CERN-LPCC-2018-03
December 12, 2018

Standard Model Physics at the HL-LHC and HE-LHC

Report from Working Group 1 on the Physics of the HL-LHC, and Perspectives at the HE-LHC

Editors:
P. Azzi[1] , *S. Farry*[2] , *P. Nason*[3] , *A. Tricoli*[4] , *D. Zeppenfeld*[5]

Contributors:
R. Abdul Khalek[6] , *J. Alimena*[7] , *N. Andari*[8] , *L. Aperio Bella*[9] , *A.J. Armbruster*[9] , *J. Baglio*[10] , *S. Bailey*[11] , *E. Bakos*[12] , *A. Bakshi*[13] , *C. Baldenegro*[14] , *F. Balli*[8] , *A. Barker*[13] , *W. Barter*[15] , *J. de Blas*[16 ,1] , *F. Blekman*[17] , *D. Bloch*[18] , *A. Bodek*[19] , *M. Boonekamp*[8] , *E. Boos*[20] , *J.D. Bossio Sola*[21] , *L. Cadamuro*[22] , *S. Camarda*[9] , *F. Campanario*[23] , *M. Campanelli*[24] , *Q.-H. Cao*[25] , *V. Cavaliere*[4] , *A. Cerri*[26] , *B. Chargeishvili*[27] , *C. Charlot*[28] , *S.-L. Chen*[29] , *T. Chen*[30] , *L. Cieri*[3] , *M. Ciuchini*[31] , *G. Corcella*[32] , *J.M. Cruz-Martinez*[33] , *M. Czakon*[34] , *A. Dainese*[1] , *N.P. Dang*[35] , *L. Darmé*[36] , *S. Dawson*[4] , *H. De la Torre*[37] , *M. Deile*[9] , *F. Deliot*[8] , *S. Demers*[38] , *A. Denner*[39] , *F. Derue*[40] , *L. Di Ciaccio*[41] , *W.K. Di Clemente*[42] , *D. Dominguez Damiani*[43] , *L. Dudko*[20] , *A. Durglishvili*[27] , *M. Dünser*[9] , *J. Ebadi*[44] , *R. B. Ferreira De Faria*[45] , *G. Ferrera*[3] , *A. Ferroglia*[99] , *T. M. Figy*[30] , *K.D. Finelli*[46] , *M.C.N. Fiolhais*[45] , *E. Franco*[47] , *R. Frederix*[48] , *B. Fuks*[49 ,50] , *B. Galhardo*[45] , *J. Gao*[51] , *J. R. Gaunt*[9] , *T. Gehrmann*[52] , *A. Gehrmann-De Ridder*[53] , *J. Giljanovic*[54] , *F. Giuli*[55] , *E.W.N. Glover*[56] , *M. D. Goodsell*[49] , *E. Gouveia*[45] , *C. Goy*[41] , *M. Grazzini*[52] , *J.F. Grosse-Oetringhaus*[9] , *P. Gunnellini*[57] , *C. Gwenlan*[11] , *L. A. Harland-Lang*[11] , *P.F. Harrison*[58] , *G. Heinrich*[59] , *C. Helsens*[9] , *C. Helsens*[9] , *M. Herndon*[60] , *O. Hindrichs*[61] , *A. Hoang*[62] , *K. Hoepfner*[34] , *J.M. Hogan*[63 ,64] , *A. Huss*[9] , *G. Isidori*[52] , *S. Jahn*[65] , *Sa. Jain*[66] , *S. P. Jones*[9] , *A.W. Jung*[13] , *H. Jung*[43] , *S. Kallweit*[67] , *D. Kar*[68] , *A. Karlberg*[52] , *M. Kerner*[52] , *M.K. Khandoga*[8] , *Hamzeh Khanpour*[69] , *S. Khatibi*[70] , *A. Khukhunaushvili*[71] , *J. Kieseler*[9] , *F. Krauss*[56] , *J. Kretzschmar*[2] , *J. Kroll*[42] , *E. Kryshen*[72] , *V.S. Lang*[43] , *L. Lechner*[73] , *C.A. Lee*[4] , *M. Leigh*[74] , *D. Lelas*[47] , *R. Les*[75] , *I. M. Lewis*[14] , *B. Li*[37] , *Y. Li*[43] , *J. Lidrych*[43] , *Z. Ligeti*[76] , *J.M. Lindert*[56] , *Y. Liu*[77] , *K. Lohwasser*[78] , *K. Long*[60] , *D. Lontkovskyi*[17] , *G. Majumder*[66] , *M. Mancini*[17] , *P. Mandrik*[79] , *M.L. Mangano*[9] , *I. Marchesini*[17] , *C. Mayer*[80] , *K. Mazumdar*[66] , *J.A. McFayden*[9] , *P. M. Mendes Amaral Torres Lagarelhos*[45] , *A.B. Meyer*[43] , *S. Mikhalcov*[81] , *S. Mishima*[82] , *A. Mitov*[83] , *M. Mohammadi Najafabadi*[44] , *M. Moreno Llácer*[9] , *M. Mulders*[9] , *M. Narain*[63] , *A. Nisati*[47] , *T. Nitta*[84] , *A. Onofre*[85] , *S. Pagan Griso*[76] , *D. Pagani*[48] , *A. Papanastasiou*[83] , *K. Pedro*[86] , *M. Pellen*[83] , *M. Perfilov*[20] , *B.A. Petersen*[9] , *M. Pierini*[9] , *J. Pires*[87] , *M.-A. Pleier*[4] , *S. Plätzer*[62] , *K. Potamianos*[43] , *S. Pozzorini*[52] , *A. C. Price*[56] , *M. Rauch*[5] , *E. Re*[9 ,88] , *L. Reina*[89] , *J. Reuter*[43] , *J. Rojo*[90] , *C. Royon*[14] , *A. Savin*[60] , *S. Sawant*[66] , *B. Schneider*[86] , *R. Schoefbeck*[73] , *M. Schoenherr*[9] , *H. Schäfer-Siebert*[5] , *M. Seidel*[9] , *T. Shears*[2] , *L. Silvestrini*[47 ,9] , *M. Sjodahl*[91] , *K. Skovpen*[17] , *D. Spitzbart*[73] , *P. Starovoitov*[92] , *C. J. E. Suster*[93] , *P. Tan*[86] , *R. Taus*[19] , *D. Teague*[60] , *K. Terashi*[94] , *J. Terron*[95] , *S. Uplap*[66] , *F. Veloso*[45] , *M. Verzetti*[52] , *M. A. Vesterinen*[58] , *V.E. Vladimirov*[58] , *P. Volkov*[20] , *G. Vorotnikov*[20] , *M. Vranjes Milosavljevic*[12] , *N. Vranjes*[12] , *E. Vryonidou*[9] , *D. Walker*[56] , *M. Wiesemann*[9] , *Y. Wu*[96] , *T. Xu*[8] , *S. Yacoob*[74] , *J. Zahreddine*[40] , *G. Zanderighi*[11] , *M. Zaro*[90] , *O. Zenaiev*[43] , *G. Zevi Della Porta*[97] , *C. Zhang*[98] , *W. Zhang*[63] , *H. Zhu*[96] , *H.L. Zhu*[96] , *R. Zlebcik*[43] , *F. N. Zubair*[9]

[1] Sezione di Padova, Istituto Nazionale di Fisica Nucleare (INFN) , [2] Department of Physics, University of Liverpool , [3] Sezione di Milano, Istituto Nazionale di Fisica Nucleare (INFN) , [4] Department of Physics, Brookhaven National Laboratory (BNL) , [5] Institut für Theoretische Physik (TP), Karlsruher Institut für Technologie (KIT) , [6] Department of Physics and Astronomy, Vrije University , [7] Ohio State University (OSU) , [8] Université Paris-Saclay , [9] European Organization for Nuclear Research (CERN) , [10] Fachbereich Physik, Eberhard Karls Universität Tübingen , [11] University of Oxford , [12] Institute of Physics Belgrade , [13] Purdue University , [14] Department of Physics and Astronomy, University of Kansas , [15] Department of Physics, Imperial College , [16] Dipartimento di Fisica, Università degli Studi di Padova , [17] Department of Physics and Astrophysics (DNTK), Vrije Universiteit Brussel (VUB) , [18] Institut Pluridisciplinaire Hubert Curien (IPHC) , [19] Rochester University , [20] Skobeltsyn Institute of Nuclear Physics (SINP), Lomonosov Moscow State University , [21] Departamento de Fisica, Universidad de Buenos Aires , [22] Department of Physics, University of Florida , [23] Universitat de Valencia-CSIC , [24] Department of Physics & Astronomy, University College London , [25] School of Physics, Peking University , [26] Department of Physics and Astronomy, University of Sussex , [27] High Energy Physics Institute (HEPI-TSU), Ivane Javakhishvili Tbilisi State University , [28] Laboratoire Leprince-Ringuet (LLR) , [29] Institute of Particle Physics, Central China Normal University (CCNU) , [30] Department of Mathematics, Statistics, and Physics, Wichita State University, Wichita , [31] Sezione di Roma Tre, Istituto Nazionale di Fisica Nucleare (INFN) , [32] Laboratori Nazionali di Frascati (LNF), Istituto Nazionale di Fisica Nucleare (INFN) , [33] Dipartimento di Fisica, Università degli Studi di Milano , [34] Rheinisch-Westfälische Technische Hochschule (RWTH) Aachen , [35] Department of Physics, University of Louisville , [36] Narodowe Centrum Badań Jądrowych (NCBJ) , [37] Department of Physics, University of Michigan , [38] Department of Physics, Yale University , [39] Department of Physics and Astronomy, Julius Maximilian University Würzburg , [40] Laboratoire de Physique Nucléaire et de Hautes Energies (LPNHE) , [41] LAPP, Université Grenoble Alpes, Université Savoie Mont-Blanc, CNRS/IN2P3, Annecy, France , [42] Department of Physics & Astronomy, University of Pennsylvania , [43] Deutsches Elektronen-Synchrotron (DESY) , [44] Institute for Research in Fundamental Sciences (IPM) , [45] Laboratorio de Instrumentacao e Fisica Experimental de Particulas (LIP) , [46] Department of Physics, Boston University , [47] Sezione di Roma, Istituto Nazionale di Fisica Nucleare (INFN) , [48] Fakultät für Physik, Technische Universität München (TUM) , [49] Sorbonne Université, CNRS, Laboratoire de Physique Théorique et Hautes Énergies, LPTHE, F-75005 Paris, France , [50] Institut Universitaire de France, 103 boulevard Saint-Michel, 75005 Paris, France , [51] Department of Physis, Shanghai Jiao Tong University , [52] Physik-Institut, Universität Zürich , [53] Departement Physik (D-PHYS), Eidgenössische Technische Hochschule (ETH) Zürich , [54] Faculty of Electrical Engineering, Mechanical Engineering and Naval Architecture in Split (FESB), University of Split , [55] Dipartimento di Fisica, Università degli Studi di Roma "Tor Vergata" , [56] Department of Physics, Durham University , [57] Fakultät für Physik, Institut für Experimentalphysik (IExpPh), Universität Hamburg , [58] Department of Physics, The University of Warwick , [59] Werner-Heisenberg-Institut, Max-Planck-Institut für Physik , [60] Department of Physics, University of Wisconsin , [61] Department of Physics and Astronomy, University of Rochester , [62] Theoretische Physik, Universität Wien , [63] Department of Physics, Brown University , [64] Bethel University, St. Paul, USA , [65] Max-Planck-Institut für Kernphysik , [66] Department of High Energy Physics (DHEP), Tata institute of fundamental research (TIFR) , [67] Dipartimento di Fisica "G. Occhialini", Università degli studi di Milano Bicocca , [68] University of the Witwatersrand , [69] Department of Physics, University of Science and Technology of Mazandaran , [70] Department of Physics, University of Tehran , [71] Cornell University , [72] Petersburg Nuclear Physics Institute (PNPI) , [73] Österreichische Akademie der Wissenschaft (OEAW) , [74] Department of Physics, University of Cape Town , [75] Department of Physics, University of Toronto , [76] Physics Division, Lawrence Berkeley National Laboratory (LBNL) , [77] Beijing Normal University (BNU) , [78] Department of Physics and Astronomy, University of Sheffield , [79] Institute of High Energy Physics (IHEP) , [80] The Henryk Niewodniczański Institute of Nuclear Physics (IFJ), Polish Academy of Sciences (PAN) , [81] Research Institute for Nuclear Problems of Byelorussian State University , [82] High Energy Accelerator Research Organization (KEK) , [83] Cavendish Laboratory, University of Cambridge , [84] Department of Physics, Waseda University , [85] Department of Mathematics, Univerisdade do Minho , [86] Fermi National Accelerator Laboratory (FNAL) , [87] CFTP, Instituto Superior Técnico, Universidade de Lisboa , [88]

Laboratoire d'Annecy-le-Vieux de Physique Théorique (LAPTH) , [89] Physics Department, Florida State University , [90] National Institute for Subatomic Physics (NIKHEF) , [91] Department of Physics, Division of Particle Physics, Lund University , [92] Ruprecht-Karls-Universität Heidelberg , [93] School of Physics, University of Sydney , [94] International Center for Elementary Particle Physics (ICEPP), University of Tokyo , [95] Departamento de Física Teórica, Universidad Autonoma de Madrid (UAM) , [96] Department of Modern Physics (DMP), University of Science and Technology of China (USTC) , [97] Department of physics, University of California (UC) , [98] Institute of High Energy Physics (IHEP), Chinese Academy of Sciences (CAS) , [99] Physics Department, New York City College of Technology, CUNY, 300 Jay Street, Brooklyn, NY 11201 USA

Abstract

The successful operation of the Large Hadron Collider (LHC) and the excellent performance ATLAS, CMS, LHCb and ALICE detectors in Run 1 and Run 2 with pp collisions at center-of-mass energies of 7, 8 and 13 TeV as well as the giant leap in precision calculations and modeling of fundamental interactions at hadron colliders have allowed an extraordinary breadth of physics studies including precision measurements of a variety physics processes. The LHC results have so far confirmed the validity of the Standard Model of particle physics up to unprecedented energy scales and with great precision in the sectors of strong and electroweak interactions as well as flavour physics, for instance in top quark physics. The upgrade of the LHC to a High Luminosity phase (HL-LHC) at 14 TeV center-of-mass energy with 3 ab^{-1} of integrated luminosity will probe the Standard Model with even greater precision and will extend the sensitivity to possible anomalies in the Standard Model, thanks to a ten-fold larger data set, upgraded detectors and expected improvements in the theoretical understanding. This document summarises the physics reach of the HL-LHC in the realm of strong and electroweak interactions and top quark physics, and provides a glimpse of the potential of a possible further upgrade of the LHC to a 27 TeV pp collider, the High-Energy LHC (HE-LHC), assumed to accumulate an integrated luminosity of 15 ab^{-1}.

Contents

1 Introduction

TO BE ADDED.

2 Theoretical tools

2.1 High Order QCD calculations

In order to exploit the full potential of the High-Luminosity LHC physics program, the high precision of experimental data must be compared to theoretical predictions that have the same accuracy. Precision calculations in QCD are typically classified into fixed-order expansions in the coupling constant α_s, and into predictions that resum large logarithms to all orders in α_s. The latter predictions are usually also subdivided into numerical parton-shower approaches and analytic resummed calculations. In recent years, a lot of work has been devoted also to matching and merging fixed-order and resummed calculations, so as to have an improved accuracy in all regions of phase space.

The technical ingredients required for a fixed-order calculations to higher order are the computation of real, virtual or, from two loop on, mixed real-virtual amplitudes, the calculations of the required master integrals and a procedure to regularize intermediate soft and collinear divergences. The first non-trivial contribution is of next-to-leading order (NLO). Here, the basis of master integrals required to compute any process at one-loop in QCD had been known for a long time, and is now available in public codes [1, 2]. In addition, two general subtraction methods (FKS [3] and CS [4]), well suited for automation, were developed. The tensor reduction of virtual amplitudes (i.e. the reduction of virtual amplitude into a combination of master integrals) proved to be the most difficult problem, since the most straightforward approaches yielded too complex results for generic processes. Around ten to fifteen years ago, a number of breakthrough ideas [5–10] led to algorithms for tensor reduction that can be automatized efficiently. With all ingredients in place, a number of tools to compute NLO cross sections for generic LHC processes in an automated way were developed. These tools are today heavily used at the LHC and will be indispensable for future phenomenology. The most widely used tools include `Gosam` [11], `MadLoop` [12], or `OpenLoops` [10]. It is interesting to note that, in the early days of NLO calculations, also slicing approaches were suggested to handle intermediate divergences (see e.g. [13]). They were however soon abandoned in favour of subtraction approaches.

While NLO tools are certainly more appropriate then LO generators to accurately predict LHC distributions, already with Run-II data it is clear that an even better perturbative accuracy is required to match the precision of data. One of the first explicit demonstration that NLO predictions are insufficient to properly describe LHC data is given by the WW cross section [14–16]. These data raised interest because of discrepancies in the extrapolated total cross section between theory and data both at 7 TeV and 8 TeV, and both at ATLAS and CMS. The comparison between data and theory was scrutinized and the discrepancy could be resolved thanks to the inclusion of NNLO corrections and thanks to the observation that the extrapolation from the fiducial to the inclusive cross section had a larger uncertainty than the estimated one. This example highlights the importance of quoting also fiducial cross sections, prior to any Monte Carlo based extrapolation, and of including NNLO corrections when comparing to high-precision data.

Current years are seeing an incredibly fast progress in the calculation of NNLO cross sections (for recent short reviews see e.g. [17, 18]). The current status is that all non-loop induced $2 \to 2$ SM processes are known at NNLO, including dijet production [19] that has the most complicated subprocess and singularity structure. This breakthrough was possible thanks to the development of new methods to compute two-loop integrals. One idea that was exploited to a great extent is the fact that polylogarithmic integrals can be calculated by means of differential equations [20–23]. Currently, the processes that are more difficult to compute are those that involve internal masses, since they lead not only to polylogarithms but also to elliptic integrals. Examples include loop-induced processes like gluon-fusion Higgs or di-Higgs production with full top-mass dependence, or gluon induced di-boson production.

With the high-luminosity run of the LHC, it will be possible to explore the Higgs transverse momentum spectrum in the region of large transverse momentum up to almost 1 TeV, where the large-m_t approximation is well-known to fail. Recently, two-loop NLO results for the Higgs transverse momen-

tum spectrum became available [24,25], but genuine NNLO predictions for these loop-induced processes are still out of reach.

The calculations of multi-scale two-loop amplitudes with massive internal particles relevant for Higgs-, top- and vector-boson production, and in particular the mathematical structures beyond multiple polylogarithms that appear in these amplitudes, is a very active area of research today [26–39]. The developments of yet new ideas and computational methods are eagerly needed. Approaches for the full numerical calculation of master integrals also exist (see e.g. [40–43] and references therein), requiring however considerable computing power as the complexity increases.

As far as the problem of canceling divergences, quite a number of different approaches are being pursued now. They can be broadly divided into subtractions methods (antenna subtraction [44], sector-improved residue subtraction [45–48], nested subtraction [49], colourful subtraction [50], projection to Born [51]) or slicing methods (q_T-subtraction [52], N-jettiness [53,54]). These methods are being scrutinized, compared, and refined, and while it is not clear yet which method will prevail, it seems realistic to assume that, by the beginning of the High-Luminosity phase, the issue of handling intermediate divergences in NNLO calculations will be considered solved. An ambitious goal is in fact to have $2 \to 3$ NNLO results by the beginning of the High-Luminosity phase. A milestone would be certainly to have NNLO prediction for ttH production. Motivated by the success at one-loop, a lot of effort is devoted to extending generalized unitarity and the OPP methods beyond one loop (see e.g. [55]). Currently, $2 \to 3$ processes is a very active subject of study, with initial results of 3-jet amplitudes starting to appear [56–62].

Beyond NNLO, two calculations of LHC processes exist today at N^{3}LO for inclusive Higgs production in the large m_t approximation [63, 64] and for VBF Higgs production in the structure function approximation [65]. The complexity of these calculations suggest that it will be very hard to extend this level of accuracy to more complicated processes, since the technology they use explicitly exploits the simplicity of these two processes, and cannot be easily extended to more complex ones.

Besides fixed-order, also resummed calculations have seen a leap in recent years. The accuracy with which particular observables can be resummed analytically reaches N^{3}LL (see e.g. [66–68]), which means three towers of logarithmic terms down compared to the leading logarithms that arise when only soft and collinear gluons are correctly accounted for. These results are properly matched to fixed order NNLO calculations.

Resummed calculations rely either on methods based upon coherent branching [69, 70] or upon Soft Collinear Effective Theory (SCET) [71]. So far, the two approaches have also been considered as complementary, in fact both methods proceed by performing a systematic expansion of the contributions to the cross section. Recent work highlights the connection between the two methods [72].

While the logarithmic accuracy of resummed calculations is impressive, the formal accuracy of parton showers is much less advanced. Unlike resummed calculations, that are targeted to a well defined cross section or distribution, Monte Carlo generators make predictions for several kind of observables at the same time, and, at present, a rigorous way to qualify their accuracy is missing. First studies in this direction can be found in [73]. Nevertheless, attempts to improve some aspects of the shower algorithms are the focus of recent work. Different approaches are taken: one can incorporate the spin-color interference into showers [74], include higher-order splitting functions and $1 \to 3$ splitting kernels into showers [75, 76] or consider different shower evolution variables [77, 78]. It seems likely that by the start of the high-Luminosity program we will have a much better theoretical control on the parton shower evolution and the uncertainty associated to it.

In the same way as the progress in NLO went hand in hand with the development of matching procedure of NLO and parton shower, a number of approaches have been suggested recently to match NNLO calculations and parton showers [79–81]. The bottleneck in these approaches is currently the fact

that they rely on a reweighing procedure that is differential in the Born phase space. Such a reweighing is possible for relatively simple processes but becomes numerically unfeasible for more complicated ones. It seems reasonable to expect that in the next years better NNLOPS approaches will be developed that do not rely on any reweighing to the NNLO. This would make it possible to have NNLOPS matched predictions to more generic processes for which an NNLO calculation is available, as is currently the case at NLO.

2.2 Electroweak corrections

Existing tools

In the last few years, the automation of EW NLO corrections has witnessed an impressive progress, for what concerns both one-loop and real-emission contributions (and their combination), by collaborations such as RECOLA [82, 83] with SHERPA [84, 85], OPENLOOPS [10] with SHERPA, GOSAM [11, 86] with either MADDIPOLE [87, 88] or SHERPA, and MadGraph5_aMC@NLO [12, 89]. For most of these codes tuned comparisons have also been published [90,91], displaying excellent agreement among them. Although the capabilities and reach in process complexity can differ from one computer program to another, recent results obtained with these tools [92–117] clearly demonstrate how automation has made it possible to tackle problems whose complexity is too great to justify their solutions through traditional approaches.

Stemming from these advances, newer applications have become possible, one of these is the computation of the so-called "complete-NLO" corrections. In general, a given scattering processes can proceed through n different coupling combinations at LO (for example, $t\bar{t}$ or dijet production receives contributions at order α_s^2, $\alpha_s\alpha$ and α^2); typically only the term with the largest power of α_s is retained, owing to the fact that $\alpha_s \gg \alpha$. This structure generates a similar one at N^{p}LO, with $n+p$ contributions, and the term "complete-NLO" means the (simultaneous) computation of all the terms entering at LO and NLO. Among the computer programs cited above, some have been employed for the computation of the complete-NLO corrections. In most of the cases the impact of the various contributions closely follows the pattern one would expect from the coupling powers, as it is the case for dijet production [106], top-pair [113] possibly with one extra jet [116]. However, there exist processes for which the coupling hierarchy is violated, or even flipped. Examples are same-sign W production with two jets [111], top-pair production in association with a W boson and four-top production [115].

Corrections beyond NLO

Similarly to the NLO case, also NNLO corrections can be organised in powers of α and α_s. At the moment, $\mathcal{O}(\alpha_s^2)$ NNLO QCD corrections have been performed for many production processes at the LHC. Conversely, complete NNLO mixed QCD-EW corrections of $\mathcal{O}(\alpha_s\alpha)$ have not been performed for any process yet. These calculations are essential in order to pin down the theoretical uncertainties for processes that at the HL- and HE-LHC will be measured with very high precision. For this reason a great effort has been already invested for achieving this result and a great progress can be expected in the next years. We recall the calculations that have been performed for the Drell-Yan production refs. [118, 119] in the resonance region via the pole approximation. For this kind of calculations two-loop amplitudes [120–124] as well regularized double-real emissions [125] are necessary ingredients. Similarly, NNLO mixed QCD-EW corrections to ggF Higgs production, which are induced by three-loop diagrams, have been estimated in ref. [126]. Further recent calculations [127] support those results and, in particular, support the fact that they can be correctly approximated via the so-called multiplicative approach. In short: NNLO mixed QCD-EW $\sim$ NLO QCD $\times$ NLO EW.

The aforementioned multiplicative approach is in general a very good approximation when the

bulk of QCD and EW corrections at NLO is dominated by soft effects and Sudakov logarithms, respectively. Given the current lack of exact NNLO mixed QCD-EW $\sim$ calculations, this approximation is already being used for estimating these corrections and/or missing higher orders uncertainties of different processes. First (N)NNLO QCD calculations including NLO EW corrections via the multiplicative approach have already appeared [63, 113, 128] and are already necessary for a correct interpretation of current data; these level of accuracy will be mandatory for more processes at HL and HE-LHC.

Besides NNLO mixed QCD-EW corrections of $\mathcal{O}(\alpha_s\alpha)$, non-negligible contributions can emerge also from large $\mathcal{O}(\alpha^n)$ corrections with $n > 1$. These typically involve final-state radiation (FSR) from massless/light particles and Sudakov logarithms. Both effects can be resummed, (at LL) via shower simulations (see the following sections on matching with QED showers and with EW showers), or analytically. In the case of Sudakov logarithms, general methods for their calculation [129, 130] and techniques for resumming them [131, 132] are already known since quite some time. Based on the study already performed for 100 TeV proton–proton collisions [133], at the HE-LHC, the resummation of Sudakov effects may be relevant in the tail of distributions.

Matching with QED shower

Fixed order computations need to be matched to parton showers, which compute a fully differential numerical resummation and implement the evolution of both QCD and EW particles from the hard scale to low scales, connecting it to the non-perturbative hadronisation stage to arrive at fully differential particle level that can be subjected to detector level data. This matching has been fully automated for NLO QCD calculations. At NLO EW accuracy only selected process specific solutions exist [134–138]. As all parton showers incorporate a joint QCD+QED parton evolution, general matching procedures, which are still lacking at the moment, will become available in the near future. This will enable precise particle level predictions that can be subjected to detector simulations for highly realistic and detailed studies.

Additionally, first solutions exist to incorporate approximate electroweak corrections in multijet merged calculations [98, 116, 139]. In these approximations, the universal nature of EW corrections in the high energy limit, where they are dominated by Sudakov-type logarithms of virtual origin, is exploited. Thus, these methods will form the cornerstone of precise particle-level predictions at large transverse momenta, which are at the basis of the increased reach of both the HL– and HE–LHC new physics search program.

Weak showers

All parton showers publicly available in the major Monte-Carlo event generators HERWIG, PYTHIA and SHERPA contain both QCD and QED splitting functions to numerically resum the respective logarithms at (N)LL accuracy. First steps towards parton showers incorporating also weak effects in their splitting functions have been taken recently [140, 141]. The now complete electroweak splitting functions suffer from their strong dependence on the helicity of the propagating parton. These parton showers, however, operate in the spin-averaged approximation, neglecting all spin-correlations. The current effort to understand the full spin dependence of the electroweak part of the evolution of partons [142, 143] in analytic resummations is complemented by efforts to keep the full colour and spin structure, including non-diagonal parts of the (now matrix-valued) evolution equations, in the parton shower community. In time for the High Luminosity Upgrade fully spin-dependent parton evolution will then be incorporated in fully differential parton shower resummations that can then produce accurate predictions for the emission probabilities of secondary weakly interacting particles and gauge bosons.

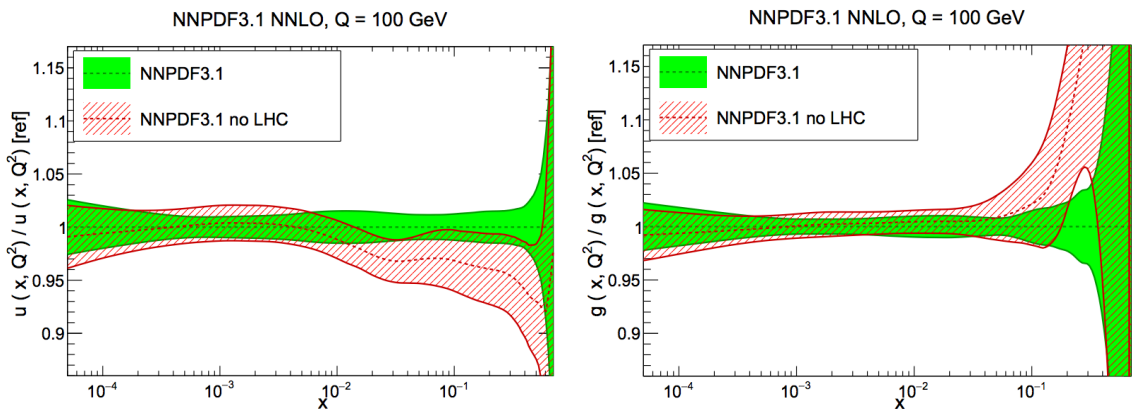

Fig. 1: Comparison of the NNPDF3.1NNLO fits with and without LHC data, normalized to the central value of the former at $Q = 100$ GeV. We show the up quark (left) and the gluon (right plot). The bands indicate the 68% confidence level PDF uncertainty.

2.3 PDF calculations and tools

At the HL-LHC, a precise knowledge of the quark and gluon structure of the proton will be essential for many analyses. These include the profiling of the Higgs boson sector [144], direct searches for new heavy BSM states [145], indirect BSM searches by *e.g.* means of the SMEFT [146], and the measurement of fundamental SM parameters such as the W boson mass [147], the Weinberg mixing angle [148] or the strong coupling constant [149] and its running.

In this section we briefly review the PDF tools that will be used in this Report for the studies of the SM chapter. We will also highlight those aspects of modern PDF fits that are more relevant for studies at the HL-LHC. At the end of this section we will provide some perspectives about the role of PDFs at the HE-LHC. We stress that this document is not intended to be a review of recent developments on PDFs, and we refer the reader to [150–152] and reference therein, for further details in this sense.

The studies presented in this Report will be based mostly on the PDF4LHC15 set [153], constructed from the statistical combination and subsequent reduction [154–156] of the CT14 [157], MMHT14 [158], and NNPDF3.0 [159] global analyses. The PDF4LHC15 set is interfaced to matrix-elements calculators and Monte Carlo shower programs by means of the `LHAPDF6` package [160].

Quantifying the impact of LHC measurements.

In recent years, one of the main developments in global PDF fits has been the increasingly significant role played by LHC processes in providing stringent PDF constraints. The combination of high precision LHC data with state-of-the art NNLO theory calculations for such hadronic processes as top-quark pair production [161], the transverse momentum spectrum of Z bosons [162], direct photon production [163], and inclusive jet production [164] is having an important impact on precision PDF fits. To illustrate this, in Fig. 1 we compare the recent NNPDF3.1 fit [165] with and without the LHC data at $Q = 100$ GeV for the up quark and gluon PDFs. The marked impact of the LHC data for $x \gtrsim 0.005$ can be observed both for central values and for the PDF uncertainties. It is of particular note that only Run I data has been included in these fits. Thus, it is clear that the addition of data from Run II and III first and then from the HL-LHC, for which the precision and reach will be greatly increased, should lead to further improvements in the determination of the proton structure. In a subsequent section of this report, we will quantify the impact of HL-LHC measurements, demonstrating that a significant reduction can be expected and providing a public PDF set including the expected constraints from the final HL-LHC

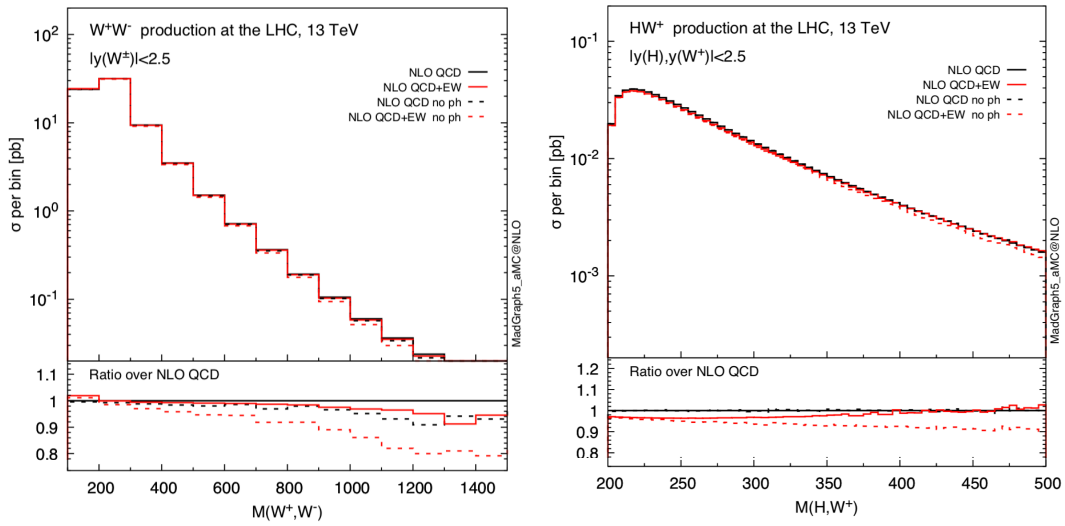

Fig. 2: Photon-initiated contributions partially cancel the NLO EW corrections in the TeV region, as shown for the case of W^+W^- production (left) and hW^+ production (right plot) at 13 TeV.

dataset.

Fast interfaces to (N)NLO calculations

To avoid the direct evaluation of the lengthy (N)NLO hadronic cross sections during the fit itself, a method of fast interfaces is generally applied, whereby the CPU time intensive part of the higher–order calculation is pre–computed once using a complete interpolation basis for the input PDFs. For a number of years, the `APPLgrid` [166] and `Fastnlo` [167] tools have been available for a range of NLO processes. The former is interfaced to the `MCFM` [168] and `NLOjet++` [169] programs. More recently, the `aMCfast` interface [170] to `MadGraph5_aMC@NLO` [12] has also been developed. Results within the `Fastnlo` framework for differential top quark production at NNLO are already available [171, 172], while work is ongoing within the `APPLfast` project to extend the `FastNLO` and `APPLgrid` technology to NNLO. This will be interfaced by default to the `NNLOJET` program [164], but will be reusable for other theory codes. Thus, for future PDF fits, relevant to HL and HE-LHC running, fast interface implementations of NNLO theory calculations are expected to be the standard.

Theoretical uncertainties

Given the high precision expected for HL-LHC data, it will be crucial to include all sources of experimental, methodological, and theoretical uncertainties associated with PDFs in order to ensure robust predictions. An important issue in this context is to estimate the theoretical uncertainties in PDFs due to missing higher orders (MHOU) in the perturbative expansion for the theory prediction [173], which are so far ignored in all global fits. There is by now some evidence that MHOUs can be comparable, if not larger, than the nominal PDF uncertainties based on the propagation of experimental and methodological uncertainties. In this context, HL-LHC projections should ideally be based on PDFs that consistently account for MHOUs in addition to other sources of uncertainties.

To keep such uncertainties to a minimum, global PDF fits will need to include higher-order perturbative corrections either at fixed-order or at all-orders using some form of resummation. In the former case, encouraging recent progress with N^{3}LO splitting functions [174] suggest that an (approximate) N^{3}LO fit might be within the reach of the HL-LHC era, to match the precision of partonic cross-sections

for processes such as Higgs production in gluon fusion [63,175]. In the latter case, one can use threshold (BFKL) resummation [176, 177] to reduce theoretical uncertainties at the large-x (small-x) kinematic regions. Indeed, several state-of-the-art predictions for LHC processes include threshold resummation, such as for example top quark pair production [178].

Electroweak effects and photon-initiated contributions

The enhanced coverage of the TeV region at the HL-LHC requires not only higher-order QCD corrections to be account for, but also electroweak ones, which can be enhanced due to Sudakov logarithms [179]. In the context of PDF studies, there are two main considerations to take into account. First of all, exploiting the constraints from the HL-LHC measurements for PDF fits will require systematically accounting for NLO EW corrections. Secondly, PDFs with QED effects and thus with photon-initiated contributions should become the baseline. It has now been demonstrated [180, 181] (see [182] for a recent implementation within a global fit) that the photon PDF can be determined with percent–level uncertainties and carry up to $\simeq 0.5\%$ of the proton's momentum. For certain processes, in the TeV region the photon-initiated contributions can have a comparable size but opposite sign to the NLO virtual EW corrections, and therefore it is crucial to include both consistently. This is illustrated in Fig. 2 in the specific cases of W^+W^- and hW^+ production at 13 TeV. A more detailed discussion of EW corrections for HL-LHC studies is presented later in the report.

Perspectives at the High Energy LHC

At a centre-of-mass energy of $\sqrt{s} = 27$ GeV, a number of novel phenomena are expected to arise, due to the increased phase space available. Much of this has already been discussed in the context of the Future Circular Collider (FCC) studies at $\sqrt{s} = 100$ TeV [133,183]. To begin with, as illustrated in Fig. 3, when going to higher energies one becomes more sensitive to the small-x region, even for electroweak-scale observables, implying that BFKL resummation effects could become relevant.

Indeed, for $M_X \simeq 100$ GeV the NNPDF3.1sx results [177] at NNLO and at NNLO+NLLx for the gg luminosities are found to differ at the $\simeq 5\%$ level at the HE–LHC. In [184] a detailed study of SM Higgs boson production via gluon fusion has been performed, consistently including BFKL resummation in the PDFs (via [177]) and coefficient functions. The role of the former is found to be dominant, and while the impact is mild at the LHC, for the HE–LHC a larger increase is seen relative to the N^{3}LO result with fixed–order NNLO PDFs, that lies outside the fixed–order PDF uncertainty bands, see Fig. 3 (right). This highlights the important role such effects will play at high energies and precision.

Another effect that might become relevant at the HE-LHC are the electroweak PDFs [142, 185] from the resummation of large collinear logarithms of the masses of the W and Z bosons, which become effectively massless at high energies. Related to this is the top quark PDF, which can be (and is) straightforwardly generated within the standard PDF framework. When included with a suitably matched flavour scheme this may provide a more accurate description of processes involving top quarks [186,187]. In addition, at $\sqrt{s} = 27$ TeV, knowledge of the small-x PDFs will be also required for the modeling of soft and semi-hard QCD dynamics in Monte Carlo event generators [133, 188]. In turn, an improved understanding of the PDFs in the ultra-low-x regime will have implications in high-energy astrophysics, for processes such as cosmic ray detection and for signal and background event rates in neutrino telescopes [189].

2.4 Effective Field Theory calculations and tools

State of the art

The success of the Standard Model Effective Theory (SMEFT) programme at the LHC relies on the availability of public tools for calculations in this framework. Among the most important of these are

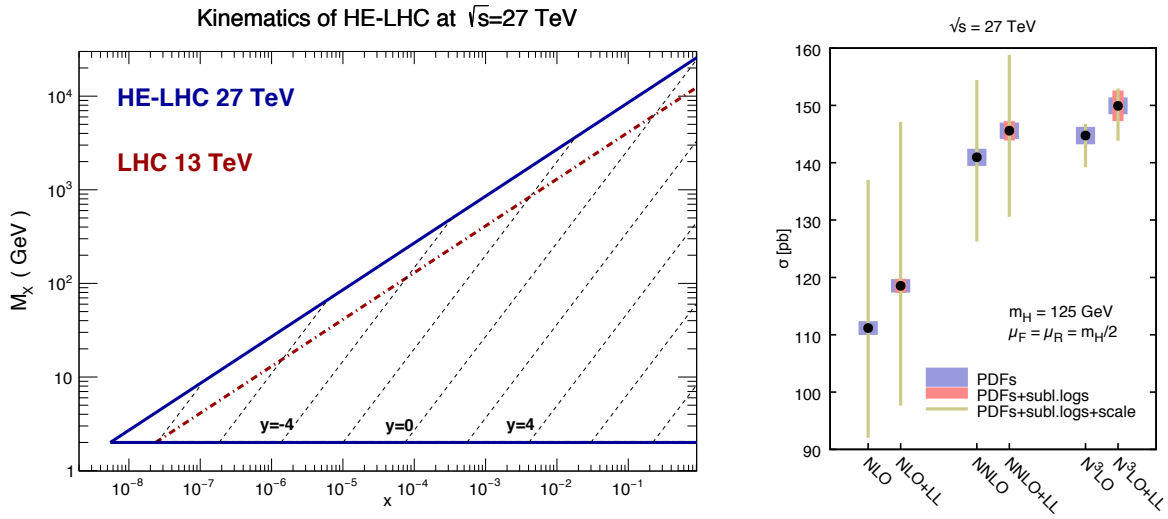

Fig. 3: Left: kinematic coverage of the HE-LHC at $\sqrt{s} = 27$ TeV compared to 13 TeV. Right: the Higgs cross section at the HE-LHC, for different orders and with/without (LL) low–x resummation, and with uncertainty bands from PDF, subleading logarithms, and scale variations [184].

Monte Carlo (MC) tools for providing realistic predictions for collider processes both for phenomenological studies and experimental analyses. In this respect, significant efforts are being made to implement the effects of dimension-6 operators in MC event generators. Concerning Leading Order (LO) predictions, recent progress includes SMEFTSIM, a complete implementation of the dimension-6 operators in the Warsaw basis [190], an alternative implementation of the Warsaw basis in the R_ξ gauge [191], DIM6TOP, an implementation of top quark operators under various flavour assumptions [192] and the Higgs Effective Lagrangian (HEL) [193] implementation of SILH basis operators. Complementary to SMEFT implementations, there also exist several models of anomalous couplings such as the Higgs Characterisation [194–196] and BSM Characterisation models [197]. These models are all made available in the Universal FeynRules Output (UFO) format that can be imported into general purpose Monte Carlo tools, such as MG5_AMC@NLO or SHERPA, to generate events and interface them to parton shower generators (PS). A powerful aspect of this workflow is that, once implemented, the model is generic enough to enable event generation for any desired process.

Implementations of particular processes in the presence of dimension-6 operators exist also in other frameworks. An example is the weak production of Higgs in association with a vector boson in POWHEG based on the NLO computation of [198], the implementation of Higgs pair production in the EFT in HPAIR (including approximate NLO corrections) [199] and in HERWIG [200, 201]. Two well-known tools for calculating cross sections for Higgs production via gluon fusion including higher order QCD corrections, HIGLU [202, 203] and SUSHI [204], can also include the effects of modified top and bottom quark Yukawas and the dimension-5 Higgs-gluon-gluon operator. The latter code also permits event generation at NLOQCD+PS accuracy via AMCSUSHI [205] including modified top and bottom quark Yukawa couplings. For a variety of processes with electroweak and Higgs bosons in the final state (VBF H, W and Z production, weak boson pair production, vector-boson-scattering processes, triboson production) the VBFNLO program [206, 207] provides NLO QCD corrections together with implementations of dimension-6 operators and, in the case of VBS and triboson production, dimension-8 operators.

There are also EFT-specific tools providing a number of useful interfaces and calculations. EHDECAY [208, 209] is a package for the calculation of Higgs boson branching fractions including SMEFT

effects parametrised by SILH basis operators. The freedom of basis choice in the SMEFT implies that arbitrarily many equivalent descriptions of the model can be formulated. This has important consequences for the development of EFT tools given that any numerical implementation of EFT effects requires choosing a specific basis. A SMEFT basis translation tool, ROSETTA [197], can be used to numerically transform points in parameter space from one basis to another. It adopts the SLHA convention for model parameter specification and provides an interface to Monte Carlo event generation tools through the aforementioned BSMC model. Furthermore, additional interfaces exist to other programs such as EHDECAY, internal routines testing compatibility of Higgs signal-strength and EW precision measurements as well as providing predictions for di-Higgs production cross sections in the SMEFT. ROSETTA provides SMEFT basis-independent access to these functionalities. A related tool is DEFT [210], a python code that can check if a set of operators forms a basis, generate a basis and change between bases. A similar implementation based on FeynRules is ALLYOURBASES, that performs the reduction of an arbitrary dimension-6 operator into the Warsaw basis operator set. Efforts are also underway to establish a common format for the Wilson coefficients [211], which will allow interfacing various programs computing the matching and running of the operators such as DIM6TOOLS [212] and WILSON [213]. A public fitting framework that can be used to obtain constraints on the EFT is HEPFIT, which is based on the Bayesian Analysis Toolkit, and includes Higgs and electroweak precision observables.

Future Developments

There is significant progress in computing NLO QCD corrections for the EFT, in both the top and Higgs sector [198, 214–221]. This progress, now on a process-by-process basis, will eventually lead to a full automation of QCD corrections for the SMEFT. As experimental measurements become increasingly systematics dominated, the importance of higher order calculations grows. The complete implementation of dimension-6 operators at NLO, including some flavour symmetry assumptions, is in preparation. This implementation will enable the computation of NLO-QCD corrections to any tree-level process, bringing the Monte Carlo automation to the same level as the Standard Model.

Another direction in which progress is expected over the coming years is the computation of weak corrections in the SMEFT. A small sample of computations has been done, e.g. weak corrections to Higgs production and decay due to top quark loops [222] and due to modified trilinear Higgs coupling [223–225] as well as Higgs and Z-boson decays [226–231]. Due to the behaviour of the Sudakov logarithms, weak corrections are typically important for high transverse momentum regions. Therefore at HE/HL-LHC their impact is expected to be enhanced. It can be expected that the recent progress on a process-by-process basis will eventually lead to the automation of the computation of weak loops in the EFT, as in the Standard Model.

Finally progress is expected in linking tools which compute the running and mixing of the operators with Monte Carlo tools. This will allow the automatic computation of cross-sections and differential distributions taking into account the mixing and running of the operator coefficients.

3 Experimental environment at HL-LHC

3.1 Analysis methods, particle reconstruction and identification

Different approaches have been used by the experiments and in theoretical prospect studies, hereafter named projections, to assess the sensitivity in searching for new physics at the HL-LHC and HE-LHC. For some of the projections, a mix of the approaches described below is used, in order to deliver the most realistic result. The total integrated luminosity for the HL-LHC dataset is assumed to be 3000 fb^{-1} at a center-of-mass energy of 14 TeV. For HE-LHC studies the dataset is assumed to be 15 ab^{-1} at a center-of-mass of 27 TeV. The effect of systematic uncertainties is taken into account based on the studies performed for the existing analyses and using common guidelines for projecting the expected improvements that are foreseen thanks to the large dataset and upgraded detectors, as described in Section 3.2.

Detailed-simulations are used to assess the performance of reconstructed objects in the upgraded detectors and HL-LHC conditions, as described in Sections 3.1.1,3.1.2. For some of the projections, such simulations are directly interfaced to different event generators, parton showering (PS) and hadronisation generators. Monte Carlo (MC) generated events are used for standard model (SM) and beyond-the-standard-model (BSM) processes, and are employed in the various projections to estimate the expected contributions of each process.

Extrapolations of existing results rely on the existent statistical frameworks to estimate the expected sensitivity for the HL-LHC dataset. The increased center-of-mass energy and the performance of the upgraded detectors are taken into account for most of the extrapolations using scale factors on the individual processes contributing to the signal regions. Such scale factors are derived from the expected cross sections and from detailed simulation studies.

Fast-simulations are employed for some of the projections in order to produce a large number of Monte Carlo events and estimate their reconstruction efficiency for the upgraded detectors. The upgraded CMS detector performance is taken into account encoding the expected performance of the upgraded detector in DELPHES [232], including the effects of pile-up interactions. Theoretical contributions use DELPHES [232] with the commonly accepted HL-LHC card corresponding to the upgraded ATLAS and CMS detectors.

Parametric-simulations are used for some of the projections to allow a full re-optimization of the analysis selections that profit from the larger available datasets. Particle-level definitions are used for electrons, photons, muons, taus, jets and missing transverse momentum. These are constructed from stable particles of the MC event record with a lifetime larger than 0.3×10^{-10} s within the observable pseudorapidity range. Jets are reconstructed using the anti-k_t algorithm [233] implemented in the Fastjet [234] library, with a radius parameter of 0.4. All stable final-state particles are used to reconstruct the jets, except the neutrinos, leptons and photons associated to W or Z boson or τ lepton decays. The effects of an upgraded ATLAS detector are taken into account by applying energy smearing, efficiencies and fake rates to generator level quantities, following parameterisations based on detector performance studies with the detailed simulations. The effect of the high pileup at the HL-LHC is incorporated by overlaying pileup jets onto the hard-scatter events. Jets from pileup are randomly selected as jets to be considered for analysis with $\sim 2\%$ efficiency, based on studies of pile-up jet rejection and current experience.

3.1.1 ATLAS and CMS performance

The expected performance of the upgraded ATLAS and CMS detectors has been studied in detail in the context of the Technical Design Reports and subsequent studies; the assumptions used for this report and a more detailed description are available in Ref. [235, 236]. For CMS, the object performance in the central region assumes a barrel calorimeter aging corresponding to an integrated luminosity of

$1000\ \text{fb}^{-1}$.

The triggering system for both experiments will be replaced and its impact on the triggering abilities of each experiment assessed; new capabilities will be added, and, despite the more challenging conditions, most of the trigger thresholds for common objects are expected to either remain similar to the current ones or to even decrease [237, 238].

The inner detector is expected to be completely replaced by both experiments, notably extending its coverage to $|\eta| < 4.0$. The performance for reconstructing charged particles has been studied in detail in Ref. [239–241].

Electrons and photons are reconstructed from energy deposits in the electromagnetic calorimeter and information from the inner tracker [242–245]. Several identification working points have been studied and are employed by the projection studies as most appropriate.

Muons are reconstructed combining muon spectrometer and inner tracker information [246, 247].

Jets are reconstructed by clustering energy deposits in the electromagnetic and hadronic calorimeters [242, 243, 248] using the anti-k_T algorithm [233]. B-jets are identified via b-tagging algorithms. B-tagging is performed if the jet is within the tracker acceptance ($|\eta| < 4.0$). Multivariate techniques are employed in order to identify $b-$jets and $c-$jets, and were fully re-optimized for the upgraded detectors [239, 241]. An 70% $b-$jet efficiency working point is used, unless otherwise noted.

High p_T boosted jets are reconstructed using large-radius anti-k_T jets with a distance parameter of 0.8. Various jet substructure variables are employed to identify boosted W/Z/Higgs boson and top quark jets with good discrimination against generic QCD jets.

Missing transverse energy is reconstructed following similar algorithms as employed in the current data taking. Its performance has been evaluated for standard processes, such as top pair production [239, 249].

The addition of new precise-timing detectors and its effect on object reconstruction has also been studied in Ref. [245, 250], although its results are only taken into account in a small subset of the projections in this report.

3.1.2 LHCb

The LHCb upgrades are shifted with respect to those of ATLAS and CMS. A first upgrade will happen at the end of Run 2 of the LHC, to run at a luminosity five times larger ($2 \times 10^{33}\text{cm}^{-2}\text{s}^{-1}$) in LHC Run 3 compared to those in Runs 1 and 2, while maintaining or improving the current detector performance. This first upgrade (named Upgrade I) will be followed by by the so-called Upgrade II (planned at the end of Run 4) to run at a luminosity of $\sim 2 \times 10^{34}\text{cm}^{-2}\text{s}^{-1}$.

The LHCb MC simulation used in this document mainly relies on the PYTHIA 8 generator [251] with a specific LHCb configuration [252], using the CTEQ6 leading-order set of parton density functions [253]. The interaction of the generated particles with the detector, and its response, are implemented using the GEANT toolkit [254, 255], as described in Ref. [256].

The reconstruction of jets is done using a particle flow algorithm, with the output of this clustered using the anti-kT algorithm as implemented in Fastjet, with a distance parameter of 0.5. Requirements are placed on the candidate jet in order to reduce the background formed by particles which are either incorrectly reconstructed or produced in additional pp interactions in the same event.

Concerning the increased pile-up, different assumptions are made, but in general the effect is assumed to be similar to the one in Run 2.

3.2 Treatment of systematic uncertainties

It is a significant challenge to predict the expected systematic uncertainties of physics results at the end of HL-LHC running. It is reasonable to anticipate improvements to techniques of determining systematic uncertainties over an additional decade of data-taking. To estimate the expected performance, experts in the various physics objects and detector systems from ATLAS and CMS have looked at current limitations to systematic uncertainties in detail to determine which contributions are limited by statistics and where there are more fundamental limitations. Predictions were made taking into account the increased integrated luminosity and expected potential gains in technique. These recommendations were then harmonized between the experiments to take advantage of a wider array of expert opinions and to allow the experiments to make sensitivity predictions on equal footing [235, 236]. For theorists' contributions, a simplified approach is often adopted, loosely inspired by the improvements predicted by experiments.

General guide-lining principles were defined in assessing the expected systematic uncertainties. Theoretical uncertainties are assumed to be reduced by a factor of two with respect to the current knowledge, thanks to both higher-order calculation as well as reduced PDF uncertainties [257]. All the uncertainties related to the limited number of simulated events are neglected, under the assumption that sufficiently large simulation samples will be available by the time the HL-LHC becomes operational. For all scenarios, the intrinsic statistical uncertainty in the measurement is reduced by a factor $1/\sqrt{\mathrm{L}}$, where L is the projection integrated luminosity divided by that of the reference Run 2 analysis. Systematics driven by intrinsic detector limitations are left unchanged, or revised according to detailed simulation studies of the upgraded detector. Uncertainties on methods are kept at the same value as in the latest public results available, assuming that the harsher HL-LHC conditions will be compensated by method improvements.

The uncertainty in the integrated luminosity of the data sample is expected to be reduced down to 1% by a better understanding of the calibration methods and their stability employed in its determination, and making use of the new capabilities of the upgraded detectors.

In addition to the above scenario (often referred to as "YR18 systematics uncertainties" scenario), results are often compared to the case where the current level of understanding of systematic uncertainties is assumed ("Run 2 systematic uncertainties") or to the case of statistical-only uncertainties.

3.3 Precision Luminosity

3.3.1 Motivation

Measurements of production cross sections provide fundamental tests of theoretical predictions. Ultimate precision both of the experimental measurements and the theoretical predictions is required in order to determine fundamental parameters of the standard model and to constrain or discover beyond-the-standard-model phenomena. At the LHC, the precision of cross section measurements is limited by the uncertainty of the integrated luminosity, currently about 2%. The impact of all other experimental uncertainties combined is smaller than $\sim$ 1% (2–3%) for Drell-Yan ($t\bar{t}$) cross section measurements, respectively [258, 259]. For the High-Luminosity LHC (HL-LHC) [260], significant improvements of the luminosity measurement are being planned. A target uncertainty of 1% has been set, and this is also assumed for many of the results presented in this report. Such improvement is expected to be achieved by combination of improved luminosity detector instrumentation, currently in the design phase, and refined analysis techniques, rapidly developing during the analysis of Run-II data. In the following, we provide a short description of the general plan towards the 1% target for the integrated luminosity at the HL-LHC.

3.3.2 *Van der Meer Scans*

At hadron colliders, the precision of theoretical predictions for inclusive cross sections, e.g. for Z/γ^* production, is limited by the knowledge of the parton density functions (PDFs) in the proton, and the uncertainty is of the order of 3–5% [261]. A more precise, and purely experimental method to determine the luminosity is based on the Van der Meer (VdM) scan technique [262]. In VdM scans, beam axes are moved in the transverse planes, x and y, across each other such that the beam overlap integral can be determined. From the measured overlap integral, and the beam currents, the instantaneous luminosity during the VdM scan is determined [263].

In practice, VdM scan data are typically recorded with a small number of low pile-up bunches well separated in time, with special interaction-region optics optimised for the measurement of the luminous-region parameters [263–265], and with the bunch intensity lowered to about 3/4 of that during physics runs so as to reduce beam-beam biases while retaining adequate statistics in the luminometers. To transfer the luminosity information from VdM scans to high-PU operation, rate measurements are performed during the VdM scan, in several detectors. The absolute scale, i.e. the relation between the measured rate in a given detector and the luminosity measurement is a detector-specific calibration constant, usually referred to as visible cross section σ_{vis}, relating the measured event rate $\mathrm{d}N/\mathrm{d}t$ to the instantaneous luminosity through the relation $\mathrm{d}N/\mathrm{d}t = L \cdot \sigma_{\text{vis}}$. The integrated luminosity for a complete data taking period, e.g. a full year of data taking is then obtained by continuous rate measurements throughout the year. The integrated normalized rate measurement then corresponds to the integrated luminosity.

3.3.3 *Systematic Uncertainties*

The uncertainty in the integrated luminosity consists of three components [265, 266]: the absolute-scale uncertainty, i.e. that on the measured visible cross-sections extracted from the VdM-scan analysis; the calibration-transfer uncertainty, which affects the extrapolation of the visible cross-section from the low pile-up, low luminosity VdM regime to the high pile-up, high luminosity physics regime; and the stability uncertainty, that arises from possible time-dependencies and degradations of the detector response affecting the rate measurement over time. Improved analysis techniques, better detectors and extended data takings dedicated to precision luminosity measurements are required to reduce the current uncertainty towards the 1% goal.

Absolute Scale Uncertainty

Dominant uncertainties in the luminosity scale arise from the modeling of, and the potential non-linear correlations between, the horizontal and vertical beam profiles; from inconsistencies between equivalent visible cross-section measurements carried out during the same calibration session or using different luminometers; from the absolute displacement scale of the beams during the scans; and from beam-orbit stability. In Run 2, these and other uncertainties have been reduced using refined methods and dedicated additional data have been recorded for such specific purposes. Improvements of the uncertainty can be achieved by combination of different complementary approaches, of results obtained using different detectors, and of datasets obtained from different VdM scans.

An alternative technique, complementary to VdM scans, was established by the LHCb experiment [267]. The shape of a single beam is measured as the distribution of beam-gas interactions. For this purpose a gas is injected into the interaction region during the VdM fill. The combination of VdM-scan and beam-gas imaging measurements leads to further reduction of the uncertainty, at least for LHCb, thanks to the exquisite performance of the VELO vertex detector.

Calibration-transfer Uncertainty

In the HL-LHC area, the VdM calibration will typically be carried out under similar conditions as in Run 2, i.e. at a pile-up level of about 0.5 interactions per bunch crossing, and with a luminosity of a few Hz/microbarn. In contrast, the physics running during the HL-LHC, will be characterized by pile-up parameters of up to 200 interactions per bunch crossing, and by average instantaneous luminosities of 50 Hz/nb, two to three times the peak instantaneous luminosity achieved so far. This will lead to an increase of the uncertainties associated with non-linearities in luminometer response. Most luminosity detectors for HL-LHC are still being designed. Drawing on Run 1 and Run 2 experience with precision luminosity measurements, the design of the future detectors aims to reduce the associated systematic uncertainties. HL-LHC detectors are required to behave linearly over several orders of magnitude in their track, energy or hit rate measurements, with residual non-linearities that are reproducible and monitorable. Special runs with scans at intermediate instantaneous luminosity can be used to pin down nonlinear behaviour further.

Long-term stability and consistency of luminosity measurements

In the past, one obvious way to determine stability and linearity effects has been to devise and compare the luminosity measurements by several detectors, using different technologies, with uncorrelated systematics. Since 2016, experiments started to exploit so-called emittance scans. These are short VdM scans (duration of minutes) performed at standard physics optics and currents, regularly at the beginning and at the end of fills [268–271]. While the emittance scans are not primarily designed for the precision determination of σ_{vis}, trends over time, or as a function of instantaneous luminosity, can be used to determine stability effects, such as aging, independently for each given detector. The combination of emittance scans and of rate comparisons between redundant and independent detector systems has been successfully used to discover and control drifts and trends throughout Run-2, the longest LHC data-taking period so far, during which 150 fb^{-1} worth of data were recorded. As a result, the uncertainty in the integrated luminosity in recent years remained at around 2-2.5% even though the pile-up extrapolation range and the duration of the integration periods increased significantly.

Recent Ideas

Additional methods are being discussed among luminosity experts of the LHC experiments and machine. One method recently developed is to use the rate measurement of $\text{Z} \to \mu\mu$ production [272]. This is a high-rate physics process with in-situ calibration capabilities. Luminosity and Z boson rate are experimentally related through the following formula: $\sigma_{\text{Z}} = N_{\text{Z}}/(L \times \epsilon_{\text{Z}\to\mu\mu})$ where N_{Z} is the number of reconstructed Z bosons, L the integrated luminosity, and $\epsilon_{\text{Z}\to\mu\mu}$ the $\text{Z} \to \mu\mu$ event reconstruction efficiency. If $\epsilon_{\text{Z}\to\mu\mu}$ and L are known, then the fiducial Z boson production cross section σ_{Z} can directly be determined from the measured event rate. To minimize the uncertainties associated with luminometer non-linearities and long-term stability, the fiducial Z boson cross section is measured from data recorded during an extended proton–proton production run at low pileup. This run should be close in time to one or two extended VdM scans. The efficiency $\epsilon_{\text{Z}\to\mu\mu}$ can be determined in situ, using the tag-and-probe method on the same event sample [272]. Once the cross section is measured at sub-percent level precision, the continuous rate measurement can be used to transfer the calibration to the high pileup dataset. The integrated luminosity will be given by the total number of produced Z bosons, corrected by the time-integrated muon identification efficiency with an uncertainty consisting of the absolute scale uncertainty from the VdM scan (or, in LHCb, beam-gas imaging scan), and a remaining uncertainty in the pileup dependency of the muon identification efficiency.

3.3.4 Conclusions Towards HL-LHC

The aim for HL-LHC is to measure luminosity with substantially improved precision. This aim can be achieved by combination of three ingredients:

1. High precision luminosity detectors are needed to provide high-granularity bunch-by-bunch luminosity measurements, with very good linearity and stability.

2. Advanced, multiple and redundant VdM scans and refined VdM analysis techniques can lead to substantial improvements.

3. Novel techniques, such as the measurement of fiducial Z boson production rates exploiting in-situ efficiency determination, provide handles for advancement of the integrated luminosity uncertainty towards the 1% target.

In order to achieve these goals during HL-LHC, a suite of tests and proof-of-concept measurements is being developed which should be carried out already during Run-3.

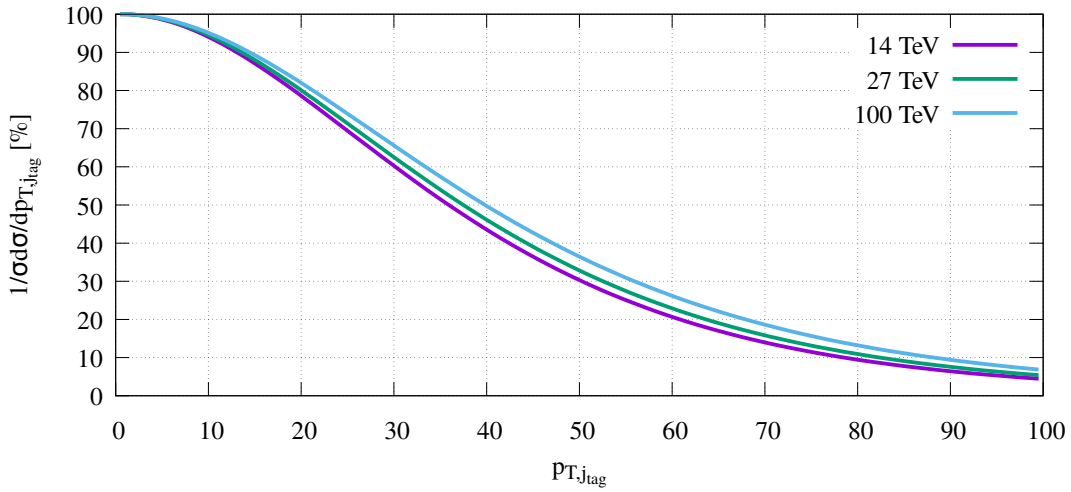

Fig. 4: Total VBF cross section after imposing a p_{T} cut on the two hardest jets of $p_{\mathrm{T,j_{tag}}}$ for three different collider energies. The results shown here are computed at LO.

4 Electroweak processes

4.1 Vector boson fusion processes

The common setup for this chapter is taken from the YR4 [144]. For completeness we repeat the relevant parameters here. The gauge boson masses and widths are set to

$$m_W = 80.385 \text{ GeV}, \qquad \Gamma_W = 2.085\text{GeV}. \tag{1}$$

$$m_Z = 91.1876 \text{ GeV}, \qquad \Gamma_Z = 2.4952 \text{ GeV}. \tag{2}$$

and the Fermi constant is

$$G_F = 1.16637 \cdot 10^{-}5 \text{ GeV}^{-2}. \tag{3}$$

We always assume the Higgs to be in the narrow width approximation and use the Higgs mass

$$m_H = 125 \text{ GeV}. \tag{4}$$

We use the parton distribution function PDF4LHC15_nnlo_100_pdfas and set the central renormalisation and factorisation scale to $\mu_0 = m_W$ unless otherwise specified.

In this chapter we discuss the prospects of studying vector boson fusion Higgs production at the HL-LHC and the HE-LHC respectively. In particular we investigate how hard and how forward the two tag jets are expected to be at 27 TeV. We also discuss the efficiency of VBF cuts, and report fiducial cross sections and differential distributions for a set of typical analysis cuts.

We also report on the quality of the VBF approximation, in particular when extra jet activity in addition to the two tag jets are required.

4.1.1 Detector requirements

In this section we discuss the impact of p_{T} and rapidity cuts on the two hardest tag jets. VBF production is characterized by two hard and forward jets. The requirement of two such jets can significantly reduce

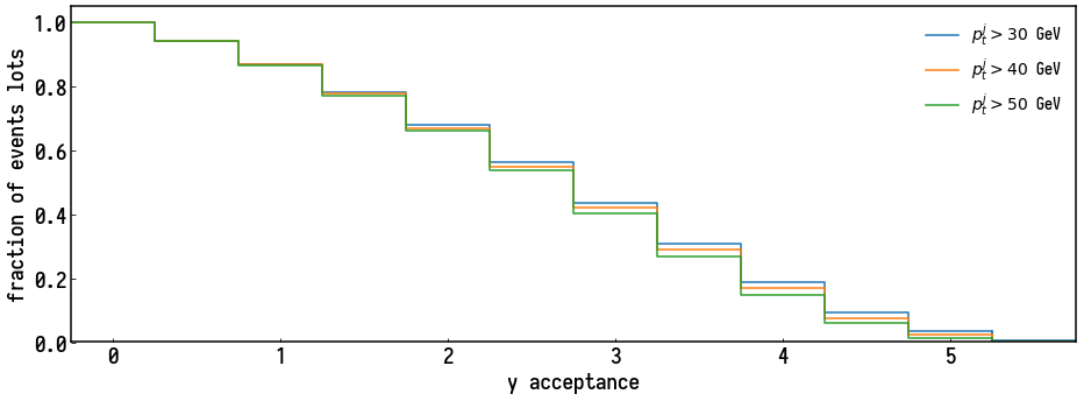

Fig. 5: Fraction of events lost as a function of the rapidity acceptance of the detector at a collider energy of $\sqrt{s} = 27$ TeV. Results shown for three different tagjet transverse momentum cuts. The results shown here are computed at LO.

the QCD induced background along with the electroweak production stemming from s-channel production. The transverse hardness of the VBF jets is fundamentally set by the mass scale of the virtual vector bosons. It is therefore expected that the jet spectrum is not very sensitive to the collider centre-of-mass energy, and in particular that the jets do not get appreciably harder when increasing the energy.

In figure 4 we show the total VBF cross section that survives the cut on the transverse momentum of the two tag jets for the three collider energies 14, 27, and 100 TeV. As can be seen, the cross section drops rapidly as the cut is increased. In particular, at 27 TeV, there is a drop from roughly 60% for $p_{T,tag} > 30$ GeV to roughly 30% for $p_{T,tag} > 50$ GeV. It will therefore be of great importance to the VBF program to be able to keep the jet definition not too hard.

Given that the two tag jets tend to be forward in the detector volume, it is of interest to study how many jets are lost above a certain rapidity threshold. In figure 5 we show the fraction of events with $\max\left|y_{j_1}\right|, \left|y_{j_2}\right|$ above some threshold at $\sqrt{s} = 27$ TeV for various jet p_T definitions. As can be seen from the plot, about 20% of the cross section has $\max\left|y_{j_1}\right|, \left|y_{j_2}\right| > 4$. For comparison, this number is $\sim 5\%$ at 14 TeV. Additionally we find that the number increases to $\sim 30\%$ when imposing the cuts of section 4.1.3. Hence, in order to maximize the potential of VBF analyses at the HE-LHC it will be crucial that the detectors have a rapidity reach beyond 4.0.

4.1.2 HL-LHC

In this section we present fiducial cross sections and differential distributions for VBF production with a centre of mass energy of $\sqrt{s} = 14$ TeV. The VBF cuts are the same as used in the YR4. We require two anti-k_{T} jets with $R = 0.4$ and

$$p_{\mathrm{T}}^j > 20 \text{ GeV}, \qquad |y_j| < 5.0, \qquad |y_{j_1} - y_{j_2}| > 3.0, \qquad M_{jj} > 130 \text{ GeV}. \tag{5}$$

The requirement on the rapidity separation and invariant mass significantly reduces background contributions to the process $pp \to Hjj$.

Fiducial cross sections and differential distributions

In Table 1 we report the fiducial VBF cross section under the above cuts. The cross section includes NNLO-QCD corrections in the DIS approximation and NLO-EW corrections including photon induced contributions. Shown separately is the s-channel contribution which is not included in the total number. The NNLO-QCD corrections have been computed with proVBFH-1.1.0 [51, 65, 273–275] and the electroweak contributions with HAWK-2.0 [276–279].

Table 1: Fiducial VBF cross sections including QCD and EW corrections and their uncertainties for collider energy $\sqrt{s} = 14$ TeV and for a Higgs-boson mass $m_H = 125$ GeV. The QCD corrections have been updated compared to those reported in the YR4.

σ^{VBF}[fb]	Δ_{scale}[%]	$\Delta_{\text{PDF}\oplus\alpha_s}$[%]	$\sigma^{\text{DIS}}_{\text{NNLOQCD}}$[fb]	δ_{EW}[%]	σ_γ[fb]	$\sigma_{s\text{-channel}}$[fb]
2259	$^{+1.5}_{-1.3}$	$\pm 2.1 / \pm 0.4 / \pm 2.1$	2401	-6.9	23.6	32.9

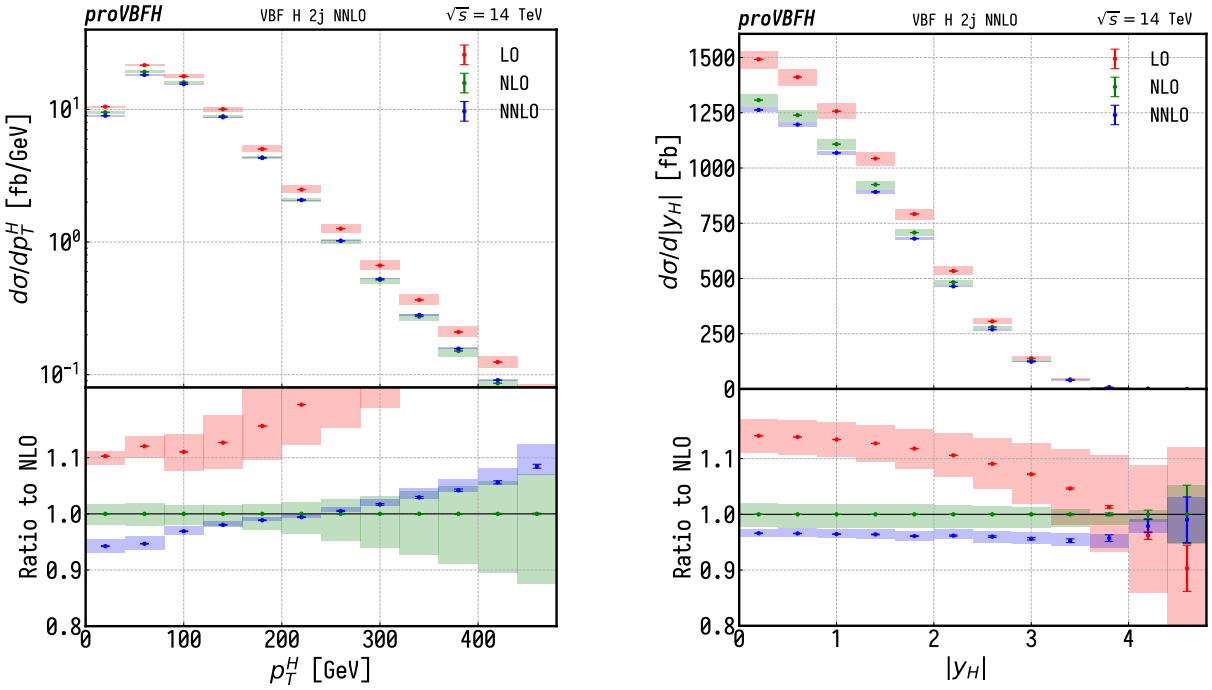

Fig. 6: Transverse momentum and rapidity of the Higgs boson after the cuts of (5) and at collider energy $\sqrt{s} = 14$ TeV.

4.1.3 HE-LHC

In this section we present fiducial cross sections for a center of mass energy of $\sqrt{s} = 27$ TeV. All physical parameters are kept unchanged with respect to the previous sections. In section 4.1.3 we compare the contributions of the gluon fusion (ggF) and VBF channels to Hjj production. In section 4.1.3 we study the effect of the NLO and NNLO QCD corrections to VBF Hjj production as computed in NNLOJET [280] with a redefined set of VBF cuts for the new energy choice.

Comparison of VBF to ggF background

For this comparison we dot not apply any kind of VBF cuts, requiring only two jets with

$$p_{\text{T}}^j > 30 \text{ GeV}, \qquad |y_j| < 5.0, \tag{6}$$

defined using the anti-k_t algorithm [281] with $R = 0.4$. The total cross section for ggF and VBF is shown in Table 2. Both the ggF and VBF contributions are computed with the parton-level Monte Carlo NNLOJET which includes ggF Higgs production in the heavy top limit (HTL) [67, 68, 282–284] among other processes [19, 164, 285–291]. The comparison of Table 2 is done at NLO QCD since Higgs plus two jets in gluon fusion is only available at this accuracy level.

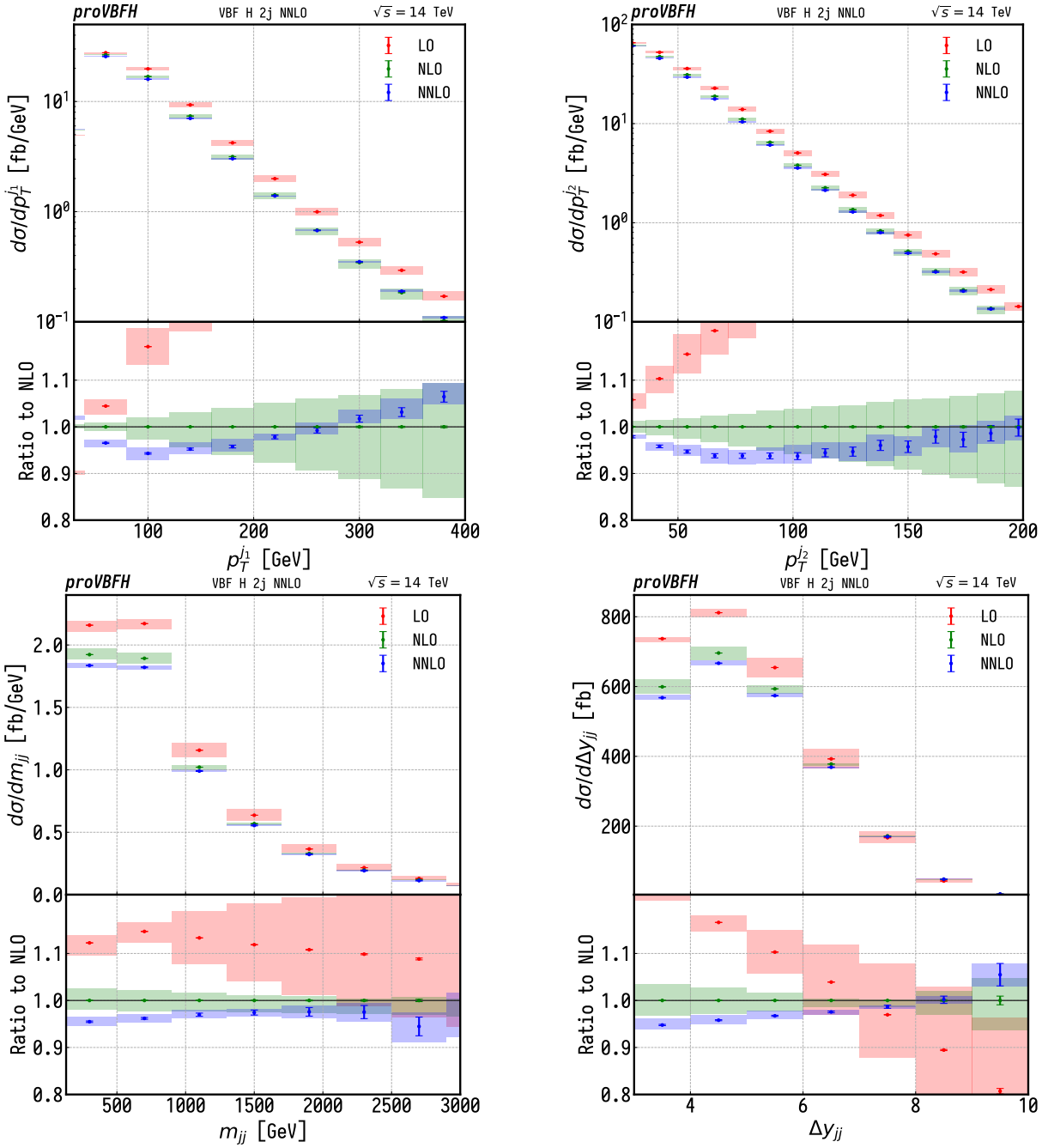

Fig. 7: In the top row the transverse momentum the two hardest jet after the cuts of (5) and at collider energy $\sqrt{s} = 14$ TeV. In the bottom row the invariant mass and absolute rapidity gap between the two hardest jets.

Table 2: Comparison between gluon fusion and vector boson fusion for a center of mass energy $\sqrt{s} = 27$ TeV.

Production mode	Total cross section (fb)	% of Total
ggF (HTL)	21984 ± 10	75.32 ± 0.04
VBF	7203 ± 2	24.68 ± 0.01

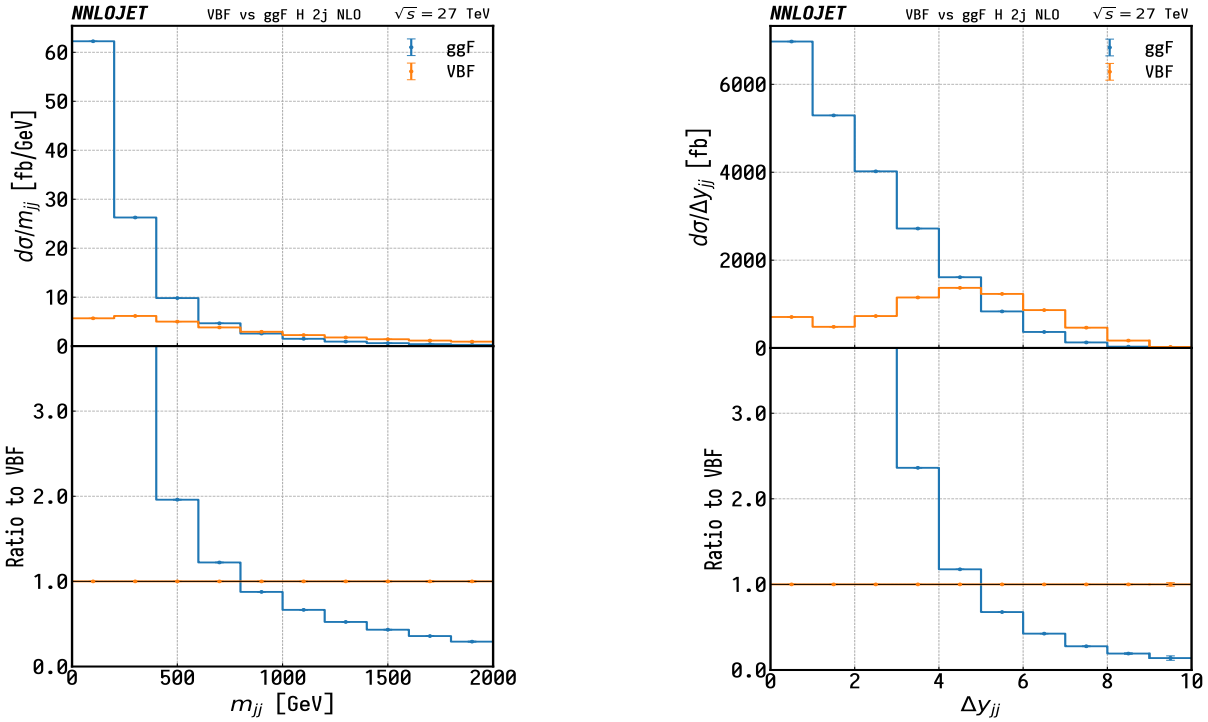

Fig. 8: Differential distributions for the invariant mass (left) and spatial distribution (right) of the dijet system. At lower values of m_{jj} and Δy_{jj} we observe a strong dominance of the ggF channel. For larger values of both observables, however, the VBF channel gains importance.

In order to define a set of cuts which enhance the VBF contribution we study the invariant mass (m_{jj}) and the spacial distribution (through the rapidity gap between both jets, Δy_{jj}) of the dijet system formed by the two leading jets. The VBF production mode dominates over ggF in the large rapidity separation region ($\Delta y_{jj} > 4.5$) as well as for moderate and high values of the dijet invariant mass ($m_{jj} > 700$ GeV).

Fiducial cross sections and differential distributions

We define the fiducial cross section for VBF at $\sqrt{s} = 27$ TeV with a set of tight VBF cuts,

$$\Delta y_{jj} > 4.5, \qquad m_{jj} > 600 \text{ GeV}, \tag{7}$$

requiring the two leading jets to be found in opposite rapidity hemispheres with a maximum rapidity of $|y_j| < 5.0$. In Table 3 the fiducial cross section is computed for three choices of the cut on the transverse momentum of the two leading jets: $p_{\mathrm{T}}^{j} > \{30, 40, 50\}$ GeV while differential distributions for $p_{\mathrm{T}}^{j} > 30$ GeV are shown in Figs. 9 to 10. The Hjj contribution in the VBF approximation as well as plots in this section are calculated at NNLO QCD accuracy with NNLOJET, electroweak corrections and the s-channel contribution shown in Table 3 are again computed with HAWK-2.0. Shaded boxes in

Table 3: Fiducial VBF cross sections including QCD and EW corrections and their uncertainties for collider energy $\sqrt{s} = 27$ TeV ($m_H = 125$ GeV). For completeness the s-channel contribution (corresponding to $pp \to HV \to q\bar{q}$) is also included.

σ^{VBF}[fb]	Δ_{scale}[%]	$\sigma^{\text{DIS}}_{\text{NNLOQCD}}$[fb]	δ_{EW}[%]	σ_γ[fb]	$\sigma_{s\text{-channel}}$[fb]	p_{T}^j cut [GeV]
2805	$^{+1.05}_{-0.02}$	3059	−9.6	39.8	5.9	30
2087	$^{+1.13}_{-1.05}$	2283	−10.0	32.3	4.4	40
1442	$^{+1.43}_{-1.61}$	1586	−10.5	22.3	3.0	50

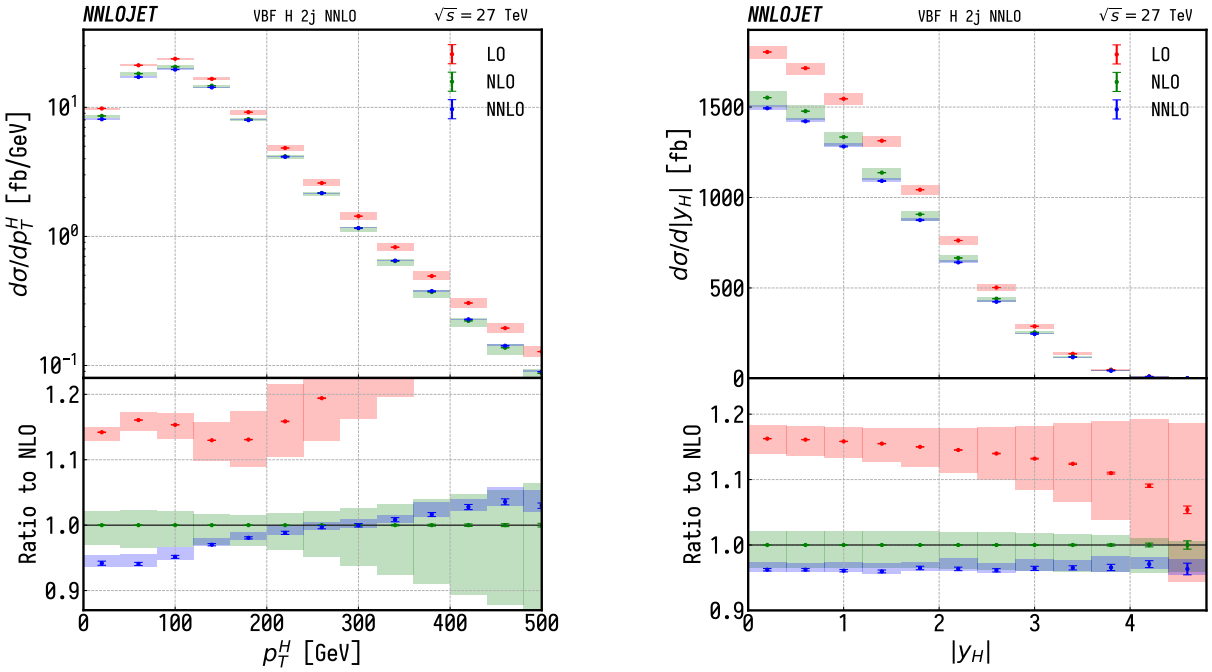

Fig. 9: Kinematical variables for the Higgs boson at $\sqrt{s} = 27$ TeV for tight VBF cuts. The NLO corrections are of more than -10 % across the whole considered range. The NNLO corrections, much smaller than NLO, show good convergence of the perturbative series. The NNLO corrections changes sign for high transverse momentum (left). For the rapidity distribution (right) they remain stable across the entire range of the observable.

all plots represent scale variations with $\mu_R = \mu_F = \{0.5, 2\}\mu_0$ with the central scale $\mu_0 = m_W$ and error bars represent statistical uncertainties from the Monte Carlo integration. In Fig. 9 the transverse momentum and rapidity distribution of the Higgs boson is shown. The kinematical variables for the system formed by the two leading jets is shown in Fig. 10.

Comparison of `HJets++` *and* `VBFNLO` *matrix elements in Higgs boson production*

The `HJets++ 1.1` module implements [292–295] electroweak Higgs boson plus two and three jet production. The one-loop integrals are computed using the techniques discussed in Ref. [296] and the colour algebra is performed using `ColorFull` [297]. For the VBF approximation we rely on the matrix elements encoded in `VBFNLO` version 3.0 beta 5 [206, 207, 298, 299]. We use `Herwig 7` for the event generator [201, 300–302]. Jet reconstruction is performed on final state partons using the anti-k_t algorithm [281] in the `fastjet` library [303]. Simulated events are analyzed via `Rivet` [304]. This

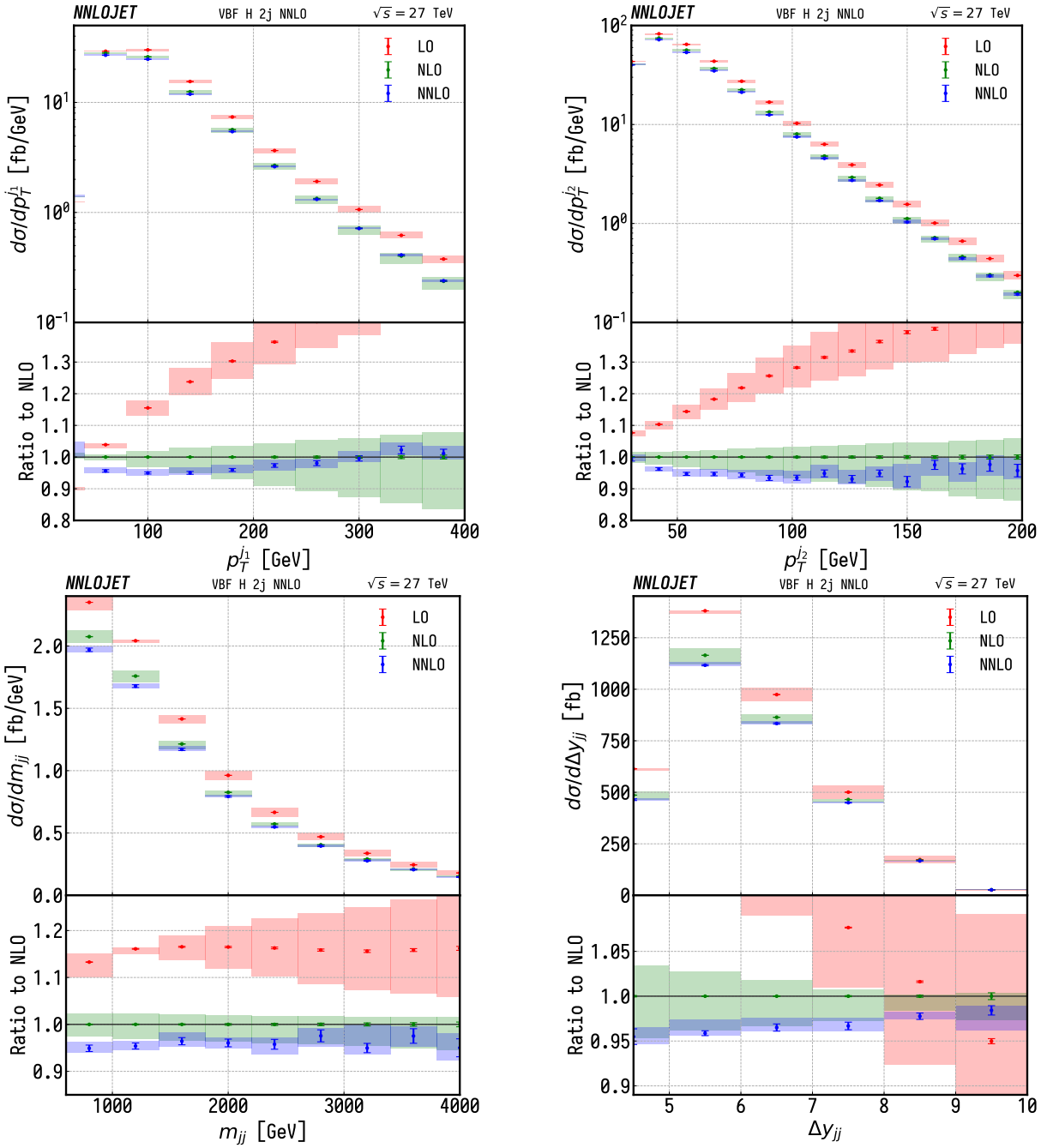

Fig. 10: In the top row we show the transverse momentum of the two leading jets ordered in rapidity at $\sqrt{s} = 27$ TeV for tight VBF cuts. In the bottom row we show the kinematical variables for the dijet system they form. Note that NNLO corrections noticeably reduce the scale uncertainties for both observables over the entire range we consider. NLO corrections are big for moderate and high transverse momentum with a scale uncertainty that grows with the transverse momentum. This behaviours is softened by the NNLO corrections.

work used the Extreme Science and Engineering Discovery Environment (XSEDE) [305] Open Science Grid [306, 307] through allocation of Wichita State University.

Higgs plus two jets

This section shows comparison plots of Higgs plus two jet calculations. The collider energy is set as $\sqrt{s} = 14$ TeV and $\sqrt{s} = 27$ TeV. Two kinematic variables: invariant mass m_{jj} and spatial distribution Δy_{jj} are chosen to present their differential distributions in this section. We use the parton distribution functions PDF4_LHC15_nlo_100 and all other input parameters are the same as shown in section 4.1. Differential distributions for leading order, leading order plus parton shower, next-to-leading order, and next-to-leading order plus parton shower are shown in the Fig. 11, with the inclusive cuts defined in Eq. (6). Comparison plots between two different matrix elements, `HJets++` and `VBFNLO` are shown in Fig. 12. The tight VBF cuts applied for $\sqrt{s} = 14$ TeV are defined as

$$p_{\mathrm{T}}^{j} > 30 \text{ GeV}, \qquad |y_j| < 5.0, \qquad |y_{j_1} - y_{j_2}| > 3.0, \qquad M_{jj} > 130 \text{ GeV}. \tag{8}$$

For $\sqrt{s} = 27$ TeV comparison plots, we used the tight VBF cuts defined in Eq. 7. The `VBFNLO` calculation is consistent with the `HJets++` calculation after applied the tight VBF cut.

Higgs plus three jets

In this section we present NLO results for Higgs boson plus three jet production for the following collider energies: $\sqrt{s} = 27$ TeV and $\sqrt{s} = 14$ TeV. Fig. 13 depicts the rapidity separation of the leading two jets Δy_{jj}, the invariant mass of the leading two jets m_{jj}, and the transverse momentum of the third hardest jet $p_T^{j_3}$, and for the full calculation using `HJets++` matrix elements for a collider energies of $\sqrt{s} = 14$ TeV and $\sqrt{s} = 27$ TeV for inclusive selection cuts. For inclusive cuts for both choices of collider energy we observe a large K-factor in the transverse momentum of the third jet $p_T^{j_3}$.

Fig. 14 shows differential distributions of kinematics variables for the NLO full and approximate results at $\sqrt{s} = 14$ TeV and $\sqrt{s} = 27$ TeV. The comparison of the full and approximate calculations are shown in the second and third rows of Fig. 14 for tight VBF cuts for the tranverse momentum of the third jet $p_T^{j_3}$ and the centrality of the third jet $y_{j_3}^{\star} = (y_{j_3} - \frac{1}{2}(y_{j_1} + y_{j_2}))/|y_{j_1} - y_{j_2}|$. For $\sqrt{s} = 27$ TeV the tight VBF cuts are: $\Delta y_{jj} > 4.5$, $m_{jj} > 600$ GeV, and $y_{j_1} \cdot y_{j_2} < 0$. For these selection cuts we see excellent agreement between the full and approximate calculation. For $\sqrt{s} = 14$ TeV the tight VBF cuts are: $\Delta y_{jj} > 3.0$, $m_{jj} > 130$ GeV, and $y_{j_1} \cdot y_{j_2} < 0$. For these selections cuts the full and approximate calculations still do not converge. However, if we had chosen $\Delta y_{jj} > 4.0$ the full and approximate calculations would compare quite well.

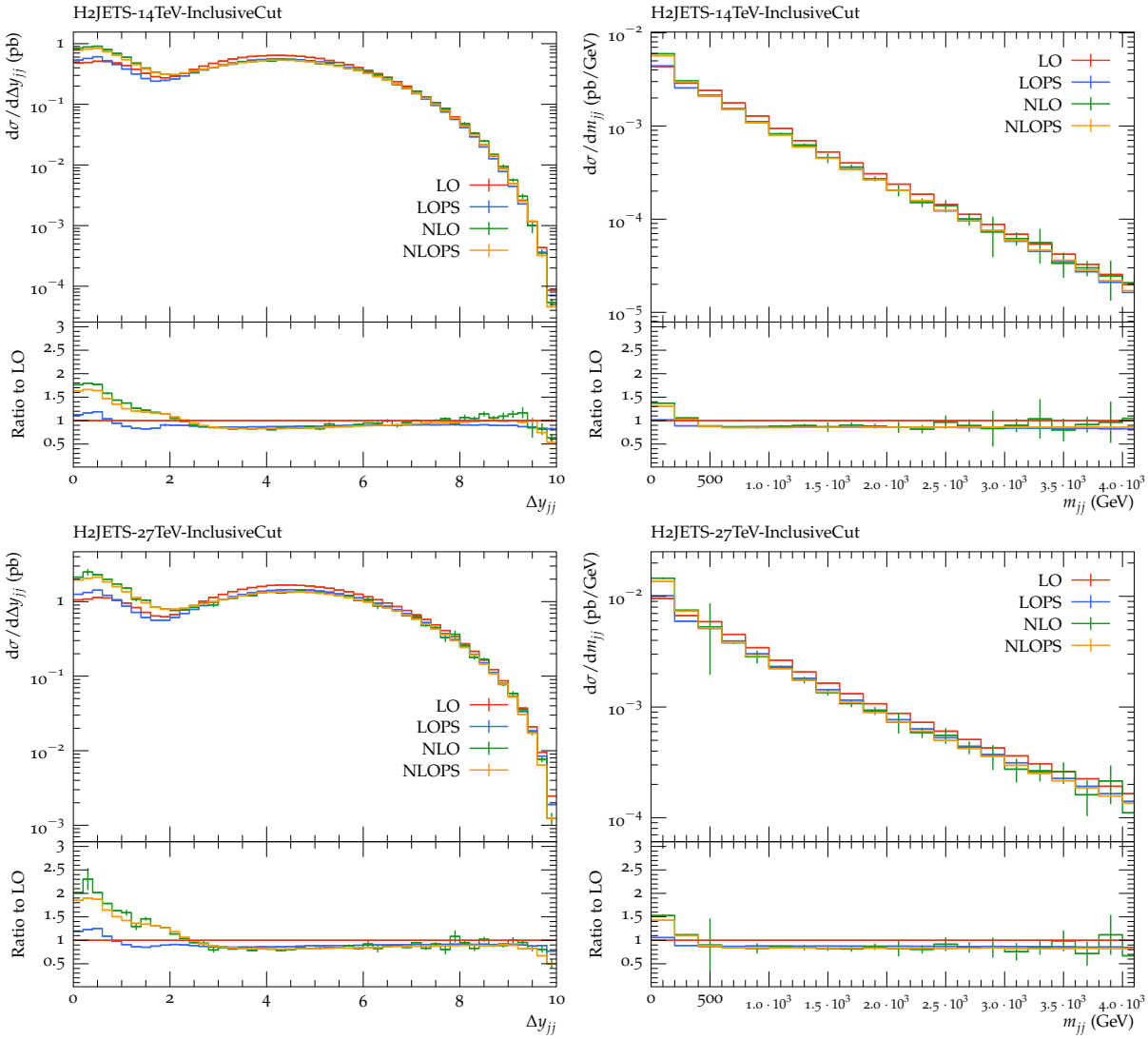

Fig. 11: Differential distributions of Δy_{jj} and m_{jj} at $\sqrt{s} = 14$ TeV (top row) and $\sqrt{s} = 27$ TeV (bottom row). `HJets++` matrix elements and inclusive cuts are used in the $H + 2$ jets calculations.

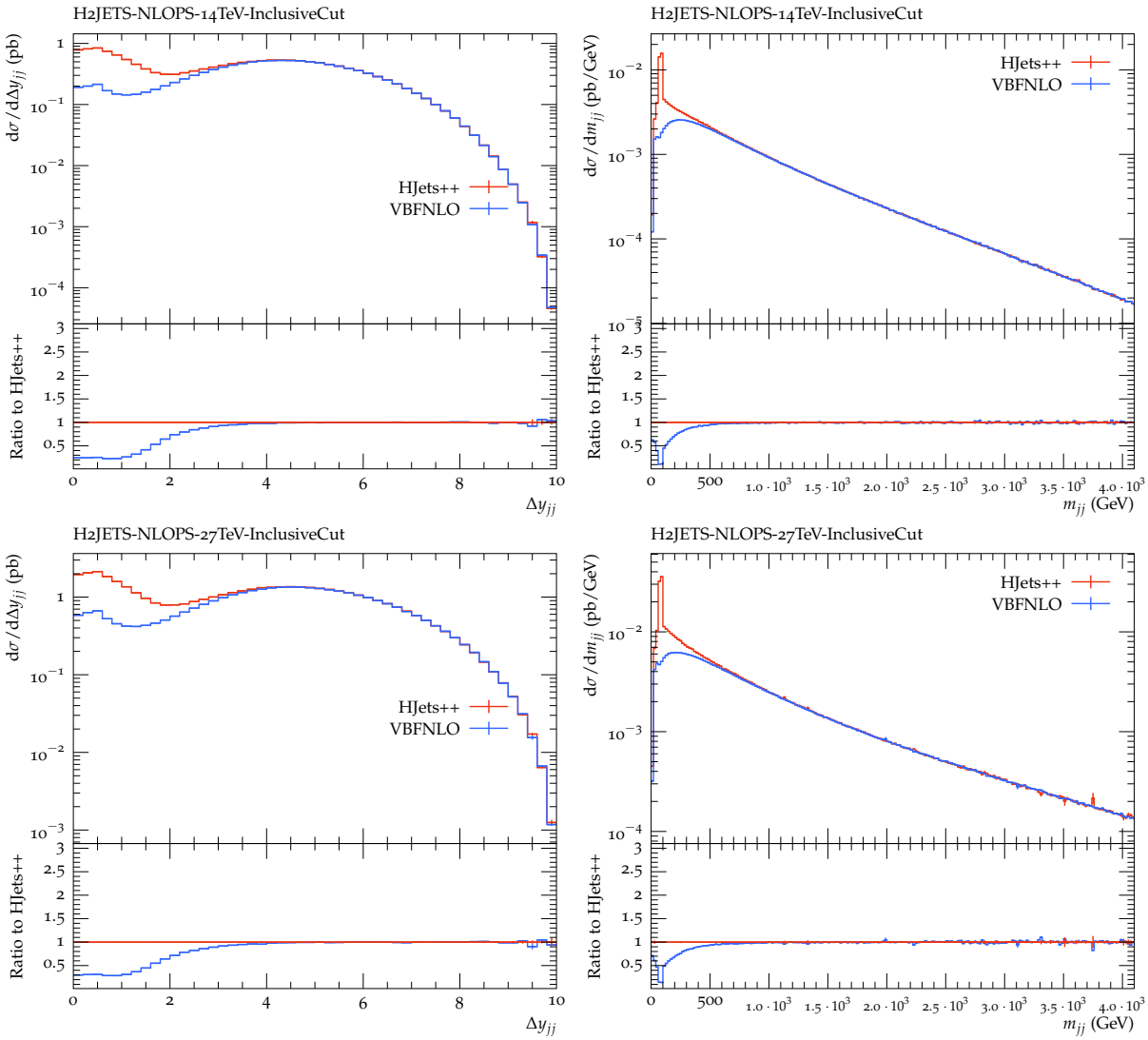

Fig. 12: The distributions of kinematic variables in $H + 2$ jets at $\sqrt{s} = 14$ TeV (top row) and $\sqrt{s} = 27$ TeV (bottom row). Comparisons are between the `HJets++` matrix elements and the `VBFNLO` matrix elements at NLO plus parton shower. Plots indicate that both `HJets++` and `VBFNLO` calculations have agreement after applied the tight VBF cuts.

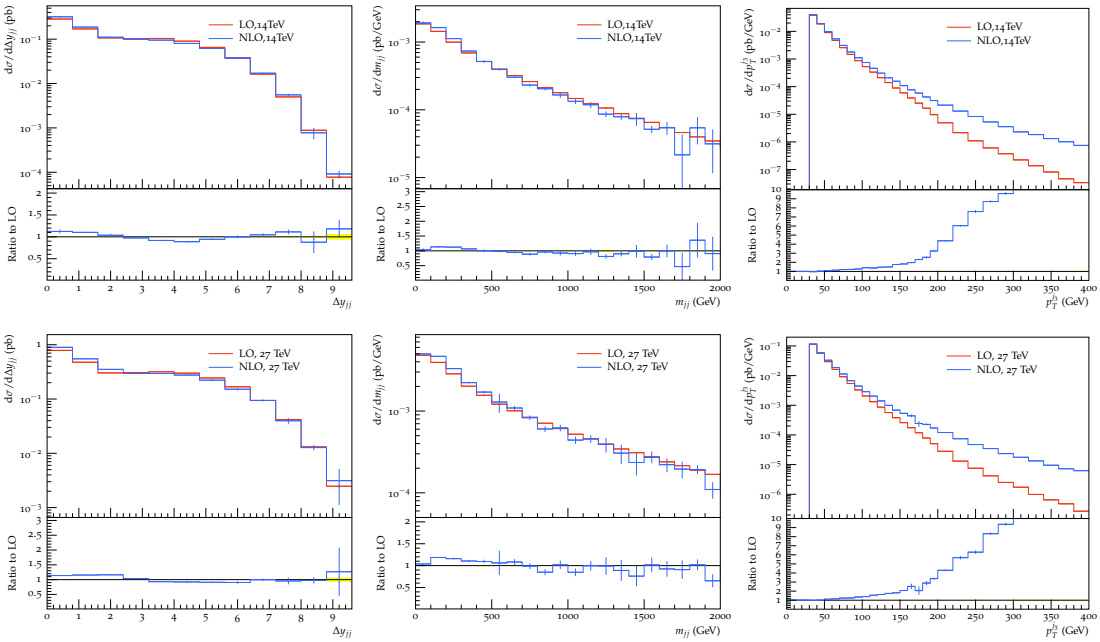

Fig. 13: Kinematic distributions for $H + 3$ jet production at LO and NLO using `HJets++` for $\sqrt{s} = 14$ TeV (top row) and $\sqrt{s} = 27$ TeV (bottom row). The selection cuts are inclusive.

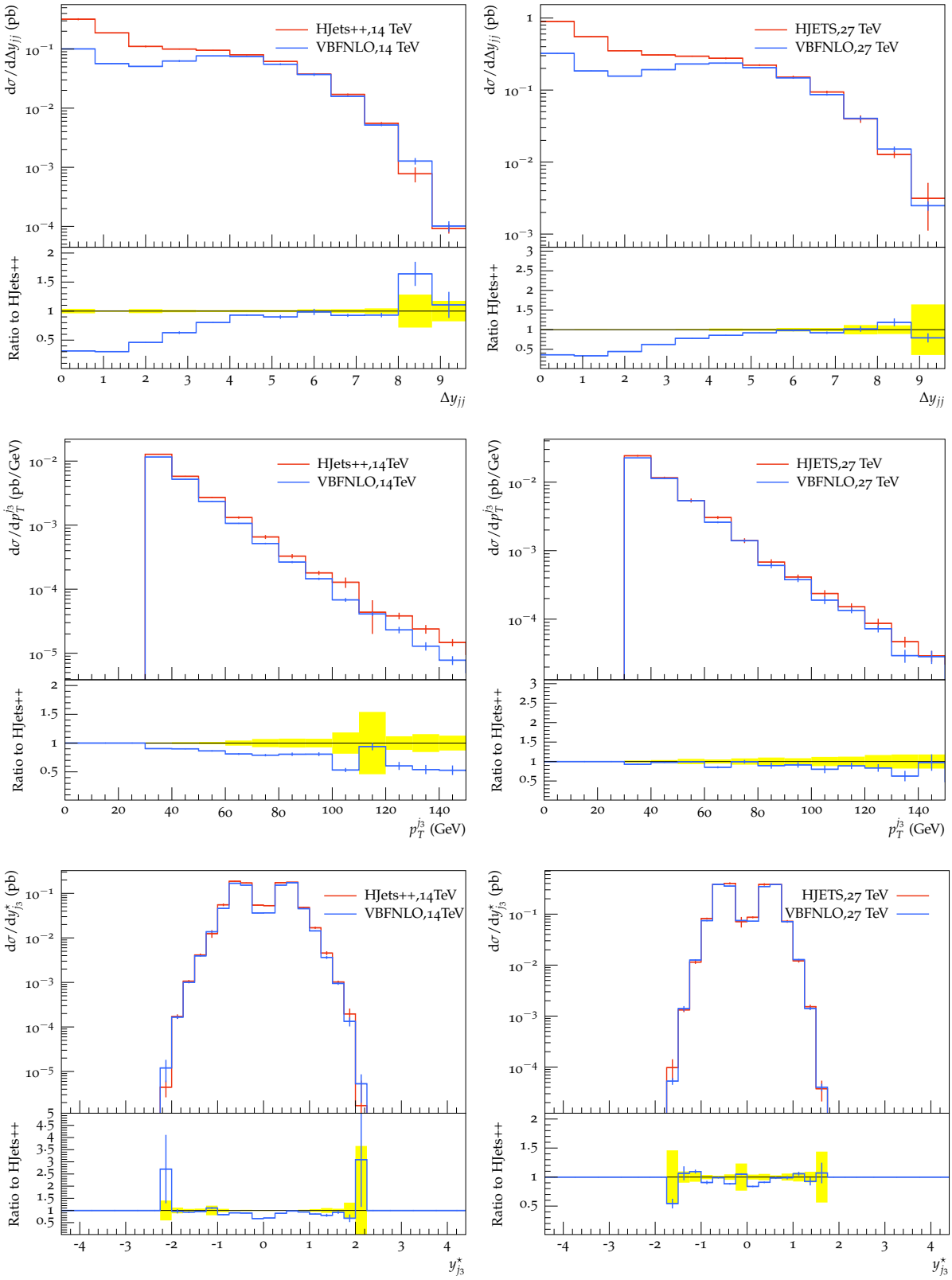

Fig. 14: Kinematics distributions at for $H+3$ jet production at NLO for the full result (`HJets++`) and the approximate result (`VBFNLO`) for $\sqrt{s} = 14$ TeV (first column) and $\sqrt{s} = 27$ TeV (second column). The kinematic distribution Δy_{jj} (top row) is shown for inclusive selection cuts. The kinematic distributions for $p_T^{j_3}$ and $y^\star_{j_3}$ are shown for VBF tight selection cuts.

4.2 Vector boson scattering processes

The study of the scattering of two massive vector bosons $V = W, Z$ (vector boson scattering, VBS) provides a key opportunity to probe the nature of the electroweak symmetry breaking (EWSB) mechanism as well as physics beyond the Standard Model (SM) [308, 309]. It is still unknown whether the discovered Higgs boson [310] preserves unitarity of the longitudinal VV scattering amplitude at all energies, or if other new physics processes are involved [311–315]. In the VBS topology, two incoming quarks radiate bosons which interact, yielding a final state of two jets from the outgoing quarks, and two massive bosons which decay into fermions. This final state can be the result of $VVjj$ electroweak (EW) production with and without a scattering topology, or of processes involving the strong interaction.

4.2.1 Measurements of the $W^{\pm}W^{\pm}$ scattering cross section and extraction of the longitudinal scattering component

With the largest cross-section ratio of electroweak to strong production [316, 317], events with $W^{\pm}W^{\pm}$ plus two jets ($W^{\pm}W^{\pm}jj$) provide one of the best opportunities to study the scattering of two vector bosons. ATLAS and CMS have both observed the EW process at 13 TeV with significances of 6.9 σ and 5.5 σ, respectively [318, 319].

This section describes the prospects for the study of $W^{\pm}W^{\pm}jj$ at $\sqrt{s} = 14$ TeV at the HL-LHC, with the Phase-2 upgraded ATLAS and CMS detectors [320, 321]. Results are presented for a range of integrated luminosities $\mathcal{L}$, from 300 fb^{-1}through 8000 fb^{-1}, where the first value corresponds to one year of data taking, and the latter to 10 years of combined data sets collected by the ATLAS and CMS experiments in the most optimistic scenario.

In both ATLAS and CMS analyses, the signal (VBS and non-VBS EW) and background (QCD) $W^{\pm}W^{\pm}jj$ events are simulated at leading order using `Madgraph5_aMC@NLO` [12, 322] with the `NNPDF3.0` set [159, 323], interfaced with `PYTHIA v8` [324] for parton showering, hadronisation and underlying event modelling. The information about the polarization of the individual W bosons in the signal process is extracted by generating a separate set of events using the DECAY package of MADGRAPH(v1.5.14). The other backgrounds – top ($t\bar{t}$ + jets, single-top), Drell-Yan, diboson ($W\gamma$, $\mathrm{W^{\pm}W^{\pm}}$ and WZ) and triboson (WWγ, WZγ, WWW, WWZ, WZZ, ZZZ) – are generated with either `Madgraph5_aMC@NLO`, POWHEG [325], or `PYTHIA v8`. The analyses use generated events obtained either using a fully simulated description of the Phase-2 CMS detector, implemented using the GEANT4 package [255] (CMS) or using a partameterised description of the detector response [326] (ATLAS). Additional details for each analysis are provided in the relevant reports from CMS [321] and ATLAS [320].

The experimental signature of the $W^{\pm}W^{\pm}jj$ scattering process consists of exactly two isolated leptons (electrons or muons) with the same electric charge, two jets well-separated in rapidity, and moderate E_T^{miss}. The event selection requirements for the two experiments are listed in Table 4. A minimum requirement on the dilepton mass reduces the contamination from low-mass Drell-Yan processes, with an additional restriction excluding the Z mass in the dielectron channel where the likelihood of charge misidentification is higher. A requirement on E_T^{miss} further reduces the background from charge misidentified events, and events containing any b-tagged jets[4] are vetoed to suppress background contribution from $\mathrm{t\bar{t}}$ production. A veto on additional preselected leptons significantly reduces background from WZ events. The two leading jets are required to have a large invariant mass, and large angular separation, to satisfy the expected VBS topology. Since leptons in the EWK $W^{\pm}W^{\pm}jj$ process are expected to be located in the central region defined by the forward-backward jets, non-VBS background

[4]The b tagging of jets in CMS is performed with the Deep Combined Secondary Vertex discriminator based on a deep neural network [329].

Table 4: ATLAS and CMS event selection criteria for $W^{\pm}W^{\pm}jj$ candidate events, with $\ell = e, \mu$ and j as the leading or sub-leading jet.

Selection requirement	ATLAS Selection	CMS Selection
Signal lepton p_{T}	$p_{\mathrm{T}} > 28(25)$[1] GeV	$p_{\mathrm{T}} > 20$ GeV
Signal lepton η	$\lvert\eta\rvert \leq 4.0$	$\lvert\eta\rvert \leq 3.0$
Tag jet p_{T}	$p_{\mathrm{T}} > 90(45)$[2] GeV	$p_{\mathrm{T}} > 50$ GeV
Tag jet η	$\lvert\eta\rvert \leq 4.5$	$\lvert\eta\rvert \leq 4.7$
Dilepton mass	$m_{\ell\ell} > 28$ GeV	$m_{\ell\ell} > 20$ GeV
Z_{ee} veto	$\lvert m_{ee} - m_Z\rvert > 10$ GeV	$\lvert m_{ee} - m_Z\rvert > 15$ GeV
E_T^{miss}	$E_T^{miss} > 40$ GeV	$E_T^{miss} > 40$ GeV
Number of b-tagged jets	0	0
Jet selection	Anti-k_t [327] jets with $\Delta R_{\ell,j} > 0.3$	Anti-k_{T} PUPPI [328] jets with $\Delta R_{\ell,j} > 0.4$
Preselected lepton veto	$p_T > 7(6)$[3] GeV	$p_T > 10$ GeV
Dijet rapidity separation	$\Delta\eta_{j,j} > 2.5$	$\Delta\eta_{j,j} > 2.5$
Dijet mass	$m_{jj} > 520$ GeV	$m_{jj} > 500$ GeV
Lepton centrality	$\zeta > -0.5$	$Z_{\mathrm{MAX}} < 0.75$

can be suppressed with a requirement on the centrality of the two leptons. CMS uses the Zeppenfeld variable [330], defined for a given lepton with pseudorapidity η_ℓ as

$$Z_\ell = \frac{[\eta_\ell - 0.5(\eta_1 + \eta_2)]}{|(\eta_1 - \eta_2)|},$$

where η_1, η_2 refer to the pseudorapidities of the leading and subleading jets. The maximum value of this variable, Z_{MAX}, for any of the leptons is required to be less than 0.75. ATLAS uses a requirement on the function ζ, where $\zeta = \min[\min(\eta_{\ell 1}, \eta_{\ell 2}) - \min(\eta_{j1}, \eta_{j2}), \max(\eta_{j1}, \eta_{j2}) - \max(\eta_{\ell 1}, \eta_{\ell 2})]$

The event selections are optimized to maximise signal acceptance (CMS) or minimise fake background (ATLAS). ATLAS uses tight electron requirements, which have a lower efficiency (around 50%, see [326]).

The expected event yields are summarized in Table 5 for CMS, and Table 6 for ATLAS. The m_{jj} distributions after the full event selection for $\mathcal{L} = 3000\,\mathrm{fb}^{-1}$ are presented in Fig. 15 . The main background contributions in the final signal region are due to inclusive $\mathrm{t\bar{t}}$ and WZ productions, where the third lepton in the event was not reconstructed within the detector acceptance. ATLAS explicitly models the background contributions from jets faking electrons and lepton charge misidentification, which also contribute significantly in the signal region, while CMS includes the fake contribution under $t\bar{t}$ and does not consider the charge-misidentified or triboson backgrounds in this study, since their contributions were found to be negligible. The integrated number of signal and background events as a function of the dilepton invariant mass is shown in Figure 17 for the ATLAS selection.

The uncertainty of the expected cross section measurement as a function of integrated luminosity is measured by fitting the m_{jj} distribution, using a binned maximum likelihood approach with all systematic uncertainties in the form of nuisance parameters with log- normal distributions. The correlations among different sources of uncertainties are taken into account while different final states are considered

Table 5: CMS expected yields for signal and background contributions for $\mathcal{L} = 3000\,\text{fb}^{-1}$.

Process	Expected yield, $\mathcal{L} = 3000\,\text{fb}^{-1}$
$W^{\pm}W^{\pm}$ (QCD)	196
$t\bar{t}$	5515
WZ	1421
Wγ	406
Total Background	7538
Signal $W^{\pm}W^{\pm}$ (EWK)	5368

Table 6: The ATLAS expected signal and background event yields after the optimised full event selection for a corresponding integrated luminosity of $\mathcal{L}$=3000 fb^{-1}. Events tagged as either "charge misidentification" or "jets faking leptons" are summed for all background samples and combined into a single entry each in the table. Remaining events are listed separately per process. Both QCD and EW production of WZ processes are included in the diboson background.

	All channels	$\mu^{\pm}\mu^{\pm}$	$e^{\pm}e^{\pm}$	$\mu^{\pm}e^{\pm}$	$e^{\pm}\mu^{\pm}$
$W^{\pm}W^{\pm}jj$(QCD)	132	58	16	24	35
Charge Misidentification	62	0.0	3.0	10	49
Jets faking electrons	210	0.0	8.7	201	0.1
Dibosons	901	207	216	182	297
Tribosons	58	22	7.1	11	17
Other non-prompt	99	23	14	48	13
Total Background	1460	310	264	476	411
Signal $W^{\pm}W^{\pm}jj$(EW)	2431	983	325	483	641

as independent channels in the fit. CMS considers three channels categorised by lepton flavour (ee, eμ and $\mu\mu$), while ATLAS uses eight channels by lepton flavour and charge (e^+e^+, e^-e^-, $e^+\mu^+$, $e^-\mu^-$, μ^+e^+, μ^-e^-, $\mu^+\mu^+$, $\mu^-\mu^-$).

The experimental uncertainties, statistical and systematic, in the CMS analysis contribute to a total uncertainty on the signal strength of 3.2% for 3000 fb^{-1}. Including a theoretical uncertainty of 3% and an uncertainty on the luminosity of 1%, the total uncertainty reaches a value of 4.5% for 3000 fb^{-1}. For the ATLAS analysis experimental systematics on the trigger, leptons, jets, and flavour tagging are taken from the 13 TeV analysis unchanged, while for the baseline estimation, rate uncertainties on the backgrounds are halved. An "optimistic" set of uncertainties is also presented, where the uncertainties on the non-data-driven backgrounds are aggressively reduced. The total uncertainty is presented in Fig. 16 as a function of the integrated luminosity. The values of $\mathcal{L}$ exceeding 3000 fb^{-1} are an estimation of a combination of the measurements from CMS and ATLAS, effectively doubling the total integrated luminosity.

The total W$^{\pm}$W$^{\pm}$ VBS cross section can be decomposed into the polarized components based on the decays of the individual W bosons. Either or both can be longitudinally (L) or transversely (T) polarized, giving rise to final states of LL, LT as well as the mixed state LT (with TL combination

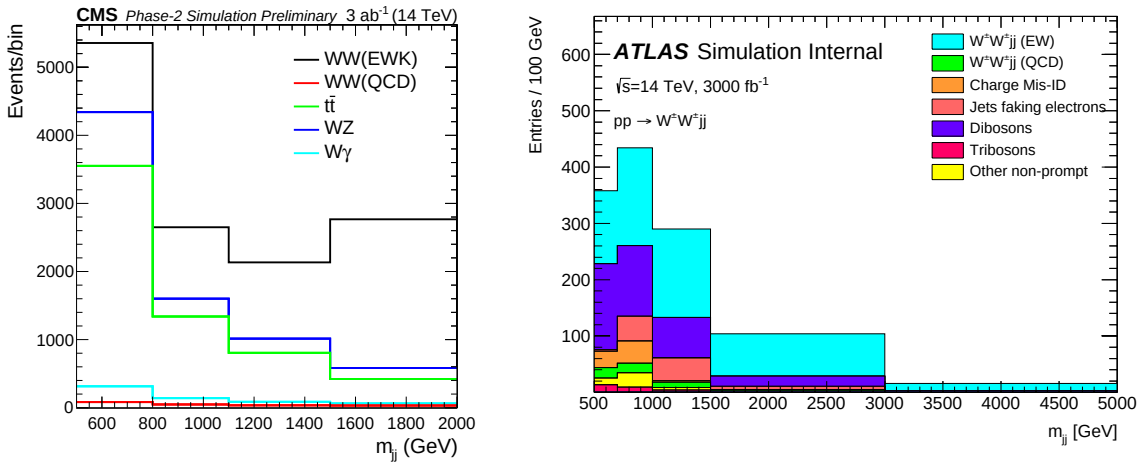

Fig. 15: The distribution of the invariant mass of the two leading jets after the selection requirements for an integrated luminosity of 3000 fb^{-1}, for CMS (left) and ATLAS (right).

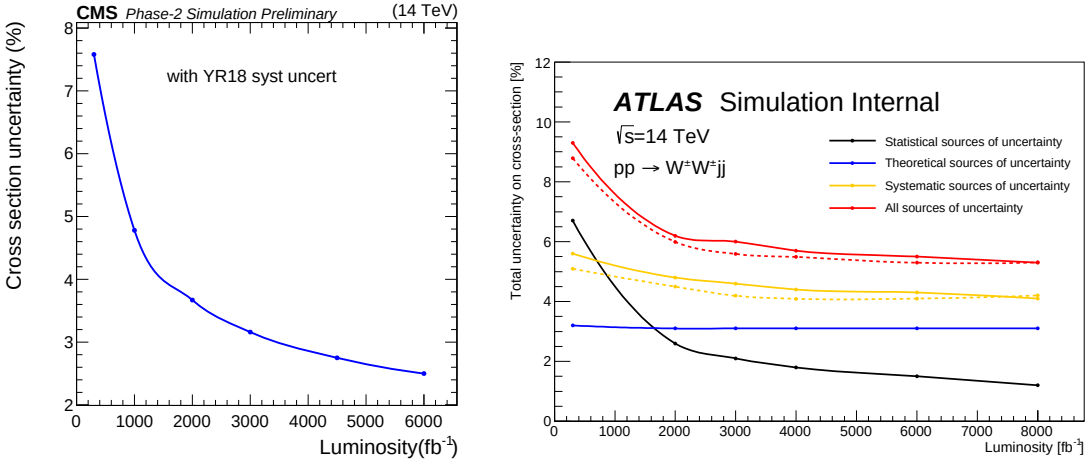

Fig. 16: The estimated uncertainty of the EWK $W^{\pm}W^{\pm}$ cross section measurement as a function of the integrated luminosity, for CMS (left), only statistical and experimental systematic uncertainties are considered, and ATLAS (right).

implied). The LL component, $W_L^{\pm}W_L^{\pm}jj$, is expected to be only about 6-7% of the total VBS cross section for jet $p_{\mathrm{T}} > 50$ GeV. The difference in azimuthal angle between the two leading jets, $\Delta\phi_{jj}$, has the potential for discriminating the LL component of the VBS scattering from TT and LT contributions. Since the signal-to-background separation for the EWK $W^{\pm}W^{\pm}jj$ process improves with increasing m_{jj} as shown in Fig. 15 (left), the $\Delta\phi_{jj}$ distributions are studied in two ranges of m_{jj}: for 500-1100 GeV and above 1100 GeV. Figure 18 shows the combination of signal and background yields as a function of $\Delta\phi_{jj}$ for high m_{jj} regions. Using a simultaneous fit to two mass regions[5], the significance for the observation of the LL process is estimated as a function of integrated luminosity. The significance is found to be up to 2.7 standard deviations for $\mathcal{L} = 3000\,\mathrm{fb}^{-1}$. The gradual improvement of signal significance as a function of integrated luminosity is shown in Fig. 19 right. A combination of ATLAS and CMS results, using fully simulated ATLAS events and improved electron efficiency, is expected to

[5]The low m_{jj} region serves to constrain the $t\bar{t}$/fake background

reach an expected significance of 3 standard deviations with 2000 fb^{-1} per experiment. In addition, recent studies [331] have shown that advances in machine learning can also improve the prospects for the measurement of the $W_L^{\pm}W_L^{\pm}jj$ process.

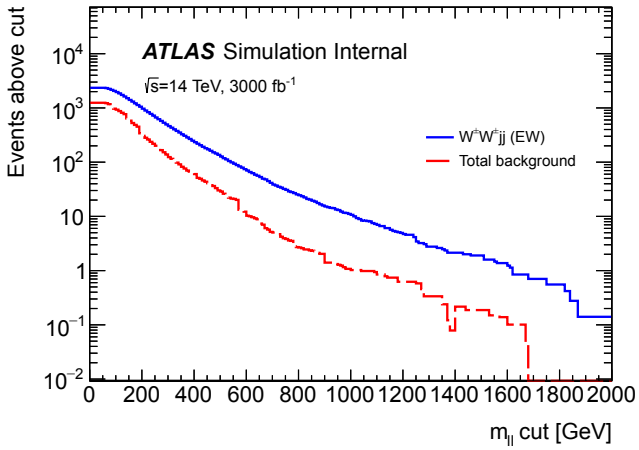

Fig. 17: Integrated number of events as a function of dilepton invariant mass for events passing all selection criteria of the ATLAS signal region.

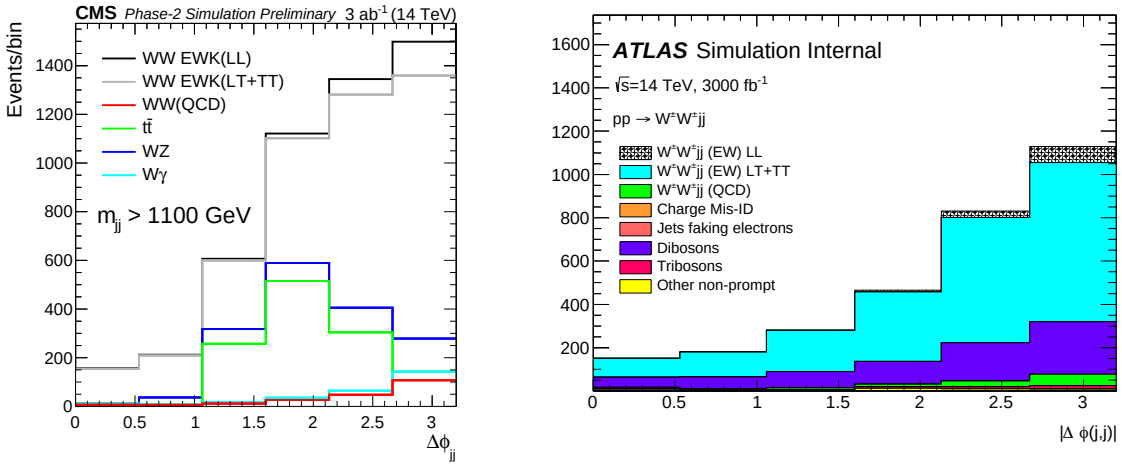

Fig. 18: Distribution of the azimuthal angle difference between two leading jets for dijet invariant mass above 1100 GeV.

4.2.2 High Order corrections in VBS $W^{\pm}W^{\pm}$ production at HL and HE LHC

The expected experimental precision in the measurement of VBS processes offers great opportunities to probe the electroweak (EW) sector and its associated symmetry breaking mechanism (see Refs. [133, 332, 333] for 100 TeV-collider studies). Therefore, it is of prime importance to make precise theoretical predictions available for the future operation of the LHC. In this sub-section, predictions for NLO QCD and EW corrections are provided for the LHC running in its high-luminosity (HL) and high-energy (HE) configurations. The HL set-up corresponds to a centre-of-mass energy of 14 TeV while the HE one refers to 27 TeV. For both centre-of-mass energies the same type of event selections has been used. These

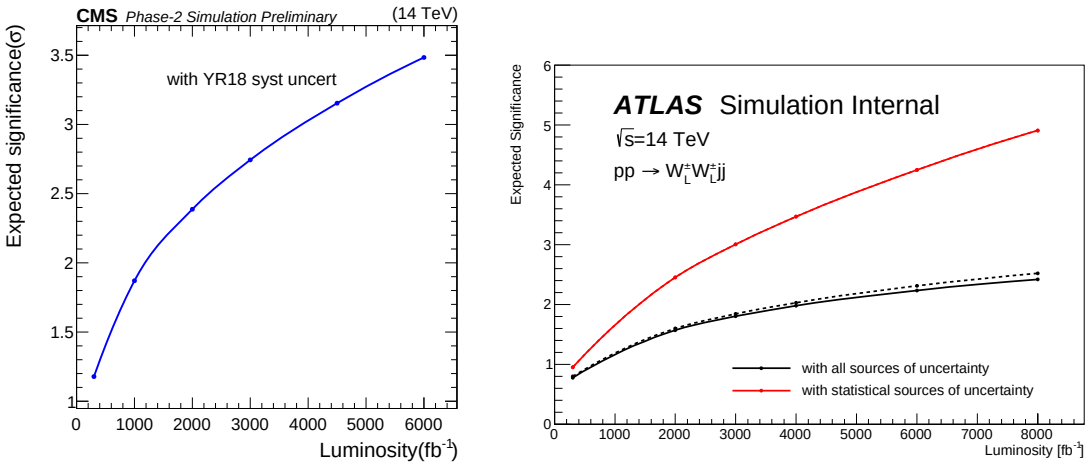

Fig. 19: Significance of the observation of the scattering of a pair of longitudinally polarized W bosons as a function of the integrated luminosity at CMS (left) and ATLAS (right).

predictions represent important benchmarks as they indicate the expected rates and the corresponding theoretical uncertainties. The QCD corrections are particularly important as they can significantly distort the shape of jet-related observables [111, 334–341]. In addition, the inclusion of NLO QCD corrections reduces the theoretical uncertainties. The NLO EW corrections have been shown to be very large for VBS processes [103] and even are the dominating NLO contribution for same-sign WW scattering [111].

In this study, the NLO QCD corrections have been obtained from VBFNLO based on Refs. [206, 207, 298] in the so-called VBS approximation [339, 341, 342]. The NLO EW corrections have been obtained from MoCaNLO+Recola [82, 82, 91] based on a full NLO computation [111]. The differences between the full computation and the one based on the VBS approximation have been found to be below the per-cent level at NLO QCD [341]. This justifies the combination of the NLO corrections from these two types of calculations. The QCD corrections have been computed for all possible VBS signatures, while the EW ones are only known for same-sign WW scattering. While the exact value of the corrections is expected to be different for other signatures, their magnitudes and nature should be similar.

Set-up

The hadronic scattering processes are simulated at the LHC with a centre-of-mass energies $\sqrt{s} = 14\,\text{TeV}$ and $\sqrt{s} = 27\,\text{TeV}$. The NNNPDF 3.1 LUXQED parton distribution functions (PDFs) [182] with five massless flavours,[6] NLO-QCD evolution, and a strong coupling constant $\alpha_s(M_Z) = 0.118$ are employed.[7] Initial-state collinear singularities are factorised according to the $\overline{\text{MS}}$ scheme, consistently with the conventions in the NNPDF set.

The other input parameters have been chosen as in Ref. [341]. For the massive particles, the following masses and decay widths are used:

$$\begin{aligned} m_t &= 173.21\,\text{GeV}, & \Gamma_t &= 0\,\text{GeV}, \\ M_Z^{OS} &= 91.1876\,\text{GeV}, & \Gamma_Z^{OS} &= 2.4952\,\text{GeV}, \\ M_W^{OS} &= 80.385\,\text{GeV}, & \Gamma_W^{OS} &= 2.085\,\text{GeV}, \end{aligned}$$

[6] For the process considered, no bottom (anti-)quarks appear in the initial or final state at LO and NLO, as they would lead to top quarks rather than light jets in the final state.

[7] The corresponding identifier `lhaid` in the program LHAPDF6 [160] is 324900.

$$M_{\mathrm{H}} = 125.0\,\mathrm{GeV}, \qquad \Gamma_{\mathrm{H}} = 4.07 \times 10^{-3}\,\mathrm{GeV}. \tag{9}$$

The measured on-shell (OS) values for the masses and widths of the W and Z bosons are converted into pole values for the gauge bosons ($V = \mathrm{W}, \mathrm{Z}$) according to Ref. [343],

$$\begin{aligned} M_V &= M_V^{\mathrm{OS}} / \sqrt{1 + (\Gamma_V^{\mathrm{OS}} / M_V^{\mathrm{OS}})^2}\,, \\ \Gamma_V &= \Gamma_V^{\mathrm{OS}} / \sqrt{1 + (\Gamma_V^{\mathrm{OS}} / M_V^{\mathrm{OS}})^2}. \end{aligned} \tag{10}$$

The EW coupling is fixed in the G_μ scheme [344] according to

$$\alpha = \frac{\sqrt{2}}{\pi} G_\mu M_{\mathrm{W}}^2 \left(1 - \frac{M_{\mathrm{W}}^2}{M_{\mathrm{Z}}^2}\right), \tag{11}$$

with

$$G_\mu = 1.16637 \times 10^{-5}\,\mathrm{GeV}^{-2}, \tag{12}$$

and M_V^2 corresponds to the real part of the squared pole mass. The complex-mass scheme [345–347] is used throughout to treat unstable intermediate particles in a gauge-invariant manner.

The central value of the renormalisation and factorisation scales is set to

$$\mu_{\mathrm{ren}} = \mu_{\mathrm{fac}} = \sqrt{p_{\mathrm{T,j_1}}\, p_{\mathrm{T,j_2}}}. \tag{13}$$

The transverse momenta are those of the two hardest jets. This choice of scale has been shown to provide stable NLO-QCD predictions [339].

Following experimental measurements [348–351] and prospect studies [352], the event selection used in the present study is:

- The two same-sign charged leptons are required to fulfil cuts on transverse momentum, rapidity, separation in the rapidity–azimuthal-angle, and the lepton-pair invariant mass,

$$p_{\mathrm{T},\ell} > 20\,\mathrm{GeV}, \qquad |y_\ell| < 4.0, \qquad \Delta R_{\ell\ell} > 0.3, \qquad m_{\ell\ell} > 20\,\mathrm{GeV}. \tag{14}$$

- The total missing transverse momentum, computed from the vectorial sum of the transverse momenta of the two neutrinos, is required to be

$$p_{\mathrm{T,miss}} > 40\,\mathrm{GeV}\,. \tag{15}$$

- QCD partons (light quarks and gluons) are clustered using the anti-k_T algorithm [233] with jet-resolution parameter $R = 0.4$. Cuts on the jets' transverse momenta and rapidities are imposed,

$$p_{\mathrm{T,j}} > 30\,\mathrm{GeV}, \qquad |y_{\mathrm{j}}| < 4.0. \tag{16}$$

  VBS cuts are applied on the two jets with largest transverse momentum. In particular, we impose a cut on the invariant mass of the di-jet system, as well as on the rapidity separation of the two jets and their separation from leptons,

$$m_{\mathrm{jj}} > 500\,\mathrm{GeV}, \qquad |\Delta y_{\mathrm{jj}}| > 2.5, \qquad \Delta R_{\mathrm{j}\ell} > 0.3. \tag{17}$$

- Finally, the centrality of the leptons is enforced according to Ref. [352]:

$$\zeta = \min\left[\min\left(y_{\ell_1}, y_{\ell_2}\right) - \min\left(y_{\mathrm{j}_1}, y_{\mathrm{j}_2}\right), \max\left(y_{\mathrm{j}_1}, y_{\mathrm{j}_2}\right) - \max\left(y_{\ell_1}, y_{\ell_2}\right)\right] > 0. \tag{18}$$

- For EW corrections, real photons and charged fermions are clustered using the anti-k_T algorithm with radius parameter $R = 0.1$. In this case, leptons and quarks are understood as *dressed fermions*.

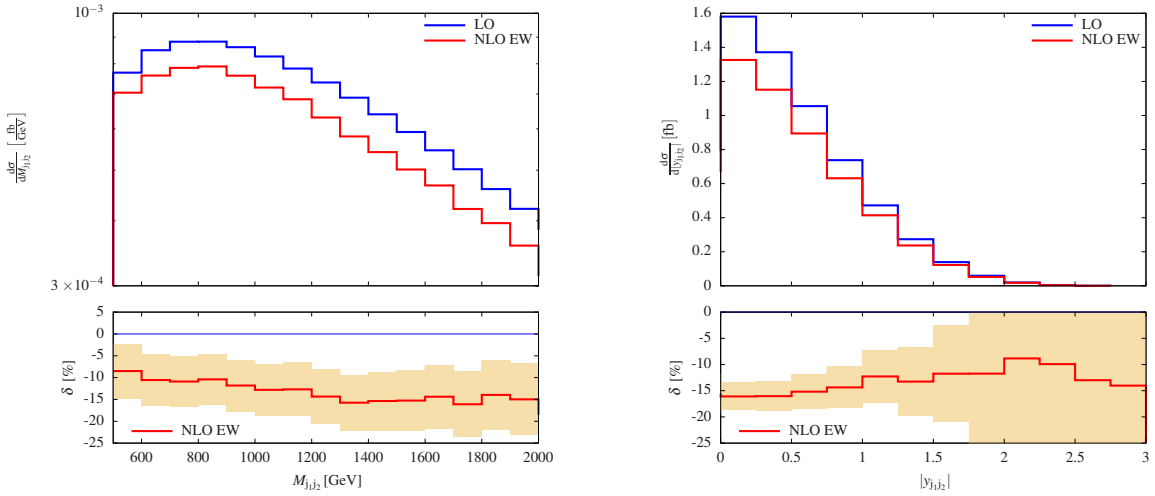

Fig. 20: Differential distributions in the invariant mass of the two jets (left) and their rapidity (right) in pp $\to \mu^+\nu_\mu e^+\nu_e jj$ at 14 TeV including NLO EW corrections (upper panel) and relative NLO EW corrections (lower panel). The yellow band describes the expected statistical uncertainty for a high-luminosity LHC collecting 3000 fb^{-1} and represents a relative variation of $\pm 1/\sqrt{N_{\text{obs}}}$ where N_{obs} is the number of observed events in each bin.

Discussion

In this section we focus on the discussion of Standard Model predictions for the HL and HE LHC. This entails both QCD and EW corrections that have been combined together.

For VBS processes EW corrections are particularly large and therefore of prime importance. The leading contributions originate from the exchange of massive gauge bosons in the virtual corrections. They tend to grow large and negative in the high-energy limit owing to so-called Sudakov double logarithms. As shown in Ref. [103], large EW corrections are an intrinsic feature of VBS at the LHC. While this study is based on the same-sign W channel, it has been further confirmed recently by the computation of large EW corrections to the WZ channel [353, 354].

Given their size and the foreseen experimental precision, these corrections are actually measurable. Because they involve interactions of the EW sector, their measurement would constitute a further test of the SM. On the left hand-side of Fig. 20, the distribution in the invariant mass of the two leading jets is shown at LO and NLO EW for the process pp $\to \mu^+\nu_\mu e^+\nu_e jj$ at 14 TeV. The yellow band describes the expected statistical uncertainty for a HL LHC collecting 3000 fb^{-1}. On the right hand-side for Fig. 20, a similar plot for the absolute rapidity of the jet pair is shown. It is thus clear that with the expected luminosity, one is not only sensitive to the VBS process but also to its EW corrections.

In Fig. 21, the distributions in the invariant mass of the visible system ($e^+\mu^+jj$) at both 14 TeV (left) and 27 TeV (right) are shown. As expected, the corrections are larger for higher centre-of-mass energy due to the higher representative scale of the process. In the tail of the distribution where new physics could play an important role, the corrections are particularly large and reach about 25% for the 27 TeV set-up. Note that in the present predictions, the real radiation of massive gauge bosons is not taken into account. This effect has been estimated to be of the order of few per cent for the HL set-up at the level of the total cross section. While this effect is for now negligible, for the HL and HE mode of the LHC, it will become relevant in the same way as the use of VBS approximations in theoretical predictions [355]. These observations are further confirmed via the cross sections for the two centre-of-mass energies at LO (using full matrix element) and NLO EW given in Table 7. At 27 TeV the EW

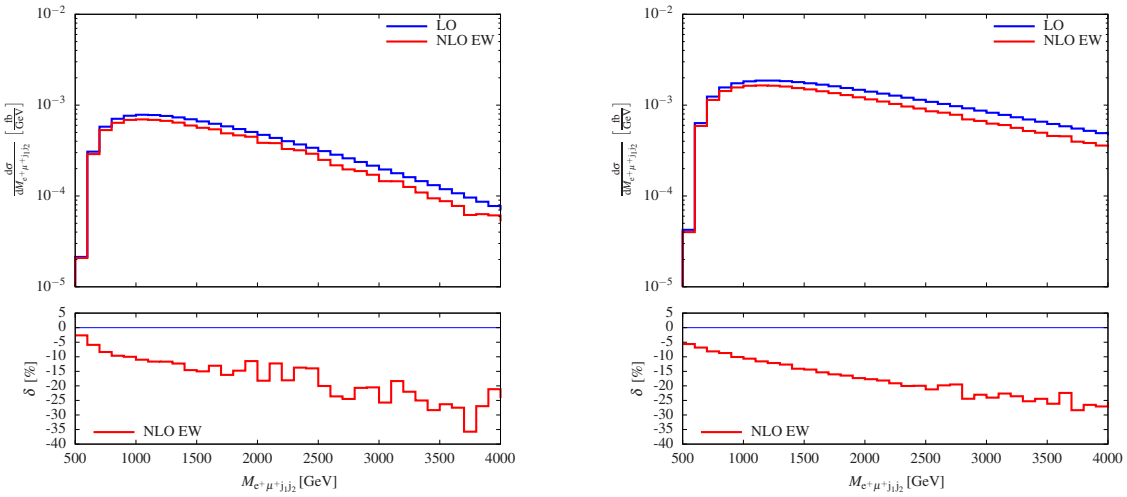

Fig. 21: Differential distribution in the invariant mass of the visible system ($e^+\mu^+jj$) in $pp \to \mu^+\nu_\mu e^+\nu_e jj$ at 14 TeV (left) and 27 TeV (right) including NLO EW corrections (upper panel) and relative NLO EW corrections (lower panel).

Table 7: Cross sections at LO ($\mathcal{O}\left(\alpha^6\right)$) and NLO EW ($\mathcal{O}\left(\alpha^7\right)$) for $pp \to \mu^+\nu_\mu e^+\nu_e jj$ at both 14 TeV and 27 TeV at the LHC. The relative EW corrections are given in per cent, and the digits in parenthesis indicate the integration error.

	σ^{LO} [fb]	$\sigma^{\text{NLO}}_{\text{EW}}$ [fb]	δ_{EW} [%]
14 TeV	1.4282(2)	1.213(5)	−15.1
27 TeV	4.7848(5)	3.881(7)	−18.9

corrections are few per cent larger than at 14 TeV (−18.9% against −15.1%, respectively). Note that the jump in energy from 14 TeV to 27 TeV is accompanied by an increase by more than a factor 3 in the cross section at LO.

4.2.3 WZ@HL-HLC

Prospects are presented for measuring the WZ electroweak production in fully leptonic final state at the HL-LHC. This work includes studies of the polarised WZ production: measurements of the vector bosons in longitudinally polarized states are of particular importance, since they give a direct access to the nature of the electroweak symmetry breaking via the exchange of a Higgs bosons in the t-channel as shown in Fig. 22. Another relevant aspect of the WZ production lies in the probe of the non-abelian structure of the standard model via the sensitivity tests to triple and quartic gauge couplings, but this topic is not developed in this section. Measurements of the electroweak production using 36 $fb^{-1}$of the proton-proton collisions at 13 TeV were reported by both the ATLAS [356] and CMS [357] collaborations. The existing results are strongly limited by the statistical uncertainties of the data samples, therefore the integrated luminosity expected at the end of the HL-LHC operation is mandatory to fully exploit the physics behind VBS in WZ production via measurement of differential distributions and the polarization of the final state bosons.

In proton-proton collisions, the VBS process results from the interaction of two bosons radiated by the initial quarks leading to a final state with two centrally produced bosons and two forward jets.

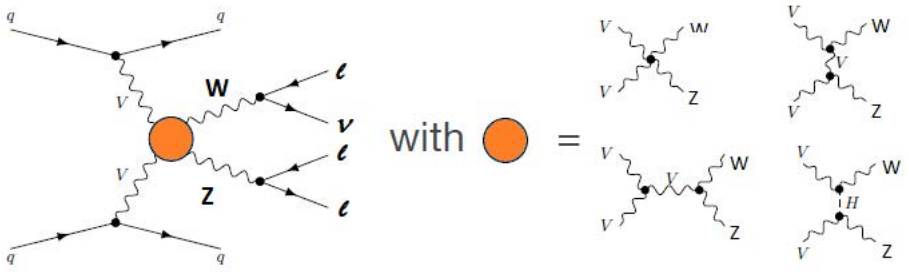

Fig. 22: Feymann diagrams describing the VBS WZ production

The main irreducible background is represented by events in which the same final state is mediated by strong interactions ($WZ - QCD$) and where the two bosons are not the direct result of a scattering process. Other backgrounds consist of different di-boson final states (ZZ, $Z\gamma$), tri-bosons and tV or $t\bar{t}V$ production , where V is a Z or a W boson. The amount of the non-prompt backgrounds, where one or more lepton candidates are coming from jets misidentified as leptons, ultimately depends on the detector geometry, reconstruction technique and event selection requirements.

The signal selection requires events with three isolated leptons with $\mathrm{p_T}$ > 15 GeV with $|\eta| < 4$ for ATLAS and $|\eta| < 2.8$ (3.0) for muons (electrons) for CMS. In addition, at least one lepton should pass the single lepton trigger (ATLAS). In order to suppress the background from ZZ processes, events containing four or more lepton candidates are discarded. At least one of the three lepton candidate is required to have $\mathrm{p_T}$ > 25 GeV. The event must have at least one pair of leptons of the same flavor and opposite charge, with an invariant mass that is consistent with the nominal Z boson mass at $M_Z = 91.188$ GeV within 10 GeV for ATLAS and 15 GeV for CMS. This pair is considered as a Z boson candidate. The third lepton is assigned to the W boson and its $\mathrm{p_T}$ is required to be greater than 20 GeV. Finally, E_T^{miss} (CMS) or the transverse mass of the W candidate computed using E_T^{miss} and the $\mathrm{p_T}$ of the third lepton (ATLAS) is required to be above 30 GeV. The VBS signature is characterized by presence of two forward jets. Jets are reconstructed with anti-k_T algorithm with distance parameter 0.4. For ATLAS, the event is selected if it contains two jets laying in opposite hemisphere with $\mathrm{p_T^{jet}}$ greater than 30 GeV and $|\eta^{\mathrm{jet}}|$ < 3.8. For CMS, the event is selected if it contains two jets with $\mathrm{p_T^{jet}}$ > 50 GeV and $|\eta^{\mathrm{jet}}|$ < 4.7 for CMS. In addition, the pseudorapidity separation between jets $\Delta\eta_{jj}$ is requested to be greater than 2.5. Finally, the dijet mass m_{jj} is required to be greater than 500 GeV. The full list of selection requirements is summarized in Tab. 8.

Distinct approaches are used by ATLAS and CMS, respectively based on simulation at 14 TeV and on extrapolation from Run2 results. ATLAS uses Monte Carlo samples generated with a fast simulation based on the parametrisation of the performance of the Phase 2 detector and where jets from PU interactions corresponding to <μ> = 200 are added to the event record; a loose event selection and a conservative background hypothesis is used. The signal events are generated at LO with Sherpa 2.2.2 [358] and the $WZ - QCD$ background is simulated at NLO with Sherpa 2.2.0: in [356], it was shown that the $WZ - QCD$ background predictions might be overestimated by 40% in certain regions of the phase-space. And with a $\mathrm{p_T^{jet}}$cut as low as 30 GeV, an $|\eta^{jet}|$ cut less than 3.8, corresponding to the Phase 2 tracker acceptance, was found necessary to maintain the contamination of PU jets in signal (resp. $WZ - QCD$) events from 18% (resp. 69%) to 2% (resp. 11%).

The CMS projection is based on MC samples with full simulation of the CMS detector at 13 TeV and data driven background estimates, see Ref. [357]. The cross sections of samples are scaled for this projection from 13 to 14 TeV using standard model predictions, for the data-driven backgrounds the scaling is done using appropriate mixture of simulated events. The performance of the CMS detector at the HL-LHC at pileup 200 is simulated using Delphes. It is proven that lepton and PUPPI jet recon-

Table 8: Summary of event selection requirements.

Variables	ATLAS	CMS
$\mathrm{p_T}(\ell)$ [GeV]	> 15	> 15
$\mathrm{p_T}(\ell_{lead})$	> 25	–
$\mathrm{p_T}(\ell_{\mathrm{Z},1})$, $\mathrm{p_T}(\ell_{\mathrm{Z},2})$ [GeV]		$> 25, > 15$
$\mathrm{p_T}(\ell_{\mathrm{W}})$ [GeV]	> 20	> 20
$\lvert\eta(\mu)\rvert$	< 4.0	< 2.8
$\lvert\eta(\mathrm{e})\rvert$	< 4.0	< 3.0
$\lvert m_{\mathrm{Z}} - m_{\mathrm{Z}}^{\mathrm{PDG}}\rvert$ [GeV]	< 10	< 15
$m_{3\ell}$ [GeV]	–	> 100
$m_{\ell\ell}$ [GeV]	–	> 4
E_T^{miss} [GeV]	–	> 30
M_T^W [GeV]	> 30	–
n_{j}	≥ 2	≥ 2
$\lvert\eta(j)\rvert$	< 3.8	< 4.7
$\mathrm{p_T^{jet}}$ [GeV]	> 30	> 50
$\Delta R(j, \ell)$	–	> 0.4
$\mathrm{p_T}(b)$ [GeV]	–	> 30
$n_{\mathrm{b-jet}}$	–	$= 0$
m_{jj}	> 500	> 500
$\Delta\eta_{jj}$	Opp. hemis.	> 2.5
$\lvert\eta_{3\ell} - \frac{1}{2}(\eta_{j_1} + \eta_{j_2})\rvert$	–	< 2.5

Table 9: Expected signal and background yields corresponding to the event selection listed in Table 8 for 3000 fb^{-1}. Background contributions are grouped differently for ATLAS and CMS.

Process	ATLAS	CMS
$WZjj - EW$	3889	2757
$WZ - QCD$	29754	3486
$t\bar{t}V$	3145	–
tZ	2221	–
tV/VVV	–	1374
Non prompt	–	1192
ZZ	1970	–
VV	–	398
Zγ	–	296

struction allow to keep the same or better level of reconstruction efficiency and background rejection as in existing data; no additional corrections are applied in the projection. An additional scaling factor is applied to account for the increased pseudorapidity coverage of the Phase 2 CMS detector. The ATLAS and CMS signal and background yields are summarized in Table 9 for the total integrated luminosity of 3000 fb^{-1}.

To extract the electroweak signal ATLAS uses nominally a final m_{jj} cut optimised at 600 GeV or a multivariate analysis (BDT) based on 25 variables that are shown to best separate the signal and background events. The shape of the BDT output is shown in Fig. 23 left. In CMS case a 2D distribution of dijet invariant mass in bins of dijet angular separation is used, as shown in Fig. 23 right. The

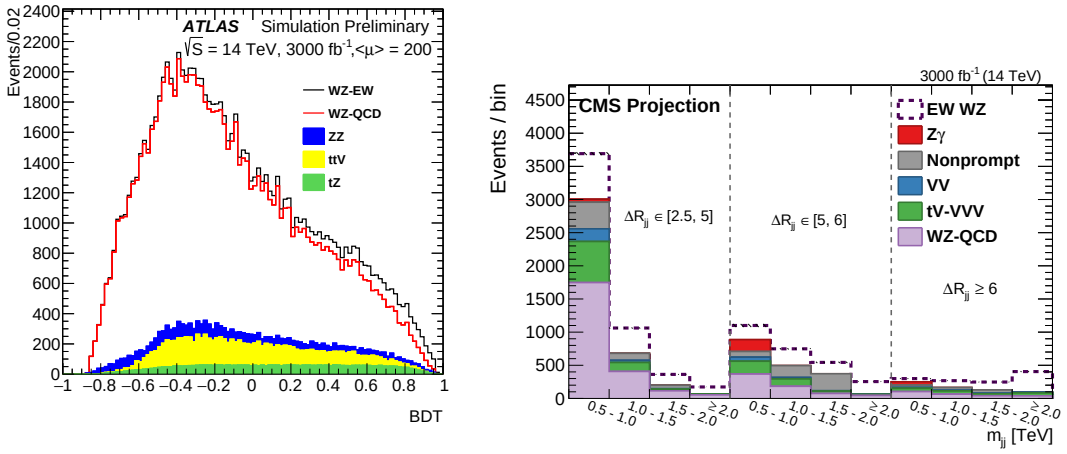

Fig. 23: Example of BDT distribution for 3000 fb^{-1}(left). The m_{jj} distributions in bins of ΔR_{jj} for 3000 fb^{-1}. (right)

measurement of the $WZjj - EW$ production cross section results from a maximum likelihood fit of this distribution performed simultaneously for four different lepton combinations in the final states, each combination being considered as independent decay channel. The systematic uncertainties are represented by nuisance parameters in the fit and are allowed to vary according to their probability density functions. The correlations across bins, between different sources of uncertainty and decay channels is taken into account. The background contributions are allowed to vary within the estimated uncertainties.

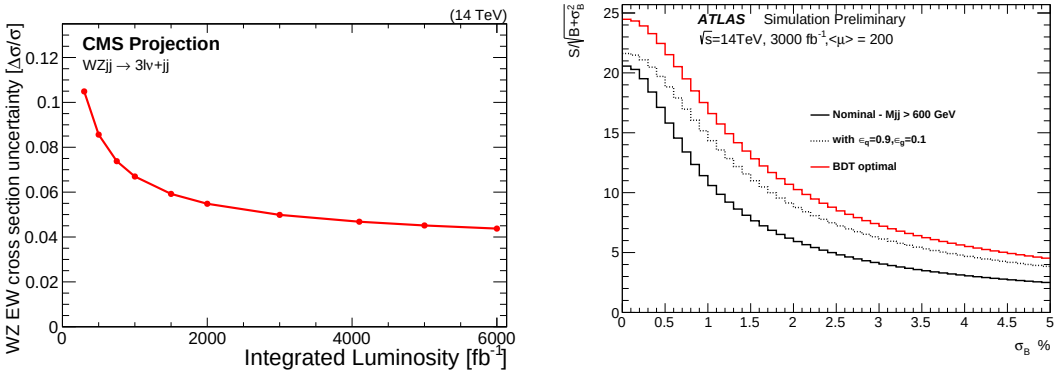

Fig. 24: Expected uncertainty on the cross-section measurement as a function of the integrated luminosity for the CMS projection (left). Signal significance versus the total background uncertainty for the ATLAS simulation (right), presented for the nominal selection, along with two alternative selections meant to mitigate the $WZ - QCD$ background.

The experimental systematic error will be dominated by the jet energy related uncertainties, and amounts to a maximum of 5%. The non-prompt background uncertainty may also be significant depending on the final state. Depending on the level of $WZ - QCD$ background, the theoretical error affecting its modeling will eventually dominant. However it is expected that the impact of these uncertainties can be controlled to less that 5% using refined and diverse control regions allowed by the large statistics at HL-LHC. The total uncertainty of the electroweak cross section measurement as a function of luminosity is shown in Fig. 24 left for the CMS projection, while the signal significance as a function

of the projected total uncertainty on background is presented in Fig. 24 right for the ATLAS simulation as it is arguable whether the theoretical uncertainty can be precisely predicted at this stage.

The polarisation of the final state bosons can be measured inclusively for each boson in two different final state configurations, ZW^+ and ZW^- or combined in a doubly longitudinally polarised final state. The $\cos\theta^*_Z$ ($\cos\theta^*_W$), where θ^*_Z represents the angle of the lepton with the Z (W) direction in the WZ rest frame, is the most sensitive differential distribution to the polarisation of the Z (W) boson. An example of the $\cos\theta^*_Z$ distribution is shown in Fig.25 left for the $WZjj-EW$ signal and the sum of backgrounds for $Z(W^+)$ final state; the distribution is fitted with three parameters: the longitudinal polarised fraction F0, the left-handed minus right-handed contributions and the number of $WZjj-EW$ events using three polarisation templates plus the two background contributions. The result of the fit is shown in Fig. 25 left, where the fraction of $WZjj-EW$ events where the Z-boson is longitudinally, left or right polarised are represented, while the log-likelihood profile corresponding to F0 is presented in Fig. 25 right. The significance to measure F0, computed as $\sqrt{-2log(\lambda(F0=0))}$, is estimated to be between 1.5 and 2.5 σ for $Z(W^+)$ and 0.7 and 1.5 σ for W^- depending on the final selection that affects the signal purity, and systematic assumptions on the total background normalisation.

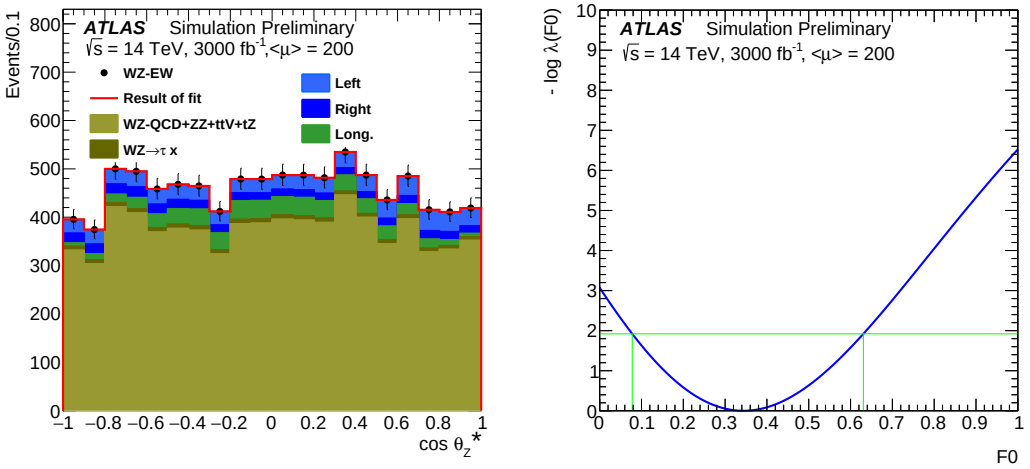

Fig. 25: Distribution of $\cos\theta^*_Z$ for 3000 fb^{-1} and result of the fit of the long. polarised contribution (F0), left and right handed contributions on top of the sum of backgrounds and of the $WZ \to x\tau$ background, both contributions taken into account with a normalisation error of 2.5% (left). Shape of the log-likelihood profile for the F0 parameter around its minimum. (right)

To measure the doubly longitudinal (LL) process, an approach based on the jets kinematics similar to this for the total $WZjj-EW$ cross-section is used by CMS. The LL fraction is expected to be of the order of 5% of the total $WZjj-EW$ production ([359]) and its unrolled 2D distribution is shown in Fig 26 left for 3000 fb^{-1}. It can be observed that the LL contribution is increasing from 2-3% to 7-8% for high angular separation between jets and for high invariant mass of the dijet system. In the fit, the LL fraction is considered as signal, while the rest of the $WZjj-EW$ process is considered as an additional background. The systematic uncertainties of the LL and non-LL fractions are considered as fully correlated within the total electroweak cross section. The significance of the LL observation as a function of integrated luminosity is shown in Fig. 26 right: the red curve presents the significance if only statistical uncertainties of the measurement are taken into account and the black line presents the results including the systematics as discussed above.

The results presented in this section confirm that the $WZjj-EW$ cross section can be measured with accuracy at the HL-LHC if the jets from pileup collisions in the events are well separated from

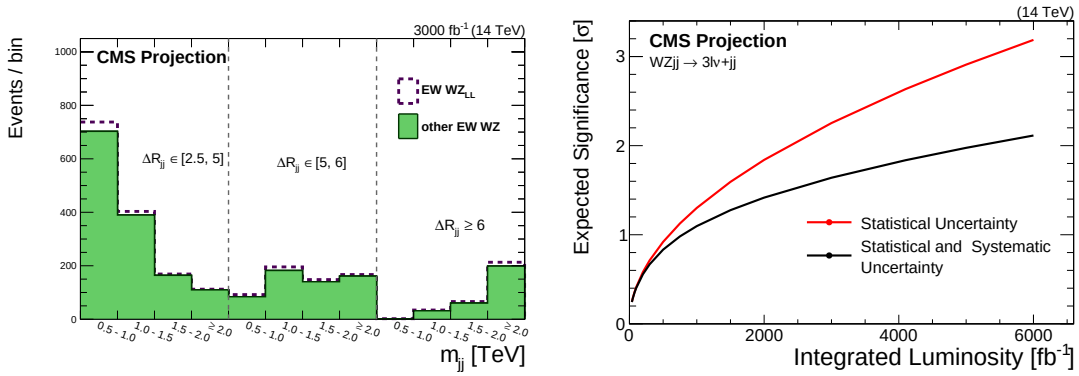

Fig. 26: Unrolled 2D ($\Delta R_{jj}; m_{jj}$) LL and non-LL distribution for 3000 fb^{-1}(left). Significance of the LL observation with and without systematic error. (right)

the jets produced in the hard interactions. Increased pseudorapidity coverage of the detectors should improve precision of such measurement. The single polarized cross sections can also be measured and the double polarized measurement requires more sophisticated methods, including development of multivariate discriminants for better separation of the signal from background. Systematic uncertainties also start to play a significant role at the HL-LHC, in particular those affecting the theoretical prediction.

4.2.4 ZZ scattering measurement at high luminosity and high energy LHC

This section presents the studies performed for VBS in the ZZ fully leptonic decay channel for HL-LHC and HE-LHC. Despite the very low cross section times branching fraction, the reconstruction of all final state leptons allows to precisely measure the angular distributions of the Z decays to optimally separate the longitudinal from the dominating transverse polarizations. In addition, a precise measurement of the hard scattering center-of-mass energy is possible from the reconstructed four-leptons invariant mass. Last but not least, the reducible background in this channel is very small, making it an ideal case for high statistics measurement since the impact of associated experimental systematics uncertainties is expected to be very small.

The ATLAS analysis is performed with simulated events at generator level at 14 TeV, where the detector effects of lepton and jet reconstruction and identification were estimated by corrections, assuming a mean number of interactions per bunch crossing of 200. The CMS analysis is based on the experimental investigation of VBS in the ZZ channel using 36fb^{-1}of data collected in 2016 [360], which is projected to HL-LHC conditions by scaling the expected yields for the signal and background processes, taking into account the increase in luminosity and scattering energy as well as the changes in acceptance and selection efficiencies between the Phase-1 (13 TeV) and the Phase-2 (14 TeV) configurations. The Delphes simulation [232] is then used to assess the sensitivity to VBS $Z_L Z_L$. The HL-LHC result is further projected to the HE-LHC configuration.

Several Monte Carlo event generators were used to simulate the signal and background contributions. In the ATLAS analysis, both the EW-ZZjj and QCD-ZZjj processes with the $ZZ \rightarrow 4\ell$ decays are modeled using SHERPA v2.2.2 [84] with the NNPDF3.0NNLO [361] parton distribution functions (PDFs) set. The signal sample is generated with two jets at Matrix Element (ME) level. The background process is modeled with next-to-leading order (NLO) QCD accuracy for events with up to one outgoing parton and with leading order (LO) accuracy for the case with two and three partons, in a phase space of $m_{\ell\ell} > 4$ GeV and at least two leptons with $p_{\mathrm{T}} > 5$ GeV. Other backgrounds have minor contributions to the 4ℓ channel and therefore are not included. The CMS analysis uses MADGRAPH5_aMC@NLO v2.3.3 [362] to simulate the EW-ZZjj signal and QCD-ZZjj background samples

with zero, one, and two outgoing partons at Born level at NLO. The different jet multiplicities are merged using the FxFx scheme [363] with a merging scale of 30 GeV, and leptonic Z boson decays were simulated using MADSPIN [364]. The gluon loop-induced production of two Z bosons (ggZZ) is simulated at LO with MCFM v.7.0.1 [365], and checked with a dedicated simulation of the loop-induced $gg \to ZZjj$ process using MADGRAPH5_aMC@NLO. The NNPDF3.0 PDF set is also used. The interference between EW-ZZjj and QCD-ZZjj processes is found to be small and is neglected in both analyses. Simulated samples with polarization information on the outgoing Z bosons are generated using MADGRAPH v5.4.2 [359] and the DECAY package from MADGRAPH5_aMC@NLO v1.5.14.

The selections are based on Run 2 analyses and have been modified according to the expected changes for the detectors at HL-LHC. The foreseen forward lepton coverage is up to $|\eta| = 4.0$ for both electrons and muons in ATLAS, while it is is up to $|\eta| = 3.0(2.8)$ for electrons (muons) in the CMS upgrade, with an option for an extension of up to $|\eta| = 4.0$ for electrons. Candidate events should contain two pairs of oppositely charged isolated leptons (electrons or muons), consistent with the decays of two on-shell Z bosons. The VBS topology is ensured by requiring at least two jets with large invariant mass and η separation in the cut based analysis, whereas an inclusive selection is used when the signal extraction is performed with a multivariate discriminant (BDT). Table 10 summarizes the details of the selection criteria used by the ATLAS and CMS collaborations.

Table 10: Event selections used in ATLAS and CMS analyses. For the leptons η and p_{T} in CMS the first number refers to electrons and the second to muons.

	ATLAS	CMS
lepton η	$\lvert\eta\rvert < 4.0$	$\lvert\eta\rvert < 3.0(2.8)$ ($\lvert\eta\rvert < 4.0(2.8)$, extended option)
lepton p_{T}	$p_{\mathrm{T}} > 20, 20, 10, 7$ GeV	$p_{\mathrm{T}} > 20, 12(10), 10, 7(5)$ GeV
N leptons	exactly 4	≥ 4
Z mass	$60 < m_{ll} < 120$ GeV	$60 < m_{ll} < 120$ GeV
Z_1 definition	m_{ll} closest to PDG [366] value	p_{T}-leading Z
jet η	$\lvert\eta\rvert < 4.5$	$\lvert\eta\rvert < 4.7$
jet p_{T}	$p_{\mathrm{T}} > 30(70)$ GeV for $\lvert\eta\rvert < 3.8(> 3.8)$	$p_{\mathrm{T}} > 30$ GeV
N jets	≥ 2, with $\eta^{j_1} \times \eta^{j_2} < 0$	≥ 2
VBS cuts	$m_{jj} > 600$ GeV and $\lvert\Delta\eta_{jj}\rvert > 2$	$m_{jj} > 100$ GeV, signal extraction from BDT

The distributions of the dijet invariant mass (m_{jj}) and ZZ invariant mass (m_{ZZ}) are shown in Fig. 27, after the ATLAS event selection. The numbers of selected signal and background events are quoted in Table 11, normalized to 3000 fb^{-1} of integrated luminosity. In addition to the baseline selection, two alternative selections are also studied to compare different detector scenarios at the HL-LHC. Uncertainties in the table refer to expected data statistical uncertainty at 14 TeV with 3000 fb^{-1}. The

Table 11: Comparison of event yields for the signal ($N_{\mathrm{EW-ZZjj}}$) and background ($N_{\mathrm{QCD-ZZjj}}$) processes, and expected significance of EW-ZZjj processes, normalized to 3000 fb^{-1} data at 14 TeV, for baseline and alternative selections.

Selection	$N_{\mathrm{EW-ZZjj}}$	$N_{\mathrm{QCD-ZZjj}}$	$N_{\mathrm{EW-ZZjj}} / \sqrt{N_{\mathrm{QCD-ZZjj}}}$
Baseline	432 ± 21	1402 ± 37	11.5 ± 0.6
Leptons with $\lvert\eta\rvert < 2.7$	373 ± 19	1058 ± 33	11.5 ± 0.6
PU jet suppression only in $\lvert\eta\rvert < 2.4$	536 ± 23	15470 ± 124	4.3 ± 0.2

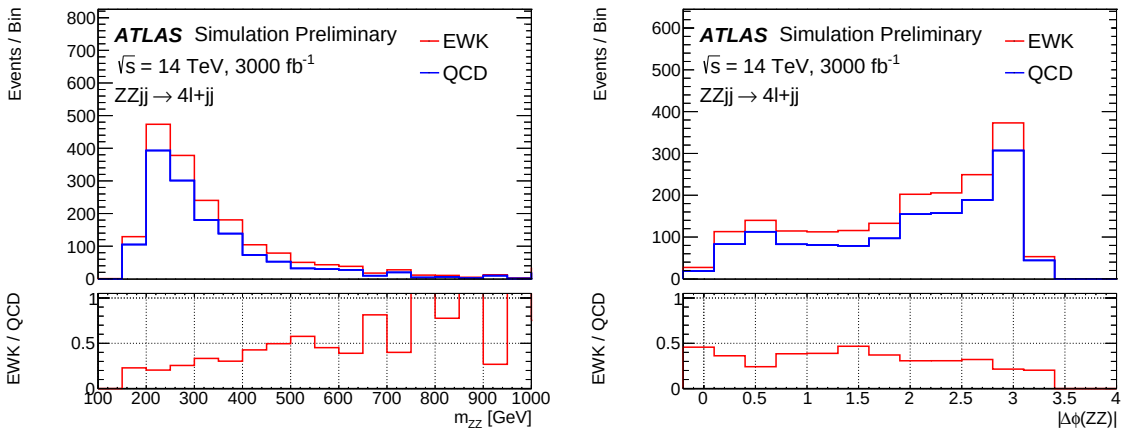

Fig. 27: Detector-level distributions of $m_{jj}$and m_{ZZ} for the EW and QCD processes after the cut-based event selection. Distributions are normalized to 3000 fb^{-1} (SF Is this caption correct?).

benefit of the extension for the rejection of PU jets is clear. The extended tracking coverage improves the lepton detection efficiency and increases the number of signal events, providing larger event yield for differential cross-section measurements and for the longitudinal scattering. However, the overall significance of observing the EW-ZZjj process does not improve as much, due to larger increase of the QCD-ZZjj background contribution. This is due to the ZZ system being more centrally produced in EW processes than in QCD processes. These results, however, do not include the gluon-induced contribution, for which the ZZ system is found to be more centrally produced than for the leading quark-induced contribution. Moreover, in the case of the longitudinal scattering, the η distribution of longitudinally polarized Z bosons is peaked in the forward region, therefore extended coverage is beneficial in this case as will be shown in the following.

The dominant systematics for 4ℓ channel are from theoretical modeling of the QCD-ZZjj background processes. The ATLAS analysis considers different sizes of systematic uncertainty in the background modeling of 5, 10 and 30%. The 30% uncertainty is a conservative estimation from direct calculation by comparing different choices of PDF sets and QCD renormalization and factorization scales, following recommendation from PDF4LHC [153]. The 5% one is an optimistic estimation where enough data events from QCD enriched control region at the HL-LHC could be used to provide constrain on the theoretical modeling of QCD-ZZjj processes. For the experimental sources, the jet uncertainties have been checked following the studies in Ref. [367] and the effect is within fluctuation of the simulated events, which is at the 5% level. Thus a 5% uncertainty is used as a conservative estimate of the experimental uncertainties. In this analysis these uncertainties are treated as uncorrelated and summed up quadratically. The CMS analysis considers two scenarios for the systematic uncertainties. The first scenario ('Run 2 scenario') consists in using the same systematic uncertainties as that used for the Run 2 analysis, apart from the uncertainty in the gluon-induced background contribution for which a 10% uncertainty is considered. In the second scenario ('YR18 scenario'), improved systematic uncertainties are assumed to be obtained from the more data and better understanding of the detector. In this scenario, the theory systematic uncertainties (PDF and QCD scales) are furthermore halved with respect to the Run 2 scenario. In this analysis the systematic uncertainties are considered as nuisances in the fit and profiled.

Figure 28 (left) shows the result of a scan over different m_{jj} cuts in addition to the ATLAS baseline selection, for an integrated luminosity of 3000 fb^{-1}. The expected significance of EW-ZZjj

production processes is calculated as Significance $= S/\sqrt{\sigma(B)^2_{stat.} + \sigma(B)^2_{syst.}}$, where S denotes the number of signal events after the selection, and $\sigma(B)_{stat.}$ and $\sigma(B)_{syst.}$ refer to the statistical and systematic uncertainties in background yield. The statistical uncertainty is estimated from expected data yield at 14 TeV with 3000 fb^{-1}.

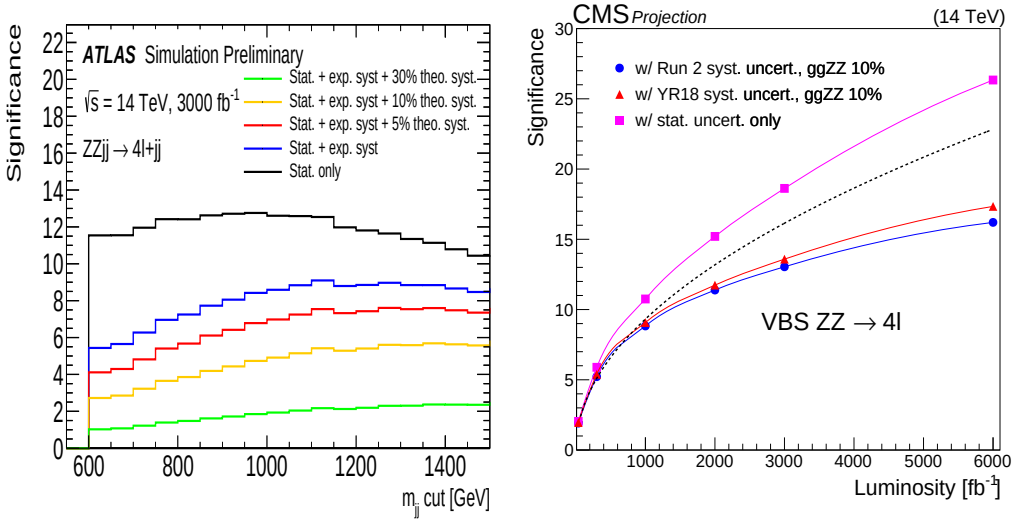

Fig. 28: Expected significance of EW-ZZjj processes as a function of different m_{jj} cuts for 3000 fb^{-1}, for different sizes of theoretical uncertainties in the QCD-ZZjj background modeling (left). Projected significance in the multivariate analysis as a function of the integrated luminosity for the two considered scenario and a 10% uncertainty in the loop-induced ggZZ background yield, as well as with only the statistical uncertainties included (right).

The CMS analysis employs a multivariate discriminant based on a boosted decision tree (BDT) to extract the EW-ZZjj signal from the QCD-ZZjj background processes. Seven observables are used in the BDT, including m_{jj}, $|\Delta\eta_{\mathrm{jj}}|$, m_{ZZ}, as well as the Zeppenfeld variables [368] $\eta^*_{\mathrm{Z}_{1,2}} = \eta_{\mathrm{Z}_{1,2}} - (\eta_{\mathrm{jet}_1} + \eta_{\mathrm{jet}_2})/2$ of the two Z bosons, and the ratio between the p_{T} of the tagging jet system and the scalar sum of p_{T} of the tagging jets ($R(p_{\mathrm{T}})^{\mathrm{jets}}$). The BDT also exploits the event balance $R(p_{\mathrm{T}})^{\mathrm{hard}}$, defined as the transverse component of the vector sum of the Z bosons and tagging jets momenta, normalized to the scalar p_{T} sum of the same objects [369]. The modeling of all these observables was checked with Run 2 data in a background-enriched region [360]. A maximum likelihood fit of the BDT distributions for signal and backgrounds is used to extract the signal strength. The shape and normalization of each distribution are allowed to vary within their respective uncertainties. Figure 28 (right) shows the projected significance for a 10% uncertainty in the loop-induced ggZZ background yield, as a function of the integrated luminosity and for the two scenarios described above, as well as for a scenario with only the statistical uncertainty included. The dashed line shows the projected significance as obtained scaling the 2016 result with statistical uncertainty only by the luminosity ratio. The impact of a multivariate analysis is clear for such small signal. The expected significance is 13.0σ (13.6σ) for the Run 2 (YR18) scenario, for a 10% uncertainty in the loop-induced ggZZ background yield and an integrated luminosity of 3000 fb^{-1}.

A fiducial phase space is defined at generator level with the same kinematic selections as listed in Table 10, and is used to study the expected precision of the cross-section measurements. Table 12 shows the expected cross-section measurement in this phase space for 3000 fb^{-1}, with the statistical only case, and the cases with different sizes of theoretical uncertainties. The statistical uncertainty is at 10% level and the integrated cross-section measurement becomes dominated by experimental and

modeling uncertainty in the QCD-ZZjj background. For the possible extension of the HL-LHC run to 4000 fb^{-1}, the statistical uncertainty will be further reduced to 8% level.

Table 12: Summary of expected cross-section measurements for different theoretical uncertainties. The statistical uncertainty is estimated from expected data yield at 14 TeV with 3000 fb^{-1}. Different uncertainties are summed up quadratically.

	Cross section [fb]	Stat. only	Plus exp.	Plus 5% theo.	Plus 10% theo.	Plus 30% theo.
EW-ZZjj	0.21	$\pm$0.02	$\pm$0.04	$\pm$0.05	$\pm$0.08	$\pm$0.21

The projected measurement uncertainty from the CMS analysis is 9.8% (8.8%) for the Run 2 (YR18) scenario and for a 10% uncertainty in the loop-induced ggZZ background yield, for an integrated luminosity of 3000 fb^{-1}and a coverage of up to $|\eta| = 3$ for electrons. Extending the coverage up to $|\eta| = 4$ for electrons, the expected measurement uncertainty becomes 9.5% and 8.5%, respectively. In these estimates it is assumed that a fiducial cross section close to the detector volume is used, such that the measurement is to first order insensitive to theoretical uncertainties in the signal cross section.

In addition, the expected differential cross-section measurements of the EW-ZZjj processes at 14 TeV have been studied in the defined phase space, as a function of m_{jj}, and m_{ZZ}, as shown in Fig. 29. The expected differential cross-section measurements are calculated bin by bin as

$$\sigma = \frac{N_{pseudo-data} - N_{QCD-ZZjj}}{L * C_{EW-ZZjj}},\ C_{EW-ZZjj} = \frac{N^{det.}_{EW-ZZjj}}{N^{part.}_{EW-ZZjj}}, \tag{19}$$

where $N_{pseudo-data}$ is the expected number of data events with 3000 fb^{-1} luminosity, and $N_{QCD-ZZjj}$ and $N_{EW-ZZjj}$ are the number of predicted events from QCD-ZZjj and EW-ZZjj processes, respectively. The $C_{EW-ZZjj}$ factor refers to the detector efficiency for EW-ZZjj processes, calculated as number of selected signal events at detector level ($N^{det.}_{EW-ZZjj}$), divided by number of selected events at particle level in the fiducial phase space ($N^{part.}_{EW-ZZjj}$). Both the statistical only case (statistical uncertainty is estimated from expected data yield at 14 TeV with 3000 fb^{-1}) and the ones with different sizes of theoretical uncertainties on the background modeling are shown in Fig. 29.

The decay angle $\cos\theta^*$ of the lepton direction in the Z decay rest frame with respect to the Z momentum direction in the laboratory frame is the most distinctive feature of longitudinal Z bosons ($\mathrm{Z_L}$). The Z boson p_{T} and η distributions also carry information on $\mathrm{Z_L Z_L}$ production, in particular longitudinal Z bosons are produced with a lower p_{T} and more forward, compared to transverse polarizations ($\mathrm{Z_T}$). The distributions of $\cos\theta^*$, p_{T} and η of both Z bosons, together with the distributions of all observables used to separate VBS processes from QCD backgrounds and described above are employed as input to a BDT to separate the VBS $\mathrm{Z_L Z_L}$ signal from all backgrounds. The BDT is trained separately to discriminate the VBS $\mathrm{Z_L Z_L}$ signal from the QCD backgrounds (QCD BDT) and to discriminate the VBS $\mathrm{Z_L Z_L}$ signal from the VBS background (VBS BDT). Cut values are defined on the QCD BDT and on the VBS BDT output values, which maximizes the overall significance estimator $S/\sqrt{B}$ for the selected events. The corresponding signal efficiency is 14.1% and the VBS, leading QCD-ZZjj and loop-induced ggZZ background efficiencies are 1.6%, 0.03% and 0.05%, respectively. It is assumed that the VBS $\mathrm{Z_L Z_L}$ fraction, defined as VBS $\mathrm{Z_L Z_L}$/VBS $(\mathrm{Z_L Z_L} + \mathrm{Z_L Z_T} + \mathrm{Z_T Z_T})$ will be measured, rather than the absolute VBS $\mathrm{Z_L Z_L}$ cross section. In such ratio measurement, the systematic uncertainties from luminosity, and selection efficiency, as well as theoretical uncertainties on the VBS and VBS background cross section cancel out, such that only the uncertainties in the QCD backgrounds yields are considered.

Figure 30 shows the expected significance for the VBS $\mathrm{Z_L Z_L}$ fraction as a function of the integrated luminosity and for the two scenarios described above and a 10% uncertainty in the loop-induced

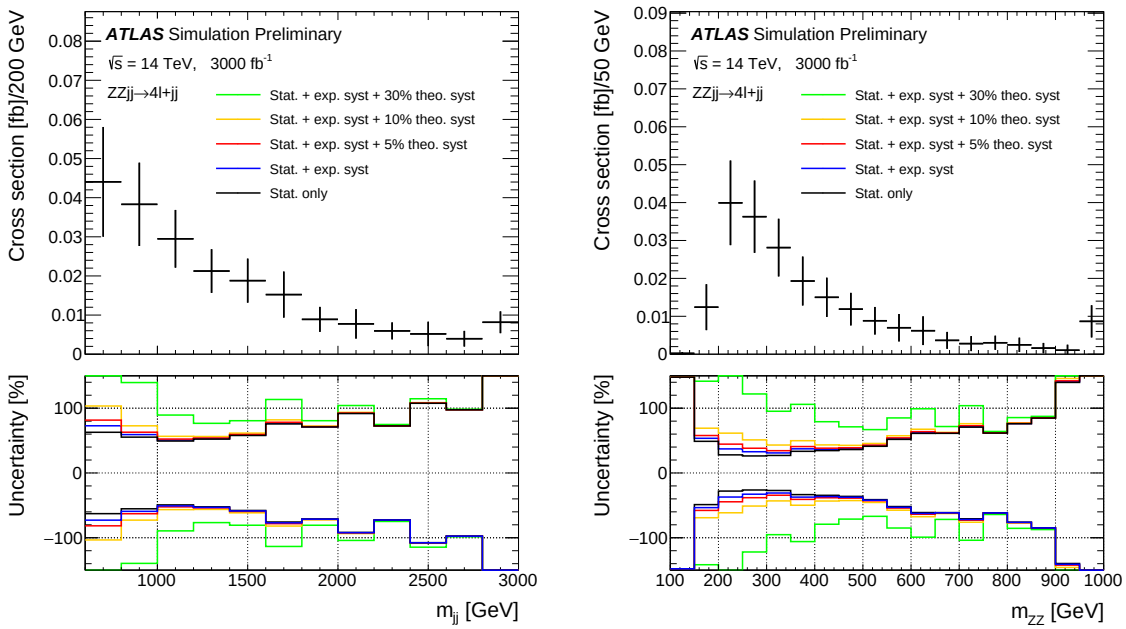

Fig. 29: Expected differential cross-sections at 14 TeV for the EW-ZZjj processes as a function of m_{jj}(left) and m_{ZZ}(right). Results are shown with different sizes of systematic uncertainties.

ggZZ background yield, as well as for a scenario with only the statistical uncertainty included. A significance of 1.4σ is reached for 3000 fb^{-1}. As expected from the ratio measurement, the effect of systematic uncertainties is very small. Results are also shown for an integrated luminosity of 6000 fb^{-1}, which would approximately correspond to combining ATLAS and CMS after 3000 fb^{-1}. Table 13

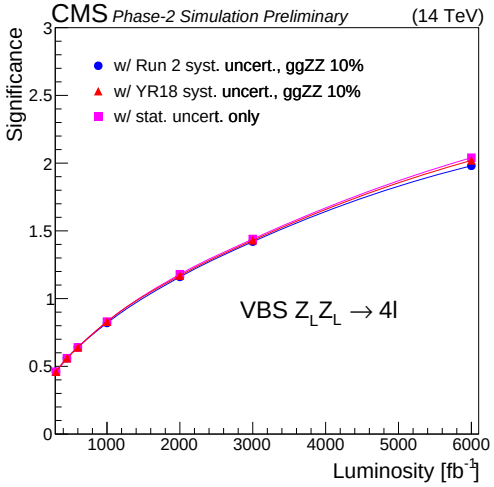

Fig. 30: Expected significance for the VBS $\mathrm{Z_L Z_L}$ fraction as a function of the integrated luminosity and for systematic uncertainties according to the Run 2 and YR18 scenario, as well as with only the statistical uncertainties included.

presents the expected significance and relative uncertainty in the VBS $\mathrm{Z_L Z_L}$ fraction for various η coverage configurations. The foreseen coverage extension of up to $|\eta| = 3\ (2.8)$ for electrons (muons) leads to a $\sim 13\%$ improvement for the significance and precision on the VBS $\mathrm{Z_L Z_L}$ fraction. An extension of

up to $|\eta| = 4$ for electrons would allow to further improve by $\sim 4\%$ both significance and cross section measurement uncertainty.

Table 13: Significance and measurement uncertainty for the VBS $\mathrm{Z_L Z_L}$ fraction for different acceptance configurations. In the quoted η coverages, the first number corresponds to electrons while the number in parentheses corresponds to muons.

η coverage	significance	VBS $\mathrm{Z_L Z_L}$ fraction uncertainty (%)
$\|\eta\| < 2.5$ (2.4)	1.22σ	88
$\|\eta\| < 3.0$ (2.8)	1.38σ	78
$\|\eta\| < 4.0$ (2.8)	1.43σ	75

Finally, a simple scaling of the signal and background cross sections is performed to assess the sensitivity to the VBS $\mathrm{Z_L Z_L}$ fraction at HE-LHC. An integrated luminosity of 15 ab^{-1} is considered, together with a c.o.m energy of 27 TeV. The cross section ratios $\sigma_{27\,\mathrm{TeV}}$ / $\sigma_{14\,\mathrm{TeV}}$ are evaluated at LO with MADGRAPH(v5.4.2) [359] for the EW signal and the leading QCD-ZZjj background, and with MCFM(v.7.0.1) [365] for the ggZZ loop-induced background. Table 14 shows the expected significance and relative uncertainty for the VBS $\mathrm{Z_L Z_L}$ fraction at HE-LHC, compared to HL-LHC. The HE-LHC machine would allow to bring the sensitivity (uncertainty) for the measurement of the VBS $\mathrm{Z_L Z_L}$ fraction at the level of $\sim 5\sigma$ ($\sim 20\%$).

Table 14: Expected significance and measurement uncertainty for the VBS $\mathrm{Z_L Z_L}$ fraction at HL-LHC and HE-LHC with and without systematic uncertainties included.

	significance		precision (%)	
	w/ syst. uncert.	w/o syst. uncert.	w/ syst. uncert.	w/o syst. uncert.)
HL-LHC	1.4σ	1.4σ	75%	75%
HE-LHC	5.2σ	5.7σ	20%	19%

4.2.5 Prospects for electroweak WW/WZ production via vector boson scattering in the semi-leptonic final states at HL-LHC and HE-LHC

The study of the high-energy scattering between the longitudinal components of the vector bosons (vector boson scattering or VBS) is a perfect case to search systematically for the presence of new particles or interactions behind the breaking of the EW symmetry. In fact, the scattering amplitude of the VBS processes, in absence of the Higgs boson, would grow indefinitely with the center-of-mass energy. This important high-energy behavior still needs to be tested experimentally and it will be one of the main drivers of the physics program for the HL-LHC. The existing Run-2 VBS measurements have focused on channels involving the fully leptonic boson decays, or decay modes involving photons. The semileptonic channels can however offer some interesting advantages: the $V \to qq$ branching fractions are much larger than the leptonic ones and the use of jet substructure techniques with large-radius jet reconstruction allows to reconstruct and identify the V-boson produced in the high-p_{T} region, which is the most sensitive to new physics effects. This section presents the sensitivity of the ATLAS experiment to VBS in the $V(qq)W(\ell\nu)$ final state, assuming an integrated luminosity of 300 or 3000 fb^{-1} of pp collisions at $\sqrt{s}$= 14 TeV.

This analyses uses generator-level samples of the main signal and background processes, combined with the parameterizations of the detector performance (muon and jet reconstruction and selection

efficiencies and momentum resolutions) expected at the HL-LHC from fully simulated samples. The parametrized detector resolutions are used to smear the generator-level particle transverse momenta, while the parametrized efficiencies are used to reweigh the selected events. All generated samples were produced at $\sqrt{s}$= 14 TeV and normalized to luminosities of 300 or 3000 fb^{-1} when the results are presented.

The electro-weak (EWK) $VVjj$ production is modeled using MADGRAPH5_AMC@NLO v2.3.3 [12], plus PYTHIA8 [251] for fragmentation. The main background sources are W bosons produced in association with jets (W+jets), with significant contributions from top-quark production (both $t\bar{t}$ pair and single-top), non-resonant vector-boson pair production (ZZ, WZ and WW) and Z bosons produced in association with jets (Z+jets). Background originating from multi-jet processes are expected to be negligible due to the event selection requirements. Details about the samples generation can be found in

To increase the purity of considered events, several requirements are placed on the constituents of an event. Events are required to have exactly one lepton. Generator-level electrons or muons are required to be isolated and pass the tight identification criteria [370] and to have $p_{\mathrm{T}} > 27$ GeV. Events are required to contain a hadronically-decaying W/Z candidate, reconstructed either from two small-R jets, defined as the resolved channel, or from one large-R jet, designated the boosted channel. Small-R jets are defined using the anti-k_t algorithm [371] with a radius parameter of R = 0.4. The identification of jets originating from b-quarks is done by finding jets with generator-level b-hadron within a cone of $\Delta R < 0.4$ around the jet direction. Similarly, the anti-k_t algorithm with a radius parameter of R = 1.0 is used to reconstruct large-R jets. The large-R jets are trimmed using the standard ATLAS trimming parameters [372]. It is assumed that the performance of a future W/Z-boson tagger at the HL-LHC conditions will have similar, if not better, performance as existing boson taggers. To simulate the effect of Run-2 W/Z-boson tagging performance [373, 374] events which contain a large-R jet are scaled by the expected boson tagging efficiency for the $V \rightarrow qq$ with kinematics corresponding to the large-R jet, calculated from fully-simulated 13 TeV Monte-Carlo (MC) samples. The missing transverse energy E_{T}^{miss} is required to be greater than 60 GeV, which suppresses the expected multijet background to a negligible level. By constraining the E_{T}^{miss} + lepton system to be consistent with the W mass, the z component of the neutrino (ν) momentum can be reconstructed by solving a quadratic equation.

Experimentally, VBS is characterized by the presence of a pair of vector bosons and two forward jets with a large separation in pseudorapidity and a large dijet invariant mass. Therefore the VBS search is required to have 2 additional forward VBS-topology tagging jets in the event in addition to jets associated with the boson decay, similar to the resonant VBF search. The VBS tagging jets are required to be non-b-tagged, be in the opposite hemispheres, $\eta(j_1^{\mathrm{tag}}) \cdot \eta(j_2^{\mathrm{tag}}) < 0$, and to have the highest dijet invariant mass among all pairs of jets remaining in the event after the $V \rightarrow jj$ jet selection. After the tagging jet pair are selected, it is required that both tagging jets should have p_{T} >30 GeV, and that the invariant mass of the two tagging jets system is greater than 400 GeV . In the merged selection, events are required to have at least one large-R jet with $p_{\mathrm{T}}(J) > 200$ GeV and $|\eta(J)| < 2$. From those candidate large-R jets, the one with the smallest $|m(J) - m(W/Z)|$ is selected as the signal large-R jet. Mass window cuts and boson tagging efficiencies are applied as described above. To suppress backgrounds with top quarks, an event is rejected if any of the reconstructed jets outside the large R jet, is identified as containing a b-quark. If events fail the merged VBS selection, the resolved selection is then applied. Signal jets are chosen as the pair with $m(jj)$ closest to the W/Z mass. The signal jet pairs are then required to have $|m(jj) - m(W/Z)| < 15$ GeV. To suppress backgrounds with top quarks, an event is rejected if any of the reconstructed jets is identified as containing a b-quark.

To optimize the signal sensitivity, Boosted Decision Trees (BDT) for the resolved and merged searches were trained on the background and signal MC samples in the respective regions. Four variables are included in the merged BDT: the invariant mass of the lvJ system, the lepton η, the second tag jet p_T and the boson centrality ζ_V. The boson centrality is defined as $\zeta_V = min(\Delta\eta_+, \Delta\eta_-)$ where $\Delta\eta_+ =$

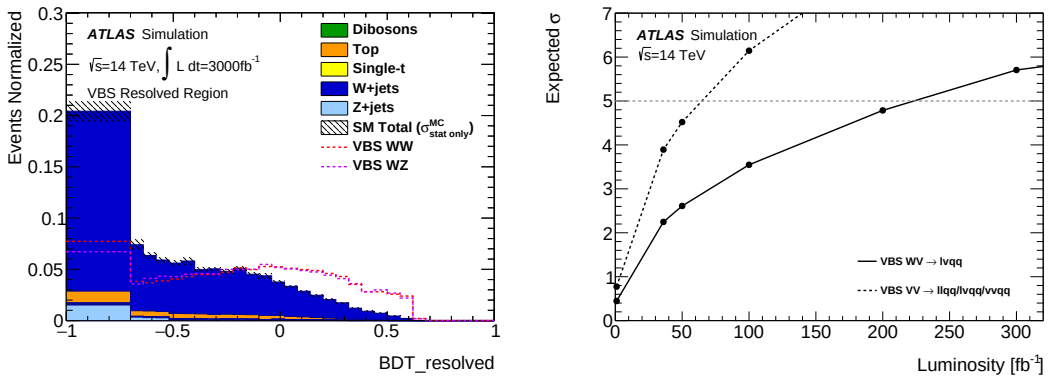

Fig. 31: Final signal and background distributions for the VBS search in the respective resolved signal region for the normalized BDT response. Background distributions are separated into production type. VBS signals in WW and WZ mode are overlayed as dashed curves where appropriate. Both background and signal BDT distributions are normalized to unity (left). Expected signal significance as a function of integrated luminosity up to 300 fb^{-1}. The solid black curve is the significance from the $\ell\nu qq$channel, while the black dashed curve shows the expected significance from all semi-leptonic channels assuming equal sensitivity (right).

$max(\eta(j_1^{\text{tag}}), \eta(j_2^{\text{tag}})) - max(\eta(\ell\nu), \eta(J))$ and $\Delta\eta_- = min(\eta(\ell\nu), \eta(J)) - min(\eta(j_1^{\text{tag}}), \eta(j_2^{\text{tag}}))$. In the resolved BDT, eight variables were used: the invariant mass of the $WVjj$ system , the lepton η, the p_T of both VBS-tagging jets and sub-leading signal jet, the boson centrality defined similarly to above, the $\Delta\eta$ between signal jets, and the ΔR between the lepton and neutrino candidate. These variables were chosen as they are the minimal subset of variables with the greatest separation between the signal and background, that provide significant improvement when added during the training. The BDT were trained using a gradient descent BDT algorithm, maximizing the the Gini index, in the TMVA package [375]. The BDT are chosen as the discriminants and their distributions are used in the final fit for the VBS search shown in Figure 31.

If an event fails either a mass-window cut or a b-veto but passes all other events then the event is categorized as a W or top control region. These regions are used to constrain the normalization and shape systematics of the background.

The results are extracted by performing a simultaneous binned maximum-likelihood fit to the BDT distributions in the signal regions and the W+jets and $t\bar{t}$ control regions. A test statistic based on the profile likelihood ratio [376] is used to test hypothesized values of the signal cross-section. The likelihood is defined as the product of the Poisson likelihoods for all signal and control regions for a given production mechanism category and channel. Systematic uncertainties are taken into account as constrained nuisance parameters with Gaussian or log-normal distributions. The main background modelling systematics, namely the W+jets and $t\bar{t}$ shape uncertainties, are constrained by the corresponding control regions and are treated as uncorrelated among the resolved and merged signal regions.

The expected significance for the SM VBS process is 5.7σ at 300 fb^{-1} as shown in Fig. 31. The expected cross-section uncertainties are 18% at 300 fb^{-1} and 6.5% at 3000 fb^{-1}. The effects of unfolding were not considered for the cross-section estimates. If control regions are not used to constrain the systematics the expected significance is reduced to 3.6σ at 300 fb^{-1}. Likewise the cross-section uncertainty are increased to 28% at 300 fb^{-1} and 10% at 3000 fb^{-1} when control regions are ignored.

4.2.5.1 *Electroweak WW/WZ production analysis at HE-LHC*

The prospect analysis at HE-LHC [Cavaliere:2018zcf] mimics the analysis at HL-LHC but the Delphes simulation is used [377]. VBS signal samples are procuded in the same manner as the HL-LHC analysis. The major backgrounds W+jets and $t\bar{t}$ production are simulated with MADGRAPH and AMC@NLO respectively, interfaced with Pythia. Z+jets, single top and diboson contribution are not simulated and are expected to contribute at most 10% to the total background.

The unprecedented energy of pp collisions at the HE-LHC will significantly improve sensitivity to new multi-TeV particles over LHC and HL-LHC. However, the experimental environment is expected to be challenging at the HE-LHC , primarily due to a significant increase of the number of pp collisions in a same and nearby bunch crossings (pile-up). The HE-LHC is planned to be operated at a centre-of-mass energy of 27 TeV with 800 pile-up collisions at the peak luminosity. Such extreme pile-up conditions are expected to be particularly challenging for identifying hadronically decaying W/Z boson as the extra contribution of particles produced from pile-up collisions into jets could degrade the performance of W/Z boson tagger significantly. It is therefore important to assess the performance of pile-up mitigation technique at the HE-LHC in order to have a reliable estimate of the search sensitivity.

The study presented here focuses on the performance of pile-up mitigation techniques and W/Z boson tagging. The VBS signal events are produced with the overlay of minimum-bias pp interactions generated using Pythia 8. The minimum-bias interactions are overlaid onto hard scattering event using Poisson probability distribution with the mean number of interactions (μ_{pileup}) varied from 0 to 100, 200, 400 and 800. Furthermore, the minimum-bias interactions are distributed randomly in z and timing using Gaussian profiles of $\sigma_z = 5.3$ cm and $\sigma_t = 160$ ps, respectively (z=0 at the detector center and t=0 for hard scattering event). The overlaid VBS signal events are processed through Delphes with two pile-up mitigation techniques: the Pile-up Per Particle Identification (PUPPI) algorithm [328] used in CMS and the trimming procedure used in ATLAS. The trimming parameters of the p_T fraction cut and the sub-jet reclustering radius are chosen to be the same as those used in ATLAS. For the PUPPI algorithm the standard Delphes implementation is used.

Figure 32 shows the leading large-R jet mass (m_J)for the PUPPI-only jets and the PUPPI+trimmed jets, both required to have $p_T > 200$ GeV. The m_J distribution get shifted towards lower values with the trimming applied, enhancing the peak around m_W . The residual pile-up effect is still visible as a shift towards larger values with increasing μ_{pileup}, but the overall signal yield after the mass-window and D_2 requirements (e.g, $D_2 < 1.5$) is largely stable. This indicates that an impact to the W/Z-boson tagging performance from expected pile-up collisions at the HE-LHC can be mitigated to the level where the tagging performance is similar to what we expect at Run 2 or the HL-LHC. Therefore, the study presented in the rest of this note is based on the W/Z-boson tagging performance at Run 2.

The sensitivity to the VBS signal at 27 TeV is extracted in the same manner as the HL-LHC analysis. The event selection is similar and a BDT is built using the same variables both in the resolved and boosted channel. For more details about the BDT and the setup used please refer to citation. Fig. 33 shows the expected cross-section uncertainty as function of integrated luminosity at 27 TeV compared to the one obtained at 14 TeV. The results are very consistent and show that given the same luminosity the same uncertainty can be reached at 27 TeV. Prospects are also presented for the extraction of the longitudinal component of the WW scattering. For the extraction of the longitudinal component in VBS processes, the electro-weak $WWjj$ samples are generated with the DECAY program to identify the polarization state of the produced V bosons. The generated events are then classified according to the polarization state: both V bosons are longitudinally (LL) or transversely (TT) polarized, or in the mixed state (LT). Each event is showered using Pythia and and then processed through the Delphes simulation.

In this case a BDT is built training the signal samples (WW LL) against the sum of the backgrounds which include the TT and LT component of the electroweak $WWjj$ samples. The observed significance expected with this simple setup is shown in the right figure of Fig. 33. One line shows

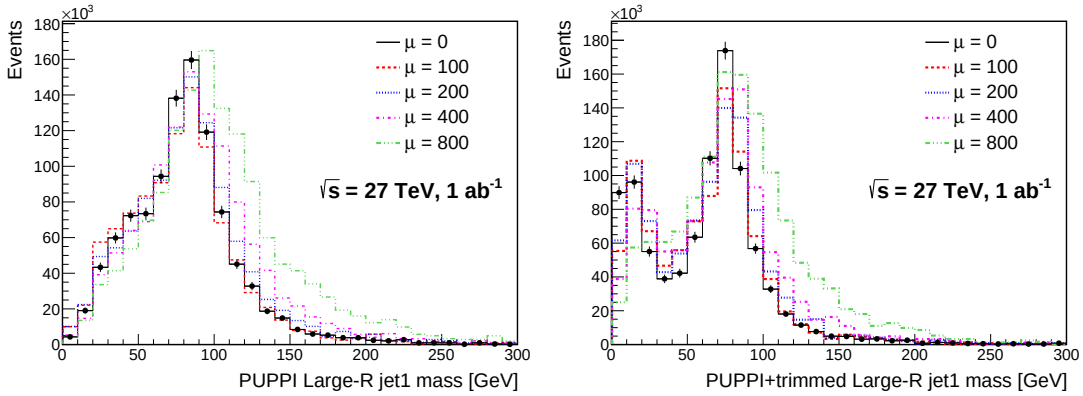

Fig. 32: Leading large-R jet mass (left) after applying the PUPPI algorithm at an integrated luminosity of 1 ab^{-1} at $\sqrt{s} = 27$ TeV with five different pile-up overlay conditions of $\mu_{\text{pileup}} = 0$, 100, 200, 400 and 800. The right plots shows the same distribution but after additionally requiring that the jets are trimmed with the conditions described in the text.

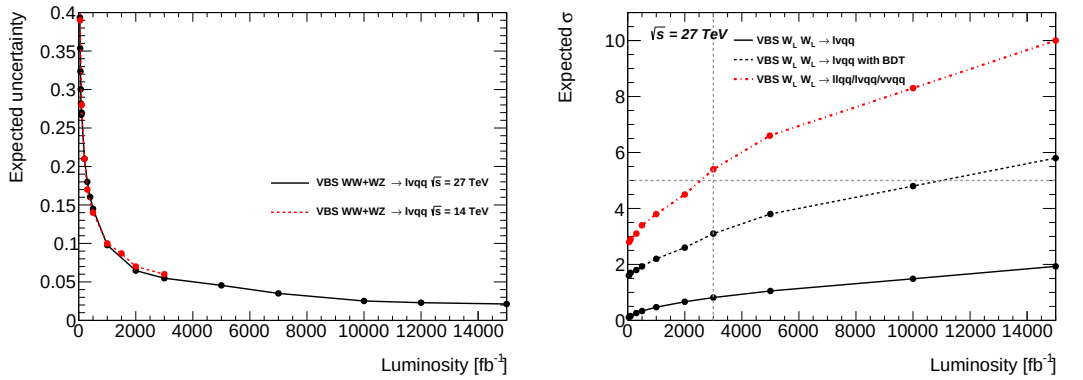

Fig. 33: The expected cross-section uncertainty as function of integrated luminosity at 27 TeV compared to the one obtained at 14 TeV (left). Right: Observed significance as a function of the luminosity and expected uncertainty for the EWK $W_L W_L$ signal assuming a 10% fraction predicted by Madgraph (right). One line shows the results obtained by fitting a single variable, the total invariant mass of the system and the other one shows the expected significance using the BDT. The third line shows the expected significance assuming the combination of all three semi-leptonic channels with the same sensitivity.

the results obtained by fitting a single variable, the total invariant mass of the system and the other one shows the expected significance using the BDT. The third line shows the expected significance assuming the combination of all three semi-leptonic channels with the same sensitivity. It's expected to reach 5σ sensitivities with 3000 fb^{-1} combining all the semileptonic channels.

4.3 Tri-boson production

The production of multiple heavy gauge bosons V (= $W^{\pm}, Z$) opens up a multitude of potential decay channels categorised according to the number of charged leptons in the final state. The sensitivity prospect studies have been performed related to the production of $W^{\pm}W^{\pm}W^{\mp}$, $W^{\pm}W^{\mp}Z$

or $W^{\pm}ZZ$ followed by the fully leptonic or semi-hadronic[8] decays: $W^{\pm}W^{\pm}W^{\mp} \to \ell^{\pm}\nu\ell^{\pm}\nu\ell^{\mp}\nu$, $W^{\pm}W^{\pm}W^{\mp} \to \ell^{\pm}\nu\ell^{\pm}\nu jj$, $W^{\pm}W^{\mp}Z \to \ell^{\pm}\nu\ell^{\pm}\nu\ell^{+}\ell^{-}$, $W^{\pm}W^{\mp}Z \to \ell^{\pm}\nu jj\ell^{+}\ell^{-}$, $W^{\pm}ZZ \to \ell^{\pm}\nu\ell^{+}\ell^{-}\ell^{+}\ell^{-}$, $W^{\pm}ZZ \to \ell^{\pm}\nu\ell^{+}\ell^{-}\nu\nu$, $W^{\pm}ZZ \to jj\ell^{+}\ell^{-}\ell^{+}\ell^{-}$ and $W^{\pm}ZZ \to \ell^{\pm}\nu\ell^{+}\ell^{-}jj$, with $\ell = e$ or μ. Prospect studies have been performed, using a cut-based analysis, corresponding to an integrated luminosity of 3000 fb^{-1} and 4000 fb^{-1} of proton–proton collisions at a centre-of-mass energy of $\sqrt{s}$ = 14 TeV, expected to be collected by the ATLAS detector at the the High-Luminosity Large Hadron Collider (HL-LHC) [378,379]. In this document we summarise only results that are expected to provide the best sensitivity according to the full prospect studies documented in [380].

Monte Carlo (MC) simulated event samples are used to predict the background from SM processes and to model the multi-boson signal production. The effects of an upgraded ATLAS detector are taken into account by applying energy smearing, efficiencies and fake rates to generator level quantities, following parameterisations based on detector performance studies with full simulation and HL-LHC conditions. The most relevant MC samples have equivalent luminosities (at 14 TeV) of at least 3000 fb^{-1}. Several MC generators are used to model the production of signal and dominant SM background processes relevant for the analysis.

For the generation of triboson signal events, matrix elements for all combinations of $pp \to VV$ ($V = W^{\pm}, Z$) have been generated using SHERPA v2.2.2 [84] with up to two additional partons in the final state, including full next-to-leading-order calculations (NLO) [381–383] accuracy for the inclusive process. All diagrams with three electroweak couplings are taken into account, including diagrams involving Higgs propagators. However, since these samples use factorised decays with on-shell vector bosons, the resonant contribution from those diagrams can not be reached from the 125 GeV Higgs. In order to account for the contribution coming from these diagrams the corresponding production of VH ($V = W, Z$) bosons is added to the signal. Electroweak NLO corrections to the signal production cross sections are not considered in this analysis. The diboson processes are generated with SHERPA event generator following the approach described in [384]. For the simulation of the top quark pair and the production of VH ($V = W, Z$) bosons POWHEG [273,385,386]+PYTHIA [387] was used as described in [388], while for the $t\bar{t}$ + V ($V = W, Z, H$) MADGRAPH5_aMC@NLO [12] interfaced to PYTHIA was used as in [389].

The expected multi-boson yields are normalised to the SHERPA predictions, while the $t\bar{t}$ + V ($V = W, Z, H$) yields are normalized to NLO. The top quark pair-production contribution is normalised to approximate NNLO+NNLL accuracy [41,390].

4.3.1 Experimental signatures

The experimental signature of the triboson processes considered in these studies consists of at least three charged leptons moderate $E_{\mathrm{T}}^{\mathrm{miss}}$ originating from the leptonic decay of W bosons, and jets in case one of the vector bosons decays hadronically. The event selection criteria starts from the one used in published analysis [**?**], but considers tighter selection criteria in terms of transverse momentum of the selected objects and missing transverse momentum of the event, in order to suppress higher pile-up contributions expected at the HL-LHC. The selection requirements used to define the signal regions are obtained from an optimization to maximize the sensitivity to $W^{\pm}W^{\pm}W^{\mp}$, $W^{\pm}W^{\mp}Z$ and $W^{\pm}ZZ$ processes and to reduce the contributions from SM background processes. In the case of $W^{\pm}W^{\pm}W^{\mp} \to \ell^{\pm}\nu\ell^{\pm}\nu\ell^{\mp}\nu$ channel, three separate signal regions are defined based on the number of same-flavour opposite-sign (SFOS) lepton pairs in the event: 0SFOS ($e^{\pm}e^{\pm}\mu^{\mp}$, $\mu^{\pm}\mu^{\pm}e^{\mp}$), 1SFOS ($e^{\pm}e^{\mp}\mu^{\pm}$, $e^{\pm}e^{\mp}\mu^{\mp}$, $\mu^{\pm}\mu^{\mp}e^{\pm}$, $\mu^{\pm}\mu^{\mp}e^{\mp}$) and 2SFOS ($e^{\pm}e^{\pm}e^{\mp}$, $\mu^{\pm}\mu^{\pm}\mu^{\mp}$). Similarly, in $W^{\pm}W^{\mp}Z \to \ell^{\pm}\nu\ell^{\pm}\nu\ell^{+}\ell^{-}$ channel, two signal regions are defined based on the selection of SFOS or different-flavour opposite-sign (DFOS) lepton-pair events: SFOS ($e^{\pm}e^{\mp}\mu^{\mp}\mu^{\pm}$, $e^{\pm}e^{\mp}e^{\pm}e^{\mp}$, $\mu^{\mp}\mu^{\pm}\mu^{\mp}\mu^{\pm}$) and DFOS ($e^{\pm}e^{\mp}\mu^{\mp}e^{\pm}$, $\mu^{\mp}\mu^{\pm}\mu^{\mp}e^{\pm}$). To

[8] In case of semi-hadronic channels we assume that one of the vector bosons decays hadronically while the other two decay leptonically.

select $W^{\pm}W^{\pm}W^{\mp} \to \ell^{\pm}\nu\ell^{\pm}\nu jj$ candidates, events are required to have exactly two leptons with the same electric charge, and at least two jets. Three different final states are considered based on the lepton flavour, namely $e^{\pm}e^{\pm}$, $e^{\pm}\mu^{\pm}$ and $\mu^{\pm}\mu^{\pm}$. In the case of $W^{\pm}ZZ$ process, separate set of selection criteria are defined in order to select events in which vector bosons undergo either fully leptonic of semi-hadronic decay. In all channels events are rejected if they have identified b-jets. This selection requirement suppresses background involving top quarks, with marginal impact on the signal efficiency. Full description to the optimized selection criteria, estimated systematic uncertainties and expected signal and background event yields for all channels considered in the study are available in [380]. Three channels, 0SFOS $W^{\pm}W^{\pm}W^{\mp} \to 3\ell\,3\nu$, DFOS $W^{\pm}W^{\mp}Z \to 4\ell\,2\nu$ and $W^{\pm}ZZ \to 5\ell\,1\nu$, for which we give details in the following, are estimated to provide best sensitivities. Tables 15 to 17 show the kinematic selection criteria used to select signal events in these channels.

Table 15: Event selection criteria for $W^{\pm}W^{\pm}W^{\mp} \to 3\ell\,3\nu$ candidate events.

$W^{\pm}W^{\pm}W^{\mp} \to \ell^{\pm}\nu\ell^{\pm}\nu\ell^{\mp}\nu$	0SFOS events: $e^{\pm}e^{\pm}\mu^{\mp}$, $\mu^{\pm}\mu^{\pm}e^{\mp}$
Preselection	Exactly 3 charged *tight* leptons with $p_{\mathrm{T}} > 30$ GeV and $\lvert\eta\rvert < 4$
SFOS dilepton mass	$m_{\ell\ell}^{\mathrm{SFOS}} > 20$ GeV
Angle between the trilepton system and $\overrightarrow{E}_{\mathrm{T}}^{miss}$	$\lvert\varphi^{3\ell} - \varphi^{\overrightarrow{E}_{\mathrm{T}}^{miss}}\rvert > 2.5$
Z boson veto	$\lvert m_{\mathrm{ee}} - m_{\mathrm{Z}}\rvert > 15$ GeV
Jet veto	At most one jet with $p_{\mathrm{T}} > 30$ GeV and $\lvert\eta\rvert < 2.5$
b-jet veto	No identified b-jets with $p_{\mathrm{T}} > 30$ GeV

Table 16: Event selection criteria for $W^{\pm}W^{\mp}Z \to 4\ell\,2\nu$ candidate events. The four-lepton mass $m_{4\ell}$ is calculated as invariant mass of the four-lepton system.

$W^{\pm}W^{\mp}Z \to \ell^{\pm}\nu\ell^{\pm}\nu\ell^{+}\ell^{-}$	DFOS events: $e^{\pm}e^{\mp}\mu^{\mp}e^{\pm}$, $\mu^{\mp}\mu^{\pm}\mu^{\mp}e^{\pm}$
Preselection	Exactly 4 charged *loose* (3^{rd} and 4^{th} *tight*) leptons with $p_{\mathrm{T}}(1,2) > 30$ GeV, $p_{\mathrm{T}}(3,4) > 25$ GeV and $\lvert\eta\rvert < 4$
SFOS dilepton mass	$\lvert m_{\ell\ell}^{\mathrm{SFOS}} - 91\text{ GeV}\rvert < 15$ GeV
DFOS dilepton mass	$m_{\ell\ell}^{\mathrm{DFOS}} > 40$ GeV
Four-lepton mass	$m_{4\ell} > 250$ GeV
b-jet veto	No identified b-jets with $p_{\mathrm{T}} > 30$ GeV

Table 17: Event selection criteria for $W^{\pm}ZZ \to 5\ell 1\nu$ candidate events. Two-lepton pairs of the same flavour and opposite charge have to satisfy same-flavour dilepton mass selection requirement. The transverse mass is calculated from the $E_{\mathrm{T}}^{\mathrm{miss}}$ and the lepton that does not pass dilepton mass requirement.

$W^{\pm}ZZ \to \ell^{\pm}\nu\ell^{+}\ell^{-}\ell^{+}\ell^{-}$	$5\ell 1\nu$
Preselection	Exactly 5 charged *loose* (4^{rd} and 5^{th} *tight*) leptons with $p_{\mathrm{T}}(1,2,3) > 30$ GeV, $p_{\mathrm{T}}(4,5) > 25$ GeV and $\lvert\eta\rvert < 4$
SFOS dilepton mass	$\lvert m_{\ell\ell}^{\mathrm{SFOS}} - 91\text{ GeV}\rvert < 15$ GeV
Transverse mass	$m_{\mathrm{T}} > 40$ GeV
b-jet veto	No identified b-jets with $p_{\mathrm{T}} > 30$ GeV

4.3.2 Results

The SM processes that mimic the multi-boson signal signatures by producing at least three prompt leptons or two prompt leptons with the same electric charge, can be grouped into the following categories:

– The WZ and ZZ processes, referred to as "diboson background";

– The WWW, WWZ, WZZ, ZZZ processes, excluding the signal process under study, referred to as "triboson background";
– The VH and $t\bar{t}H$ processes, excluding the processes which are added to the signal, referred to as "Higgs+X background";
– The production of four top quarks, top quark associated with WZ bosons or $t\bar{t}$ associated with W, Z, WZ or $W^{\pm}W^{\mp}$ bosons, referred to as "top background";
– Processes that have non-prompt leptons (electrons) originating from misidentified jets (referred to as "fake-lepton background");
– Processes that produce prompt charged leptons, but the charge of one lepton is misidentified (referred to as "charge-flip background").

The contributions from the WW and $t\bar{t}$ processes are accounted for in the fake-lepton and charge-flip backgrounds. The diboson, triboson, Higgs+X and top background sources are estimated using simulated events, with the dominant irreducible background in most of the channels originating from the diboson processes. In some channels the contribution of the fake-lepton background, which is derived by applying the pre-defined (p_{T}, η)-dependent likelihood as described in Section 7.3, becomes significant. The charge-flip background has been investigated and found to be negligible in all considered processes.

In $W^{\pm}W^{\pm}W^{\mp} \to 3\ell\,3\nu$ channel, the background is dominated by the irreducible diboson background and fake-lepton contribution. The contribution of signal events containing Higgs decays are the level of 40%. In $W^{\pm}W^{\mp}Z \to 4\ell\,2\nu$ channel with two leptons being of different flavour, this requirement suppresses a large fraction of the diboson background. Contribution of Higgs decays is quite smaller with respect to the one in $W^{\pm}W^{\pm}W^{\mp} \to 3\ell\,3\nu$ due to smaller lepton p_{T} and invariant mass requirement $m_{\ell\ell}^{\mathrm{DFOS}} > 40$ GeV. In $W^{\pm}ZZ$ channel the most promising signal region is the one with five charged leptons. In this case, the fake-lepton contribution becomes significant. The background is dominated by rare top production of $t\bar{t}ZW$.

Figure 34 shows relevant distributions in the three channels: the $m_{\mathrm{T}}^{3\ell}$ distribution for the $W^{\pm}W^{\pm}W^{\mp} \to 3\ell\,3\nu$ channel, the distribution of transverse momenta of the two-lepton system $p_{\mathrm{T}}^{\ell\ell}$ in $W^{\pm}W^{\mp}Z \to 4\ell\,2\nu$ channel and the distribution of two lepton invariant mass $p_{\mathrm{T}}^{\ell\ell}$ selected to give the mass closest to the mass of the Z boson in $W^{\pm}ZZ \to 5\ell\,1\nu$ channel.

Systematic uncertainties in the signal and background predictions arise from the uncertainties in the measurement of the integrated luminosity, from the experimental modelling of the signal acceptance and detection efficiency, and from the background normalisation. With the much larger integrated luminosity and a sophisticated understanding of the detector performance and backgrounds at the HL-LHC, we expect experimental uncertainties related to the lepton reconstruction and identification efficiencies as well as lepton energy/momentum resolution and scale modelling of 1%, to the $E_{\mathrm{T}}^{\mathrm{miss}}$ modelling of 1%, to the jet energy scale and resolution of 1.5% and 5% in the fully leptonic and leptons+jets channels, respectively, to the luminosity measurement of 1% and to the expected pileup of 1% [391]. Based on the extrapolations of current ATLAS measurements and assuming a reduction of the uncertainty at the level of 15–80%, depending on the process and the origin of the systematics, the following systematic uncertainties on the cross-section normalisation for each of the background processes are assumed: 4% on $\sigma_{\mathrm{diboson}}$, 30% on $\sigma_{\mathrm{triboson}}$, 3% on $\sigma_{t\bar{t}}$, 20% on $\sigma_{t\bar{t}H}$, 6% on $\sigma_{t\bar{t}Z}$, and 11% on $\sigma_{t\bar{t}W}$. The uncertainty on the level of the fake-lepton background is estimated to be 10%. Taking these assumptions into account, we estimate the total systematic uncertainty on the background of 9% for $W^{\pm}W^{\pm}W^{\mp} \to 3\ell 3\nu$ and $W^{\pm}ZZ \to 5\ell 1\nu$ channels and 6% in $W^{\pm}W^{\mp}Z \to 4\ell 2\nu$ channel. Assuming that the number of signal events follows a Poissonian distribution and taking into account an estimated systematic uncertainty on the background, the signal significance Z_{σ} and the estimated precision on the signal strength measurement, $\frac{\Delta\mu}{\mu}$ are calculated using the asymptotic formula from [376]. Only experimental uncertainties are taken into account for the signal. Uncertainties related to the limited number of MC events

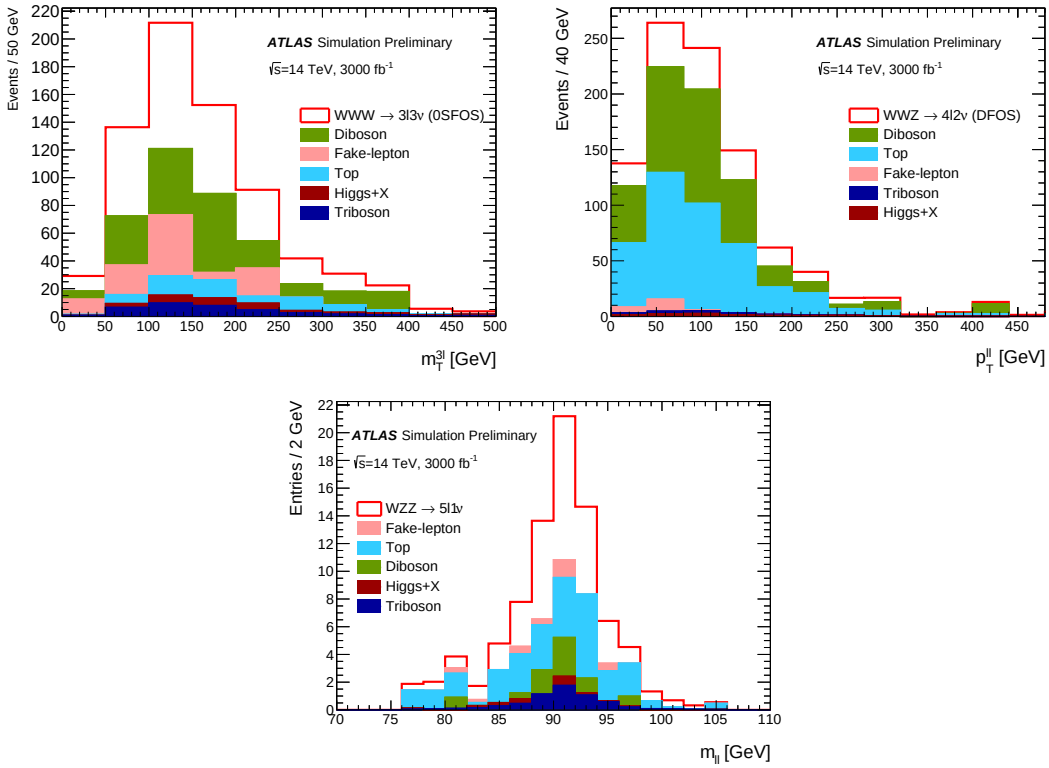

Fig. 34: The distribution of $m_{\mathrm{T}}^{3\ell}$ for the $W^{\pm}W^{\pm}W^{\mp} \rightarrow 3\ell\ 3\nu$ channel (top left), the distribution of transverse momenta of the two-lepton system $p_{\mathrm{T}}^{\ell\ell}$ in $W^{\pm}W^{\mp}Z \rightarrow 4\ell\ 2\nu$ channel (top right) and the distribution of two lepton invariant mass $p_{\mathrm{T}}^{\ell\ell}$ selected to give the mass closest to the mass of the Z boson in $W^{\pm}ZZ \rightarrow 5\ell\ 1\nu$ channel (bottom) as expected from the signal and background processes at 3000 fb^{-1} after applying the selection criteria from Tables 15 to 17.

are neglected. The total number of signal and background events expected after applying the full set of selection requirements from Tables 15 to 17 in three selected channels, the corresponding signal significance and the expected precision on the signal strength measurement, for an integrated luminosity of 3000 fb^{-1} are shown in Table 18.

The HL-LHC offers a large improvement to multi-boson production, where this simple cut-and-count approach provides the sensitivities larger than 3σ in three channels considered in this analysis. It should be noted that more mature analysis techniques such as MVA, would likely improve these results further. However high level of background control, mainly diboson background as well as instrumental background arising from fake-leptons, will be needed in order to maintain desired level of precision.

Table 18: Expected number of signal and background events, the expected signal significance Z_σ and the estimated precision on the signal strength measurement, $\frac{\Delta\mu}{\mu}$ in $W^\pm W^\pm W^\mp \to 3\ell 3\nu$, $W^\pm W^\mp Z \to 4\ell 2\nu$ and $W^\pm ZZ \to 5\ell 1\nu$ channels after applying the selection criteria from Tables 15 to 17.

	$W^\pm W^\pm W^\mp \to 3\ell 3\nu$	$W^\pm W^\mp Z \to 4\ell 2\nu$	$W^\pm ZZ \to 5\ell 1\nu$
Signal	312	168	19
Diboson	208	357	4.0
Triboson	37	11	3.0
Higgs+X	25	10	0.3
Top	60	390	15
fake-lepton	97	16	3.0
Total:	427	784	25
Significance Z_σ	6.7	3.0	3.0
Significance Z_σ (4000 fb^{-1})	7.0	3.1	3.4
Precision $\frac{\Delta\mu}{\mu}$	11%	27%	36%
Precision $\frac{\Delta\mu}{\mu}$ (4000 fb^{-1})	10%	25%	31%

4.3.3 Cross-section for off-shell WWW production including NLO electroweak corrections

TO BE UPDATED

Introduction

Triboson production processes allow for a measurement of triple and quartic couplings of the Standard Model gauge bosons, which can be used to constain anomalous gauge couplings that frquently appear in BSM theories [392]. In this section we calculate the production yields to fully off-shell $W^-W^+W^+$ production, ie. a $\ell_1^-\ell_2^+\ell_3^+\bar{\nu}_{\ell_4}\nu_{\ell_5}\nu_{\ell_6}$ final state with $\ell_i = e, \mu$, including all triple, double and single resonant topologies and interferences of diagrams with different vector boson (W, Z, γ) intermediate states.

This calculation makes use of the automated tools SHERPA [84, 85, 393] and RECOLA [82, 83]. While SHERPA provides the tree-level matrix elements, infrared subtraction, process management and phase-space integration of all contributions to all processes, RECOLA provides the renormalised virtual corrections. It follows the parameters of the original publication [**?**]

In the following, the production yields for the High Luminosity and the proposed High Energy upgrade of the LHC are presented in Sections 4.3.3 and 4.3.3, respectively. For both collider setups we use the `NNPDF31_nlo_as_0118_luxqed` PDF [182] containing QED effects calculated in the LUXqed scheme [180,181]. The calculation is performed in the Standard Model using the complex mass scheme, defining the electroweak parameters in the G_μ-scheme with the following input parameters

$$
\begin{aligned}
G_\mu &= 1.16637 \times 10^{-5}\ \text{GeV}^2 & & \\
m_W &= 80.385\ \text{GeV} & \Gamma_W &= 2.0897\ \text{GeV} \\
m_Z &= 91.1876\ \text{GeV} & \Gamma_Z &= 2.4955\ \text{GeV} \\
m_h &= 125.0\ \text{GeV} & \Gamma_h &= 0.00407\ \text{GeV} \\
m_t &= 173.2\ \text{GeV} & \Gamma_t &= 1.3394\ \text{GeV}\,.
\end{aligned}
$$

We choose $\mu_R = \mu_F = 3\,m_W$ and a diagonal CKM matrix. The lepton acceptance cuts specifying the fiducial region are listed in Table 19. They are applied on dressed leptons, defined through recombining the bare lepton four-momenta with all photons in a cone of $\Delta R_{\text{dress}} = 0.1$ around it. At most one jet is allowed to be present, which, however, does not affect the present next-to-leading order calculation.

Table 19: Definition of the fiducial region. All selection cuts are applied to dressed leptons, defined with $\Delta R_{\text{dress}} = 0.1$.

Selection	Cut	Value
General	$p_{\text{T}}(\ell)$	$[30\,\text{GeV}, \infty)$
	$y(\ell)$	$[-4.0, 4.0]$
	$\Delta R(\ell, \ell)$	$[0.2, \infty)$
1, 2 SFOS	$\not{p}_{\text{T}}$	$[50\,\text{GeV}, \infty)$
	$m_{\ell\ell}^{\text{SFOS}}$	$[0, 70\,\text{GeV}] \wedge [100\,\text{GeV}, \infty)$

Fig. 35: Event yields at the High Luminosity LHC at 14 TeV with 300 fb^{-1} depending on a minimum transverse mass (left) or a minimum missing transverse momentum (right).

Fig. 36: Event yields at the High Energy LHC at 27 TeV with 15 ab^{-1} depending on a minimum transverse mass (left) or a minimum missing transverse momentum (right).

Cross sections for 14 TeV

In this section the integrated production yields for $W^-W^+W^+$ production are presented for the High Luminosity upgrade of the LHC at a centre-of-mass energy of 14 TeV and an integrated luminostiy of 300 fb^{-1}.

About 2/3 pages figures and short description.

Cross sections for 27 TeV

In this section the integrated production yields for $W^-W^+W^+$ production are presented for the High Luminosity upgrade of the LHC at a centre-of-mass energy of 27 TeV and an integrated luminosity of 15 ab^{-1}.

About 2/3 pages figures and short description.

Conclusions

About 1/3 pages short summary.

4.4 Precision electroweak measurements

4.4.1 NNLO predictions for Z-boson pair production at the LHC and HE-LHC

The results presented in this section are produced using the program described in Ref. [394] with the NNPDF3.0 [159] set of parton distribution functions. The parton densities and α_s are evaluated at each corresponding order (i.e. we use $(n{+}1)$-loop α_s at N^nLO, with $n = 0, 1, 2$) and we consider $N_f = 5$ massless quark flavours. For the renormalisation (μ_R) and factorisation (μ_F) scales we investigate two choices: $\mu_R = \mu_F = m_Z$ and the dynamic scale $\mu_R = \mu_F = m_{ZZ}/2$. We use the G_μ EW scheme where the EW input parameters have been set to $G_F = 1.16639 \times 10^{-5}$, $m_W = 80.399$ GeV and $m_Z = 91.1876$ GeV. The top quark and Higgs boson masses that are included in the real-virtual one-loop contributions and in the loop-induced gg channel have been set to $m_t = 173.2$ GeV and $m_H = 125$ GeV, respectively. The one-loop contributions are calculated with the program GoSam [11, 86]. For the NNLO real radiation we employ the N-jettiness subtraction scheme [53, 54, 395, 396]. The process dependent hard function has been extracted from the two-loop amplitude computed in Ref. [397] and

cross-checked with an in-house calculation. The top quark contributions in the double virtual two-loop diagrams are not included in the results below. Table 20 shows cross section results for the central scale $\mu_R = \mu_F = m_Z$, including 7-point scale variations. In Table 21 results for the dynamic scale $\mu_R = \mu_F = m_{ZZ}/2$ are given.

	σ_{LO} [pb]	σ_{NLO} [pb]	σ_{NNLO} [pb]	$gg \to ZZ$ [pb]
14 TeV	$10.80^{+5.7\%}_{-6.7\%}$	$15.55^{+3.0\%}_{-2.4\%}$	$18.50^{+3.0\%}_{-3.2\%}$	$1.56^{+25\%}_{-18\%}$
27 TeV	$23.59^{+10.0\%}_{-10.9\%}$	$35.59^{+3.2\%}_{-4.2\%}$	$44.52^{+3.7\%}_{-4.1\%}$	$4.81^{+25\%}_{-18\%}$

Table 20: Inclusive cross section for ZZ production at the LHC for $\sqrt{s}$ =14 TeV and $\sqrt{s}$ =27 TeV at LO, NLO and NNLO with $\mu_R = \mu_F = m_Z$. The uncertainties are obtained by varying the renormalisation and factorisation scales in the range $m_Z/2 < \mu_R, \mu_F < 2m_Z$ with the constraint $0.5 < \mu_F/\mu_R < 2$.

	σ_{LO} [pb]	σ_{NLO} [pb]	σ_{NNLO} [pb]	$gg \to ZZ$ [pb]
14 TeV	$11.03^{+5.2\%}_{-6.1\%}$	$15.38^{+2.5\%}_{-2.0\%}$	$18.20^{+3.3\%}_{-2.3\%}$	$1.41^{+23\%}_{-18\%}$
27 TeV	$24.68^{+9.0\%}_{-9.8\%}$	$35.43^{+2.6\%}_{-3.7\%}$	$43.71^{+3.3\%}_{-3.2\%}$	$4.41^{+23\%}_{-17\%}$

Table 21: Inclusive cross section for ZZ production at the LHC for $\sqrt{s}$ =14 TeV and $\sqrt{s}$ =27 TeV at LO, NLO and NNLO with the dynamic scale choice $\mu_R = \mu_F = m_{ZZ}/2$. The uncertainties are obtained by varying the renormalisation and factorisation scales in the range $m_{ZZ}/4 < \mu_R, \mu_F < m_{ZZ}$ with the constraint $0.5 < \mu_F/\mu_R < 2$.

Figs. 37 and 38 show largely non-overlapping scale uncertainty bands between NLO and NNLO, both for a fixed central scale choice $\mu = m_Z$ as well as for a dynamic central scale choice $\mu = m_{ZZ}/2$. This demonstrate that for this process, the scale variations are insufficient to estimate missing higher order terms in the perturbative expansion. This is mostly due to the fact that at NNLO, the loop-induced gluon fusion channel $gg \to ZZ$ opens up, and due to the large gluon flux it represents a numerically significant contribution, about 8% at $\sqrt{s} = 14$ TeV and 11% at $\sqrt{s} = 27$ TeV of the total NNLO cross section, for both central scale choices. For further studies of the gluon channel we refer to Refs. [398, 399]. Since this new channel contributes for the first time at NNLO its contribution cannot be captured by the scale variations of the NLO cross section. Therefore, with increasing perturbative order, we can observe a systematic reduction of the factorisation scale dependence of the cross section (indicated by the thickness of the scale uncertainty band), while there is no significant reduction of the renormalisation scale dependence. To show that this effect can be attributed to the gluon fusion channel opening up at NNLO, we also show the NNLO result excluding this channel in Figs. 37 and 38.

4.4.2 Diboson production

We present NNLO QCD predictions for W^+W^-, $W^\pm Z$ and ZZ production in proton–proton collisions. We consider two LHC upgrade scenarios, namely a high-luminosity (HL) LHC running at $\sqrt{s} = 14$ TeV with an assumed integrated luminosity of $3\,\text{ab}^{-1}$, and a high-energy (HE) LHC at $\sqrt{s} = 27$ TeV with

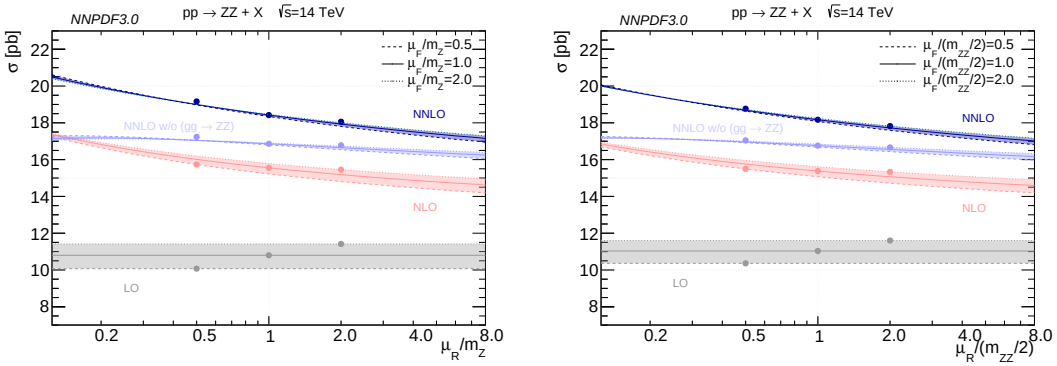

Fig. 37: Renormalisation and factorisation scale dependence of the ZZ cross section for $\sqrt{s} = 14\,\text{TeV}$ at LO, NLO and NNLO for the fixed central scale choice $\mu_R = \mu_F = m_Z$ (left) and for the dynamic central scale choice $\mu_R = \mu_F = m_{ZZ}/2$ (right). We also show the NNLO result without the gluon fusion contributions in light blue. The thickness of the bands shows the variation with the factorisation scale, while the slope shows the renormalisation scale dependence. The scale uncertainties are the envelope of scale variations by a factor of two up and down with the constraint $0.5 < \mu_F/\mu_R < 2$, i.e. 7-point scale variations.

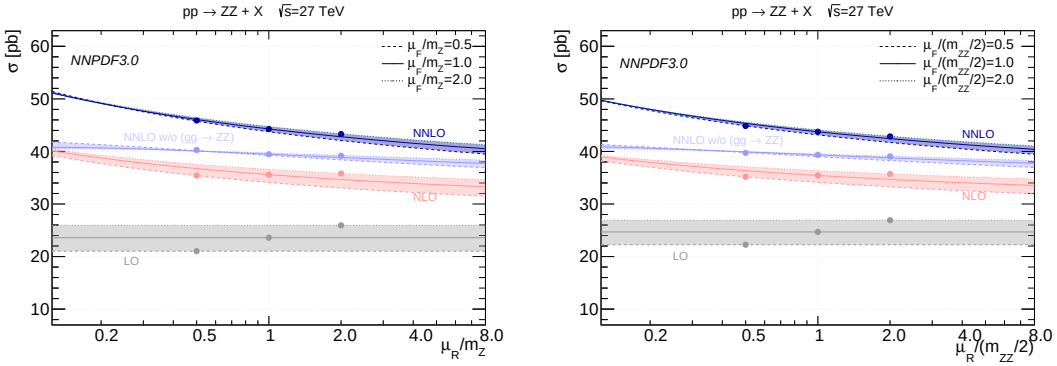

Fig. 38: Renormalisation and factorisation scale dependence of the ZZ cross section for $\sqrt{s} = 27\,\text{TeV}$ at LO, NLO and NNLO for the fixed central scale choice $\mu_R = \mu_F = m_Z$ (left) and for the dynamic central scale choice $\mu_R = \mu_F = m_{ZZ}/2$ (right). The NNLO result without the gluon fusion contributions is shown in light blue, and the bands are produced in the same way as in Fig.37.

$15\,\text{ab}^{-1}$. More precisely, we investigate the inclusive hard-scattering processes

$$
\begin{aligned}
pp &\to \ell^+\nu_\ell\,\ell'^-\bar{\nu}_{\ell'} + X\,,\\
pp &\to \ell\nu_\ell\,\ell'^+\ell'^- + X\,,\\
pp &\to \ell^+\ell^-\ell'^+\ell'^- + X\,,
\end{aligned}
$$

where all off-shell effects and interference contributions are fully accounted for.

All results are obtained with the public parton-level NNLO framework MATRIX. This program, and earlier versions of it, have been used to compute state-of-the-art QCD predictions for gauge-boson pair production processes [400–408].[9] All tree-level and one-loop amplitudes are evaluated with OPENLOOPS[10] [10, 414]. At two-loop level we use the $q\bar{q} \to VV'$ amplitudes of Ref. [397].

[9] It was also used in the NNLL+NNLO computation for W^+W^- and ZZ production of Ref. [409], and in the NNLOPS computation for W^+W^- production of Ref. [410].

[10] OPENLOOPS which relies on the fast and stable tensor reduction of COLLIER [411, 412], supported by a rescue system

We apply the complex mass scheme [346] throughout, i.e. we use complex W- and Z-boson masses and define the EW mixing angle as $\cos\theta_W^2 = (m_W^2 - i\Gamma_W m_W)/(m_Z^2 - i\Gamma_Z m_Z)$. For the input of the weak parameters we employ the G_μ scheme with $\alpha = \sqrt{2}\,G_\mu |(m_W^2 - i\Gamma_W m_W)\sin^2\theta_W|/\pi$. We set $G_F = 1.16639 \times 10^{-5}\,\text{GeV}^{-2}$, $m_W = 80.399\,\text{GeV}$, $\Gamma_W = 2.1054\,\text{GeV}$, $m_Z = 91.1876\,\text{GeV}$, $\Gamma_Z = 2.4952\,\text{GeV}$, $m_H = 125\,\text{GeV}$ and $\Gamma_H = 0.00407\,\text{GeV}$. Furthermore, we use a diagonal CKM matrix.

The number of light quarks is chosen differently for the processes under consideration: All W^+W^- results are obtained by applying the four-flavour scheme (4FS) with massive top and bottom quarks in order to consistently remove top-quark contamination by omitting the (separately IR finite) partonic processes with real bottom-quark emissions. In the 4FS, we use the on-shell bottom mass $m_b = 4.92\,\text{GeV}$. For all other processes we apply the five-flavour scheme (5FS) with a vanishing bottom mass $m_b = 0$. The top quark is treated as massive and unstable throughout, and we set $m_t = 173.2\,\text{GeV}$ as well as $\Gamma_t = 1.44262\,\text{GeV}$.[11]

We use the MMHT2014 [158] sets of parton distribution functions (PDFs) with $n_f = 4$ or $n_f = 5$ active quark flavours, consistently with the flavour scheme under consideration. N^{n}LO ($n = 0, 1, 2$) predictions are obtained by using PDFs at the same perturbative order and the evolution of α_S at $(n+1)$-loop order, as provided by the corresponding PDF set. To be precise, in the 5FS we use `MMHT2014lo68cl`, `MMHT2014nlo68cl`, and `MMHTnnlo68cl` at LO, NLO, and NNLO. In the 4FS we use `MSTW2008lo68cl_nf4`, `MMHT2014nlo68cl_nf4`, and `MMHT2014nnlo68cl_nf4` at LO, NLO, and NNLO.

Our central predictions are obtained by setting the factorization and renormalization scales to $\mu_F = \mu_R = \mu_0 \equiv E_{\text{T},V_1} + E_{\text{T},V_2}$, with $E_{\text{T},V_i} = \sqrt{M_{V_i}^2 + p_{\text{T},V_i}^2}$, where M_{V_i} is the invariant mass and p_{T,V_i} the transverse momentum of the respective vector boson. Uncertainties from missing higher-order contributions are estimated in the usual way by independently varying μ_F and μ_R in the range $0.5\mu_0 < \mu_F, \mu_R < 2\mu_0$ with the constraint $0.5 < \mu_F/\mu_R < 2$.

In Table 22 we present cross sections for W^+W^-, $W^\pm Z$ and ZZ production, inclusive over the phase space of the final-state leptons, for pp collisions at $\sqrt{s} = 14\,\text{TeV}$ and $\sqrt{s} = 27\,\text{TeV}$. Throughout, we apply only a basic selection cut on Z bosons, by requiring the invariant masses of all opposite-sign same-flavour lepton pairs to be within a Z-mass window of $66\,\text{GeV} < m_{\ell^-\ell^+} < 116\,\text{GeV}$, which is necessary to avoid divergencies induced by soft intermediate photons. The gain in the inclusive cross section at $\sqrt{s} = 27\,\text{TeV}$ is roughly a factor of 2.5 for all processes under consideration, see last column of Table 22. We further see the importance of QCD corrections: Higher-order contributions are huge, especially for $W^\pm Z$ production. The NLO corrections range from about $+36\%$ to $+82\%$ depending on process and collider energy, while NNLO QCD corrections are still sizeable and induce a further increase of the cross sections of 13% to 20%. The cross-section ratio for W^+Z/W^-Z production is about 1.55 at NNLO for $\sqrt{s} = 14\,\text{TeV}$, changes to 1.42 for $\sqrt{s} = 27\,\text{TeV}$, and is essentially independent on the perturbative order.

We stress that QCD radiative corrections may change quite significantly as soon as fiducial cuts on the leptonic final state are applied, or when kinematical distributions are considered. The corrections for the inclusive cross sections in Table 22 should therefore be understood as illustrative, and the use of inclusive K-factors to obtain NNLO predictions from lower order results with different sets of cuts should be avoided in general.

It is interesting to quantify the size of the loop-induced gluon fusion contribution of the charge-neutral processes, which is part of the NNLO QCD corrections. By NLO′+gg we denote its sum with

based on quad-precision CutTools [413] with OneLOop [2] to deal with exceptional phase-space points.

[11] Massive top-quark contributions are neglected in the virtual two-loop corrections, but are kept everywhere else in the computations.

Table 22: Inclusive cross sections for W^+W^-, $W^\pm Z$ and ZZ production.

σ [fb] (correction)		LO	NLO (NLO/LO−1)	NLO′+gg (NLO′+gg/NLO−1)	NNLO (NNLO/NLO−1)	$\frac{\sigma_{\text{NNLO}}(27\,\text{TeV})}{\sigma_{\text{NNLO}}(14\,\text{TeV})}$
W^+W^-	$\sqrt{s} = 14\,\text{TeV}$	$897.27(9)^{+4.3\%}_{-5.3\%}$	$1303.3(1)^{+2.7\%}_{-2.2\%}$ (+45.3%)	$1386.1(2)^{+3.7\%}_{-2.9\%}$ (+6.4%)	$1485.(1)^{+2.4\%}_{-2.2\%}$ (+13.9%)	2.33
	$\sqrt{s} = 27\,\text{TeV}$	$2091.5(2)^{+7.6\%}_{-8.6\%}$	$2988.4(3)^{+2.8\%}_{-2.9\%}$ (+42.9%)	$3213.0(4)^{+4.1\%}_{-3.2\%}$ (+7.0%)	$3457.(4)^{+2.8\%}_{-2.4\%}$ (+15.6%)	
W^+Z	$\sqrt{s} = 14\,\text{TeV}$	$60.322(6)^{+3.4\%}_{-4.3\%}$	$106.15(1)^{+3.6\%}_{-3.0\%}$ (+76.0%)	—	$120.5(1)^{+2.0\%}_{-1.9\%}$ (+13.5%)	2.35
	$\sqrt{s} = 27\,\text{TeV}$	$136.66(1)^{+6.8\%}_{-7.8\%}$	$248.51(2)^{+4.0\%}_{-3.3\%}$ (+81.8%)	—	$283.4(3)^{+2.1\%}_{-2.1\%}$ (+14.0%)	
W^-Z	$\sqrt{s} = 14\,\text{TeV}$	$39.182(4)^{+3.7\%}_{-4.7\%}$	$68.430(7)^{+3.7\%}_{-3.0\%}$ (+74.6%)	—	$77.63(7)^{+1.9\%}_{-1.9\%}$ (+13.4%)	2.57
	$\sqrt{s} = 27\,\text{TeV}$	$96.70(1)^{+7.2\%}_{-8.2\%}$	$175.44(2)^{+4.0\%}_{-3.3\%}$ (+81.4%)	—	$199.7(2)^{+2.0\%}_{-2.0\%}$ (+13.8%)	
ZZ	$\sqrt{s} = 14\,\text{TeV}$	$24.500(2)^{+4.3\%}_{-5.3\%}$	$34.201(3)^{+2.0\%}_{-1.8\%}$ (+39.6%)	$37.531(4)^{+3.3\%}_{-2.6\%}$ (+9.7%)	$39.64(4)^{+2.4\%}_{-2.1\%}$ (+15.9%)	2.40
	$\sqrt{s} = 27\,\text{TeV}$	$58.622(6)^{+7.9\%}_{-8.9\%}$	$79.757(8)^{+2.2\%}_{-3.0\%}$ (+36.1%)	$89.89(1)^{+3.7\%}_{-3.0\%}$ (+12.7%)	$95.20(9)^{+2.9\%}_{-2.4\%}$ (+19.4%)	

the NLO cross section computed with NNLO PDFs. The NLO′+gg result for W^+W^- production is 6.4% (7.0%) larger than the NLO result at $\sqrt{s} = 14\,(27)\,\text{TeV}$, while their difference is even 9.7% (12.7%) for ZZ production. These numbers amount to roughly half of the full NNLO correction of the W^+W^- process, and even about two-thirds for ZZ production. However, one has to bear in mind that under typical fiducial selection requirements on the leptons and missing transverse energy, the impact of the loop-induced contribution decreases significantly, especially for W^+W^- production. Furthermore, its relative contribution is strongly suppressed as far as the tails of the kinematical distributions are concerned, due to the large-x suppression of the gluon density.

To illustrate how strongly the radiative corrections may depend on the fiducial cuts, in Table 23 we show cross sections with a minimum $p_{\text{T,min}} = 100\,\text{GeV}$ cut on the transverse momentum of the charged leptons and the missing energy. More precisely, depending on the process we have applied the following cuts, as shown in Tab.24:

As we can read from the table, radiative corrections at NLO can be enormous for some processes with $p_{\text{T,min}} = 100\,\text{GeV}$, ranging from +51% to even +281%. Also the NNLO corrections are significantly increased with respect to the inclusive case, and can be as large as +27%. It is also apparent that the importance of the loop-induced gluon fusion contribution is significantly reduced. For W^+W^- production, due to the applied $p_{\text{T,miss}}$ cut the NLO′+gg contribution is even smaller than the NLO cross section by −1.2% (−1.6%) at $\sqrt{s} = 14\,(27)\,\text{TeV}$ (i.e. the positive impact of the gg channel is smaller than the negative effect from using NNLO PDFs instead of NLO PDFs in the NLO′+gg prediction). For ZZ production, it is still sizeable with 7.7% (12.3%), but its relative contribution at $\mathcal{O}(\alpha_S^2)$ has decreased from roughly two-thirds in the inclusive case to less than half of the NNLO corrections for $p_{\text{T,min}} = 100\,\text{GeV}$. Furthermore, compared to the inclusive results we observe an even more substantial increase of the cross sections from $\sqrt{s} = 14\,\text{TeV}$ to $\sqrt{s} = 27\,\text{TeV}$ of roughly a factor of four. This can be understood by the fact, that the additional energy enlarges the available phase-space, especially at high momentum transfer.

Table 23: Cross sections with a $p_{\mathrm{T,min}} = 100\,\mathrm{GeV}$ cut on the transverse momentum of the charged leptons and the missing energy for W^+W^-, $W^\pm Z$ and ZZ production.

σ [fb] (correction)		LO	NLO (NLO/LO−1)	NLO′+gg (NLO′+gg/NLO−1)	NNLO (NNLO/NLO−1)	$\frac{\sigma_{\mathrm{NNLO}}(27\,\mathrm{TeV})}{\sigma_{\mathrm{NNLO}}(14\,\mathrm{TeV})}$
W^+W^-	$\sqrt{s} = 14\,\mathrm{TeV}$	$0.920(1)^{+2.7\%}_{-2.7\%}$	$2.827(5)^{+9.7\%}_{-8.0\%}$ (+207.1%)	$2.793(7)^{+9.9\%}_{-8.1\%}$ (−1.2%)	$3.51(1)^{+5.2\%}_{-5.0\%}$ (+24.3%)	3.93
	$\sqrt{s} = 27\,\mathrm{TeV}$	$2.847(3)^{+0.08\%}_{-0.5\%}$	$10.83(2)^{+8.2\%}_{-6.9\%}$ (+280.5%)	$10.66(2)^{+8.4\%}_{-7.1\%}$ (−1.6%)	$13.80(4)^{+5.3\%}_{-4.8\%}$ (+27.3%)	
W^+Z	$\sqrt{s} = 14\,\mathrm{TeV}$	$0.06524(8)^{+3.3\%}_{-3.2\%}$	$0.1273(3)^{+7.1\%}_{-5.8\%}$ (+95.2%)	—	$0.1485(9)^{+3.4\%}_{-3.3\%}$ (+16.6%)	3.82
	$\sqrt{s} = 27\,\mathrm{TeV}$	$0.1919(2)^{+0.1\%}_{-0.5\%}$	$0.4642(8)^{+7.0\%}_{-5.8\%}$ (+141.9%)	—	$0.568(3)^{+3.8\%}_{-3.6\%}$ (+22.5%)	
W^-Z	$\sqrt{s} = 14\,\mathrm{TeV}$	$0.03289(4)^{+3.1\%}_{-3.1\%}$	$0.0641(2)^{+7.5\%}_{-6.0\%}$ (+94.9%)	—	$0.0767(5)^{+3.4\%}_{-3.5\%}$ (+19.7%)	4.34
	$\sqrt{s} = 27\,\mathrm{TeV}$	$0.1121(1)^{+0.\%}_{-0.3\%}$	$0.2719(5)^{+7.2\%}_{-5.9\%}$ (+142.7%)	—	$0.333(2)^{+3.7\%}_{-3.5\%}$ (+22.5%)	
ZZ	$\sqrt{s} = 14\,\mathrm{TeV}$	$0.02108(3)^{+3.1\%}_{-3.1\%}$	$0.0318(1)^{+3.8\%}_{-3.2\%}$ (+50.6%)	$0.0342(1)^{+5.4\%}_{-4.3\%}$ (+7.7%)	$0.0371(3)^{+3.6\%}_{-3.0\%}$ (+16.9%)	3.70
	$\sqrt{s} = 27\,\mathrm{TeV}$	$0.0675(1)^{+0.\%}_{-0.2\%}$	$0.1100(3)^{+3.5\%}_{-2.8\%}$ (+62.9%)	$0.1235(3)^{+5.4\%}_{-4.3\%}$ (+12.3%)	$0.1371(7)^{+4.3\%}_{-3.5\%}$ (+24.7%)	

Table 24: Selection cuts applied in the analysis for the different processes.

	W^+W^-	$W^\pm Z$	ZZ
lepton cuts	$p_{\mathrm{T},\ell_{1/2}} > p_{\mathrm{T,min}}$	$p_{\mathrm{T},\ell_{1/2/3}} > p_{\mathrm{T,min}}$	$p_{\mathrm{T},\ell_{1/2/3/4}} > p_{\mathrm{T,min}}$
neutrino cuts	$p_{\mathrm{T,miss}} > p_{\mathrm{T,min}}$	$p_{\mathrm{T,miss}} > p_{\mathrm{T,min}}$	—

From the results in Table 22 and 23 it is clear that the perturbative uncertainties at NLO cannot account for the additional loop-induced gluon fusion contribution that appears at NNLO. Besides that, also the genuine NNLO corrections to the quark–antiquark production mechanism cannot be anticipated from NLO scale variations, which in turn means that the NLO uncertainties are underestimated. The inclusion of NNLO corrections is therefore crucial. At this order all partonic channels are included for the first time, and scale variations can be used to obtain an estimate of the actual size of missing higher-order terms. However, the NLO corrections to the loop-induced gluon fusion contribution are relevant and should be included when possible, especially at $\sqrt{s} = 27\,\mathrm{TeV}$ where gluons with smaller x are probed. In particular in tails of high-energy observables, the inclusion of NLO EW corrections and their interplay with QCD corrections will also need to be investigated. Nevertheless we restrict ourselves to presenting NNLO QCD results in the following, but the above-mentioned extensions will become available well before the start of the HL-LHC.

We now turn to discussing differential results in diboson processes in the light of the HL and HE upgrades of the LHC. Since the importance of highest-order predictions is evident from the previous discussion, we concentrate on NNLO QCD accurate results here. We first consider the cumulative cross section with a minimum $p_{\mathrm{T,min}}$ cut, as introduced above. In order to analyse the number of expected

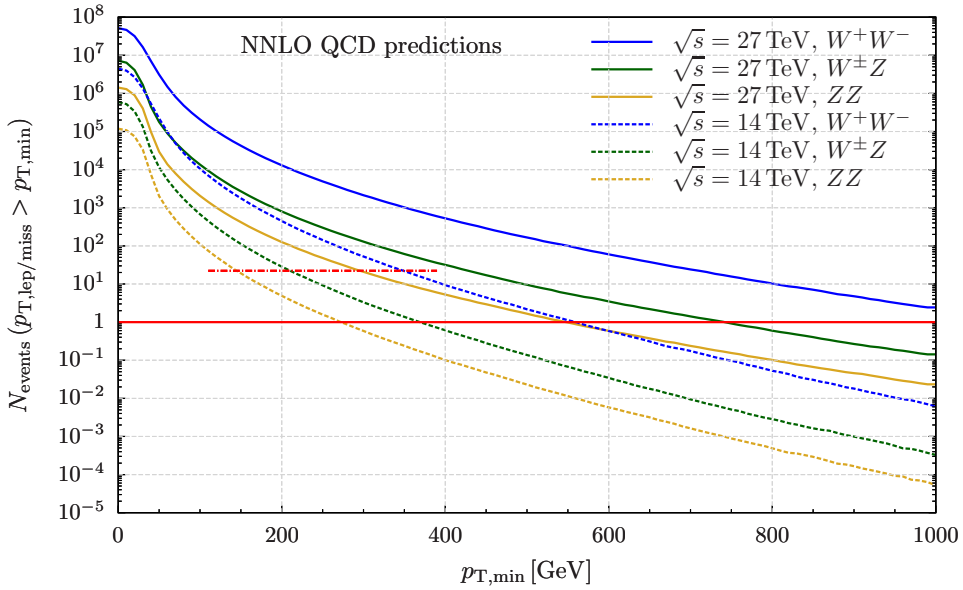

Fig. 39: Cumulative number of events as a function of $p_{\text{T,min}}$.

events as a function of $p_{\text{T,min}}$, we have translated the cross sections to event numbers by assuming an integrated luminosity of $3\,\text{ab}^{-1}$ at 14 TeV and of $15\,\text{ab}^{-1}$ at 27 TeV.

Figure 39 shows the expected number of events as a function of $p_{\text{T,min}}$. Since we are restricting the transverse momentum of all leptonic final states simultaneously, the reach in the tails may appear smaller than expected, and would be significantly larger if we were to consider a cut on the transverse momentum of the leading lepton or the missing energy only. However, the toy scenario we are considering is well suited to compare the three diboson production processes, and to quantify the relative gain of the additional energy and luminosity.

The curves in Figure 39 show all production processes under consideration: W^+W^- (blue), $W^\pm Z$ (green), and ZZ (orange); at 14 TeV (dashed) and 27 TeV (solid). The horizontal red line shows the one-event threshold, below which no events are expected anymore. We read the following features from the plot: At $\sqrt{s} = 14\,\text{TeV}$ we expect events up to $p_{\text{T,min}}$ values of roughly 550 GeV, 370 GeV, and 270 GeV for W^+W^-, $W^\pm Z$, and ZZ production, respectively. At $\sqrt{s} = 27\,\text{TeV}$ these values read >1000 GeV, 740 GeV, and 550 GeV. To put these numbers into perspective, we have added a dash-dotted red line for the present status at the end of Run II, which represents the one-event threshold for $150\,\text{fb}^{-1}$ at 13 TeV (14 TeV $\to$ 13 TeV conversion approximated by a constant cross-section correction factor of 0.9). Its intersection points with the $\sqrt{s} = 14\,\text{TeV}$ curves indicates the current reach of the LHC, which is roughly up to 350 GeV, 210 GeV, and 140 GeV for W^+W^-, $W^\pm Z$, and ZZ production, respectively. The improved reach in the tails at 27 TeV is not only related to the larger inclusive cross section and higher luminosity, but also the enlarged phase-space available with higher energies plays an important role: Whereas the solid curves fall only by $7-8$ orders of magnitude in the range of $0\,\text{GeV} \le p_{\text{T,min}} \le 1000\,\text{GeV}$, the dashed 14 TeV curves fall by more than 9 orders of magnitude in the same region. This also explains why the 14 TeV W^+W^- result, which has a much larger inclusive cross section, crosses the red one-event line at almost the same point as the 27 TeV ZZ result.

In Figure 40 we study the reach of the three vector-boson pair production processes for future LHC upgrades in the invariant-mass distributions of all produced charged leptons. We choose a scenario where $p_{\text{T,min}}$, defined as before in the three processes, is 20 GeV in order to have at least a rough definition of the fiducial phase-space. We show the expected number of events, assuming the same integrated

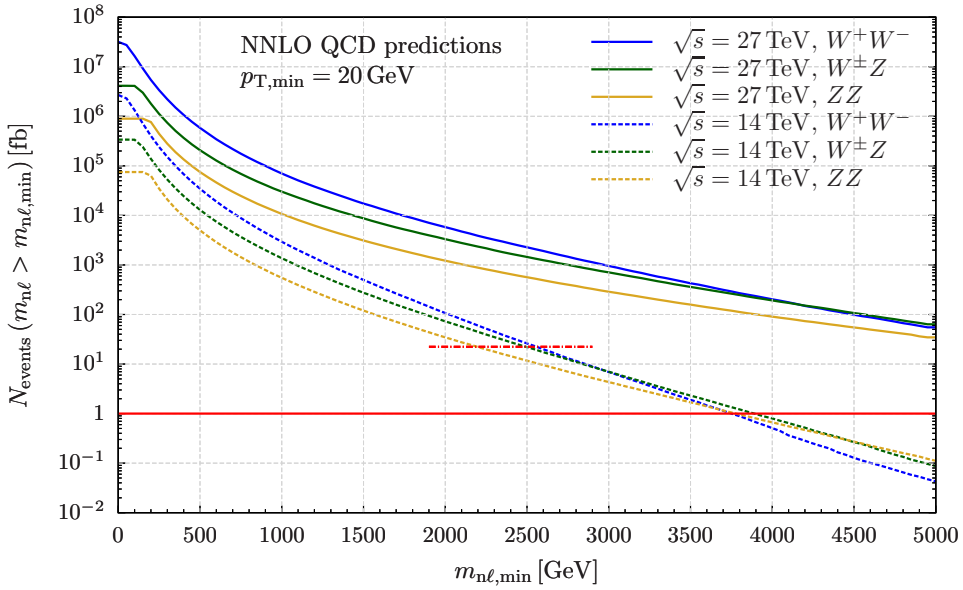

Fig. 40: Cumulative number of events as a function of $m_{n\ell,\mathrm{min}}$.

luminosities as stated above, for $\sqrt{s} = 14\,\mathrm{TeV}$ (dashed) and $\sqrt{s} = 27\,\mathrm{TeV}$ (solid) with a lower cut $m_{n\ell} > m_{n\ell,\mathrm{min}}$, where n is the number of leptons in the respective process, i.e., for W^+W^- production it is the distribution in $m_{2\ell}$ (blue), for $W^\pm Z$ it is the one in $m_{3\ell}$ (green), and for ZZ in $m_{4\ell}$ (orange). The significant reach in energy for both the HL run of the LHC and a potential HE upgrade is evident. With "reach" we refer to the point where the curves cross the red horizontal one-event threshold. A resonance in the tails of the invariant masses of two leptons (plus missing transverse momentum) or of four leptons is indeed a realistic signature predicted by many BSM theories. While with the current Run II data (red, dash-dotted line crossing the 14 TeV results) searches can hardly pass the two TeV frontier, future LHC upgrades will allow us to probe mass scales of a few TeV at 14 TeV with $3\,\mathrm{ab}^{-1}$, or potentially even up to ten TeV at 27 TeV with $15\,\mathrm{ab}^{-1}$. We also notice that despite $\sigma_{W^+W^-} \gg \sigma_{W^\pm Z} \gg \sigma_{ZZ}$ holds inclusively, the point where the three lines fall below one event is much closer. This is simply caused by the fact that the phase space of the four-lepton system in ZZ production is larger than the one of the three-lepton system in $W^\pm Z$ production, where some energy is taken by the additional neutrino. An analogous interpretation applies to W^+W^- production. Furthermore, also here the significantly enlarged phase space induced by the increase in energy at 27 TeV is evident: The 27 TeV results drop by roughly $4-5$ orders of magnitude in the displayed range, while the 14 TeV ones drop by more than 6 orders.

We continue our study by analysing the importance of the additional fiducial phase space that becomes available with detector upgrades to enlarge the accessible rapidity range of charged leptons. Since we found very similar results for W^+W^-, $W^\pm Z$ and ZZ production in that respect, in Figure 41 we show the rapidity efficiency of the four-lepton signature for ZZ production only. The rapidity efficiency is defined as the ratio of the cross section with an absolute-rapidity cut η_{cut} on all four charged leptons, divided by the inclusive cross section. As for $\eta_{\mathrm{cut}} \to \infty$ no cut is applied, the ratio tends to unity for large η_{cut} values. The efficiency as a function of η_{cut} is studied for three $p_{\mathrm{T,min}}$ scenarios: inclusive (light blue), $p_{\mathrm{T,min}} = 20\,\mathrm{GeV}$ (blue), and $p_{\mathrm{T,min}} = 100\,\mathrm{GeV}$ (dark blue); at 14 TeV (dashed) and 27 TeV (solid). We directly observe that the efficiency decreases with the machine energy. In other words, a small rapidity threshold at 27 TeV results in a much larger (relative) reduction of the cross section than at 14 TeV. This is because the additional energy induces more forward (and boosted) leptons, and it shows

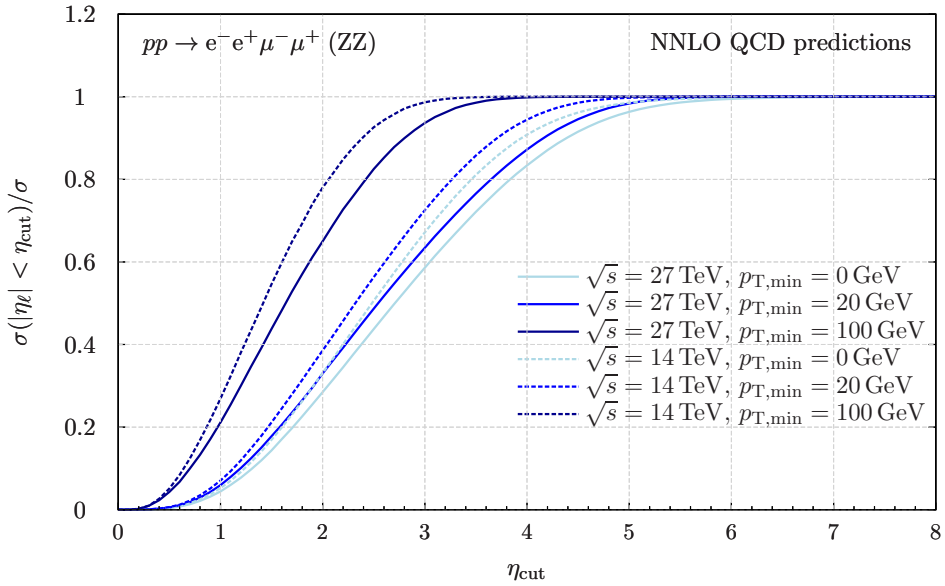

Fig. 41: Rapidity efficiency of the charged leptons.

that detector upgrades that enlarge the measurable rapidity range become even more important at the HE LHC. Requiring minimum transverse-momentum cuts, on the other hand, has the effect of increasing the rapidity efficiency, which is particularly striking for $p_{\text{T,min}} = 100\,\text{GeV}$. The reason for this is simple: Leptons with high transverse momentum are predominantly produced at central rapidities.

Let us focus on the scenario with $p_{\text{T,min}} = 20\,\text{GeV}$ as it provides the most realistic fiducial setup, which is actually not much different from the fully inclusive case. Typical rapidity cuts on charged leptons with the current LHC detectors are of the order of $\eta_\ell = 2.5$. Future detector upgrades for the HL phase of the LHC can be expected to reach rapidities at the level of $\eta_\ell = 4$. At $14\,(27)$ TeV this would allow us to improve measurements of fiducial cross from a $<60\%$ ($\sim 50\%$) efficiency for $\eta_{\text{cut}} = 2.5$ to a $>90\%$ ($\lesssim 90\%$) efficiency for $\eta_{\text{cut}} = 4$. This implies that the available inclusive cross section will be hardly reduced by fiducial rapidity requirements anymore once the detectors have been upgraded. This statement holds even more when considering scenarios with boosted leptons: For $p_{\text{T,min}} = 100\,\text{GeV}$ the efficiency is practically 100% for $\eta_{\text{cut}} = 4$.

Projections for measurements of anomalous 3-gauge boson couplings

The $SU(2) \times U(1)$ structure of the electroweak sector of the Standard Model determines the W^+W^-V interactions ($V = \gamma, Z$). The amplitudes for the production of W^+W^- pairs involve subtle cancellations between contributions that grow with energy, so the pair production of gauge bosons is extremely sensitive to new physics interactions. Assuming CP conservation, the most general Lorentz invariant $3-$gauge boson couplings can be written as [415,416]

$$\begin{aligned}\mathcal{L}_V &= -ig_{WWV}\Big\{(1+\delta g_1^V)\left(W^+_{\mu\nu}W^{-\mu}V^\nu - W^-_{\mu\nu}W^{+\mu}V^\nu\right) + (1+\delta\kappa^V)W^+_\mu W^-_\nu V^{\mu\nu}) \\ &\quad + \frac{\lambda^V}{M_W^2}W^+_{\rho\mu}W^{-\mu}{}_\nu V^{\nu\rho}\Big\}, \end{aligned} \tag{20}$$

where $V = \gamma, Z$, $g_{WW\gamma} = e$, $g_{WWZ} = g\cos\theta_W$, $s_W \equiv \sin\theta_W$, $c_W \equiv \cos\theta_W$, and in the SM, $\delta g_1^V = \delta\kappa^V = \lambda^V = 0$. Because of gauge invariance, This form can be translated into the language of effective field theory, where δg_1^V , $\delta\kappa^V$, $\lambda^V \sim \frac{v^2}{\Lambda^2}$, with Λ the scale of BSM physics, $\Lambda >> v$.

The effective couplings of fermions to gauge fields are parameterised as,

$$\begin{aligned}\mathcal{L} &= \frac{g}{c_W} Z_\mu \left[g_L^{Zq} + \delta g_L^{Zq} \right] \bar{q}_L \gamma_\mu q_L + g_Z Z_\mu \left[g_R^{Zq} + \delta g_R^{Zq} \right] \bar{q}_R \gamma_\mu q_R \\ &+ \frac{g}{\sqrt{2}} \left\{ W_\mu \left[(1 + \delta g_L^W) \bar{q}_L \gamma_\mu q'_L + \delta g_R^W \bar{q}_R \gamma_\mu q'_R \right] + h.c. \right\}, \end{aligned} \tag{21}$$

where Q_q is the electric charge of the quarks, and q denotes up-type or down-type quarks. The anomalous fermion couplings also scale as $\delta g_{L,R}^{Zq}, \delta g_{L,R}^{W} \sim \frac{v^2}{\Lambda^2}$. The SM quark couplings are $g_R^{Zq} = -s_W^2 Q_q$ and $g_L^{Zq} = T_3^q - s_W^2 Q_q$ with $T_3^q = \pm\frac{1}{2}$. $SU(2)$ invariance relates the coefficients, $\delta g_L^W = \delta g_L^{Zf} - \delta g_L^{Zf'}$, $\delta g_1^Z = \delta\kappa^Z + \frac{s_W^2}{c_W^2}\delta\kappa^\gamma$ and $\lambda^\gamma = \lambda^Z$, where f denotes up-type quarks and f' down-type quarks.

We have implemented both the anomalous 3-gauge boson and fermion couplings into the POWHEG BOX framework [417,418] for W^+W^- production and generated samples of events with $pp \to W^+W^- \to \mu^\pm e^\mp \nu\nu$. Fits to 8 TeV data [419, 420] illustrate the importance of including both anomalous fermion and 3-gauge boson couplings. The sensitivity to anomalous couplings results almost entirely from contributions quadratic in the anomalous couplings and the effects of anomalous 3-gauge boson and fermion couplings are numerically similar.

To probe the sensitivity to anomalous couplings, we generate events using the cuts

$$p_T^l > 30\ GeV,\ |\ \eta^l\ | < 2.5,\ m_{ll} > 10\ \text{GeV}, \not{E}_T > 20\ \text{GeV}\,. \tag{22}$$

These cuts are similar to those applied in the ATLAS [421] and CMS [422] extractions of anomalous coupling limits using the 8 TeV data. We postulate a hypothetical future systematic uncertainty of $\delta_{sys} = 16\%$ and set a cut on the p_T of the leading lepton such that the systematic error is smaller than the statistical error, $\delta_{stat} = \frac{1}{\sqrt{L\sigma(p_{l,T}^{lead} > p_T^{cut})}} > \delta_{sys}$,where L is the integrated luminosity. We look at the integrated cross section above a p_T^{cut}, assume a 50 % efficiency and set the cuts as

$$27\ \text{TeV with}\ 15\ ab^{-1}:\quad p_T^{cut} = 750\ \text{GeV}, \qquad 14\ \text{TeV with}\ 3\ ab^{-1}: p_T^{cut} = 1350\ \text{GeV}\,. \tag{23}$$

We work at NLO QCD, use CT14qed-inc-proton PDFs, and take the renormalisation/factorisation scales to be $M_{WW}/2$. We assume the $Wl\nu$ couplings in the decays are SM-like.

The results of the scans are shown in Figs. 42 and 43; the allowed regions are within the ellipses. We see a significant improvement going from 14 TeV to 27 TeV, while the improvement from reducing the systematic error, $\delta_{sys} = .16 \to .04$, is marginal. We allow the fermion couplings to vary around 0, assuming the 2σ errors from fits to LEP data. As can be seen, by including the anomalous fermion couplings, the sensitivity of the scan is significantly reduced [419, 423]. This effect is quite pronounced at 27 TeV and implies that global fits to both anomalous fermion and 3 gauge boson couplings are necessary.

4.4.3 Prospects for the measurement of the W-boson mass

Special low pile-up proton-proton collision data at the HL-LHC (and HE-LHC) will be of large interest for W boson physics. At $\sqrt{s} = 14$ TeV and for an instantaneous luminosity of $\mathcal{L} \sim 5 \times 10^{32}$ cm^{-2}s^{-1}, corresponding to two collisions per bunch crossing on average, about $2{\times}10^6$ W boson events can be collected in one week. Such a sample provides a statistical sensitivity at the permille level for cross section measurements, at the percent level for measurements of the W boson transverse momentum distribution, and of about 10 MeV for a measurement of m_W. The increased acceptance provided by the new inner detector in ATLAS, the ITk [424], extends the coverage in pseudorapidity from $|\eta| < 2.5$ to

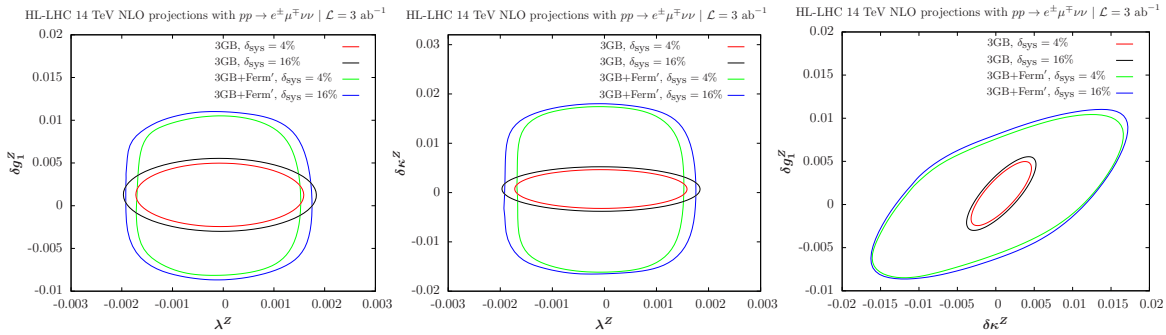

Fig. 42: Projections for 14 TeV with 3 ab^{-1}. We take $p_{T,cut} = 750$ GeV, corresponding to $\delta_{stat} = 16\%$ and consider $\delta_{sys} = 4\%$ and $\delta_{sys} = 16\%$. The curves labelled 3GB have SM Z-fermion couplings, while the curves labelled 3GB +Ferm' allow the Z-fermion couplings to vary around a central value of 0.

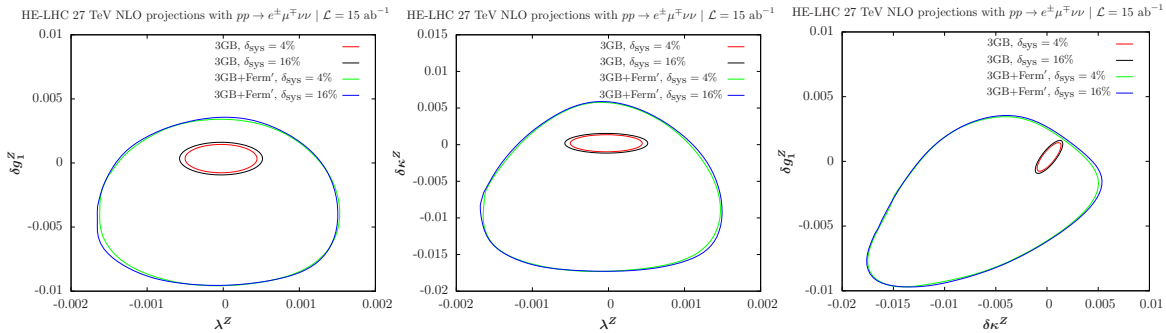

Fig. 43: Projections for 27 TeV with 15 ab^{-1}. We take $p_{T,cut} = 1350$ GeV, corresponding to $\delta_{stat} = 16\%$ and consider $\delta_{sys} = 4\%$ and $\delta_{sys} = 16\%$. The curves labelled 3GB have SM Z-fermion couplings, while the curves labelled 3GB +Ferm' allow the Z-fermion couplings to vary around a central value of 0.

$|\eta| < 4$ and allows further constraints on the parton density functions (PDFs) from cross section measurements, reducing the corresponding uncertainties in the measurement of m_W. An energy increase at the HE-LHC to $\sqrt{s} = 27$ TeV [425] could play a similar role. A first quantitative study of the potential improvement in the W-boson mass using low pile-up data at the HL-LHC and HE-LHC is discussed in [426] considering only statistical and PDF uncertainties. Experimental systematic uncertainties can be maintained at a level similar to the statistical uncertainty, since they are largely dominated by the statistics of the low pile-up samples. Other theoretical uncertainties in the modelling of the W-boson production, like the description of the boson transverse momentum distribution, will also be constrained by measurements using these data.

Leptonic W boson decays are characterised by an energetic, isolated electron or muon, and significant missing transverse momentum reflecting the decay neutrino. The hadronic recoil, $u_{\rm T}$, is defined from the vector sum of the transverse momenta of all reconstructed particles in the event excluding the charged lepton, and provides a measure of the W boson transverse momentum. The lepton transverse momentum, $p_{\rm T}^{\ell}$, the missing transverse momentum, $E_{\rm T}^{\rm miss}$, and the hadronic recoil are related through $\vec{E}_{\rm T}^{\rm miss} = -(\vec{p}_{\rm T}^{\,\ell} + \vec{u}_{\rm T})$. The $p_{\rm T}^{\ell}$ and $E_{\rm T}^{\rm miss}$ distributions have sharp peaks at $p_{\rm T}^{\ell} \sim E_{\rm T}^{\rm miss} \sim m_W/2$. The transverse mass $m_{\rm T}$, defined as $m_{\rm T} = \sqrt{2p_{\rm T}^{\ell} E_{\rm T}^{\rm miss} \cos(\phi_{\ell} - \phi_{\rm miss})}$, peaks at $m_{\rm T} \sim m_W$.

Events are generated at $\sqrt{s} = 14$ and 27 TeV using the W_EW_BMNNP process [135] of the POWHEG V1 event generator [273], with electroweak corrections switched off. The CT10 PDF set [427] is used, and parton shower effects are included using the PYTHIA8 event generator [324] with parameters set according to the AZNLO tune [428]. Final-state QED corrections are applied using PHOTOS [429]. The energy resolutions of the lepton and hadronic recoil are parameterised as a function of the truth-related observables in order to emulate detector effects. These parameterised resolutions are checked against simulated distributions at the reconstructed level, and they agree at a few percent level.

Events are selected applying the following cuts to the object kinematics, after resolution corrections: $p_{\mathrm{T}}^{\ell} > 25$ GeV, $E_{\mathrm{T}}^{\mathrm{miss}} > 25$ GeV, $m_{\mathrm{T}} > 50$ GeV and $u_{\mathrm{T}} < 15$ GeV; $|\eta_{\ell}| < 2.4$ or $2.4 < |\eta_{\ell}| < 4$. The first set of cuts selects the range of the kinematic peaks of the W boson decay products, restricting to the region of small p_{T}^{W} to maximise the sensitivity of the distributions to m_W. Two pseudorapidity ranges are considered, corresponding to the central region accessible with the current ATLAS detector, and to the forward region accessible in the electron channel with the ITk.

The Monte Carlo samples are produced using the CT10 PDF set, $m_W^{\mathrm{ref}} = 80.399$ GeV, and the corresponding Standard Model prediction for Γ_W. Kinematic distributions for the different values of m_W are obtained by applying an event weight to the reference samples based on the ratio of the Breit–Wigner densities corresponding to m_W and m_W^{ref}, for a given value of the final state invariant mass. A similar event weight, calculated internally by POWHEG and corresponding to the ratio of the event cross sections predicted by CT10 and several alternate PDFs, is used to obtain final state distributions corresponding to the CT14 [157], MMHT2014 [158], HL-LHC [257] and LHeC [430] PDF sets and their associated uncertainties. Compared to current sets such as CT14 and MMHT2014, the HL-LHC set incorporates the expected constraints from present and future LHC data; it starts from the PDF4LHC convention [153] and comes in three scenarios corresponding to more or less optimistic projections of the experimental uncertainties. The LHeC PDF set represents the impact of a proposed future high-energy, high-luminosity ep scattering experiment [431] on the uncertainties in the proton structure, using the theoretically best understood process for this purpose.

The shift in the measured value of m_W resulting from a change in the assumed PDF set is estimated as follows. Considering a set of template distributions obtained for different values of m_W and a given reference PDF set, and "pseudo-data" distributions obtained for $m_W = m_W^{\mathrm{ref}}$ and an alternate set i (representing, for example, uncertainty variations with respect to the reference set), the preferred value of m_W for this set is determined by minimising the χ^2 between the pseudo-data and the templates. The preferred value is denoted m_W^i, and the corresponding variation is defined as $\delta m_W^i = m_W^i - m_W^{\mathrm{ref}}$. The statistical uncertainty on the measurement is estimated from the half width of the χ^2 function one unit above the minimum.

The present study considers measurements of m_W in separate categories, corresponding to W^+ and W^- events; five pseudorapidity bins, $|\eta_{\ell}| < 0.6$, $0.6 < |\eta_{\ell}| < 1.2$, $1.2 < |\eta_{\ell}| < 1.8$, $1.8 < |\eta_{\ell}| < 2.4$, and $2.4 < |\eta_{\ell}| < 4$; p_{T}^{ℓ} and m_{T} distribution fits; and two centre-of-mass energies ($\sqrt{s} = 14$ and 27 TeV). For each category α and for the PDF sets considered here, the Hessian uncertainty corresponding to a given set is estimated as $\delta m_{W\alpha}^{+} = \left[\sum_i \left(\delta m_{W\alpha}^i\right)^2\right]^{1/2}$, if $\delta m_{W\alpha}^i > 0$, and as $\delta m_{W\alpha}^{-} = \left[\sum_i \left(\delta m_{W\alpha}^i\right)^2\right]^{1/2}$, if $\delta m_{W\alpha}^i < 0$, where i runs over the uncertainty sets, and $\delta m_{W\alpha}^i$ is calculated with respect to the reference PDF set. For CT10 and CT14, the uncertainties are divided by a factor 1.645 to match the 68% CL. Only symmetrised uncertainties, $\delta m_{W\alpha} = (\delta m_{W\alpha}^{+} + \delta m_{W\alpha}^{-})/2$, are considered for simplicity. The correlation of PDF uncertainties between different measurement categories is calculated as $\rho_{\alpha\beta} = \frac{\sum_i \delta m_{W\alpha}^i \delta m_{W\beta}^i}{\delta m_{W\alpha} \delta m_{W\beta}}$.

PDF variations generate correlated variations in the p_{T}^{W} and p_{T}^{Z} distributions, while the latter are strongly constrained by experimental data [428, 432]. These constraints were used in the ATLAS measurement

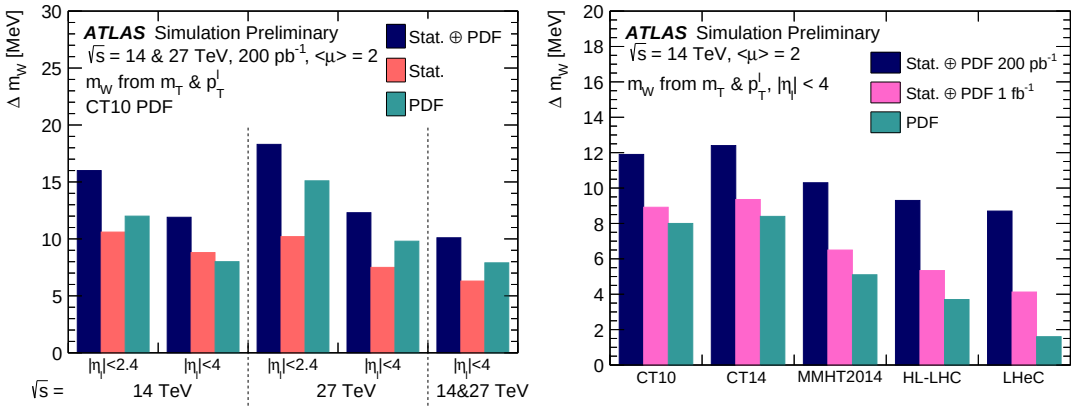

Fig. 44: Measurement uncertainty for combined fits to the p_{T}^{ℓ} and m_{T} distributions (a) in different lepton acceptance regions and for different centre-of-mass energies, using the CT10 PDF set and for 200 pb^{-1}collected at each energy and (b) for different PDF sets in $|\eta_{\ell}| < 4$, for 200 pb^{-1}and 1 fb^{-1}collected at $\sqrt{s} = 14$ TeV. The numbers quoted for $0 < |\eta_{\ell}| < 2.4$ correspond to the combination of the four pseudorapidity bins in this range.

of m_W [433], bringing significant reduction in the PDF uncertainties. The uncertainties estimated here are thus conservative from this perspective, and partly account for uncertainties in the p_{T}^{W} distribution.

The overall measurement precision is evaluated by combining the results obtained in the different categories using the BLUE prescription [434]. Only statistical and PDF uncertainties are considered. The former are assigned assuming an integrated luminosity of 200 pb^{-1}, and normalising the samples to the expected cross-sections. The expected measurement uncertainties, together with their statistical and PDF components, are summarised in Figure 44 (a) for CT10. The numbers quoted for $0 < |\eta_{\ell}| < 2.4$ correspond to the combination of the four pseudorapidity bins in this range. Moderate or negative PDF uncertainty correlations, leading to reduced combined uncertainties, are observed between categories of different W-boson charges, and between central and forward pseudorapidities, at given $\sqrt{s}$. On the other hand, PDF uncertainty correlations tend to be large and positive between $\sqrt{s} = 14$ and 27 TeV, for a given boson charge and lepton pseudorapidity range. With 200 pb^{-1}of data collected at each energy, a total uncertainty of about 10 MeV is obtained.

Table 25 and Figure 44 (b) compare the uncertainties obtained for different PDF sets. The CT10 and CT14 sets display similar uncertainty correlations, leading to similar improvements under combination of categories, and yielding comparable final PDF uncertainties. The MMHT2014 uncertainties are about 30% lower. The three projected HL-LHC PDF sets give very similar uncertainties; the most conservative one is shown here. Compared to CT10 and CT14, a reduction in PDF uncertainty of about a factor of two is obtained. The LHeC projection results from a QCD fit to 1 ab^{-1} of ep scattering pseudodata, with $E_e = 60$ GeV and $E_p = 7$ TeV. Such a sample could be collected in about five years, synchronously with the HL-LHC operation. In this configuration, the neutral- and charged-current DIS samples are sufficient to disentangle the first and second generation parton densities without ambiguity, and reduce the PDF uncertainty below 2 MeV, a factor 5–6 compared to present knowledge. Also in this case the m_W measurement will benefit from the large W boson samples collected at the LHC, and from the anti-correlation between central and forward categories. In this context, PDF uncertainties would still be sub-leading with 1 fb^{-1} of low pile-up data.

Table 25: Measurement uncertainty for different lepton acceptance regions, centre-of-mass energies and PDF sets, combined fits to the p_{T}^{ℓ} and m_{T} distributions, and for 200 pb^{-1}collected at each energy. The numbers quoted for $0 < |\eta_\ell| < 2.4$ correspond to the combination of the four pseudorapidity bins in this range. In each case, the first number corresponds to the sum of statistical and PDF uncertainties, and the numbers between parentheses are the statistical and PDF components, respectively.

$\sqrt{s}$ [TeV]	Lepton acceptance	Uncertainty in m_W [MeV]		
		CT10	CT14	MMHT2014
14	$\|\eta_\ell\| < 2.4$	16.0 (10.6 $\oplus$ 12.0)	17.3 (11.4 $\oplus$ 13.0)	15.4 (10.7 $\oplus$ 11.1)
14	$\|\eta_\ell\| < 4$	11.9 (8.8 $\oplus$ 8.0)	12.4 (9.2 $\oplus$ 8.4)	10.3 (9.0 $\oplus$ 5.1)
27	$\|\eta_\ell\| < 2.4$	18.3 (10.2 $\oplus$ 15.1)	18.8 (10.5 $\oplus$ 15.5)	16.5 (9.4 $\oplus$ 13.5)
27	$\|\eta_\ell\| < 4$	12.3 (7.5 $\oplus$ 9.8)	12.7 (8.2 $\oplus$ 9.7)	11.4 (7.9 $\oplus$ 8.3)
14+27	$\|\eta_\ell\| < 4$	10.1 (6.3 $\oplus$ 7.9)	10.1 (6.9 $\oplus$ 7.4)	8.6 (6.5 $\oplus$ 5.5)

$\sqrt{s}$ [TeV]	Lepton acceptance	Uncertainty in m_W [MeV]	
		HL-LHC	LHeC
14	$\|\eta_\ell\| < 2.4$	11.5 (10.0 $\oplus$ 5.8)	10.2 (9.9 $\oplus$ 2.2)
14	$\|\eta_\ell\| < 4$	9.3 (8.6 $\oplus$ 3.7)	8.7 (8.5 $\oplus$ 1.6)

4.4.4 Prospects for measurement of the effective weak mixing angle

At leading order dilepton pairs are produced through the annihilation of a quark and antiquark via the exchange of a Z boson or a virtual photon: $q\bar{q} \rightarrow Z/\gamma^* \rightarrow \ell^+\ell^-$. The definition of the forward-backward asymmetry, $\mathrm{A_{FB}}$, is based on the angle θ^* of the lepton (ℓ^-) in the Collins-Soper [435] frame of the dilepton system:

$$\mathrm{A_{FB}} = \frac{\sigma_{\mathrm{F}} - \sigma_{\mathrm{B}}}{\sigma_{\mathrm{F}} + \sigma_{\mathrm{B}}}, \tag{24}$$

where σ_{F} and σ_{B} are the cross sections in the forward ($\cos\theta^* > 0$) and backward ($\cos\theta^* < 0$) hemispheres, respectively. In this frame the θ^* is the angle of the ℓ^- direction with respect to the axis that bisects the angle between the direction of the quark and opposite direction of the anti-quark. In pp collisions the direction of the quark is assumed to be in the boost direction of the dilepton pair. Here, $\cos\theta^*$ is calculated using laboratory-frame quantities as follows:

$$\cos\theta^* = \frac{2(p_1^+ p_2^- - p_1^- p_2^+)}{\sqrt{M^2(M^2 + P_{\mathrm{T}}^2)}} \times \frac{P_{\mathrm{z}}}{|P_{\mathrm{z}}|}, \tag{25}$$

where M, P_{T}, and P_{z} are the mass, transverse momentum, and longitudinal momentum, respectively, of the dilepton system, and $p_1(p_2)$ are defined in terms of energy, $e_1(e_2)$, and longitudinal momentum, $p_{\mathrm{z},1}(p_{\mathrm{z},2})$, of the negatively (positively) charged lepton as $p_{\mathrm{i}}^{\pm} = (e_i \pm p_{\mathrm{z},i})/\sqrt{2}$ [435].

A non-zero $\mathrm{A_{FB}}$ in dilepton events arises from the vector and axial-vector couplings of electroweak bosons to fermions. At tree level, the vector v_{f} and axial-vector a_{f} couplings of Z bosons to fermions (f) are:

$$v_{\mathrm{f}} = T_3^{\mathrm{f}} - 2Q_{\mathrm{f}} \sin^2\theta_{\mathrm{W}}, \tag{26}$$

$$a_{\mathrm{f}} = T_3^{\mathrm{f}}, \tag{27}$$

where T_3^{f} and Q_{f} are the third component of the weak isospin and the charge of the fermion, respectively, and $\sin^2\theta_{\mathrm{W}}$ is the weak mixing angle, which is related to the masses of the W and Z bosons by the relation $\sin^2\theta_{\mathrm{W}} = 1 - M_{\mathrm{W}}^2/M_{\mathrm{Z}}^2$. Electroweak radiative corrections affect these leading-order relations.

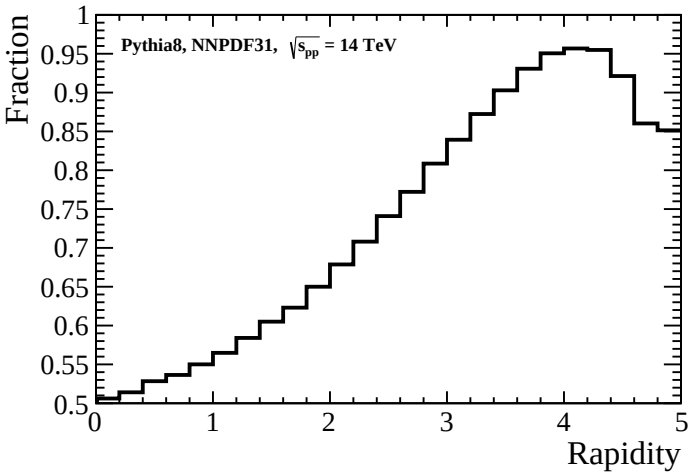

Fig. 45: The fraction of events where the Z boson travels in the same direction along the z-axis as the colliding quark, in proton-proton collisions with $\sqrt{s} = 14$ TeV. This increases as the event becomes more forward, reaching a maximum in the region probed by LHCb. The decrease once the rapidity is greater than 4 is because the fraction of collisions involving valence quarks decreases (the Bjorken-x value of the high momentum quark in these collisions is typically greater than 0.3). No detector effects are simulated for this figure.

An effective weak mixing angle, $\sin^2\theta^{\rm f}_{\rm eff}$, is defined based on the relation between these couplings: $v_{\rm f}/a_{\rm f} = 1 - 4|Q_{\rm f}|\sin^2\theta^{\rm f}_{\rm eff}$, with $\sin^2\theta^{\rm f}_{\rm eff} = \kappa_{\rm f}\sin^2\theta_{\rm W}$, where flavour-dependent $\kappa_{\rm f}$ is determined by electroweak corrections. Consequently, precise measurements of $\rm A_{FB}$ can be used to extract the effective leptonic weak mixing angle ($\sin^2\theta^{\rm lept}_{\rm eff}$).

The most precise previous measurements of $\sin^2\theta^{\rm lept}_{\rm eff}$ were performed by the LEP and SLD experiments [436]. There is, however, a known tension of about 3 standard deviations between the two most precise measurements. Measurements of $\sin^2\theta^{\rm lept}_{\rm eff}$ have also been performed by the LHC and Tevatron experiments [437–442].

In measurements of $\rm A_{FB}$ (or associated angular variables) in leptonic decays of Z bosons at a pp collider, the assignment of the z-axis is crucial. At low rapidities, there is a two-fold ambiguity in the direction of the initial state quark and anti-quark; the colliding quark is equally likely to be in either proton and the parton level asymmetry is diluted. However, at higher rapidities, the Z boson tends to be produced in the direction of travel of the quark, since the (valence) quark tends to be at higher Bjorken-x than the anti-quark. This means that the dilution between parton level and proton level quantities is significantly smaller at larger rapidities, illustrated in Fig.45, and consequently a larger forward-backward asymmetry is induced. Consequently, the forward acceptance of LHCb, in addition to the increased forward coverage of the ATLAS and CMS detectors in the HL-LHC will be crucial to achieving the most precise measurement of $\sin^2\theta^{\rm lept}_{\rm eff}$ possible.

The uncertainties on the parton distribution functions translate into sizeable variations in the observed $\rm A_{FB}$ values, which have limited the precision of current measurements of $\sin^2\theta^{\rm lept}_{\rm eff}$ at the LHC. However, the changes in PDFs affect the $\rm A_{FB}(M_{\ell\ell}, Y_{\ell\ell})$ distribution in a different way from changes in $\sin^2\theta^{\rm lept}_{\rm eff}$. Because of this behaviour, the distribution of $\rm A_{FB}$ can itself be used to constrain the PDF uncertainties on the extraction of $\sin^2\theta^{\rm lept}_{\rm eff}$ using either a Bayesian χ^2 reweighting method [443–445] (in the case of PDFs with Monte Carlo replicas) or through a profiling procedure [446] (in the case of PDFs with Hessian error sets).

Prospects for the measurement of the effective weak mixing angle using the forward-backward asym-

metry, A_{FB}, in Drell-Yan di-lepton events at the HL-LHC at ATLAS [447], CMS [448] and LHCb [449] have been performed and are reported here. The leptonic effective weak mixing angle is extracted from measurements of A_{FB} in dilepton events by minimising the χ^2 value between the simulated data and template A_{FB} distributions representing different $\sin^2\theta^{lept}_{eff}$ values and PDF variations. The LHCb and CMS analyses consider the dimuon final state, while the ATLAS analysis considers the dielectron final state. For CMS and LHCb the samples and different $\sin^2\theta^{lept}_{eff}$ templates are generated at next-to-leading order using the POWHEG event generator [450–453], where the NNPDF3.0 [454] PDF set is used in the case of the CMS analysis, and the NNPDF31 PDF set [165] for LHCb. For CMS, the analysis is performed at generator level without the effect of smearing due to detector effects[12] while for LHCb, a smearing is performed where the momentum resolution and reconstruction efficiency is assumed to be similar to the performance of the current detector [455]. In the case of ATLAS, events are generated with POWHEG and overlaid with additional inelastic pp collisions per bunch-crossing simulated with Pythia. Parameterisations of the expected ATLAS detector performances during the HL-LHC runs [456] are then applied on particle-level objects to emulate the detector response. Lepton trigger and identification efficiencies are derived as a function of η and p_T and used to estimate the likelihood of a given lepton to fulfil either the trigger or identification requirements, which have been optimised for the level of pile-up expected at the HL-LHC [367]. The A_{FB} distributions are generated, at leading order (LO) in QCD, with DYTURBO, an optimised version of DYRES/DYNNLO [457] with NNLO CT14 PDF and the world average value for $\sin^2\theta^{lept}_{eff} = 0.23153$.

The HL-LHC CMS detector will extend the pseudorapidity, η, coverage of the muon reconstruction from the current configuration of 2.4 to 2.8. In the CMS analysis an event is selected if there are at least two muons with $|\eta| < 2.8$ and with the leading (i.e. having the largest transverse momentum p_T muon $p_T > 25$ GeV and the second leading muon $p_T > 15$ GeV. Figure 46 shows the A_{FB} distributions in bins of dimuon mass and rapidity for different energies and pseudorapidity acceptances. As expected, at higher center-of-mass energies the observed A_{FB} is smaller because the interacting partons have smaller x-values which results in a smaller fraction of dimuon events produced by the valence quarks, which also means more dilution. The samples are normalised to the integrated luminosities of 19 fb^{-1} for $\sqrt{s} = 8$ TeV and to 10 – 3000 fb^{-1} for $\sqrt{s} = 14$ TeV samples and the simulated data are shown for $\sqrt{s} = 8$ TeV and $\sqrt{s} = 14$ TeV for two different selection requirements, $|\eta| < 2.4$ and 2.8. Extending the pseudorapidity acceptance significantly increases the coverage for larger x-values in the production and reduces both the statistical and PDF uncertainties, as shown below.

In the case of the 14 TeV analysis with a large number of events (> 200 fb^{-1}), the pseudo-data are too precise to estimate the PDF uncertainties with the Bayesian reweighting approach because the replica distributions are too sparse compared to the statistical uncertainties. Therefore, the PDF uncertainties after the Bayesian reweighting are estimated by extrapolating from the lower values of integrated luminosities.

The corresponding values for various luminosities at CMS are summarized in Table 26. One can see from the Table that with the extended pseudorapidity coverage of $|\eta| < 2.8$, the statistical uncertainties are reduced by about 30% and the PDF uncertainties are reduced by about 20%, compared to $|\eta| < 2.4$ regardless of the target integrated luminosity and for both nominal and constrained PDF uncertainties.

The LHCb detector has coverage in the pseudorapidity range $2 < \eta < 5$ and expects to install its 'Upgrade II' in Long Shutdown 4. Following this upgrade, LHCb will collect at least 300 fb^{-1} of data, allowing high precision measurements. The forward acceptance of LHCb brings a number of benefits in measurements of $\sin^2\theta^{lept}_{eff}$ at the LHC. The lower level of dilution in the forward region results in a larger sensitivity to $\sin^2\theta^{lept}_{eff}$ and the PDF effects are (in relative terms) smaller, providing both statistical precision in measurements of the weak mixing angle and a reduction in PDF uncertainties. In addition, LHCb does not simply probe forward rapidities of the Z boson: the leptons themselves are located over

[12] A comparison of 8 TeV predictions and measured values suggests the effect is not significant

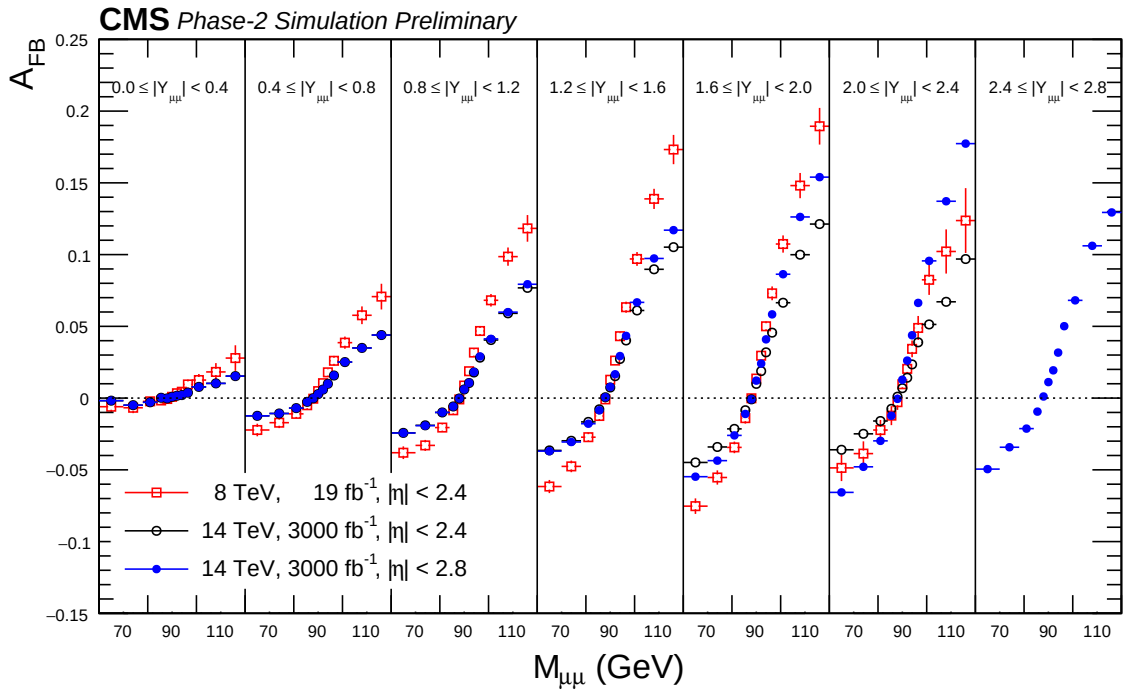

Fig. 46: Forward-backward asymmetry distribution, $\mathrm{A_{FB}}(M_{\mu\mu}, Y_{\mu\mu})$, in dimuon events at $\sqrt{s} = 8$ TeV and 14 TeV. The distributions are made with POWHEG event generator using NNPDF3.0 PDFs and interfaced with PYTHIA8 for parton-showering, QED final-state radiation (FSR) and hadronization. Following acceptance selections are applied to the generated muons after FSR: $|\eta| < 2.4$ (or $|\eta| < 2.8$), $p_{\mathrm{T}}^{\mathrm{lead}} > 25$ GeV, $p_{\mathrm{T}}^{\mathrm{trail}} > 15$ GeV. The error bars represent the statistical uncertainties for the integrated luminosities corresponding to 19 fb^{-1} at $\sqrt{s} = 8$ TeV and 3000 fb^{-1} at $\sqrt{s} = 14$ TeV.

a significant range of rapidities, allowing extremal values of $\cos\theta^*$ to be probed, increasing sensitivity to the weak mixing angle. Finally, LHCb has the ability to select events at low momentum using a flexible full software trigger and real time analysis scheme (from Run-3 onwards). It is therefore foreseen that the LHCb Upgrade II will be able to select Z boson decays where one lepton has transverse momentum above 20 GeV, while the other lepton has a transverse momentum above 5 GeV. Such low thresholds again increase the sensitivity to asymmetric events at high $|\cos\theta^*|$. In addition to the advantages of the extended forward acceptance for such measurements, as part of Upgrade II LHCb is expected to undergo a significant calorimeter upgrade[13] allowing similar precision to be achived in both the dielectron and dimuon final states.

LHCb has performed a study of projected sensitivities [**?**], considering the dimuon final state. The experiment is assumed to have coverage in the region $2.0 < \eta < 5$. Toy measurements of the forward-backward asymmetry are used to determine the sensitivity of measurements at LHCb Upgrade II to the weak mixing angle. Only statistical uncertainties are considered alongside the effects of knowledge of PDFs. The statistical uncertainty on $\sin^2\theta^{\mathrm{lept}}_{\mathrm{eff}}$ is expected to be below 5×10^{-5} with 300 fb^{-1} of data. The expected PDF uncertainty from current PDF knowledge is $\sim 20 \times 10^{-5}$, but with Bayesian reweighting this can be reduced to the level of about 10×10^{-5} (with analysis of a dataset corresponding to an integrated luminosity of 300 fb^{-1}). This reduction assumes systematic effects are negligible in comparison to statistical uncertainties, though the current knowledge of PDFs means that any measurement in the forward region is expected to offer a smaller PDF uncertainty than the total uncertainties in

[13] This upgrade will offer an extended dynamic range within the ECAL, offering improved electron momentum resolution.

Table 26: Statistical, nominal NNPDF3.0, and constrained NNPDF3.0 uncertainties of extracted $\sin^2\theta^{\text{lept}}_{\text{eff}}$ at 14 TeV for muon acceptance of $|\eta| < 2.4$ and $|\eta| < 2.8$ and for the different values of integrated luminosity. For comparison, results of the 8 TeV estimate of this analysis are compared to the results obtained from 8 TeV measurement [448].

L_{int}	$\delta_{\text{stat}}[10^{-5}]$		$\delta^{\text{nominal}}_{\text{nnpdf3.0}}[10^{-5}]$		$\delta^{\text{constrained}}_{\text{nnpdf3.0}}[10^{-5}]$	
(fb^{-1})	$\|\eta\| < 2.4$	$\|\eta\| < 2.8$	$\|\eta\| < 2.4$	$\|\eta\| < 2.8$	$\|\eta\| < 2.4$	$\|\eta\| < 2.8$
10	76	51	75	57	39	29
100	24	16	75	57	27	20
500	11	7	75	57	20	16
1000	8	5	75	57	18	14
3000	4	3	75	57	15	12
19	43		49		27	
19 (from [448])	44		54		32	

the previous best measurements of the weak mixing angle. The main challenge of such measurements at LHCb Upgrade II will therefore be to control systematic uncertainties in order to ensure the overall measurement also achieves high precision; however, the large dataset of J/ψ and Υ mesons to be recorded is expected to aid the understanding of effects such as the momentum scale (which introduced the largest systematic uncertainty in the Run-1 analysis at LHCb). This should enable a measurement at LHCb Upgrade II with a precision similar to or better than that achieved in the combination of measurements at LEP and SLD.

A new inner tracking system (ITk) will extend the tracking coverage of the ATLAS detector from $|\eta| \leq 2.5$ up to $|\eta| \leq 4.0$ at the HL-LHC, providing the ability to reconstruct forward charged particle tracks, which can be matched to calorimeter clusters for forward electron reconstruction.

In the ATLAS analysis di-electron candidates are selected where each electron has p_{T} in excess of 25 GeV and the combined invariant mass is in the region of the Z pole. The data sample is then split into three channels, where both electrons are in the central region, satisfying $|\eta| < 2.47$ (the CC channel), where one electron is central and the other is forward, satisfying $2.5 < \eta < 4.2$ (the CF channel), and finally where both electrons are forward (the FF channel). Events are selected by requiring at least one electron firing the single electron trigger, except in the FF channel, where a dielectron trigger is required.

As Fig. 47 shows, the CF channel selects events at high $\cos\theta^*$ values where the forward-backward asymmetry is more pronounced, and consequently the sensitivity to $\sin^2\theta^{\text{lept}}_{\text{eff}}$ is higher in this channel. While the LHCb and CMS analyses consider only uncertainties due to statistics and PDFs, the ATLAS analysis considers also various sources of experimental uncertainty which affect the precision of the extraction of A_{FB}. The main contributions arise from the limited knowledge of the momentum scale and resolution of the electrons, and the background contributions, which are mostly relevant in the CF and FF channels.

The extraction of $\sin^2\theta^{\text{lept}}_{\text{eff}}$ is performed by minimising the χ^2 value comparing particle-level A_{FB} distributions with different weak mixing angle hypotheses in invariant mass and rapidity bins combining CC, CF and FF channels. A global fit is performed where $\sin^2\theta^{\text{lept}}_{\text{eff}}$ is extracted while constraining the PDF uncertainties using a profiling procedure following that used in a previous ATLAS publication [458] and implemented in the xFitter package [459].

With this analysis, a significant reduction of the light quarks uncertainties at low x is seen and combining the three channels together, the measurement reaches a precision of $18{\cdot}10^{-5}$ ($\pm 16{\cdot}10^{-5}$ (PDF) $\pm 9{\cdot}10^{-5}$ (exp.)). The uncertainty of the results remains dominated by the limited knowledge of the PDFs.

In the context of the Yellow Report for the HL-LHC, prospect PDF fits including HL-LHC pseudo-data

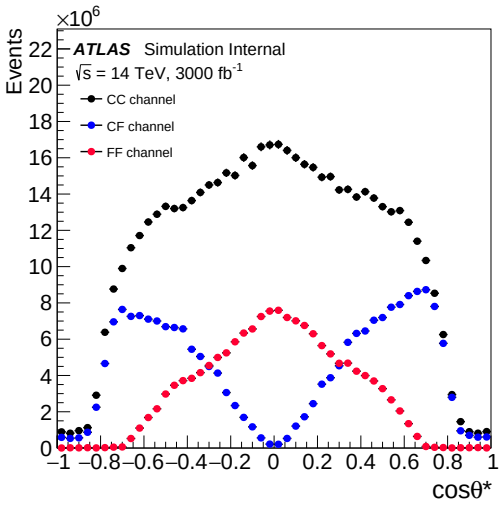

Fig. 47: The $\cos\theta^*$ distribution for CC, CF and FF channels for selected Drell-Yan di-electron events expected for 3000 fb^{-1} of data at $\sqrt{s} = 14$ TeV. SF: Still internal?

of future PDF-sensitive measurements from ATLAS, CMS and LHCb were performed (see Sec. 5.2). Three prospect PDF scenarios were considered and compared with the reference PDF set PDF4LHC15 [153]. The expected sensitivity of the $\sin^2\theta^{\text{lept}}_{\text{eff}}$ measurements with 3000 fb^{-1} at $\sqrt{s} = 14$ TeV is improved by 10-25% depending on the prospect PDFs scenario considered. In Table 27 the precision on $\sin^2\theta^{\text{lept}}_{\text{eff}}$ obtained with the "ultimate" HL-LHC PDF set is compared with the with the one obtained with CT14NNLO PDF set.

The sensitivity of the analysis to the $\sin^2\theta^{\text{lept}}_{\text{eff}}$ extraction is also estimated with a prospect PDF set including expected data from the LHeC collider [430]. In this case the PDF uncertainty is reduced by an additional factor of 5 with respect to the one obtained with the HL-LHC prospect PDFs.

Table 27: The value of $\sin^2\theta^{\text{lept}}_{\text{eff}}$ with the breakdown of uncertainties from the ATLAS preliminary results at $\sqrt{s} = 8$ TeV with 20 fb^{-1} [460] is compared to the projected $\sin^2\theta^{\text{lept}}_{\text{eff}}$ measurements with 3000 fb^{-1} of data at $\sqrt{s} = 14$ TeV for two PDF sets considered in this note. All the numbers values are given in units of 10^{-5}. Note that other sources of systematic uncertainties, such as the impact of the MC statistical uncertainty, evaluated in Ref. [460] are not considered in this prospect analysis. For the HL-LHC prospect PDFs the "ultimate" scenario is chosen.

	ATLAS $\sqrt{s} = 8$ TeV	ATLAS $\sqrt{s} = 14$ TeV	ATLAS $\sqrt{s} = 14$ TeV
$\mathcal{L}$ [fb^{-1}]	20	3000	3000
PDF set	MMHT14	CT14	PDF4LHC15$_{HL-LHC}$
$\sin^2\theta^{\text{lept}}_{\text{eff}}$ [$\times 10^{-5}$]	23140	23153	23153
Stat.	$\pm$ 21	$\pm$ 4	$\pm$ 4
PDFs	$\pm$ 24	$\pm$ 16	$\pm$ 13
Experimental Syst.	$\pm$ 9	$\pm$ 8	$\pm$ 6
Other Syst.	$\pm$ 13	-	-
Total	$\pm$ 36	$\pm$ 18	$\pm$ 15

To conclude, the accuracy of measurements of the weak mixing angle obtained with an analysis of the A_{FB} in Z-events at $\sqrt{s} = 14$ TeV with $3000\,\text{fb}^{-1}$ at ATLAS and CMS and $300\,\text{fb}^{-1}$ at LHCb at the HL-LHC exceed the precision achieved in all previous single-experiment results to date and the measurements are dominated by PDF uncertainties. To explore the full potential of the HL-LHC data it will be therefore essential to reduce PDF uncertainties. A significant improvement of the sensitivity of the measurement is observed in the ATLAS analysis when using prospect PDF sets including ancillary Drell-Yann measurements performed with the data collected during the high luminosity phase of the LHC and at the LHeC collider.

4.4.5 The global EW fit

The measurement of the Higgs Boson mass (M_H) at the Large Hadron Collider (LHC) has provided the last input to the global fit of electroweak (EW) precision observables (EWPO), which can now be used to effectively constrain new physics. Moreover, the measurement of Higgs-boson production and decay rates that is at the core of the physics program of the LHC Run 2 will further constrain those interactions that directly affect Higgs-boson physics.

The high-luminosity LHC (HL-LHC) will have the potential to provide more constraining bounds on new physics via the global fit to EWPO and Higgs data, thanks to the higher precision it will reach both in the measurement of some of the crucial input parameters of global EW fits (e.g. M_W, m_t, M_H, and $\sin^2\theta^{\text{lept}}_{\text{eff}}$), and in the measurement of Higgs-boson total and differential rates. In this study we would like to explore the reach of the HL-LHC in constraining new physics via a global fit to EWPO.

In the following, we first provide details on the parameters and procedure of the global EW fit. Next we present the results interpreted within the Standard Model (SM). Finally, we use the EW fit to constrain new physics beyond the SM. We present the results for both current data and the projections in the HL-LHC scenario.

General framework and HEPfit

The global fit of EWPO is performed using the `HEPfit` package [461], a general tool to combine direct and indirect constraints on the SM and its extensions in any statistical framework. The default fit procedure, which we use here, follows a Bayesian statistical approach and uses BAT (Bayesian Analysis Toolkit) [462]. We use flat priors for all input parameters, and build the likelihood assuming Gaussian distributions for all experimental measurements. The output of the fit is therefore given as the posterior distributions for each input parameters and observables, calculated using a Markov Chain Monte Carlo method.

All EWPO are calculated as a SM core plus corrections. The SM core includes all available higher-order corrections, including the latest theoretical developments in the calculation of radiative corrections to the EWPO of [463, 464].[14] New-physics corrections are computed at the leading order. The `HEPfit` code allows for the implementation of different models of new physics. In particular, as explained below, we will specialize our study to the general framework of the so called SM effective field theory (SMEFT), where the SM Lagrangian is extended by the addition of operators of canonical mass dimension higher than four (limited to the basis of operators of canonical dimension six in this study).

As far as EWPO are concerned, this study updates the EWPO fit of Refs. [465–467], including recent updates on the theory calculations [464] and experimental measurements [148, 468–475]. We further reduce the uncertainties on some input parameters that have been obtained by including hadron collider data, in order to account for the level of accuracy expected for the HL-LHC. In all these projections we assume the central values for the HL-LHC measurements will not change with respect to current data.

[14] The uncertainties associated to missing higher-order corrections to the SM predictions for the EWPO are also taken into account in the fits, via nuisance parameters with Gaussian priors.

In particular we have assumed that:

1. The W mass, whose uncertainty obtained by combining ATLAS and Tevatron+LEP2 measurements is currently around 12 MeV [467], could be measured at the HL-LHC with a precision of 7 MeV. This number is derived from the current estimate of the statistical plus PDF uncertainty using 1 fb^{-1} of data reported in Sec. 4.4.3, and assuming systematic errors to be of similar size to the statistical ones. In this fit we therefore add to the current combination an HL-LHC measurement of $M_W = 80.379 \pm 0.007$ GeV.

2. An aggressive estimate of the current uncertainty on the top-quark mass, obtained by combining current Tevatron and LHC measurements, puts the error of m_t at the level of 0.4 GeV. It will be difficult to further reduce this number at the HL-LHC, since the remaining uncertainty is mainly of systematic and theoretical origin. In the current fit we use $m_t = 172.8 \pm 0.4$ GeV.

3. The measurements of the effective angle $\sin^2\theta^{\rm lept}_{\rm eff}$ can also be improved at the HL-LHC. Currently, a combination of the latest LHC and Tevatron results returns a precision for this observable of $\sim 0.00022 - 0.00027$, depending on the assumptions made in combining common uncertainties. For the HL-LHC fit, we repeat the combination assuming that statistical uncertainties become subdominant. This results in a total uncertainty of ± 0.00018. This number is consistent with preliminary ATLAS results using CT14 PDFs. Using the HL-LHC PDF set this number could be further reduced to ± 0.00015. We therefore use $\sin^2\theta^{\rm lept}_{\rm eff} = 0.23143 \pm 0.00015$ as the input for our fits.

4. The error on the Higgs-boson mass, currently around 0.20 GeV, can be reduced to 0.05 GeV [476].

5. The HL-LHC should also be able to improve the current knowledge on the W width, whose precision of 42 MeV is currently given by the combination of LEP2 and Tevatron measurements. This uncertainty is dominated by the hadron collider measurement. While there is no available information about a possible determination of this quantity at the (HL-)LHC, we will use the conservative assumption that the HL-LHC can achieve a precision on Γ_W at least as good as the one on the current average. We therefore add an independent HL-LHC measurement of $\Gamma_W = 2.085 \pm 0.042$ GeV. This gives a 30 MeV uncertainty when combined with the current average.

Finally, apart from the improved precision of the HL-LHC measurements, we will assume that, by the end of the HL-LHC run, better measurements of some of the SM input parameters are possible from other experiments. In particular, following Ref. [465, 466], we assume that: 1) the uncertainty on $\Delta\alpha^{(5)}_{\rm had}(M_Z)$ can be reduced to $\pm 5 \times 10^{-5}$ by using data from currently ongoing and future experiments that measure the cross section for $e^+e^- \to$ hadrons, and 2) future lattice QCD measurements will provide a determination of the strong coupling constant with accuracy $\delta\alpha_S(M_Z) = \pm 0.0002$. The measurements of all other EWPO and input parameters have been kept to their currently available values. The current values of all EWPO measurements, as well as the corresponding HL-LHC projected uncertainties, are listed in the second and third columns of Table 28, respectively.

Global Fit: Standard Model fit results

The results of the SM global fit to EWPO for both the present (LHC) and future (HL-LHC) scenarios are collected in Table 28. These are given in the form of the mean and standard deviation for each of the observables, as derived from the posterior of the fits. For each EWPO we also compute the "pull", defined as the difference between the experimental value and the SM prediction computed by removing each observable from the fit (not shown in the table), normalized to the total uncertainty. As it is apparent, the differences in the posteriors between both fits are quite small. However, looking at the pulls one can see

Table 28: Current experimental measurement, HL-LHC projected uncertainty, posterior, and pull for the five input parameters ($\alpha_s(M_Z)$, $\Delta\alpha^{(5)}_{\rm had}(M_Z)$, M_Z, m_t, M_H), and for the main EWPO considered in the SM fit. The pulls in the last column are obtained comparing the experimental measurements with the predictions from a fit *removing* the corresponding observable(s) (See, e.g., [465] for details.).

	Measurement	HL-LHC uncertainty	Posterior		Pull
			Current	HL-LHC	Current/HL-LHC
$\alpha_s(M_Z)$	0.1180 ± 0.0010	± 0.0002	0.1180 ± 0.0009	0.1180 ± 0.0002	$0/0.5$
$\Delta\alpha^{(5)}_{\rm had}(M_Z)$	0.027611 ± 0.000111	± 0.00005	0.02758 ± 0.00011	0.02759 ± 0.00005	$1.1/2.1$
M_Z [GeV]	91.1875 ± 0.0021		91.1880 ± 0.0020	91.1890 ± 0.0020	$-1.3/-2.6$
m_t [GeV]	172.8 ± 0.7	± 0.4	173.2 ± 0.66	173.1 ± 0.38	$-1.7/-2.9$
M_H [GeV]	125.13 ± 0.17	± 0.05	125.13 ± 0.17	125.13 ± 0.05	$1.4/3$
M_W [GeV]	80.379 ± 0.012	± 0.007	80.362 ± 0.006	80.367 ± 0.004	$1.6/2.7$
Γ_W [GeV]	2.085 ± 0.042	± 0.042	2.0885 ± 0.0006	2.0889 ± 0.0003	-0.1
$\mathrm{BR}_{W\to\ell\nu}$	0.1086 ± 0.0009		0.10838 ± 0.00002	0.10838 ± 0.000005	0.2
$\mathrm{BR}_{W\to\mathrm{had}}$	0.6741 ± 0.0027		0.67486 ± 0.00007	0.67486 ± 0.00001	-0.3
$\sin^2\theta^{\rm lept}_{\rm eff}(Q^{\rm had}_{\rm FB})$	0.2324 ± 0.0012		0.23151 ± 0.00006	0.23150 ± 0.00005	0.7
$P^{\rm pol}_\tau = A_\ell$	0.1465 ± 0.0033		0.14711 ± 0.0005	0.14713 ± 0.0004	-0.2
Γ_Z [GeV]	2.4952 ± 0.0023		2.4946 ± 0.0007	2.4947 ± 0.0005	0.3
σ^0_h [nb]	41.540 ± 0.037		41.492 ± 0.008	41.491 ± 0.006	1.3
R^0_ℓ	20.767 ± 0.025		20.749 ± 0.008	20.749 ± 0.006	0.7
$A^{0,\ell}_{\rm FB}$	0.0171 ± 0.0010		0.01623 ± 0.0001	0.016247 ± 0.00008	0.9
A_ℓ (SLD)	0.1513 ± 0.0021		0.14711 ± 0.0005	0.14718 ± 0.0004	1.9
R^0_b	0.21629 ± 0.00066		0.21586 ± 0.0001	0.21586 ± 0.0001	$0.7/0.6$
R^0_c	0.1721 ± 0.0030		0.17221 ± 0.00005	0.17221 ± 0.00005	0
$A^{0,b}_{\rm FB}$	0.0992 ± 0.0016		0.10313 ± 0.00032	0.10319 ± 0.00026	$-2.4/-2.5$
$A^{0,c}_{\rm FB}$	0.0707 ± 0.0035		0.07369 ± 0.00024	0.07373 ± 0.0002	-0.9
A_b	0.923 ± 0.020		0.93475 ± 0.00004	0.93476 ± 0.00004	-0.6
A_c	0.670 ± 0.027		0.66792 ± 0.0002	0.66794 ± 0.0002	0.1
$\sin^2\theta^{\rm lept}_{\rm eff(Had.coll.)}$	0.23143 ± 0.00027	± 0.00015	0.23151 ± 0.00006	0.23150 ± 0.00005	$-0.5/-0.9$

that, should the central values of the SM input parameters remain the same, the expected improvements in their experimental uncertainties, combined with the more precise measurements of some EWPO at the HL-LHC, would significantly increase the tension between the indirect determinations of M_Z, m_t, and M_H from the EW fit and the corresponding experimental measurements, pushing them to the 3σ level. The improvement in the precision on m_t would also reduce the parametric uncertainty on some observables, e.g. the W mass, bringing the total residual error very close to the intrinsic uncertainty associated to missing higher-order corrections in the calculation of M_W. As in the case of some of the SM inputs, the expected improvement on the experimental precision of M_W, without a significant deviation on the central value, would add some tension between theory and experiment, pushing the pull for this observable well beyond the 2σ level. The impact of the HL-LHC measurements on the EW fit is well illustrated in Figure 48 where one can see the comparison between direct (i.e. experimental) and indirect constraints on the fit input parameters given for both the current and HL-LHC scenarios in the M_W vs. m_t and the M_W vs. $\sin^2\theta^{\rm lept}_{\rm eff}$ planes respectively.

Global Fit: constraints on new physics

The EWPO, being measured in processes mediated by the exchange of a Z or W boson, are extremely sensitive to any new physics that modifies the propagation of such particles. This results in a universal modification of the interactions between the EW gauge bosons and the SM fermions, which, from the point of view of EWPO, can be described in terms of only three parameters: the well-known S, T, and

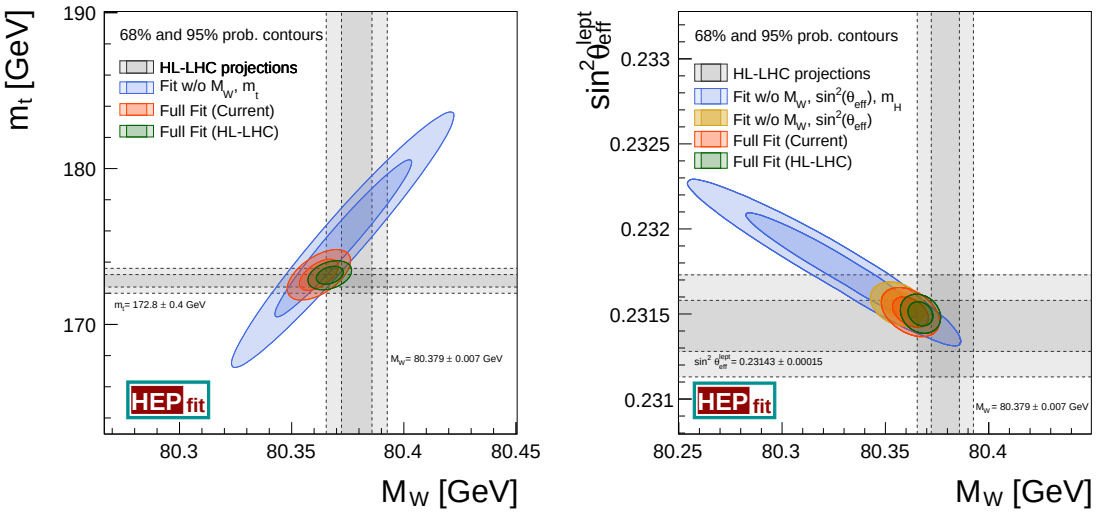

Fig. 48: Comparison of the indirect constraints on M_W and m_t with the current experimental measurements and the expected improvements at the HL-LHC (left). The same in the M_W-$\sin^2\theta^{\rm lept}_{\rm eff}$ plane (right).

U oblique parameters [477]. The study of the constraints on the S, T, and U parameters is one of the classical benchmarks in the study of EW precision constraints on new physics, and it is well motivated from a theory point of view, within the context of universal theories. The results of the fit to the S, T, and U parameters are given in Table 29. We show the results in terms of the full (S,T,U) fit and also assuming $U = 0$, which is motivated in theories where EW symmetry breaking is realised linearly, since in that case $U \ll S, T$. In both cases the current constraints are compared with the expected precision at the HL-LHC, which, in some cases, could improve the sensitivity to such new physics effects by up to $\sim 30\%$. The results for the ST fit ($U = 0$) are shown in Figure 49, illustrating also the constraints imposed by the different EWPO.

Table 29: Results of the fit for the oblique parameters S, T, U; and S, T ($U = 0$). Projections for the uncertainties at the HL-LHC are given in the last column.

	Result	Correlation Matrix			Precision at HL-LHC
S	0.04 ± 0.10	1.00			0.09
T	0.08 ± 0.12	0.90	1.00		0.12
U	0.00 ± 0.09	-0.62	-0.84	1.00	0.08
S	0.04 ± 0.08	1.00			0.06
T	0.08 ± 0.06	0.90	1.00		0.05
($U = 0$)					

As stressed above, the STU parameterisation only describes universal deformations with respect to the SM predictions. In order to systematically explore the impact of global EW precision fits on new physics, we will adopt in what follows the framework of the SMEFT. In this formalism, the SM Lagrangian is extended via operators of dimension five and higher, i.e.

$$\mathcal{L}_{\rm eff} = \mathcal{L}_{\rm SM} + \sum_{d>4} \frac{1}{\Lambda^{d-4}} \mathcal{L}_d, \quad \text{with} \quad \mathcal{L}_d = \sum_i C_i \mathcal{O}_i^{(d)}, \quad \left[\mathcal{O}_i^{(d)}\right] = d\,, \tag{28}$$

where Λ denotes the cut-off scale of the SMEFT. This new physics scale introduces a first hierar-

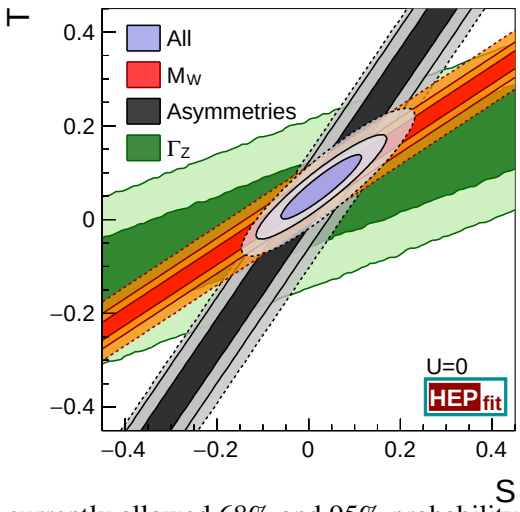

Fig. 49: Comparison of the currently allowed 68% and 95% probability regions in the S, T fit ($U = 0$) (dashed contours) with the HL-LHC projections (solid contours). The different bands illustrate the bounds from the different EWPO included in the fit and the projected improvements at the HL-LHC.

chical ordering between contributions of operators of lower versus higher dimension, where higher-dimension operators are suppressed by inverse powers of Λ. Each term in $\mathcal{L}_d$ is a linear combination of d-dimensional operators $O_i^{(d)}$ built in terms of SM fields, with Wilson coefficients C_i that can depend on both SM masses and couplings, as well as new physics parameters. For the analysis of EWPO the leading new physics corrections come from dimension-six operators ($\mathcal{L}_6$). We will limit our study to this order in the effective theory expansion. Using the complete basis of dimension-six interactions presented in Ref. [478], the Z-pole and W observables in Table 28 are corrected at the leading order by 10 different operators. The bosonic operators

$$\mathcal{O}_{\phi D} = |\phi^\dagger D^\mu \phi|^2 \quad \text{and} \quad \mathcal{O}_{\phi WB} = (\phi^\dagger \sigma_a \phi) W^a_{\mu\nu} B^{\mu\nu},$$

modify the gauge-boson propagators in a way similar to the T and S parameters, respectively. Among the remaining operators,

$$\mathcal{O}^{(1)}_{\phi\psi} = (\phi^\dagger \overleftrightarrow{D^\mu} \phi)(\overline{\psi}\gamma_\mu \psi) \quad \text{and} \quad \mathcal{O}^{(3)}_{\phi F} = (\phi^\dagger \sigma_a \overleftrightarrow{D^\mu} \phi)(\overline{F}\gamma_\mu \sigma_a F),$$

with $\psi = l,\ e,\ q,\ u\ , d$ and $F = l, q$ (where l and q denote the SM left-handed fermion doublets, e, u, d the SM right-handed fermion singlets, and flavor universality is assumed), correct, upon EW symmetry breaking, the EW couplings of the Z and W bosons to quarks and leptons. Finally, the four-lepton operator $\mathcal{O}_{ll} = \left(\bar{l}\gamma_\mu l\right)\left(\bar{l}\gamma^\mu l\right)$ modifies the muon decay amplitude and, by affecting the extraction of the Fermi constant, propagates its effect to all the different observables considered in the EW global fit.

The aim of a global fit to EWPO data is to constrain the corresponding Wilson coefficients. Of the ten operators considered, only eight combinations can be constrained using EW precision data in the case of flavour universal couplings. This means that in the basis of [478] there are two flat directions which, for simplicity, we lift by performing a field redefinition to exchange $C_{\phi D}$ and $C_{\phi WB}$ with two interactions that do not enter in EWPO. The results of the fit to EWPO using the projected HL-LHC data are shown in Figure 50, both for the case in which the eight remaining coefficients are active and fitted simultaneously and for the case in which only one coefficient at a time is active and independently fitted. The results of both fits are also summarised in Table 30 where the HL-LHC bounds are additionally compared to current bounds. We can see that the HL-LHC could improve the current bounds on some of

the considered Wilson coefficients by up to a 10-30%, although for most coefficients the effect is much milder both when different effective interactions are fitted simultaneously and individually.

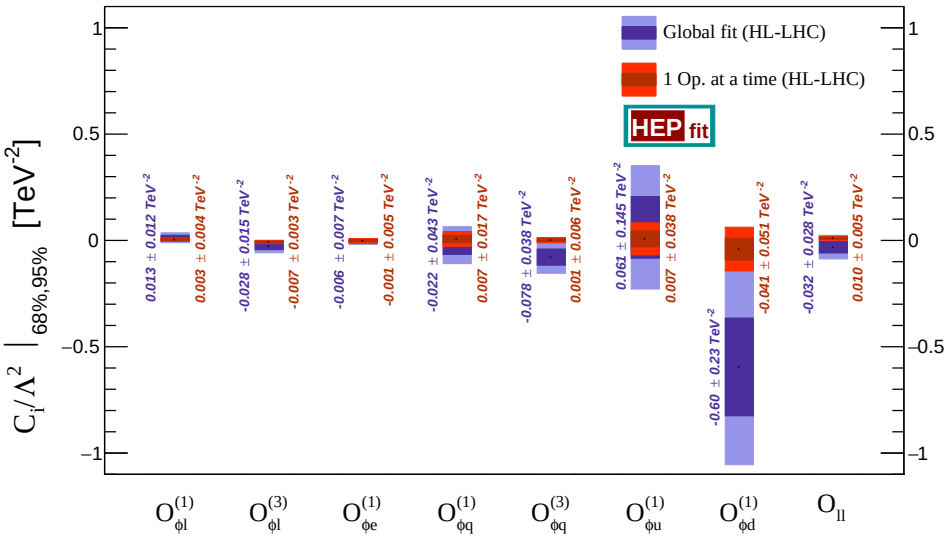

Fig. 50: 68% and 95% probability limits on the dimension-six operator coefficients C_i/Λ^2 [TeV^{-2}] from the global fit to EWPO at HL-LHC including all operators (in blue), compared with the limits obtained assuming only one operator at a time (in red). See Table 30 for the comparison with current uncertainties.

Table 30: Results of the fit to the coefficients of the SMEFT dimension-six Lagrangian. The uncertainties shown refer to the fit performed assuming the presence of only one effective operator at a time and to the case when all (eight) operators are active at the same time (global fit). Projections for the uncertainties at the HL-LHC are given in the last two columns. Result shown for the ratios $\overline{C}_i \equiv C_i/\Lambda^2$. See text for details.

	Current uncertainty [TeV^{-2}]		Precision at HL-LHC [TeV^{-2}]	
Operator Coefficient	1 op. at a time	Global fit	1 op. at a time	Global fit
$\overline{C}_{\phi l}^{(1)}$	0.004	0.012	0.004	0.012
$\overline{C}_{\phi q}^{(1)}$	0.018	0.044	0.017	0.043
$\overline{C}_{\phi e}$	0.005	0.009	0.005	0.007
$\overline{C}_{\phi u}$	0.040	0.146	0.038	0.145
$\overline{C}_{\phi d}$	0.054	0.237	0.051	0.230
$\overline{C}_{\phi l}^{(3)}$	0.004	0.017	0.003	0.015
$\overline{C}_{\phi q}^{(3)}$	0.007	0.040	0.006	0.038
$\overline{C}_{ll}$	0.007	0.028	0.005	0.028
$\overline{C}_{\phi WB}$	0.003	–	0.002	–
$\overline{C}_{\phi D}$	0.007	–	0.005	–

5 Strong interactions

5.1 Jet and photon production

We perform a phenomenological study of inclusive jet and photon production at hadron colliders. We investigate in particular the reach in cross section for these processes at future upgrades at the High-Luminosity and High-Energy stages of the Large Hadron Collider (LHC). We assess the experimental conditions that can be achieved for three HL-LHC scenarios discussed below. Theoretical predictions are obtained using perturbative calculations in QCD. In order to assess the perturbative uncertainty of the calculations, we perform independent variations of the renormalization and factorization scales by factors of 1/2 and 2 with the constraint $1/2 \leq \mu_R/\mu_F \leq 2$. The resulting scale uncertainty band for the perturbative QCD prediction is obtained from the envelope of these 7 points. A comparison between the results obtained at the future design center-of-mass energies of $\sqrt{s} = 14$ TeV and $\sqrt{s} = 27$ TeV is presented.

5.1.1 Inclusive jet production

Jets are reconstructed using the anti-k_t algorithm [233] with distance parameter R=0.4 as implemented in the FastJet software package [303], and calibrated following the procedure described in [479]. The total jet energy scale (JES) uncertainty in Run-2 measurements is compiled from 88 sources, and all need to be propagated through the analysis in order to correctly account for uncertainty correlations in the jet calibration in the final result.

A reduced set of uncertainty components (nuisance parameters) is derived from eigenvectors and eigenvalues of the diagonalised total JES covariance matrix on the jet-level. The globally reduced configuration with 19 nuisance parameters (NPs) is used in this study. Eight NPs coming from the in situ techniques are related to the detector description, physics modelling and measurements of the Z/γ energies in the ATLAS calorimeters. Three describe the physics modelling, the statistics of the dijet MC sample and the non-closure of the method used to derive the η-intercalibration [479]. Single-hadron response studies [480] are used to describe the JES uncertainty in the high-p_T jet regions, where the in situ studies have limited statistics. Four NPs are due to the pile-up corrections of the jet kinematics that take into account mis-modelling of N_{PV} and $\langle\mu\rangle$ distributions, the average energy density ρ, and the residual p_T dependence. Finally, two uncertainty components take into account the difference in the calorimeter response to the quark- and gluon-initiated jets (flavour response) and the jet flavour composition, and one uncertainty estimates the correction for the energy leakage beyond the calorimeter, the "punch-through" effect.

In order to estimate the precision in the jet cross section measurements at the HL-LHC, three scenarios of possible uncertainties in the jet energy scale calibration are defined.

In all three scenarios, the high-p_T uncertainty, the punch-through uncertainty and the flavour composition uncertainty are considered to be negligible. The JES uncertainty in the high-p_T range will be accessed using the multi-jet balance (MJB) method, rather than single hadron response measurements, since the high statistics at the HL-LHC will allow precision JES measurements in the high-p_T region. Flavour composition and flavour response uncertainties are derived from the MC generators. With the advances in the MC modelling and tunes development, these uncertainties could be significantly reduced. The flavour composition uncertainties in the jet energies measurements are set to zero to highlight the maximal possible effect of progress in parton shower and hadronisation modeling on the precision of the jet energy measurements. The flavour response uncertainties are kept the same as in Run-2 or reduced by a factor of two in conservative and optimistic scenarios, respectively.

The pile-up uncertainties, except the ρ topology uncertainty, are considered to be negligible. Current small uncertainties in the JES due to mis-modelling of N_{PV} and $\langle\mu\rangle$ distributions and the residual p_T dependence lead to a very small uncertainties at the HL-LHC conditions. With the advances of new

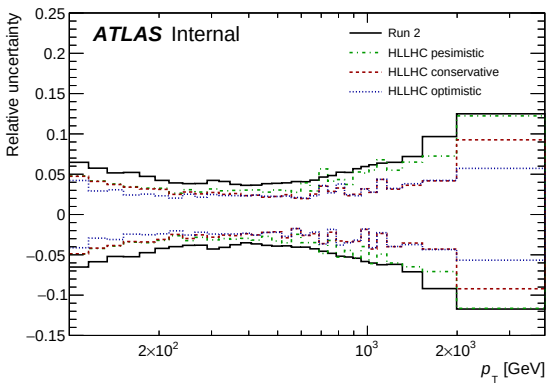

Fig. 51: Relative uncertainties in the inclusive jet cross section measurements at the HL-LHC due the JES uncertainties. Three HL-LHC scenarios are compared to the Run-2 performance. Black line corresponds to the Run-2 performance. Green, red and blue lines represent pessimistic, conservative and optimistic scenarios, respectively.

pile-up rejection techniques, the ρ topology uncertainty could be maintained at a level comparable to the one in Run-2 or reduced by a factor of two. This is addressed in conservative and optimistic scenarios.

Since the Run-2 jet energy resolution (JER) uncertainty estimation is conservative, the final Run-2 JER uncertainty is expected (based on Run-1 experience) to be about twice as small as the current one. Therefore, the JER uncertainty is estimated to be half of that in Run-2.

The remaining uncertainty sources are fixed in different scenarios as follows:

- Conservative scenario:
  - All in situ components are kept the same as in Run-2, except the uncertainties related to the photon energy measurement in the high-E_T range and the MJB method uncertainties. Relevant uncertainties are reduced by a factor of two, since those are expected to be improved at the HL-LHC;
  - MC modelling uncertainty in the η-intercalibration is reduced by a factor of two while the other two are neglected. Currently, MC modelling uncertainty is derived by comparison of leading-order (LO) pQCD generators. With future advances in next-to-leading-order MC generators this uncertainty will be improved;
  - Flavour response uncertainty is set to the Run-2 value;
  - ρ-topology uncertainty is unchanged compared to Run-2 results;
- Optimistic scenario:
  - All in situ components are treated identically to the conservative scenario;
  - All three uncertainty sources in the η-intercalibration method are set to zero;
  - Flavour response uncertainty is reduced by a factor of two compared to Run-2 results;
  - ρ-topology uncertainty is two times smaller as in Run-2;
- Pessimistic scenario:
  - same as optimistic scenario, but all uncertainty sources of in situ methods are retained from Run-2.

All components of the JES uncertainty are propagated from the jet-level to the cross section level as follows. The jet p_T is scaled up and down by one standard deviation of each source of uncertainty.

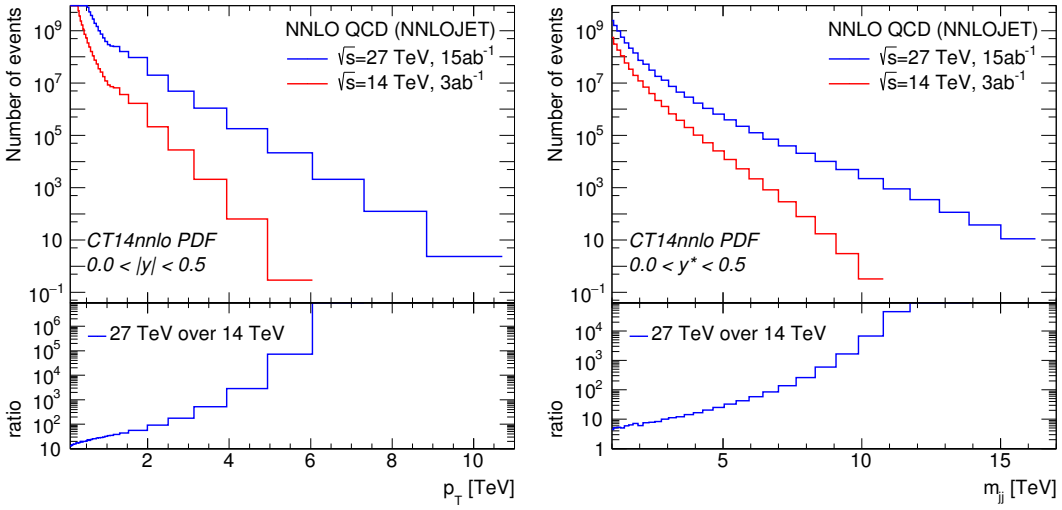

(a) (b)

Fig. 52: Predicted number of inclusive jet events as a function of the jet p_T (left) and dijet events as a function of dijet mass m_{jj} (right) at NNLO, assuming an integrated luminosity of 3 ab^{-1} (15 ab^{-1}) of pp collision data at $\sqrt{s}$=14 TeV ($\sqrt{s}$=27 TeV).

The difference between the nominal reco-level spectrum and the systematically shifted one is taken as a systematic uncertainty. All JES uncertainties are treated as bin-to-bin correlated and independent from each other in this procedure. The unfolding of the reconstruction-level distributions to the particle-level spectrum is not performed is this study. A possible modification of the shapes of uncertainty components during the unfolding procedure is expected to be small and neglected in this study.

The inclusive jet cross-sections are studied as a function of the jet transverse momentum for jets with $p_T > 100$ GeV and within $|y| < 3$. The total JES uncertainty in the inclusive jet cross section measurement for the three HL-LHC scenarios is depicted in Figure 51 and is compared to the total JES uncertainty estimate for the Run-2 jet cross section measurements. Total JES uncertainty in the low p_T range is same as in Run-2 and is about 2% better in the high-p_T region. In conservative and pessimistic scenarios JES uncertainties in the cross section are very similar in the intermediate and high-p_T range, while JES uncertainty is about 1% better in the low-p_T range for the optimistic scenario.

The predicted number of events estimated using the program NNLOJET [285], which includes next-to-next-to-leading order QCD calculations for both single jet inclusive [164] and dijet inclusive [19] production is shown in Figure 52 (left) and (right) respectively. In the dijet analysis, a second jet with $p_T >$75 GeV is required in the event. The lower panels show the ratio 27 TeV/14 TeV. In the ratio plot we observe an enhancement of the cross section growing with the jet p_T (left) and dijet mass (right). In summary, assuming $\mathcal{L}_{int} = 3ab^{-1}$ of pp collision data at $\sqrt{s}$=14 TeV the p_T reach of the measurement is 5 TeV with the observation of dijet events of mass up to 9 TeV. At the HE-LHC upgrade, an increase in cross section by a factor between 10^3 and 10^6 in the tails of the distributions extends the p_T range of the measurement by a factor of 2 up to 9 TeV with the observation of dijet events of mass up to 16 TeV reachable.

The increase in cross section in these scenarios will allow for a very precise multi-differential measurement of inclusive jet production. Working at a fixed center-of-mass energy, we probe at high-p_T the high-x and the large Q^2 region which increases our sensitivity to higher order QCD/EW effects and BSM signals. On the other hand, at fixed-p_T, an increase in the collider energy and a focus on the

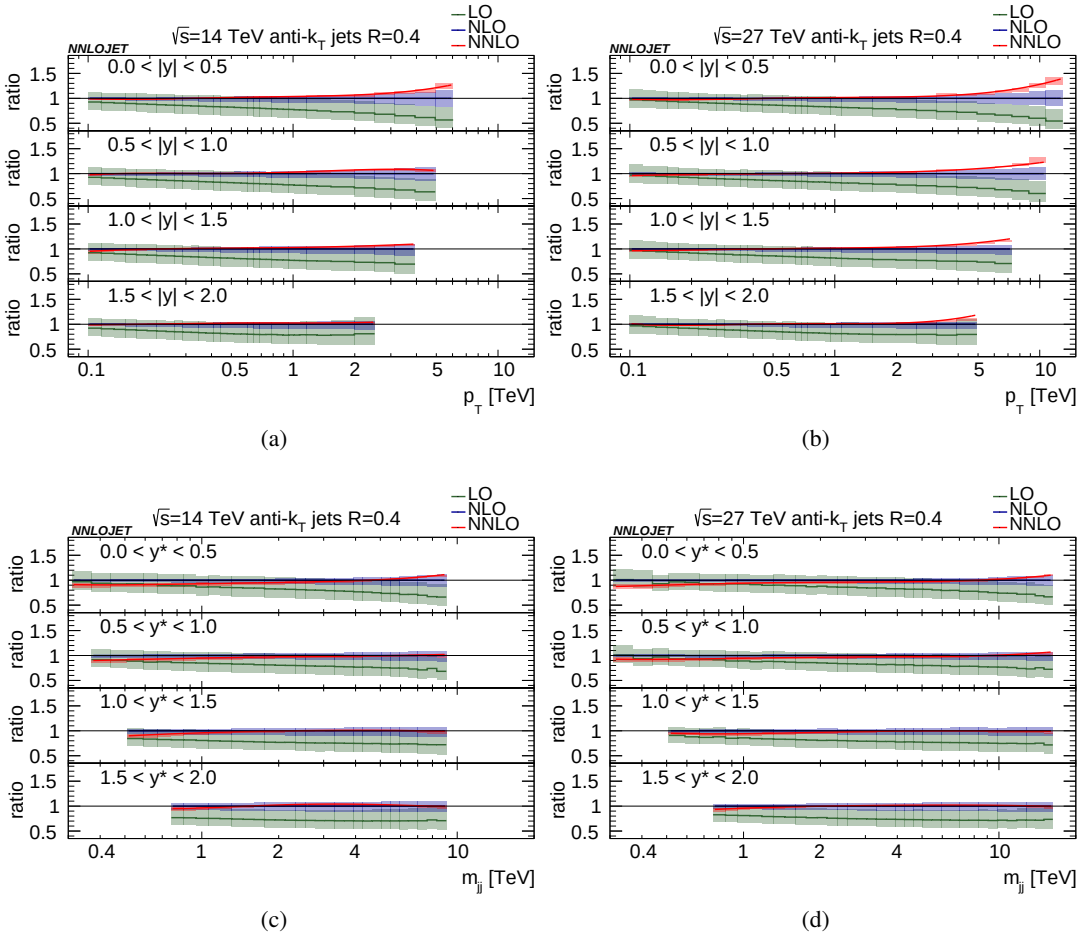

Fig. 53: Predictions for the inclusive jet p_T top and dijet mass m_{jj} (bottom) at LO (green), NLO (blue) and NNLO (red) at (a) $\sqrt{s} = 14$ TeV and (b) $\sqrt{s} = 27$ TeV normalised to the NLO result.

forward region increases the coverage in the low-x region, where we are sensitive to the role of small-x resummation effects. For these reasons, it will be necessary to have accurate jet predictions covering both regions.

To this end we present in Fig. 53 the double-differential k-factors at $\sqrt{s} = 14$ TeV (left) and $\sqrt{s} = 27$ TeV (right) for the inclusive jet p_T (top), differentially in p_T and rapidity $|y|$ and dijet mass (bottom) differentially in dijet mass m_{jj} and rapidity difference $y^* = 1/2\,|y_{j1} - y_{j2}|$. The shaded bands assess the scale uncertainty at each perturbative order, LO (green), NLO (blue) and NNLO (red). As for the value of the renormalization (μ_R) and factorization (μ_F) scales we use $\mu = \hat{H}_T$, the scalar sum of the p_T of all partons in the event as recommended in [291] for the inclusive jet p_T, and the dijet mass $\mu = m_{jj}$ for the dijet mass distribution as recommended in [19].

For the inclusive jet p_T we observe large NLO effects at high-p_T and central rapidity of approximately 90% (14 TeV) and 50% (27 TeV), with large NLO scale uncertainties of $\mathcal{O}(20-30\%)$. At NNLO we observe moderate corrections across the entire p_T and rapidity range, except at high-p_T in the central rapidity slices where the NNLO effects can reach between 10 to 30%. We observe an excellent convergence of the perturbative result and a significant reduction in the scale uncertainty of the cross section when going from NLO to NNLO. We estimate NNLO scale uncertainties at the $< 5\%$ level. Similarly to the inclusive jet p_T case we observe an excellent convergence of the perturbative result for the dijet

mass. The NNLO/NLO k-factors are typically $< 10\%$ and alter the shape of the prediction at low m_{jj} and low y^*. We generally observe a large reduction in the scale variation and estimate NNLO scale uncertainties at the $< 5\%$ level even at large m_{jj}. We note that scale uncertainties at this level are well below the PDF uncertainty, highlighting the huge potential to constrain PDFs with inclusive jet data.

Measurements of weak bosons [481], top quarks [482], photon and jet production [483] (and many others) performed by the ATLAS collaborations have been already used by the global PDF groups [157, 158, 165, 484] in the determination of the proton structure. Comparisons of inclusive jet and dijet production cross sections using different PDF sets at $\sqrt{s} = 14$ and 27 TeV, show 5–10% differences respectively between central values in the low and intermediate p_T and m_{jj} regions, consistent with current PDF uncertainties. Larger differences between the predictions of the various PDF sets in the high-p_T and m_{jj} range highlight the expected constraining power of future measurements at the HL-LHC and HE-LHC.

A study to estimate the impact of future PDF-sensitive measurements at the HL-LHC on PDFs determination was performed in [257]. Three possible scenarios for the experimental systematic uncertainties were considered. This study concluded that HL-LHC measurements will further reduce the PDF uncertainties, and published dedicated PDF sets, PDF4LHC HL-LHC, with the inclusion of HL-LHC pseudo-data in the fits. Figure 54 depicts the comparison of PDF uncertainties in the inclusive jet and di-jet production cross sections for CT14 and PDF4LHC HL-LHC (conservative scenario) in pp collisions at $\sqrt{s} = 14$ (left) and 27 TeV (right). A significant reduction in the PDF uncertainty is expected with the inclusion of PDF-sensitive measurements in HL-LHC PDF fits.

5.1.2 Inclusive b-jets at the HL-LHC

Measurements of high-p_T jets originated from b-quarks are sensitive to the higher-order corrections, parton shower modeling and the parton densities of the proton. In Fig. 55 (left), the inclusive b-jet cross section differential in p_T is shown for centre-of-mass energy of 13 and 14 TeV and rapidity $|y| < 0.5$. The depicted statistical uncertainties correspond to the luminosity 300 fb^{-1} (13 TeV) and 3 ab^{-1} (14 TeV). The systematic uncertainty of the measurement is dominated by the jet energy scale uncertainty which is of similar size as for inclusive jets and the b-tagging uncertainty which is expected to play a role mainly at higher p_T where it is about 10%. It can be seen that the p_T reach at HL-LHC for the inclusive b-jets is about 3 TeV, where about 30 events with $p_T > 3$ TeV are expected.

It is worth noticing that at high-p_T the mass of the b-quark is nearly negligible with respect to the jet momentum. This leads to the high probability that the b-quark is not produced in the hard sub-process, but in the parton shower. As the mass of the b becomes negligible, the probability of gluon splitting into $b\bar{b}$-pairs is similar to any other flavour (excluding top). In this case, we expect to see the pair of the B-hadrons inside the b-jet, where one consists of a b-quark, the second a $\bar{b}$. The fraction of such jets as a function of p_T as predicted by PYTHIA 8 MC is shown on Fig. 55 (right). In the future, it will be crucial to disentangle between b-jets with b-produced in the shower, and b-jets with b-produced in the hard sub-process.

5.1.3 Inclusive photon production

The study of photon production is done via the analysis of inclusive isolated photons and that of photon production in association with at least one jet. In both analyses the photon is required to have a transverse energy in excess of 400 GeV and the pseudorapidity to lie in the range $|\eta^\gamma| < 2.37$ excluding the region $1.37 < |\eta^\gamma| < 1.56$. The photon is required to be isolated by imposing an upper limit on the amount of transverse energy inside a cone of size $\Delta R = 0.4$ in the η–ϕ plane around the photon, excluding the photon itself: $E_{\mathrm{T}}^{\mathrm{iso}} < E_{\mathrm{T,max}}^{\mathrm{iso}}$.

In the inclusive photon analysis, the goal is the measurement of the differential cross section

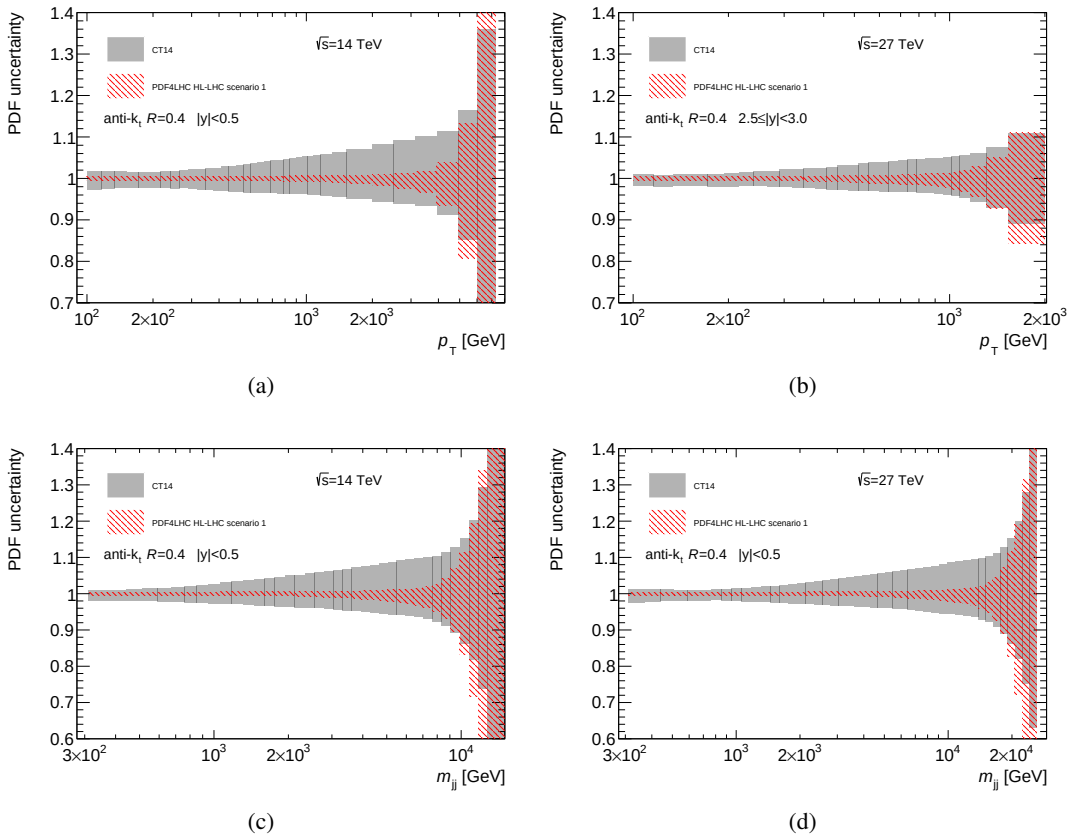

Fig. 54: Comparison of PDF uncertainty in the inclusive jet (a,b) and dijet (c,d) cross sections calculated using the CT14 PDF and PDF4LHC HL-LHC [257] sets at $\sqrt{s} = 14$ TeV (left) and $\sqrt{s} = 27$ TeV (right).

as a function of E_{T}^{γ} in four regions of the photon pseudorapidity: $|\eta^{\gamma}| < 0.6$, $0.6 < |\eta^{\gamma}| < 1.37$, $1.56 < |\eta^{\gamma}| < 1.81$ and $1.81 < |\eta^{\gamma}| < 2.37$. Photon isolation is enforced by requiring $E_{\mathrm{T}}^{\mathrm{iso}} < 4.2 \cdot 10^{-3} \cdot E_{\mathrm{T}}^{\gamma} + 4.8$ GeV.

In the photon+jet analysis, jets are reconstructed using the anti-k_t algorithm [233] with a radius parameter $R = 0.4$. Jets overlapping with the photon are not considered if the jet axis lies within a cone of size $\Delta R = 0.8$. The leading jet is required to have transverse momentum above 300 GeV and rapidity in the range $|y^{\mathrm{jet}}| < 2.37$. No additional condition is used for the differential cross section as a function of $p_{\mathrm{T}}^{\mathrm{jet}}$. For the differential cross section as a function of the invariant mass of the photon+jet system additional constraints are imposed: $m^{\gamma-\mathrm{jet}} > 1.45$ TeV, $|\cos\theta^{*}| < 0.83$ and $|\eta^{\gamma} \pm y^{\mathrm{jet}}| < 2.37$. These additional constraints are imposed to remove the bias due to the rapidity and transverse-momentum requirements on the photon and the leading jet [485, 486]. Photon isolation is enforced by requiring $E_{\mathrm{T}}^{\mathrm{iso}} < 4.2 \cdot 10^{-3} \cdot E_{\mathrm{T}}^{\gamma} + 10$ GeV.

The yields of inclusive isolated photons and of photon+jet events are estimated using the program JETPHOX 1.3.1_2 [487, 488]. This program includes a full next-to-leading-order QCD calculation of both the direct-photon and fragmentation contributions to the cross sections for the $pp \to \gamma + \mathrm{X}$ and $pp \to \gamma + \mathrm{jet} + \mathrm{X}$ reactions. The number of massless quark flavours is set to five. The renormalisation (μ_{R}), factorisation (μ_{F}) and fragmentation (μ_{f}) scales are chosen to be $\mu_{\mathrm{R}} = \mu_{\mathrm{F}} = \mu_{\mathrm{f}} = E_{\mathrm{T}}^{\gamma}$. The calculations are performed using the MMHT2014 [489] parameterisations of the proton parton distribution functions (PDFs) and the BGF set II of parton-to-photon fragmentation functions at NLO [490]. The

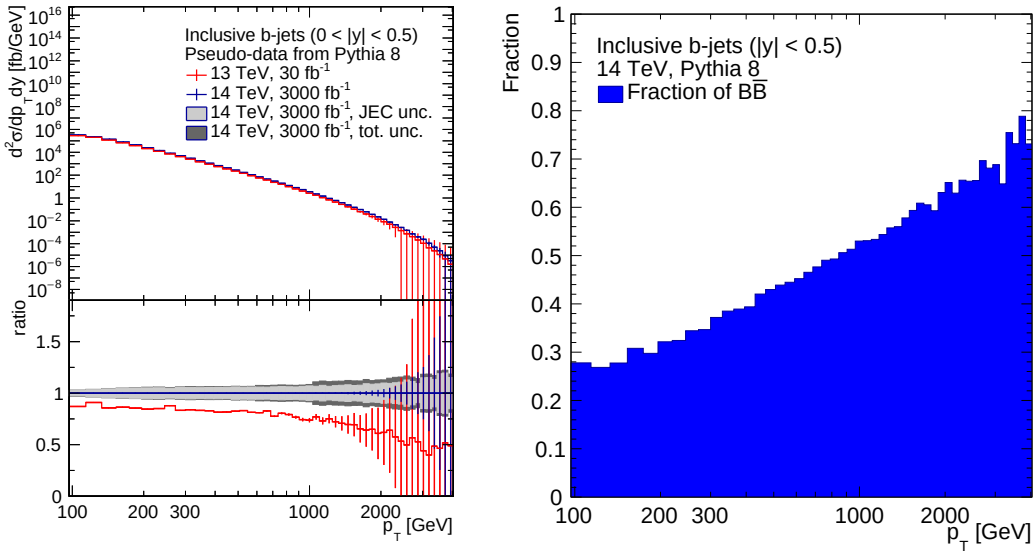

Fig. 55: The inclusive b-jet cross section differential in the p_T (left). The error bars show the statistical uncertainty corresponding to the given luminosity, while the gray band represent the systematic uncertainty from the jet-energy-scale and the total systematic uncertainty. The fraction of b -jets containing both B and $\bar{B}$ hadrons as a function of p_T (right).

strong coupling constant $\alpha_s(m_Z)$ is set to the value assumed in the fit to determine the PDFs. The reliability of the estimated yields using the program JETPHOX is supported by the high purity of the signal photons, the mild unfolding corrections and the fact that the NLO QCD predictions describe adequately the measurements of these processes using pp collisions at $\sqrt{s} = 13$ TeV [491, 492].

The predicted number of inclusive isolated photon events as a function of E_{T}^{γ} in the different ranges of $|\eta^{\gamma}|$ assuming an integrated luminosity of 3 ab^{-1} (15 ab^{-1}) of pp collision data at $\sqrt{s} =$ 14 TeV (27 TeV) is shown in Fig. 56a (56b). For HL-LHC (HE-LHC), the reach in E_{T}^{γ} is (a) 3–3.5 (5) TeV for $|\eta^{\gamma}| < 0.6$, (b) 2.5–3 (5) TeV for $0.6 < |\eta^{\gamma}| < 1.37$, (c) 1.5–2 (3–3.5) TeV for $1.56 < |\eta^{\gamma}| < 1.81$ and (d) 1–1.5 (2.5–3) TeV for $1.81 < |\eta^{\gamma}| < 2.37$. This represents a significant extension of the region measured so far with pp collisions at $\sqrt{s} = 13$ TeV [491]; as an example, at the HL-LHC (HE-LHC) the E_{T}^{γ} reach is extended from 1.5 TeV to 3–3.5 (5) TeV for $|\eta^{\gamma}| < 0.6$.

The predicted number of photon+jet events as a function of $p_{\mathrm{T}}^{\mathrm{jet}}$ and $m^{\gamma-\mathrm{jet}}$ assuming an integrated luminosity of 3 ab^{-1} (15 ab^{-1}) of pp collision data at $\sqrt{s} = 14$ TeV (27 TeV) is shown in Figs. 56c and 56d. In comparison with the latest measurements [492], the expectations obtained at the HL-LHC (HE-LHC) extend significantly the reach in $p_{\mathrm{T}}^{\mathrm{jet}}$ from 1.5 TeV to 3.5 (5) TeV and $m^{\gamma-\mathrm{jet}}$ from 3.3 TeV to 7 (12) TeV.

5.1.4 Diphoton production

The production of photon pairs (diphotons) with high invariant mass is a very relevant process for physics studies at high-energy hadron colliders. Photons are very clean final states and photon energies and momenta can be measured with high precision in modern electromagnetic calorimeters. Therefore *prompt* photons represent ideal probes to test the properties of the Standard Model (SM) [493]– [494] and they are also important in searches for new-physics signals (see, e.g., Refs. [495]– [496]). Owing to the above reasons, it is important to provide accurate theoretical predictions for diphoton production at LHC energies. This task requires in particular, the calculation of QCD and EW radiative corrections at high

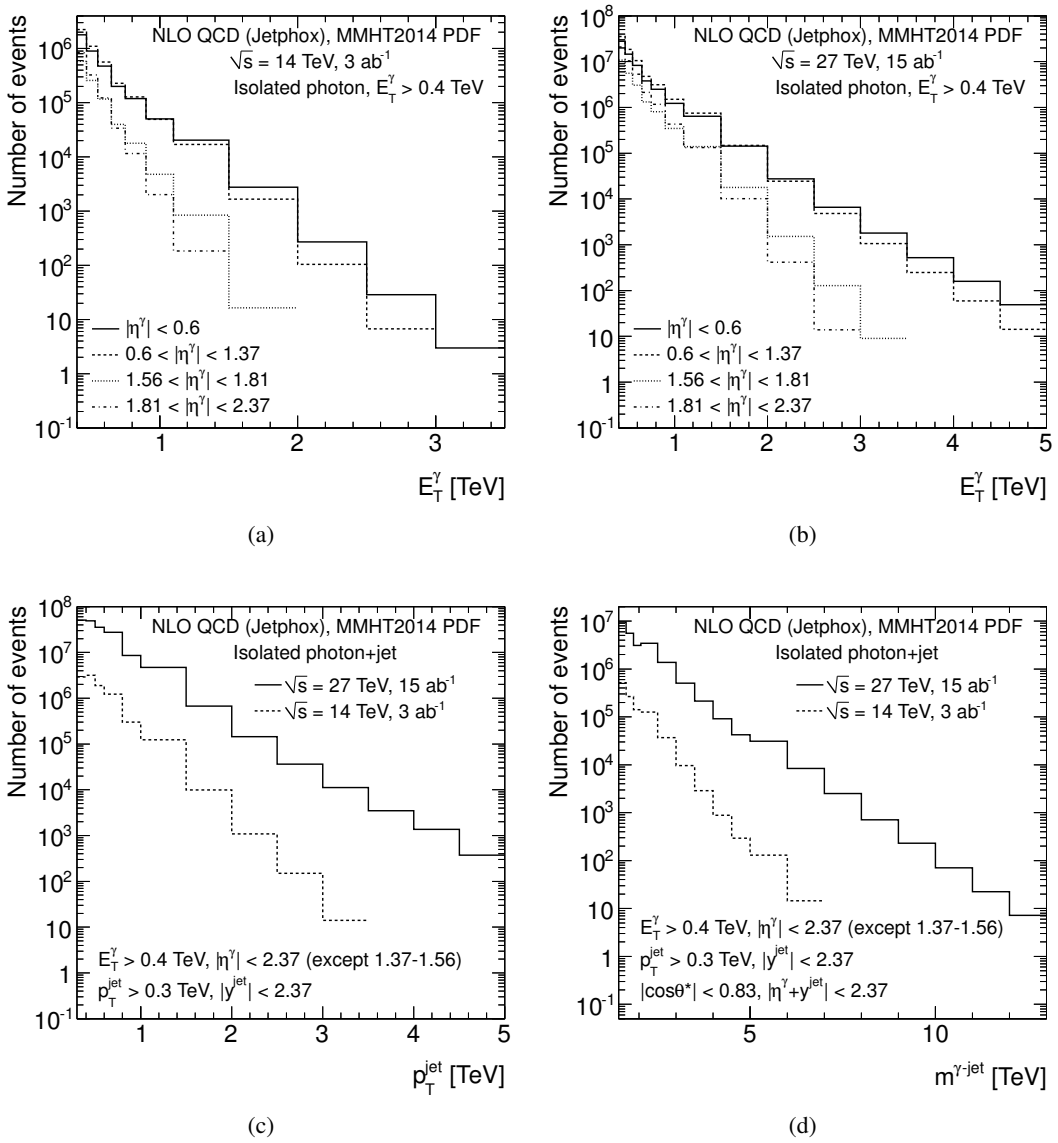

Fig. 56: (a,b) Predicted number of inclusive isolated photon events as a function of E_{T}^{γ} assuming an integrated luminosity of 3 ab^{-1} (15 ab^{-1}) of pp collision data at $\sqrt{s} = 14$ TeV (27 TeV) in different ranges of photon pseudorapidity: $|\eta^{\gamma}| < 0.6$ (solid histogram), $0.6 < |\eta^{\gamma}| < 1.37$ (dashed histogram), $1.56 < |\eta^{\gamma}| < 1.81$ (dotted histogram) and $1.81 < |\eta^{\gamma}| < 2.37$ (dot-dashed histogram). (c,d) Predicted number of photon+jet events assuming an integrated luminosity of 3 ab^{-1} (15 ab^{-1}) of pp collision data at $\sqrt{s} = 14$ TeV (27 TeV) as a function of (c) $p_{\mathrm{T}}^{\mathrm{jet}}$ and (d) $m^{\gamma-\mathrm{jet}}$.

perturbative orders.

In this contribution we consider diphoton production in pp collisions at the $\sqrt{s} = 14$ GeV and $\sqrt{s} = 27$ GeV energies, and we present perturbative QCD results up to the NNLO by using the smooth cone isolation criterion [15]. Detailed comparison between standard and smooth cone isolation criteria

[15] The NNLO QCD calculation within the standard cone isolation criterion has not yet been performed

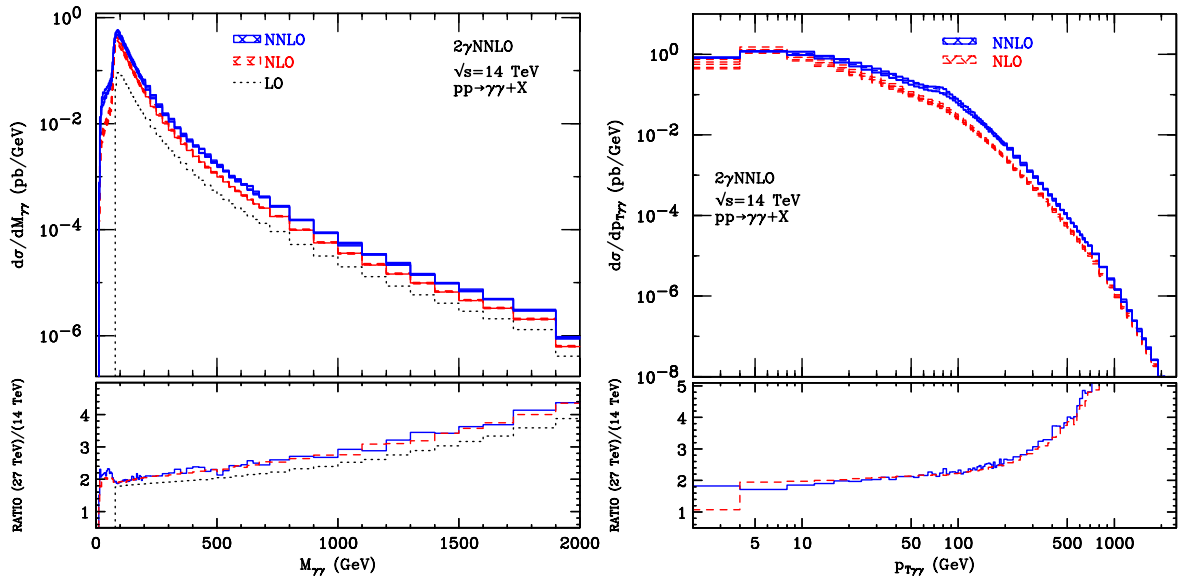

Fig. 57: The differential cross sections $d\sigma/dM_{\gamma\gamma}$ (left) and $d\sigma/dp_{T\gamma\gamma}$ (right) at $\sqrt{s} = 14$ TeV is shown in the upper panel at LO (black dotted), NLO (red dashed) and NNLO (blue solid). The NLO and NNLO scale variation bands are obtained as detailed in the text. In the lower subpanel the ratio between cross sections at two different centre–of–mass energies ($\sqrt{s} = 27$ TeV and $\sqrt{s} = 14$ TeV) is also shown. The selection cuts are described in the text.

have been presented in Refs. [90, 497–499]. We apply the following kinematical cuts:

$$p_T^{\gamma;\,hard} > 40\ GeV, \qquad p_T^{\gamma;\,soft} > 30\ GeV, \qquad |y_\gamma| < 2.8\,, \tag{29}$$

where $p_T^{\gamma;\,hard}$ and $p_T^{\gamma;\,soft}$ are respectively the transverse momenta of the harder and softer photon and $|y_\gamma|$ is the photon rapidity. The minimum angular distance between the two photons is $R_{\gamma\gamma}^{\rm min} = 0.4$. Within the smooth cone isolation criterion [500] (see also Refs. [501, 502]) photons are selected by fixing the size R of the isolation cone and imposing a maximal amount of hadronic energy ($E_T^{had}(r)$) allowed inside the cone

$$E_T^{had}(r) \leq E_{T\,\rm max}\,\chi(r;R)\,, \quad \text{in } \textit{all} \text{ cones with } r \leq R\ , \tag{30}$$

with a suitable choice of the r dependence of the isolation function $\chi(r;R)$. The smooth isolation function $\chi(r;R)$ we use is [16]

$$\chi(r;R) = \left(\frac{1-\cos(r)}{1-\cos(R)}\right)^n\ , \tag{31}$$

and the value of the power n is set to the $n = 1$. This value of n avoids the sensitivity of the cross section to soft (collinear) photons for large (small) value of n [497]. The radius of the photon isolation cone is set at the value $R = 0.4$ and $E_{T\,\rm max} = 10$ GeV. We implement a lower limit $r_{\rm cut}$ on the ratio $p_{T\gamma\gamma}/M_{\gamma\gamma}$ ($p_{T\gamma\gamma} > r_{\rm cut} M_{\gamma\gamma}$) [505], and we use values in the range $r_{\rm cut} = 0.08\%$–0.15%. We compute the perturbative uncertainty as the envelope of three-point scale variation by considering the two asymmetric scale configurations with $\{\mu_R = \mu_0/2, \mu_F = 2\mu_0\}$ and $\{\mu_R = 2\mu_0\,, \mu_F = \mu_0/2\}$ and the central scale $\{\mu_R = \mu_F = \mu_0\}$.

We begin the presentation of our quantitative results by considering the invariant mass ($M_{\gamma\gamma}$) distribution up to value of 2 TeV. The LO (black dotted), NLO (red dashed) and NNLO (blue solid)

[16] The same form of the isolation function is used in the NNLO predictions reported in Refs. [494, 503, 504]

QCD results for a centre–of–mass energy of $\sqrt{s} = 14$ TeV are presented in Fig. 57 (left). We first observe the presence of a LO threshold at an invariant mass $M^{LO} = 2p_T^{\gamma;\,hard}$. The bulk of the cross section is concentrated in the region around M^{LO} while for large values of $M_{\gamma\gamma}$ the distribution rapidly decreases. At high invariant mass, $M_{\gamma\gamma} > 1$ TeV, the cross section is dominated by the quark annihilation ($q\bar{q}$) partonic subprocess (the other partonic subprocesses are suppressed by one order of magnitude or more). The NNLO K factor, $K^{NNLO} = \sigma^{NNLO}/\sigma^{NLO}$, is flat at large values of $M_{\gamma\gamma}$ and it is roughly equal to the NNLO K factor of the $q\bar{q}$ channel. In the lower subpanel of Fig. 57 we present results for the ratio (R) between the invariant mass distribution at $\sqrt{s} = 27$ TeV and $\sqrt{s} = 14$ TeV. At LO (black dotted curve) the dynamic enhancement of the ratio can be described roughly as $\mathcal{G}(M^2_{\gamma\gamma}/27^2\ \mathrm{TeV}^2)/\mathcal{G}(M^2_{\gamma\gamma}/(14^2\ \mathrm{TeV}^2)$, where $\mathcal{G}(\tau) = \log(\tau) \times \mathcal{L}_{q\bar{q}}(\tau, \mu_f)$ and $\mathcal{L}$ are the integrated parton luminosities. We observe that the ratio at NLO and NNLO is numerically similar to the corresponding LO one. The enhancement of the ratio R at large values of invariant mass is directly related to the increasing the centre–of–mass energy and it reaches the value $R \sim 4$ at $M_{\gamma\gamma} \simeq 1$ TeV.

Finally we present theoretical results for the transverse momentum ($p_{T\gamma\gamma}$) distribution. The NLO (red dashed) and NNLO (blue solid) predictions with a centre–of–mass energy of $\sqrt{s} = 14$ TeV are shown in the upper panel of Fig. 57 (right). Given the LO kinematical constraint $p_{T\gamma\gamma} = 0$, the (N)NLO correction represent *effectively* an (N)LO prediction. Moreover, in the small $p_{T\gamma\gamma}$ region, the convergence of the fixed order expansion is spoiled by the presence of large logarithmic corrections. Reliable perturbative results require an all order resummation of these enhanced logarithmic contributions.

In the lower subpanel of Fig. 57 (right) we present results for the ratio (R) between the transverse momentum distribution at $\sqrt{s} = 27$ TeV and $\sqrt{s} = 14$ TeV. The ratio increases at large value of $p_{T\gamma\gamma}$, reaching $R \sim 4$ for $p_{T\gamma\gamma} \simeq 1$ TeV.

We add a comment on the perturbative uncertainty of our calculation. We observe that the uncertainty bands for the NLO and NNLO results fail to overlap in most of the kinematical regions. This suggests that the computed scale dependence at NNLO cannot be considered a reliable estimate of the true perturbative uncertainty. As an alternative approach the perturbative uncertainty of the NNLO result can be estimated by considering half of the difference between the NNLO and NLO results at central values of the scales [497].

We finally observe that the photon fragmentation component (which is absent in the case of smooth cone isolation) mainly affects the the low invariant mass region, where the cross section is strongly suppressed. Conversely, the intermediate and high invariant mass region, the transverse momentum distribution and the value of total cross section, are less sensitive to photon fragmentation effects. In particular, for isolation parameters commonly used in the experimental analysis at the LHC, the quantitative differences between smooth and standard isolation predictions are much smaller than the corresponding perturbative uncertainties. This observation justifies the use of the smooth cone criterion in the theoretical calculations.

5.2 Ultimate Parton Densities

The goal of this study is to quantify the precision that can be expected in the determination of the parton distribution functions (PDFs) of the proton in the HL-LHC era. Such "ultimate PDFs" will provide an important ingredient for the physics projections at the HL-LHC with a robust estimate of theoretical uncertainties, including some of those presented in other chapters of this Yellow Report. With this motivation, we have generated HL-LHC pseudo-data for a number of PDF-sensitive measurements such as top-quark, Drell-Yan, isolated photon, and W+charm production, and then studied the constraints that these pseudo-data impose on the global PDF analysis by means of the Hessian profiling method. While such studies have been performed in the context of future lepton-hadron colliders, see *e.g.* [431, 506] for the LHeC, to the best of our knowledge this is the first time that such a systematic effort has been directed to the projections for a future hadron collider. The study below is described in further detail

in [507].

5.2.1 *HL-LHC measurements for PDF studies.*

Let us start by listing the PDF-sensitive processes that will be considered in this study. In all cases, pseudo-data is generated for a center-of-mass energy of $\sqrt{s} = 14$ TeV assuming a total integrated luminosity of $\mathcal{L} = 3$ ab^{-1} for the CMS and ATLAS experiments, and of $\mathcal{L} = 0.3$ ab^{-1} for the LHCb experiment. With these settings, HL-LHC pseudo-data has been generated for the following processes:

- High-mass Drell-Yan, specifically the dilepton invariant mass differential distributions $d\sigma(pp \to ll)/dm_{ll}$ for $m_{ll} \gtrsim 110$ GeV for a central rapidity acceptance, $|\eta^l| \leq 2.4$. This process is particularly useful for quark flavour separation, in particular of the poorly known large-x sea quarks.
- Differential distributions in top-quark pair production, providing direct information on the large x gluon [161]. Specifically, we have generated pseudo-data for the top-quark transverse momentum p_T^t and rapidity y_t as well as for the top-quark pair rapidity $y_{t\bar{t}}$ and invariant mass $m_{t\bar{t}}$.
- The transverse momentum distribution of the Z bosons in the large p_T^Z region for central rapidity $|y_Z| \leq 2.4$ and different bins of the dilepton invariant mass m_{ll}. This process is relevant to constrain the gluon and the antiquarks at intermediate values of x [162].
- The production of W bosons in association with charm quarks (both in the central and forward region). This process provides a sensitive handle to the strangeness content of the proton [508, 509]. The pseudo-data for this process has been generated as function of the pseudorapidity η_l of the charged lepton from the W boson decay.
- Prompt isolated photon production, which represents a complementary probe of the gluon PDF at intermediate values of x [163, 510]. Here the pseudo-data have been generated as differential distributions in the photon transverse momentum p_T^γ for different bins in the photon pseudorapidity η^γ.
- Differential distributions for on-peak W and Z boson production in the forward region, $2.0 \leq \eta_l \leq 4.5$, covered by the LHCb experiment. These measurements constrain quark flavour separation, including the strange and charm content of the proton, in the large and small x region [511].
- The inclusive production of jets in different bins of rapidity (both in the central and forward region) as a function of $p_T^{\rm jet}$. Jets have been reconstructed using the anti–k_t algorithm [233] with $R = 0.4$, and provide information on the large-x gluon and valence quarks [512].

In all cases, we have taken as a baseline the binning and kinematic cuts from the most recent $\sqrt{s} = 13$ TeV analyses, or the corresponding 8 TeV analyses if the former are not available. We have then suitably extended this binning to account for the extended kinematical coverage achieved with $\mathcal{L} = 3\ (0.3)$ ab^{-1}. Statistical uncertainties are computed from the number of events per bin, while systematic errors are rescaled as compared to the 13 (or 8) TeV baseline analysis, see below. We consider various scenarios for the reduction of systematic errors, from a more conservative one to a more optimistic one. The overall acceptance of the selection cuts (which affects the final event yield per bin) is estimated globally again based on the reference experimental analysis.

As mentioned above, this list of processes is not exhaustive: several other important processes will provide useful information on the parton distributions in the HL-LHC era, from inclusive dijet production [19] to single top quark [513] and D meson production [189], see also [151]. In addition, we may expect that progress from both the experimental and theory sides leads to novel processes, not considered so far, being added to the PDF fitting toolbox. Even with these caveats, the list above is extensive enough to provide a reasonable snapshot of the PDF-constraining potential of the HL-LHC.

We also emphasise that our projections are based on pseudo-data which have been generated specifically for this study. They are thus not endorsed by the LHC experiments, although we have

accounted for the feedback received from the ATLAS, CMS, and LHCb contact persons.

5.2.2 Generation of HL-LHC pseudo-data.

For each of the HL-LHC processes listed above, we have generated theoretical predictions at next-to-leading order (NLO) using `MCFM` [168] interfaced to `APPLgrid` [166] to produce the corresponding fast grids. The central value of the pseudo-data is first produced according the central prediction of the PDF4LHC15 NNLO set [153], and then fluctuations as expected by the corresponding experimental uncertainties are included. Since the present study is based on pseudo-data, it is not to account for higher-order QCD effects or electroweak corrections. As in the case of PDF closure tests [159], here we are only interested in the relative reduction of PDF uncertainties once the HL-LHC data are added, while by construction the central value will be mostly unaffected.

To be more specific, if $\sigma_i^{\rm th}$ is the theoretical cross-section for bin i of a given process, computed with PDF4LHC15 NNLO, then the central value of the HL-LHC pseudo-data $\sigma_i^{\rm exp}$ is constructed by means of

$$\sigma_i^{\rm exp} = \sigma_i^{\rm th} \times \left(1 + r_i \cdot \delta_{{\rm tot},i}^{\rm exp} + \lambda \cdot \delta_{\mathcal{L}}^{\rm exp}\right) \, , \tag{32}$$

where r_i, λ are univariate Gaussian random numbers, $\delta_{{\rm tot},i}^{\rm exp}$ is the total (relative) experimental uncertainty corresponding to this specific bin, and $\delta_{\mathcal{L}}^{\rm exp}$ is the luminosity uncertainty related to the experiment. The later are taken to be 1.5% for each of the CMS, ATLAS, and LHCb experiments. The motivation for adding the fluctuations on top of the central theoretical predictions is to simulate the statistical and systematic uncertainties of an actual experimental measurement. In Eq. (32) the total experimental error is defined as

$$\delta_{{\rm tot},i}^{\rm exp} \equiv \left(\left(\delta_{{\rm stat},i}^{\rm exp}\right)^2 + \left(f_{\rm corr} \times f_{\rm red} \times \delta_{{\rm sys},i}^{\rm exp}\right)^2 \right)^{1/2} \, . \tag{33}$$

In this expression, the relative statistical error $\delta_{{\rm stat},i}^{\rm exp}$ is computed as

$$\delta_{{\rm stat},i}^{\rm exp} = \left(f_{\rm acc} \times N_{{\rm ev},i}\right)^{-1/2} \, , \tag{34}$$

where $N_{{\rm ev},i} = \sigma_i^{\rm th} \times \mathcal{L}$ is the expected number of events in bin i at the HL-LHC with $\mathcal{L} = 3\ (0.3)$ ab^{-1}, and $f_{\rm acc} \leq 1$ is an acceptance correction which accounts for the fact that, for some of the processes considered, such as top quark pair production, there is a finite experimental acceptance and/or one needs to include the effects of branching fractions. The value of $f_{\rm acc}$ is then determined by extrapolation using the reference dataset. The one exception to this is the case of forward W+charm production, for which no baseline measurement has so far been performed by LHCb; here we set the acceptance to $f_{\rm acc} = 0.3$ to account for the anticipated c–jet tagging efficiency at LHCb. In Eq. (33), $\delta_{{\rm sys},i}^{\rm exp}$ indicates the total systematic error of bin i taken from the reference LHC measurement at either 8 TeV or 13 TeV. The correction factor $f_{\rm red} \leq 1$ accounts for the expected improvement in the average systematic uncertainties at the HL-LHC in comparison to Run II, due to both detector improvements and the enlarged dataset for calibration.

We note that with the exception of the luminosity in Eq. (33) the systematic uncertainties have simply been added in quadrature with the statistical ones. That is, we do not account for the correlations between systematic errors. The full inclusion of such correlations goes beyond the scope of the closure tests being pursued in this exercise, which aim simply to provide a reasonable extrapolation of the expected PDF reach at the HL-LHC. In particular, the expected improvements in the overall size of the systematic uncertainties can only be based on the estimates and expectations provided by the LHC collaborations, and cannot be predicted with absolute certainty. The situation is certainly even more challenging in the case of the specific mutual correlations of the systematic uncertainties, which will be sensitive to the precise experimental setup in the future. However, simply excluding the effects of correlations would artificially reduce the impact of the pseudo-data into the fit.

For this reason, we introduce an effective correction factor $f_{\rm corr}$ that accounts for the fact that data with correlated systematics is more constraining than the same data where all errors are added in quadrature. The value of $f_{\rm corr}$ has been checked against the available $\sqrt{s} = 8$ TeV top quark [514,515] and the 13 TeV W+charm [516] differential distributions, that is we vary $f_{\rm corr}$ until the PDF impact is in line with the result including full experimental correlations. This turns out to have a value of between $f_{\rm corr} \simeq 1.0$ and 0.3 depending on the data set and observable. We take a factor of $f_{\rm corr} = 0.5$ in what follows.

In Table 31 we collect a summary of the features of the HL-LHC pseudo-data generated for the present study. For each process, we indicate the kinematic coverage, the number of pseudo-data points used $N_{\rm dat}$, the values of the correction factors $f_{\rm acc}$, $f_{\rm corr}$, and $f_{\rm red}$; and finally the reference from the 8 TeV or 13 TeV measurement used as baseline to define the binning and the systematic uncertainties of the HL-LHC pseudo-data. A total of $N_{\rm dat} = 768$ pseudo-data points are then used in the PDF profiling. The values of the reduction factor for the systematic errors $f_{\rm red}$ is varied between 1 (0.5) and 0.4 (0.2) in the conservative and optimistic scenarios for a 8 TeV (13 TeV) baseline measurement. This choice is motivated because available 13 TeV measurements are based on a relatively small $\mathcal{L}$ and therefore cannot be taken as representative of the systematic errors expected at the HL-LHC, even in the most conservative scenario.

5.2.3 Hessian profiling.

There exist a number of techniques that can be used to quantify the impact on PDFs of the pseudo-data listed in Table 31. In the case of Monte Carlo sets such as NNPDF, the Bayesian reweighting method [522,523] reproduces the result of a direct fit, but it is restricted by the fact that information loss limits its reliability when the measurements provide significant new information. For Hessian sets such as PDF4LHC15_100 instead, the profiling technique [446] is more suitable to achieve the same purpose. This Hessian profiling is based on the minimization of

$$\chi^2\left(\beta_{\rm exp},\beta_{\rm th}\right) = \sum_{i=1}^{N_{\rm dat}} \frac{1}{\left(\delta_{{\rm tot},i}^{\rm exp}\sigma_i^{\rm th}\right)^2}\left(\sigma_i^{\rm exp} + \sum_j \Gamma_{ij}^{\rm exp}\beta_{j,\rm exp} - \sigma_i^{\rm th} + \sum_k \Gamma_{ik}^{\rm th}\,\beta_{k,\rm th}\right)^2 + \sum_j \beta_{j,\rm exp}^2 + T^2\sum_k \beta_{k,\rm th}^2\,, \tag{35}$$

with $\sigma_i^{\rm exp}$ ($\sigma_i^{\rm th}$) are the central values of a given experimental measurement (theory prediction), $\beta_{j,\rm exp}$ are the nuisance parameters corresponding to the set of fully correlated experimental systematic uncertainties, $\beta_{k,\rm th}$ are the nuisance parameters corresponding to the PDF Hessian eigenvectors, $N_{\rm dat}$ is the number of data points and T is the tolerance factor. The matrices $\Gamma_{ij}^{\rm exp}$ and $\Gamma_{ik}^{\rm th}$ encode the effects of the corresponding nuisance parameters on the experimental data and on the theory predictions, respectively.

As mentioned above, in this study we add in quadrature statistical and experimental uncertainties excluding the luminosity, and then account for the effects of the missing correlations by means of the factor $f_{\rm corr}$. For this reason there are only nuisance parameters for the luminosity errors, and for an overall normalization uncertainty of 5% in forward W+charm production due to charm-jet tagging. If we minimise Eq. (35) with respect to these nuisance parameters, we get:

$$\chi^2\left(\beta_{\rm th}\right) = \sum_{i,j=1}^{N_{\rm dat}}\left(\sigma_i^{\rm exp} - \sigma_i^{\rm th} + \sum_k \Gamma_{ik}^{\rm th}\,\beta_{k,\rm th}\right)\left(\rm cov\right)_{ij}^{-1}\left(\sigma_j^{\rm exp} - \sigma_j^{\rm th} + \sum_m \Gamma_{jm}^{\rm th}\,\beta_{m,\rm th}\right) + T^2\sum_k \beta_{k,\rm th}^2\,, \tag{36}$$

where we have defined:

$$\left(\rm cov\right)_{ij} = \delta_{ij}\left(\delta_{{\rm tot},i}^{\rm exp}\sigma_i^{\rm th}\right)^2 + \sum \Gamma_{i,\rm lumi/norm}^{\rm exp}\Gamma_{j,\rm lumi/norm}^{\rm exp}. \tag{37}$$

Table 31: Summary of the features of the HL-LHC pseudo-data generated for the present study. For each process we indicate the kinematic coverage, the number of pseudo-data points used $N_{\rm dat}$ across all detectors, the values of the correction factors $f_{\rm corr}$ and $f_{\rm red}$; and finally the reference from the 8 TeV or 13 TeV measurement used as baseline to define the binning and the systematic uncertainties of the HL-LHC pseudo-data, as discussed in the text.

Process	Kinematics	$N_{\rm dat}$	$f_{\rm corr}$	$f_{\rm red}$	Baseline
$Z\ p_T$	$20\,\text{GeV} \le p_T^{ll} \le 3.5\,\text{TeV}$ $12\,\text{GeV} \le m_{ll} \le 150\,\text{GeV}$ $\lvert y_{ll}\rvert \le 2.4$	338	0.5	$(0.4, 1)$	[517] (8 TeV)
high-mass Drell-Yan	$p_T^{l1(2)} \ge 40(30)\,\text{GeV}$ $\lvert\eta^l\rvert \le 2.5, m_{ll} \ge 116\,\text{GeV}$	32	0.5	$(0.4, 1)$	[518] (8 TeV)
top quark pair	$\lvert y_t\rvert \le 2.4$	110	0.5	$(0.4, 1)$	[515] (8 TeV)
W+charm (central)	$p_T^\mu \ge 26\,\text{GeV}, p_T^c \ge 5\,\text{GeV}$ $\lvert\eta^\mu\rvert \le 2.4$	12	0.5	$(0.2, 0.5)$	[516] (13 TeV)
W+charm (forward)	$p_T^\mu \ge 20\,\text{GeV}, p_T^c \ge 20\,\text{GeV}$ $p_T^{\mu+c} \ge 20\,\text{GeV}$ $2 \le \eta^\mu \le 5, 2.2 \le \eta^c \le 4.2$	10	0.5	$(0.4, 1)$	LHCb projection
Direct photon	$E_T^\gamma \lesssim 3\,\text{TeV}, \lvert\eta_\gamma\rvert \le 2.5$	118	0.5	$(0.2, 0.5)$	[519] (13 TeV)
Forward W, Z	$p_T^l \ge 20\,\text{GeV}, 2.0 \le \eta^l \le 4.5$ $2.0 \le y_{ll} \le 4.5$ $60 \le m_{ll} \le 120\,\text{GeV}$	90	0.5	$(0.4, 1)$	[520] (8 TeV)
Inclusive jets	$\lvert y\rvert \le 3, R = 0.4$	58	0.5	$(0.2, 0.5)$	[521] (13 TeV)
Total		712			

We then minimise Eq. (36) with respect to the Hessian PDF nuisance parameters $\beta_{k,\rm th}$, which can be interpreted as leading to PDFs that have been optimized to describe this new dataset. The resulting Hessian matrix on $\beta_{k,\rm th}$ at the minimum can be diagonalized to construct the new eigenvector directions. Finally, the PDF uncertainties are determined from the $\Delta\chi^2 = T^2$ criteria. In the studies presented here, we use a global $T = 3$ which approximately corresponds to the average tolerance determined dynamically in the CT14 and MMHT14 analyses.

5.2.4 Results for individual processes.

We now turn to present the results of the Hessian profiling of PDF4LHC15 from individual processes, and subsequently we will study the corresponding results from the combination of all the HL-LHC processes considered in different scenarios. Let us begin with the top-quark pair production case listed in Table 31. In Fig. 58 we show the comparison of the predictions for the $m_{t\bar{t}}$ distribution in top-quark pair production at the HL-LHC using PDF4LHC15 with the associated pseudo-data and with the profiled results with $F \equiv f_{\rm corr} \cdot f_{\rm red} = 0.2$. We also present the corresponding impact at the level of the gluon PDF at $Q = 100$ GeV before and after profiling with all $t\bar{t}$ data in Table 31. It is clear that the HL-LHC

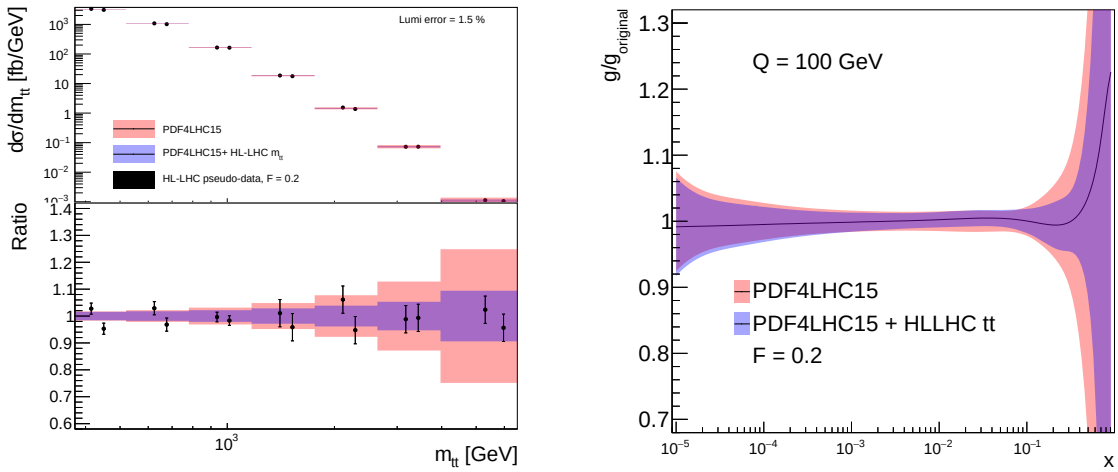

Fig. 58: Comparison of the predictions for the $m_{t\bar{t}}$ distribution in top-quark pair production at the HL-LHC using PDF4LHC15 with the associated pseudo-data and with the profiled results with $F \equiv f_{\rm corr} \cdot f_{\rm red} = 0.2$ (left). The corresponding differences at the level of the gluon PDF at $Q = 100$ GeV before and after profiling all top-quark pair production observables (right).

pseudo-data in this scenario will have much smaller uncertainties than the PDF uncertainties, so there is a marked reduction on the PDF errors on the gluon at large-x. Note that the two points in each of the bins in Fig. 58 (left) correspond to the ATLAS and CMS pseudo-data.

We next consider two other representative processes: W+charm quark production in central rapidity region and the high-mass Drell-Yan process. In Fig. 59 we show the same comparison as in Fig. 58 for these two processes. In the case of the W+charm quark production, we observe a clear reduction of PDF errors in the strangeness, $s + \bar{s}$, at intermediate values of x, highlighting the sensitivity of this measurement to the strange content of the proton. For the case of high-mass Drell-Yan, we show how the uncertainties on the $\bar{u}$ quark PDF are reduced at large x region. Here the impact is rather moderate, as experimental and PDF errors are comparable even in the high m_{ll} region.

5.2.5 Ultimate PDFs from HL-LHC data.

The final profiled PDF sets are based combined dataset listed in Table 31; these provide an estimate of the impact of future HL-LHC measurements into our knowledge of the quark and gluon structure of the proton. In Table 32 we list the three scenarios for the systematic uncertainties of the HL-LHC pseudo-data that we assume in the present exercise. These scenarios, ranging from more conservative to more optimistic, differ among them in the reduction factor $f_{\rm red}$, Eq. (33), applied to the systematic errors of the reference 8 TeV or 13 TeV measurements. In particular, in the optimistic scenario we assume a reduction of the systematic errors by a factor 2.5 compared to the reference 8 TeV measurements. We assume a large factor of 5 for the 13 TeV measurements, correcting for the fact that these are based in the initial datasets which generally have larger systematic errors in comparison to the 8 TeV case. We also indicate in each case the name of the corresponding `LHAPDF` grid.

Then in Fig. 60 we present a comparison of the baseline PDF4LHC15 set with the profiled sets based on HL-LHC pseudo-data from scenarios A and C in Table 32. Specifically, we show the gluon, down quark, up anti-quark, and total strangeness at $Q = 10$ GeV, normalized to the central value of the baseline. We observe that the predictions of scenarios A and C (optimistic and conservative respectively) are reasonably similar. This demonstrates that our results are relatively robust against the projections of how experimental errors will be reduced in HL-LHC measurements. A marked reduction of PDF

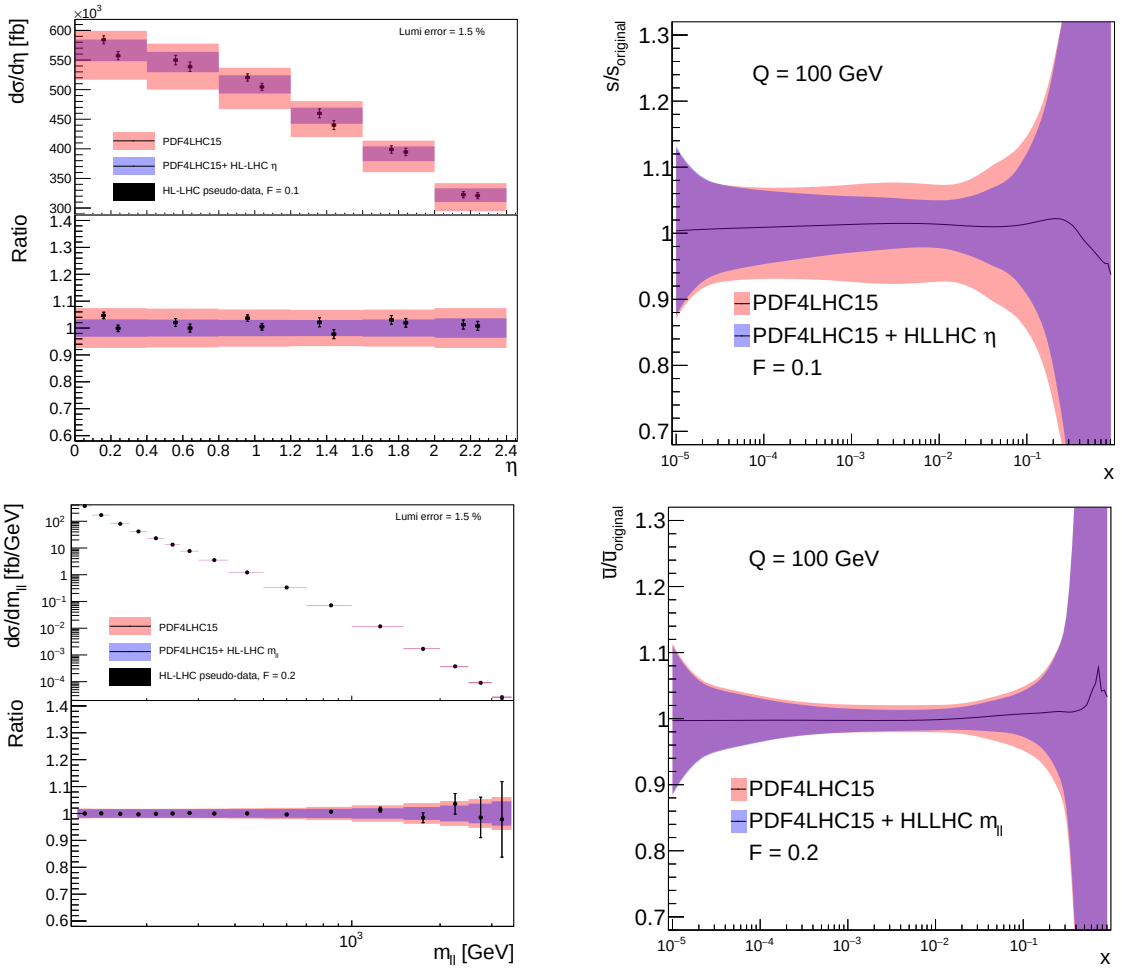

Fig. 59: Same as Fig. 58 for W+charm quark production with impact on strange quark PDF (upper) and the high-mass Drell-Yan process with impact on $\bar{u}$ PDF (lower).

Table 32: The three scenarios for the systematic uncertainties of the HL-LHC pseudo-data that we assume in the present exercise. These scenarios, ranging from conservative to optimistic, differ among them in the reduction factor $f_{\rm red}$, Eq. (33), applied to the systematic errors of the reference 8 TeV or 13 TeV measurements. We also indicate in each case the name of the corresponding `LHAPDF` grid.

Scenario	$f_{\rm red}$ (8 TeV)	$f_{\rm red}$ (13 TeV)	`LHAPDF` set	Comments
A	0.4	0.2	`PDF4LHC_nnlo_hllhc_scen3`	Optimistic
B	0.7	0.36	`PDF4LHC_nnlo_hllhc_scen2`	Intermediate
C	1	0.5	`PDF4LHC_nnlo_hllhc_scen1`	Conservative

uncertainties is visible in all cases, and is particularly significant for the gluon and the sea quarks, which are worse known than the valence quarks.

Next, we take a look at the partonic luminosities, in particular quantifying the improvement in the PDF uncertainties in different initial-state partonic combinations from the HL-LHC pseudo-data. In Fig. 61 we show the reduction of PDF uncertainties in the gg, qg, $q\bar{q}$, and qq luminosities at $\sqrt{s} = 14$

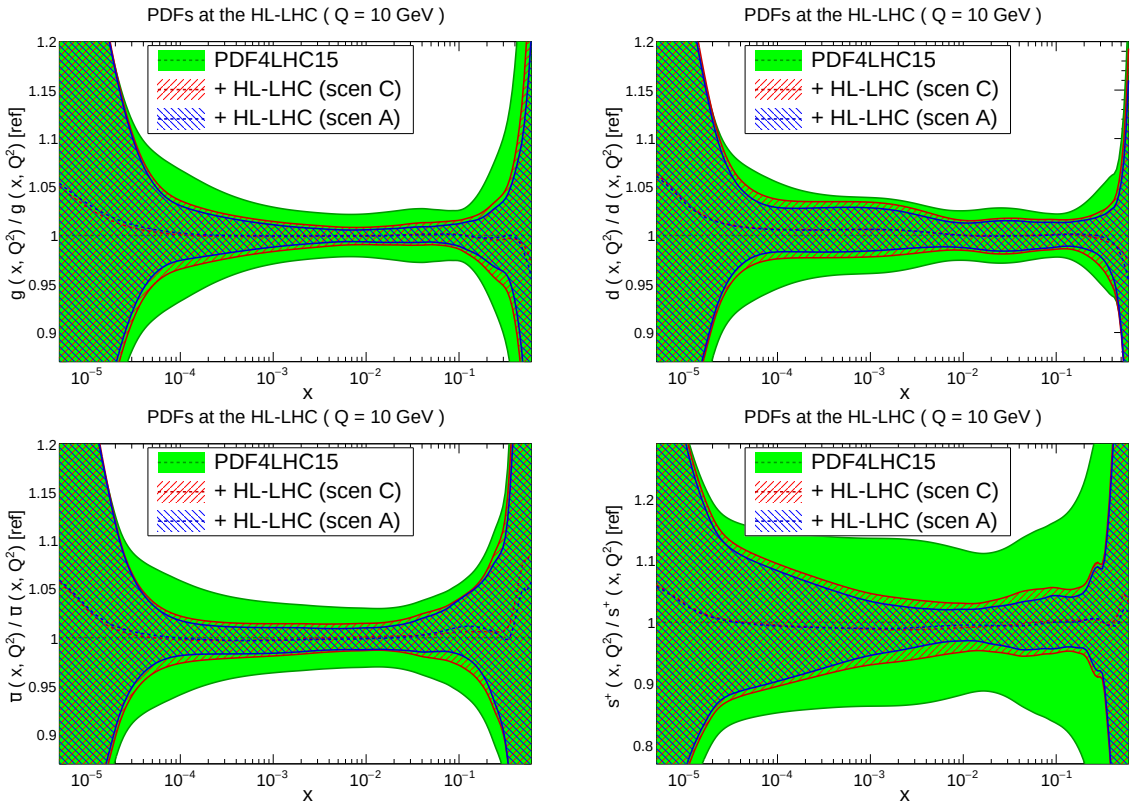

Fig. 60: Comparison of PDF4LHC15 with the profiled sets with HL-LHC data in scenarios A and B (see text). We show the gluon, down quark, up anti-quark, and total strangeness at $Q = 10$ GeV, normalized to the central value of the baseline.

TeV due to the HL-LHC pseudo-data (in scenarios A and C) with respect to the PDF4HC15 baseline. The average values of this PDF error reduction for three different invariant mass bins (low, medium, and high values of M_X) is shown in Table 62.[17] The value outside (inside) brackets correspond to scenario C (A). Note that in this table we have also listed the us luminosity, which contributes to processes such as inclusive W^+ production.

From the comparisons in Fig. 61 and in Table 62 we confirm that the overall error reduction is not too sensitive to the specific projections assumed for the experimental systematic uncertainties. We find that in the intermediate mass bin, $40\ \text{GeV} \leq M_X \leq 1\ \text{TeV}$, the reduction of PDF uncertainties ranges roughly between a factor of 2-4, depending on the partonic channel and the scenario for the systematic errors. For example, for the gg luminosity in the range relevant for Higgs production, one finds a reduction by a factor $\simeq 3$ in scenario A. A similar improvement is found in the high mass region, $M_X \geq 1$ TeV, directly relevant for bSM searches. In the optimistic scenario, the PDF error reduction at high masses ranges between a factor 4 for the gg luminosity to around a factor 2 for the qq and $q\bar{q}$ ones. On the other hand, the PDF error reduction is more moderate in the low mass region, $M_X \lesssim 20$ GeV, since none of the processes in Table 31 is directly sensitive to it.

5.2.6 Implications for LHC phenomenology

Now we turn to present some selected phenomenological implications of these "ultimate" PDFs at the HL-LHC for a variety of processes, both within the SM and beyond. We start by considering high-

[17] The average is computed from 10 points per mass bin, log-spaced in M_X.

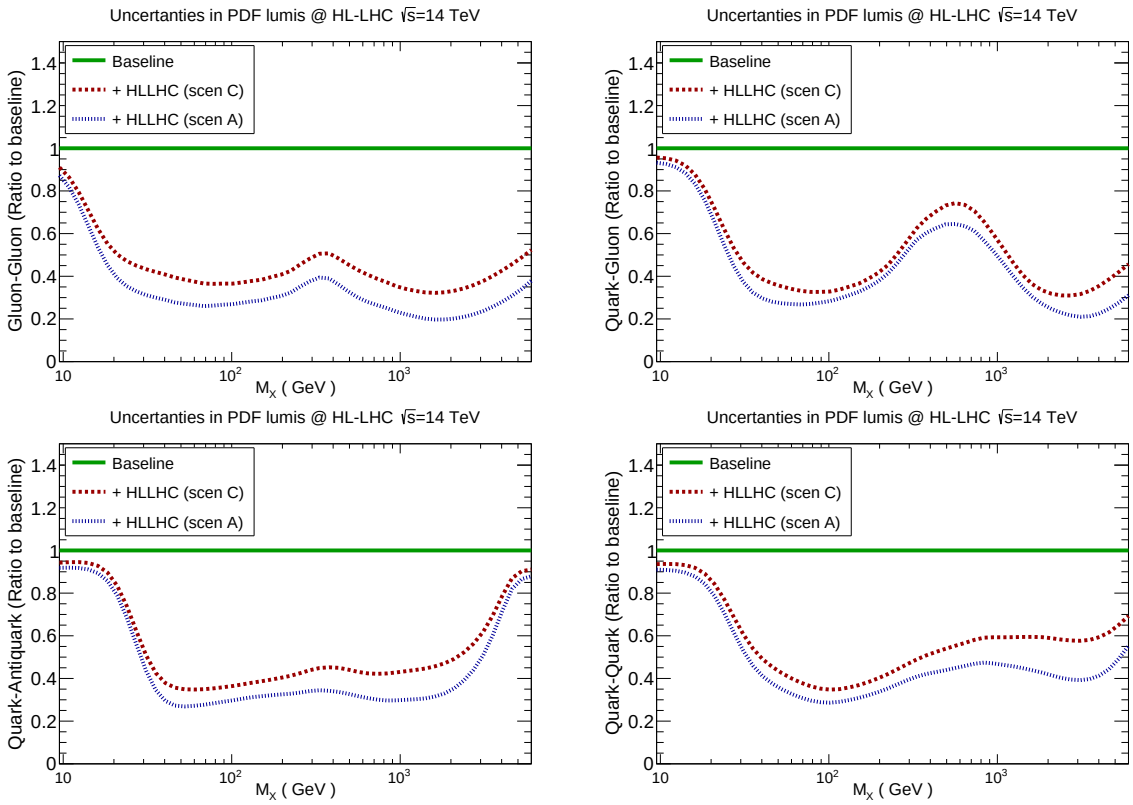

Fig. 61: The reduction of PDF uncertainties in the gg, qg, $q\bar{q}$, and qq luminosities at $\sqrt{s} = 14$ TeV due to the HL-LHC pseudo-data (in scenarios A and C) with respect to the PDF4HC15 baseline.

mass supersymmetric (SUSY) particle production at the HL-LHC, where sparticles masses up to $\simeq 3$ TeV can be searched for. While we consider this SUSY scenario for concreteness, similar results will hold for the production of new BSM states within other models. In Fig. 63 we show the comparison between the baseline PDF4LHC15 predictions with the corresponding HL-LHC results corresponding to scenarios C and A (conservative and optimistic respectively), normalised to the central value of the former. Specifically, we show the cross-sections for gluino-gluino and squark-gluino at $\sqrt{s} = 14$ TeV. Theoretical predictions have been computed at leading order (LO) using `Pythia8.235` [251] with the SLHA2 benchmark point [524] for a range of sparticle masses. For simplicity, underlying event and multiple interactions have been switched off.

From the comparisons in Fig. 63, we find that the constraints on the PDFs from the HL-LHC pseudo-data lead to a marked reduction to the uncertainties in the high-mass SUSY cross-sections, consistent with the corresponding reduction at the level of luminosities reported in Fig. 61. For instance, for gluino pair-production with $M_{\tilde{g}} = 3$ TeV, the PDF uncertainties are reduced from $\simeq 60\%$ to $\simeq 25\%$ in the optimistic scenario. An even more marked reduction is found for the squark-gluino cross-section, specially at large sparticle masses. More moderate improvements are found in the case of squark-antisquark production, due to the limited constraints that the HL-LHC provides on the large-x antiquarks, at least for the processes considered here. In this case, we find an error reduction by a factor of $\simeq 25\%$ for $M_{\tilde{q}} = 3$ TeV.

Next, in Fig. 64 we present a similar comparison as that of Fig. 63 now for various SM processes. The upper plots display diphoton (dijet) production as a function of the minimum invariant mass $M_{\gamma\gamma}^{\rm min}$ ($M_{jj}^{\rm min}$). The bottom plots show Higgs boson production in gluon fusion, first inclusive and decaying

PDF uncertainties HLLHC / Current	10 GeV < M_X < 40 GeV	40 GeV < M_X < 1 TeV	1 TeV < M_X < 6 TeV
g-g luminosity	0.58 (0.49)	0.41 (0.29)	0.38 (0.24)
q-g luminosity	0.71 (0.65)	0.49 (0.42)	0.39 (0.29)
quark-quark luminosity	0.78 (0.73)	0.46 (0.37)	0.60 (0.45)
quark-antiquark luminosity	0.73 (0.70)	0.40 (0.30)	0.61 (0.50)
up-strange luminosity	0.73 (0.67)	0.38 (0.27)	0.42 (0.38)

Fig. 62: The uncertainties associated to different PDF luminosities, normalised to the uncertainties of the current baseline (PDF4LHC15). We have computed the average for three different invariant mass M_X bins. The numbers outside (inside) brackets correspond the conservative (optimistic) scenario.

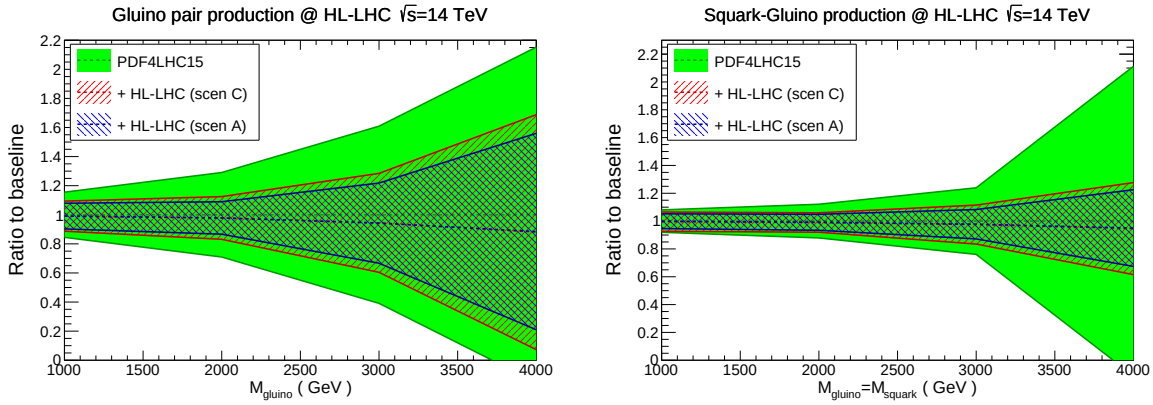

Fig. 63: Comparison between the baseline PDF4LHC15 predictions for high-mass supersymmetric particle production at the HL-LHC with the corresponding HL-LHC projections corresponding to scenarios C and A, normalised to the central value of the baseline. We show the results for gluino-gluino and squark-gluino, production cross-sections at $\sqrt{s} = 14$ TeV.

into $b\bar{b}$ as a function of $p_b^{T,\min}$, and then in association with a hard jet as a function of $p_{\rm jet}^{T,\min}$. These cross-sections have been computed at LO with `MCFMv8.2` [168] with the basic ATLAS/CMS acceptance cuts. The use of leading-order theory is justified since we only aim to illustrate the relative impact of the PDF error reduction, rather than providing state-of-the-art predictions for the rates.

From the comparisons in Fig. 64, we find again that the two scenarios, A and C, give similar results. In the case of dijet production, which at large masses is dominated by the qq and qg luminosities, we see that one expects to reduce PDF errors down to $\simeq$2% even for invariant masses as large as $M_{jj} = 6$ TeV. A similar conclusion can be drawn for diphoton production, also sensitive to the qq partonic initial state. Concerning Higgs boson production in gluon fusion, we see that in the inclusive case the HL-LHC constraints should lead to PDF errors below the percent level. For Higgs boson production in association with a hard jet, we also find a marked error reduction, suggesting that PDF uncertainties in the p_T^h distribution should be down to at most the $\simeq$2% level at the HL-LHC in the entire relevant kinematical range.

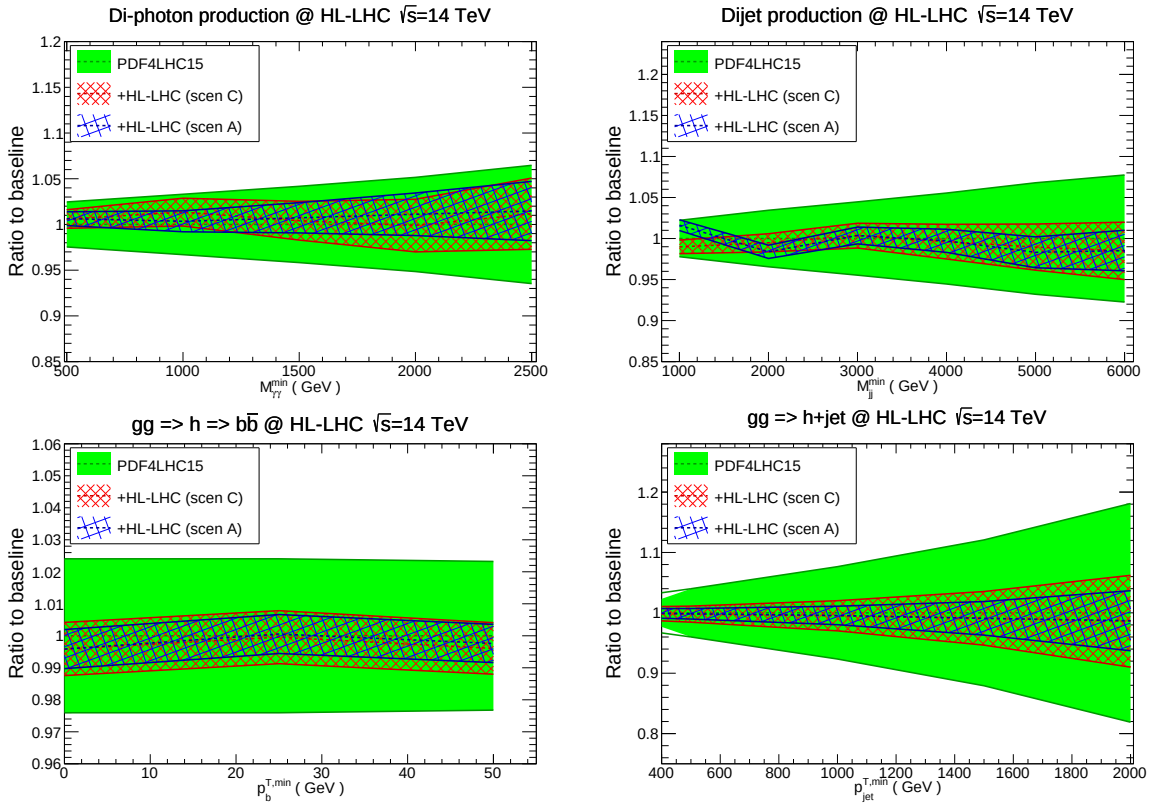

Fig. 64: Same as Fig. 63 for Standard Model processes. The upper plots show diphoton (dijet) production as a function of the minimum invariant mass $M_{\gamma\gamma}^{\rm min}$ ($M_{jj}^{\rm min}$). The bottom plots show Higgs boson production in gluon fusion, first inclusive and decaying into $b\bar{b}$ as a function of $p_b^{T,\rm min}$, and then in association with a hard jet as a function of $p_{\rm jet}^{T,\rm min}$.

5.2.7 Summary and outlook.

In this study, we have quantified the constraints that HL-LHC measurements are expected to impose on the quark and gluon structure of the proton. We have assessed the impact of a range of physical processes, from weak gauge boson and jet production to top quark and photon production, and studied the robustness of our results with respect to different projections for the experimental systematic uncertainties. We find that, in the invariant mass region $M_X \gtrsim 100$ GeV, the HL-LHC measurements can be expected to reduce the PDF uncertainties in processes such as Higgs boson or SUSY particle production by a factor between 2 and 4, depending on the dominant partonic luminosity and on the scenario for the systematic errors. Therefore, we have demonstrated how the exploitation of the HL-LHC constraints on PDFs will feed into improved theoretical predictions for a range of phenomenologically relevant processes both within and beyond the SM.

Two caveats are relevant at this point. First, we have only considered a non–exhaustive subset of all possible measurements of relevance for PDF fits. Other processes not considered here, due to currently anticipated measurements and those not foreseen but which may well added to the PDF toolbox in the future, will certainly increase the PDF impact in some regions. Second, we have ignored any possible issues such as data incompatibility, theoretical limitations, or issues with the data correlation models, which may limit the PDF impact in some cases. All these issues can only be tackled once the actual measurements are presented.

The results of this study are made publicly available in the `LHAPDF6` format [160], with the grid

names listed in Table 32. This way, the "ultimate" PDFs produced here can be straightforwardly applied to related physics projections of HL-LHC processes taking into account our improved knowledge of the partonic structure of the proton which is expected by then.

5.3 Underlying Event and Multiple Parton Interactions

5.3.1 Double Parton Scattering

Double parton scattering (DPS) is said to occur when one has two distinct hard parton-parton collisions in a single proton-proton interaction. In terms of the total cross section to produce a final state AB that may be divided into two subsets A and B, DPS is formally power suppressed by $\sim \Lambda^2_{QCD}/\min(Q^2_A, Q^2_B)$ compared to the more-familiar single parton scattering (SPS) mechanism. However, in practice there are various processes and kinematic regions where DPS contributes at a similar (or greater) level than SPS. Processes include those in which the SPS is suppressed by small/multiple coupling constants, such as same-sign WW production, and processes where at least one part of the final state can be produced via a comparatively low scale scattering – e.g. those involving a charm/bottom quark pair.

The full theoretical description of DPS in QCD is rather complex, and many of the steps towards its formulation were achieved only recently [525–530]. As a result, many past studies of DPS have taken a strongly simplified approach in which it is assumed that the two colliding partons from each proton are entirely uncorrelated with one another, and that the (single) parton density in momentum fraction x and impact parameter $\mathbf{b}$ may be factorised into the PDF and a transverse profile depending only on $\mathbf{b}$. In this case the DPS cross section simplifies into the so-called 'pocket formula':

$$\sigma^{AB}_{\text{DPS}} \simeq \frac{\sigma^{A}_{\text{SPS}}\sigma^{B}_{\text{SPS}}}{\sigma_{\text{eff}}} \tag{38}$$

The quantity σ_{eff} is a geometrical factor of order of the proton radius squared. The modelling of more general multiple parton interactions (MPI) in Monte Carlo event generators such as Herwig and Pythia is based on similar approximations.

Eq. (38) does not take into account the possibility that the two partons from either or both protons may have arisen as the result of a perturbative $1 \to 2$ splitting of a single parton into two. It also does not take into account a multitude of possible correlations between two partons in a proton, in spin, colour, and momentum fraction x_i, correlations between x_i and the transverse separation between partons $\mathbf{y}$, as well as potential interference contributions in parton type. These correlations and QCD effects can result in a DPS cross section differing from the prediction of eq. (38), both in terms of overall rate and also, crucially, in distributions.

Studies of DPS at the LHC and earlier colliders have essentially been restricted to extractions of a single number, the DPS rate, for several processes. From these early studies, in which the error bars are large and multiple factors change between measurements (x values, parton channels, scales...), nothing conclusive can be determined thus far concerning correlations. However, the increased luminosity of the HL-LHC will provide us with the statistics needed to study differential distributions with sufficiently small uncertainties that we will be able to probe quantum correlations between partons in the proton and the dynamics of the $1 \to 2$ splitting for the first time. The results of these studies can be fed back and used to improve the theoretical modelling of DPS (and more general MPI), yielding improved DPS signal or background predictions.

As can be inferred from eq. (38), DPS very roughly scales as the fourth power of a parton distribution, whilst SPS only scales as the second power. This means that for given hard scales Q_A, Q_B, the DPS cross section grows faster than the SPS one as we increase collider energy (and decrease x), meaning that at a HE-LHC DPS will be more prominent and easily measurable than at the LHC. At the same time, at the lower x values involved the effects of the correlations and $1 \to 2$ splittings will

be different - a combination of measurements of different processes at both the HL-LHC and HE-LHC should help us to separate out the effects of the different correlations.

Let us illustrate the general points above using a concrete process – namely same-sign WW production, where both Ws decay leptonically into e or μ. A simple correlation-sensitive observable for this process is the asymmetry a_{η_l}:

$$a_{\eta_l} = \frac{\sigma(\eta_1 \cdot \eta_2 < 0) - \sigma(\eta_1 \cdot \eta_2 > 0)}{\sigma(\eta_1 \cdot \eta_2 < 0) + \sigma(\eta_1 \cdot \eta_2 > 0)}, \tag{39}$$

where $\eta_{1,2}$ are the rapidities of the two leptons. This quantity measures the discrepancy between the number of times the produced leptons emerge into opposite hemispheres of the detector and the number of times they emerge into the same hemisphere, normalised by the total number of lepton pairs produced. In the absence of parton correlations, we have $a_{\eta_l} = 0$; any departure from this value indicates the presence of correlations. A more differential version of this asymmetry is the cross section differential in the product $\eta_1 \cdot \eta_2$. Here an absence of correlations yields a symmetric distribution under $\eta_1 \cdot \eta_2 \leftrightarrow -\eta_1 \cdot \eta_2$, and an asymmetric distribution indicates correlations. In the below studies a cut of $|\eta_i| < 2.4$ is always applied.

One type of correlation that will clearly affect these observables are correlations in momentum fraction x between the partons. This type of effect was investigated in [531]. Here, the double parton distributions (DPDs) were calculated at an input scale of $Q_0^2 = 0.26\,\text{GeV}^2$ from a constituent quark model calculation where the proton is taken as being composed only from the three quarks uud. At this scale there are necessarily strong correlations in x space from the fact that we have only three quarks and the constraint $\sum_i x_i = 1$. These inputs were then evolved up to the W mass scale via the double DGLAP equations, with effects of $1 \to 2$ splittings being ignored. In figure 65, the green band represents their result at $\sqrt{s} = 14$ TeV for a quantity equal to $\sigma(\eta_1 \cdot \eta_2 < 0)/\sigma(\eta_1 \cdot \eta_2 > 0)$ – their result corresponds to $a_{\eta_l} \sim 0.05$. On the same plot is given the anticipated sensitivity of the CMS experiment at the HL-LHC (3ab^{-1}) [532] (the black and yellow error bars) and the lowest values of this ratio that would allow one to reject the hypothesis of eq. (38) at the 95% confidence level (start points of black/yellow arrows). These results indicate good prospects of the HL-LHC measuring a_{η_l} values on the few per cent level for this process.

One simple feature that must necessarily be present in the true DPDs, and is taken into account by the DPDs of [531] but not by eq. (38), is the fact that removing one valence u quark from the proton halves the probability to find another, and there is no chance to find two valence d quarks (this requirement is formally expressed in the number sum rules of [533]). This effect is highly relevant to a_{η_l} as it results in a reduction of cross section for large $\eta_1 \cdot \eta_2$ (which probes the 'double valence' region in one DPD) whilst leaving the cross section elsewhere unchanged. To investigate the size of a_{η_l} resulting from this effect only, we constructed DPD inputs at $Q_0 = 1$ GeV based on a factorised ansatz of a product of MSTW2008LO PDFs times a transverse factor, except that in the uu and dd cases the PDF part is given by $D^u(x_1)D^u(x_2) - \frac{1}{2}D^{u_v}(x_1)D^{u_v}(x_2)$ and $D^d(x_1)D^d(x_2) - D^{d_v}(x_1)D^{d_v}(x_2)$ respectively. Evolving these inputs and using them to calculate the W^+W^+ cross section at $\sqrt{s} = 13$ TeV, we observe an asymmetry of ~ 0.017, indicating that these simple 'valence number effects' are at least one important driving force in the asymmetry of [531].

Correlations in (longitudinal) spin can affect the rapidity distributions of the produced leptons [534] and result in a nonzero a_{η_l}. The potential size of effects from spin correlations was investigated recently in [535]. In this study the unpolarised double parton distributions were constructed according to an uncorrelated ansatz at an initial scale of 1 GeV. The polarised double parton distributions, encoding parton spin correlations, were chosen at the initial scale to correspond to the maximal possible spin correlations (technically, saturate the positivity bounds [536]), in such a way that the effects on the cross section would be maximal. These distributions were evolved to the W mass and used to compute

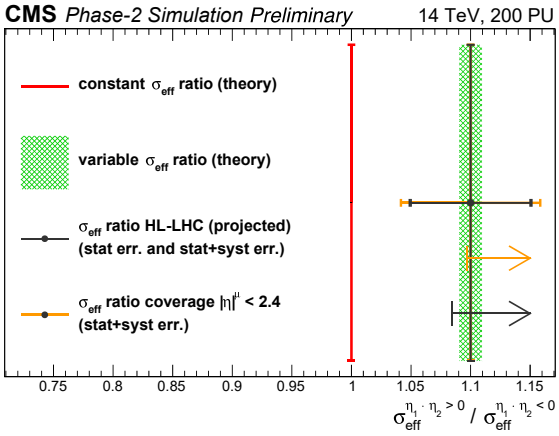

Fig. 65: Ratio of σ_{eff} for $\eta_1 \cdot \eta_2 > 0$ and $\eta_1 \cdot \eta_2 < 0$, which is equal to the inverse ratio for σ_{DPS}. The value of this in the absence of parton correlations is 1 (red line), whilst the prediction of [531] is given by the green band. The black error bars indicate systematic uncertainty attainable by the CMS experiment at 3ab^{-1}, the orange bars include systematic uncertainties assuming a conservative correlation of 0.8 between them for $\eta_1 \cdot \eta_2 > 0$ and $\eta_1 \cdot \eta_2 < 0$. The vertical line on the arrows indicates the lowest measured value of the ratio that would allow the exclusion of the uncorrelated parton hypothesis (i.e. eq. (38) with constant σ_{eff}) at 95% CL. The black arrow corresponds to muon rapidity coverage $|\eta| < 2.8$, and the orange arrow $|\eta| < 2.4$.

polarised and unpolarised W^+W^+ cross sections at $\sqrt{s} = 13$ TeV. The resulting $\eta_1 \cdot \eta_2$ distribution is shown in figure 66(a) – the corresponding value of a_{η_l} is 0.07, which is even larger than that resulting from x correlations. One should, however, bear in mind that this is a maximal value, and that there are possibilities for the polarised distributions at the input scale, compatible with the positivity bounds, that also ultimately yield negative values for a_{η_l} [537]. Figure 66(b) shows the expected significance of a measured non-zero asymmetry as a function of luminosity L, using a rapidity cut $|\eta_i| > 0.6$ imposed such that the asymmetry a_{η_l} rises to 0.11 (but overall W^+W^+ cross section reduces from 0.51 fb to 0.29 fb). The blue band shows the sensitivity achievable using the $\mu^+\mu^+$ channel only, whilst the red band shows the sensitivity attainable using $\mu^+\mu^+$, μ^+e^+, and e^+e^+ assuming a similar sensitivity can be achieved for electrons as for muons. This plot reinforces the notion that a few per cent level asymmetry can be measured at the HL-LHC.

To investigate how $1 \to 2$ splittings may affect the asymmetry a_{η_l}, we upgraded the code discussed in section 9 of [527] to include charm and bottom quarks above the appropriate mass thresholds (chosen here to be equal to the MSTW 2008 values of 1.40 GeV and 4.75 GeV respectively). The 'intrinsic' and 'splitting' part of the DPDs were initialised as in [527] – in particular, the intrinsic part was initialised according to an uncorrelated ansatz, up to a suppression factor near the phase space boundary $x_1 + x_2 = 1$, that does not have a strong impact on a_{η_l}. Then, any nonzero value of a_{η_l} will be almost entirely due to $1 \to 2$ splitting effects. Computing W^+W^+ cross sections at $\sqrt{s} = 13$ TeV we obtained $a_{\eta_l} \sim 0.028$, which is of similar size to the asymmetry arising from other sources.

Note that the asymmetries from x correlations, valence number effects and $1 \to 2$ splitting are in the same direction (favouring $\eta_1 \cdot \eta_2 < 0$ over $\eta_1 \cdot \eta_2 > 0$), whilst polarisation effects can potentially either favour a positive or negative asymmetry.

At the HE-LHC, the asymmetry should be smaller for the same cuts on $|\eta_i|$ – as x is lowered, we move away from the 'double valence' region where valence number effects are important, and the ratio

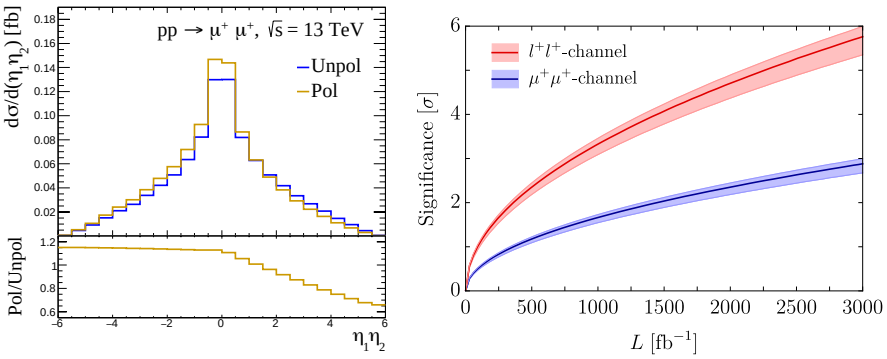

Fig. 66: Distribution in product of rapidites for two positively charged muons arising from W^+W^+ DPS. The blue plot includes only the unpolarised contribution, whilst the yellow also includes longitudinally polarised contributions (left). Estimated significance of a nonzero asymmetry as the distance in standard deviations of a measured asymmetry from zero, when the W^+W^+ cross section is 0.29 fb and asymmetry is 0.11 (right). This corresponds to the calculation of [535] with polarised contributions, and a cut on muon $|\eta| > 0.6$. The uncertainty bands indicate dependence of the sensitivity on assumptions regarding the subtraction of SPS backgrounds. More details regarding the set-up for both panels may be found in [535].

of polarised to unpolarised quark distributions reduces (see figure 6 of [538]). Repeating the study above where a minimal modification of the uncorrelated ansatz at the input scale is made to take account of number effects, but at $\sqrt{s} = 27$ TeV, we obtain $a_{\eta_l} \sim 0.008$. Including instead the effects of the $1 \to 2$ splittings yields $a_{\eta_l} \sim 0.013$ at $\sqrt{s} = 27$ TeV. At the HE-LHC (and the HL-LHC) it could be interesting to compare same-sign WW, which is comparatively weakly affected by $1 \to 2$ parton splitting (due to the fact there is no direct LO splitting yielding, for example uu), with processes that should receive stronger contributions from parton splitting, such as low mass Drell-Yan or $b\bar{b}b\bar{b}$ production, to probe in detail the effects of the $1 \to 2$ parton splitting and compare to theoretical predictions. More detailed studies in this direction are needed.

In conclusion, the HL-LHC offers the opportunity to measure the effects of correlations between partons, via measurements of DPS processes, for the first time. In same-sign WW production a good observable to probe correlations is the lepton pseudorapidity asymmetry a_{η_l}, which can only be nonzero in the presence of correlations – theoretical calculations indicate values of a_{η_l} at LHC energies on the order of a few per cent, which should be measurable at the HL-LHC. By combining measurements of various processes sensitive to DPS at the HL-LHC, and later and the HE-LHC, we should ultimately be able to build up a picture of the various correlatons existing between partons in the proton.

5.3.2 Underlying Event at 27 TeV

Underlying event (UE), defined as a accompanying activity to hard proton-proton scattering process, is an unavoidable background to collider observables for most measurements and searches. The UE activity is not constant on an event-by-event basis, so the contribution from UE cannot be subtracted. However by using measurements sensitive to UE activity, the modelling of it in Monte Carlo (MC) event generators is *tuned*.

Multiple parton interactions (MPI) are one of the most important contributors to UE. The dependence of MPI on the center-of-mass energy ($\sqrt{s}$) cannot be derived from first principles, rather modelled by looking at data at different centrer-of-mass energies, from Tevatron to LHC. At the start of LHC, it was found that the this energy extrapolation of MPI based in Tevatron Run I and II data (at $\sqrt{s} = 1.8$ TeV

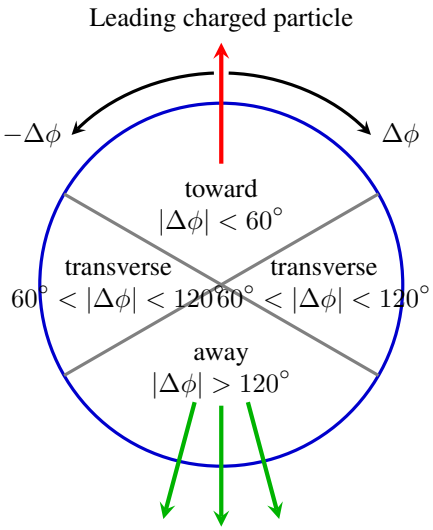

Fig. 67: Definition of UE regions in the azimuthal angle with respect to the leading charged particle

and $\sqrt{s} = 1.96$ TeV) did not describe the LHC data at $\sqrt{s} = 900$ GeV and at $\sqrt{s} = 7$ TeV [539], and predictions of different MC generators varied significantly. These generators were then tuned using LHC Run 1 and Run 2 ($\sqrt{s} = 13$ TeV) data.

To get a sense of the UE activity at HE-LHC, two state-of-the-art MC generators, PYTHIA8 [251] (v235) with Monash tune [188] and HERWIG7 [201, 540] (v713) with default tune were used. As the first measurements at a new center-of-mass energy data is easiest to perform in inclusive (i.e minimum-bias) events, 5 million such events were generated in each case. The UE activity is measured using the leading charged particle as the reference object, and defining the usual UE regions with respect to it, as shown in Fig. 67.

In Fig. 68, the scalar sum (density in per unit η-ϕ area) of charged particles and charged particle multiplicity (density) as a function of leading charged particle p_T are shown. The data is from ATLAS measurement at $\sqrt{s} = 13$ TeV [541], while MC predictions both at $\sqrt{s} = 13$ TeV and $\sqrt{s} = 27$ TeV are shown. A few conclusions can be drawn. The activity increases by about 25 - 30% by roughly doubling the center-of-mass energy, and the predictions by both generators are extremely consistent. The typical plateau-like behaviour of the activity with increasing leading charged particle p_T can be seen at $\sqrt{s} = 27$ TeV as well.

The similarity in predictions by two different generators is a welcoming sign, and perhaps indicates that the modelling of MPI evolution with center-of-mass energy is mature enough. Of course at $\sqrt{s} = 27$ TeV, the events will be very active, and disentangling the effect of MPI in even typical UE observables will be a challenge, and innovative topologies and observables will be have to be devised in order perform UE measurements.

The analysis and plots are done using the Rivet [304] analysis framework.

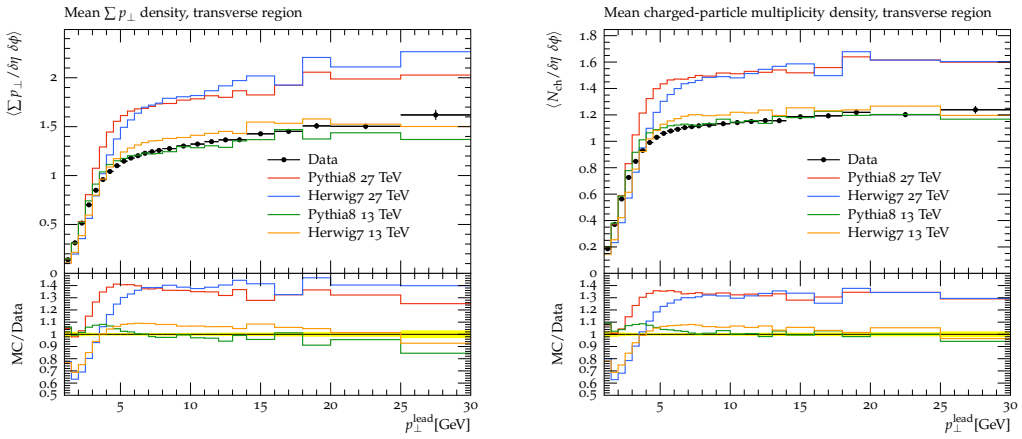

Fig. 68: Comparison of the UE activities in different center-of-mass energies.

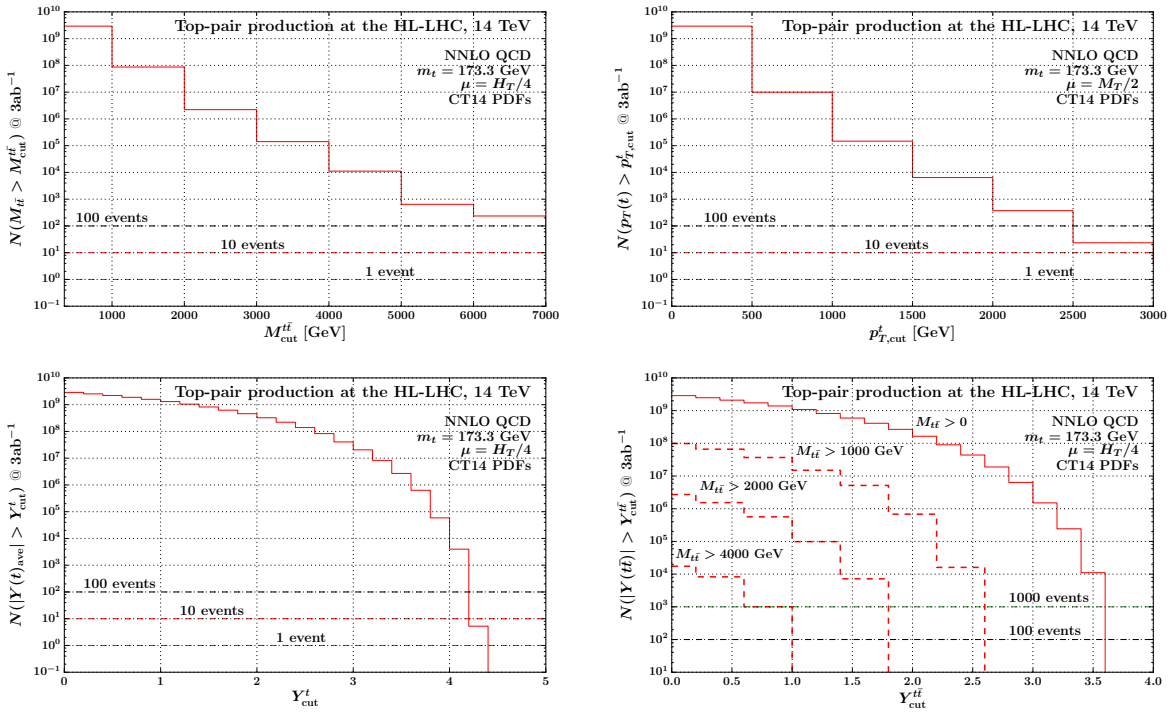

Fig. 69: Cumulative differential distributions for HL LHC at 14 TeV.

6 Top quark physics

6.1 Top quark cross section

6.1.1 The $t\bar{t}$ production cross section: theoretical results

Precision measurements of top quark properties present an important test of the SM. As the heaviest particle in the SM, the top quark plays an important role for the electroweak symmetry breaking and becomes a sensitive probe for physics beyond the SM.

This section provides a quick reference for the kinematic reach of the main $t\bar{t}$ differential distributions for both HL and HE LHC. The figures are given in terms of expected events for the proposed ultimate luminosities for both colliders: $3ab^{-1}$ for the HL LHC running at 14 TeV and $15ab^{-1}$ for the 27 TeV HE LHC. The results are presented as plots of cumulative differential distributions and should be interpreted as follows: the histograms show the numbers of expected events (for the luminosities given above) above a given cut in any one of the four kinematic variables: $m_{t\bar{t}}, p_{T,\rm avt}, y_{\rm avt}$ and $y_{t\bar{t}}$. The predictions are based on the CT14 parton distributions [157] with value of the top quark mass $m_t = 173.3$ GeV which is close to the current world average. The calculation is based on ref. [542] and uses the dynamical scales of ref. [171].

$t\bar{t}$ production at the HL LHC (14 TeV)

In fig. 69 we present predictions for the four cumulative distributions specified above, computed in NNLO QCD. We conclude that the HL LHC allows detailed studies of top quark pair production with $m_{t\bar{t}}$ of up to about 7 TeV. Events with even larger values of $m_{t\bar{t}}$ are kinematically accessible and one expects about 100 events with $m_{t\bar{t}} > 7$ TeV. Therefore, the region $m_{t\bar{t}} > 7$ TeV provides a low SM background for, for example, searches for decays of BSM heavy particles to $t\bar{t}$ pairs. A detailed understanding of the SM background - at the level of one expected event - will require a dedicated future effort due to the significant MC error in that region.

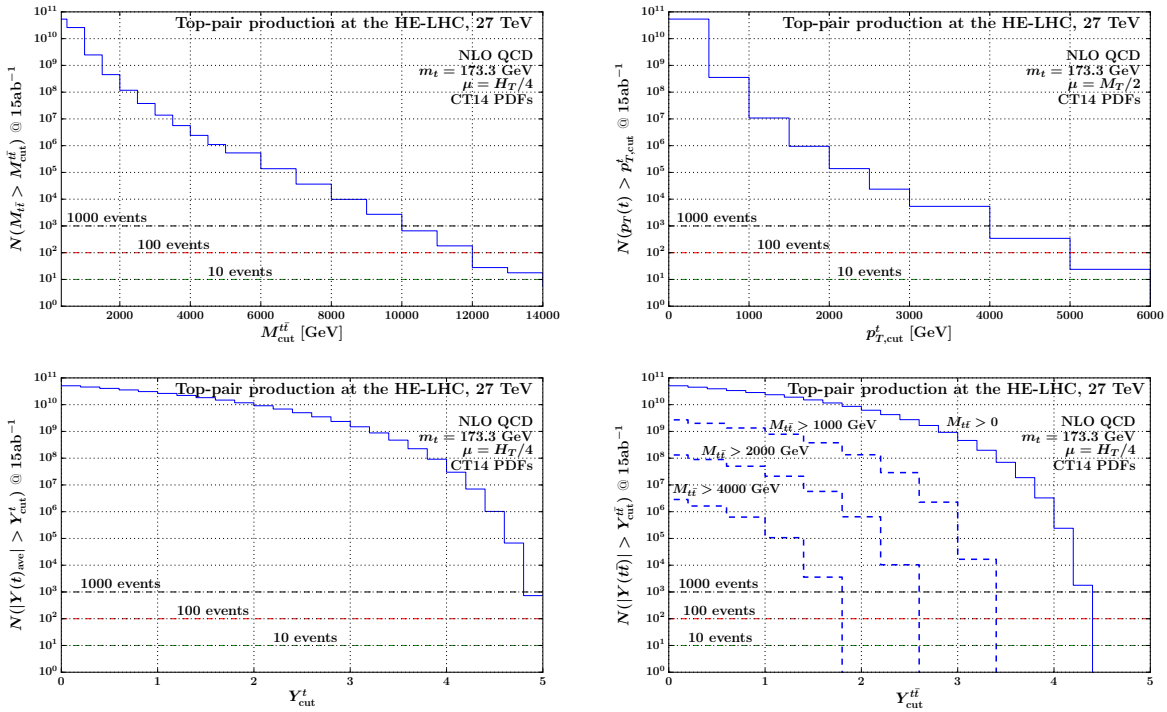

Fig. 70: Cumulative differential distributions for HE LHC at 27 TeV.

The top quark p_T distribution can probe p_T values as high as 2.5 TeV, with a total of about 100 events expected beyond that value.

The HL LHC offers the possibility to access top production at high rapidity which might provide a link between top measurements at LHCb on one hand and ATLAS and CMS on the other. Indeed, in fig. 69 we observe that top quarks with rapidity $y_{\rm avt}$ as large as 4 will be copiously produced. The cross-section is a steeply falling function at large rapidity with a maximum attainable value of around 4.2 or so. Similarly, the rapidity of top quark pairs can be measured in detail up to values exceeding 3.5 with the maximum reach at about $y_{t\bar{t}} \sim 3.8$. In fig. 69 we have shown the $y_{t\bar{t}}$ distribution for a set of cuts on the top pair invariant mass. One should bear in mind that the NNLO $y_{t\bar{t}}$ calculation has significant MC error in the bins with 10 events or less.

$t\bar{t}$ production at the HE LHC (27 TeV)

In fig. 70 we present the predictions for the same four cumulative distributions but in NLO QCD. From this figure one can easily conclude that the increase in the kinematic reach over the HL LHC is very substantial. There will be few hundred events with $m_{t\bar{t}}$ above 12 TeV and a similar number of events can be measured with p_T above 5 TeV. For the reliable description of such kinematics the inclusion of EW corrections as well as yet higher order soft and or collinear radiation will be essential; see refs. [113,178].

Very large rapidities can be attained at the HE LHC. In particular, the top quark rapidity $y_{\rm avt}$ distribution can be measured to values as high as 5.0 with excellent statistics. Indeed, about 1000 events are expected above $y_{\rm avt} = 5.0$. The top pair rapidity can reach values as high as 4.4 and, if no additional cuts are applied, few thousand events will be produced with $y_{t\bar{t}} > 4.0$. As for the case of 14 TeV we also show in fig. 70 the expected number of events as a function of $y_{t\bar{t}}$ for several cuts in $m_{t\bar{t}}$.

6.1.2 *Measurement of differential $\mathrm{t\bar{t}}$ cross section*

We present a study of the resolved reconstruction of top quark pairs in the e/μ+jets channels and a projection of differential $\mathrm{t\bar{t}}$ cross sections measurements with an integrated luminosity of 3 ab^{-1} at 14 TeV. The analysis techniques are based on previous measurements of differential $\mathrm{t\bar{t}}$ cross sections at 13 TeV [543, 544]. It is shown that such a measurement is feasible at the HL-LHC despite the expected large number of pileup interactions. The precision of the differential cross section can profit from the enormous amount of data and the extended η-range of the Phase-2 CMS detector. The results are used to estimate the improvement of measurements of parton distribution functions.

This study is based on a DELPHES simulation of the Phase-2 CMS detector [545–548] using the Monte Carlo program POWHEG [273, 325, 385, 386] (v2,hvq) in combination with PYTHIA [251, 387] (v8.219) for the generation of $\mathrm{t\bar{t}}$ events at NLO accuracy. Events with a single isolated electron or muon with $p_\mathrm{T} > 30\,\mathrm{GeV}$ and $|\eta| < 2.8$ are selected. Events with additional isolated electrons or muons with $p_\mathrm{T} > 15\,\mathrm{GeV}$ and $|\eta| < 2.8$ are rejected. At least 4 jets with $p_\mathrm{T} > 30\,\mathrm{GeV}$ and $|\eta| < 4.0$ are required, where at least 2 of the jets have to be identified as b jets. It is essential that the PUPPI algorithm [549] is used for the mitigation of pileup contribution when the jets are clustered and the $\vec{p}_\mathrm{T}^{\,\mathrm{miss}}$ is calculated.

A detailed description of the $\mathrm{t\bar{t}}$ reconstruction is presented in [543,544]. For the reconstruction all possible permutations of assigning detector-level jets to the corresponding $\mathrm{t\bar{t}}$ decay products are tested and a likelihood that a certain permutation is correct is evaluated. In each event, the permutation with the highest likelihood is selected. The likelihood is constructed from the 2 dimensional m_t–m_W distribution of correctly assigned jets for the hadronically decaying top quark and the distribution of $D_{\nu,\mathrm{min}}$ obtained when calculating the neutrino momentum [550] for the leptonically decaying top quark. A comparison of the expected event yields and the migration matrices together with their properties are shown in Fig. 71 for the HL-LHC expectation. Despite the high pileup a performance of the $\mathrm{t\bar{t}}$ reconstruction similar to the one in 2016 [544] can be reached, while the portion of the direct measurable phase-space is increased due to the extended η-range.

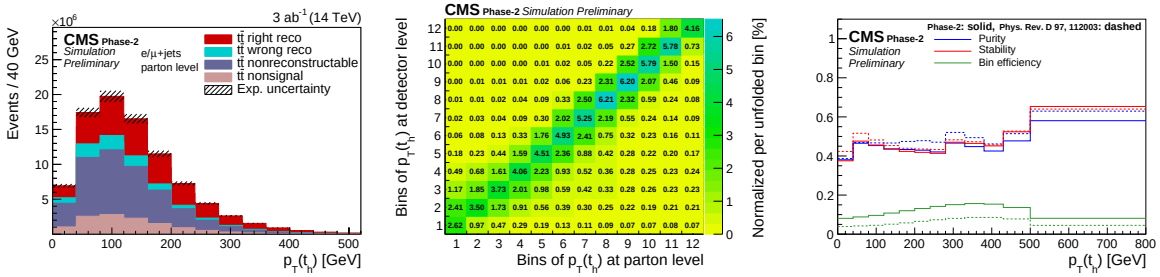

Fig. 71: Expected signal yields (left), migration matrices (middle), and its properties (right) for measurements of $p_\mathrm{T}(\mathrm{t_h})$ for the Phase-2 simulation. The purity is defined as the fraction of parton-level top quarks in the same bin at the detector level, the stability as the fraction of detector-level top quarks in the same bin at the parton level, and the bin efficiency as the ratio of the number of events found in a certain bin at detector level and the number of events found at parton-level in the same bin.

The following experimental uncertainties are estimated based on the expected performance of the Phase-2 CMS detector [TODO cite performances]: electron and muon identification, b-tagging efficiencies, jet energy and $\vec{p}_\mathrm{T}^{\,\mathrm{miss}}$ calibration, and luminosity.

Theoretical uncertainties have been studied in the 2016 analysis [544] and are taken from there. For the extended rapidity range, the uncertainties in the highest available rapidity bins of the 2016 analysis are used. We consider this as a conservative estimate, since several improvements of the theoretical predictions are expected and further measurements can reduce modeling uncertainties. Therefore, we also provide a more optimistic version, where a reduction of all theoretical and modeling uncertainties

uncertainties by a factor of two is assumed.

The unfolded results of the differential $\mathrm{t\bar{t}}$ cross section measurements as a function of p_{T} and rapidity y of the hadronically decaying top quark ($\mathrm{t_h}$) are shown in Fig. 72. In Fig. 73 the normalized double-differential cross section as a function of $M(\mathrm{t\bar{t}})$ vs $|y(\mathrm{t\bar{t}})|$ is shown. The strong impact of these measurement on PDF constraints is studied in Section 6.1.3. The high amount of data and the extended η-range of the Phase-2 detector allow for fine-binned measurements in phase-space regions — especially at high rapidity — that are not accessible in current measurements. The most significant reduction of uncertainty is expected due to an improved jet energy calibration.

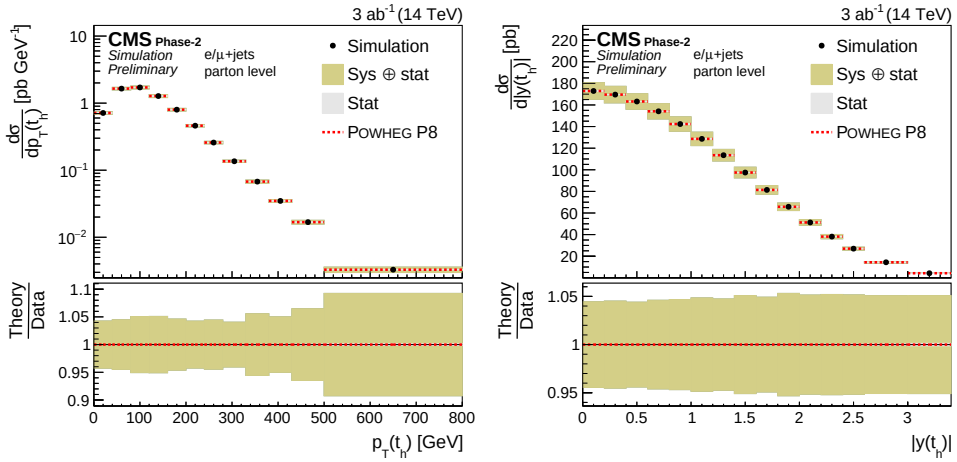

Fig. 72: Projections of the differential cross sections as a function of $p_{\mathrm{T}}(\mathrm{t_h})$ (right) and $|y(\mathrm{t_h})|$ (left). The projections are shown with conservative (Sys con.) and optimistic (Sys opt.) assumptions on theoretical uncertainties.

6.1.3 PDF constraints from double-differential $\mathrm{t\bar{t}}$ cross sections

The impact of differential $\mathrm{t\bar{t}}$ cross section measurements at the HL-LHC on the proton PDFs is quantitatively estimated using a profiling technique [446], which is based on minimizing χ^2 between data and theoretical predictions taking into account both experimental and theoretical uncertainties arising from PDF variations. The analysis is performed using the XFITTER program [459], with the theoretical predictions for the $\mathrm{t\bar{t}}$ cross sections calculated at NLO QCD using the MG5_AMC@NLO [12] framework, interfaced with the AMCFAST [551] and APPLGRID [166] programs. Three NLO PDF sets were chosen for this study: ABMP16 [552], CT14 [157], and NNPDF3.1 [165]. The normalized double-differential $\mathrm{t\bar{t}}$ production cross sections as a function of $M(\mathrm{t\bar{t}})$ vs $|y(\mathrm{t\bar{t}})|$ are used which are expected to impose stringent constraints on the gluon distribution [553]. The χ^2 value is calculated using the full covariance matrix representing the statistical and systematic uncertainties of the data, while the PDF uncertainties are treated through nuisance parameters. The values of these nuisance parameters at the minimum are interpreted as optimized or profiled PDFs, while their uncertainties determined using the tolerance criterion of $\Delta\chi^2 = 1$ correspond to the new PDF uncertainties. The profiling approach assumes that the new data are compatible with theoretical predictions using the existing PDFs, such that no modification of the PDF fitting procedure is needed. Under this assumption, the central values of the measured cross sections are set to the central values of the theoretical predictions. The original and profiled ABMP16, CT14, and NNPDF3.1 uncertainties of the gluon distribution at the scale $\mu_{\mathrm{f}}^2 = 30\,000\,GeV^2 \simeq m_{\mathrm{t}}^2$ are shown in Fig. 74. A consistent impact of the $\mathrm{t\bar{t}}$ data on the PDFs is observed for the three PDF sets. The uncertainties of the gluon distribution are drastically reduced once the $\mathrm{t\bar{t}}$ data are included in the fit.

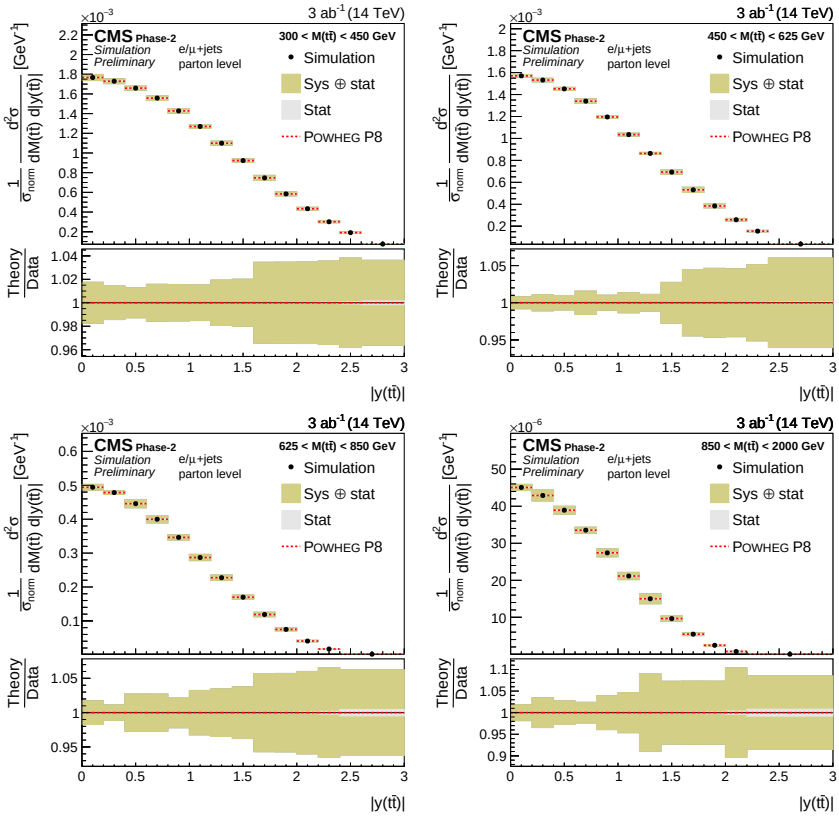

Fig. 73: Projections of the double-differential cross section as a function of $|y(\mathrm{t\bar{t}})|$. The projection is shown with conservative (Sys con.) and optimistic (Sys opt.) assumptions on theoretical uncertainties.

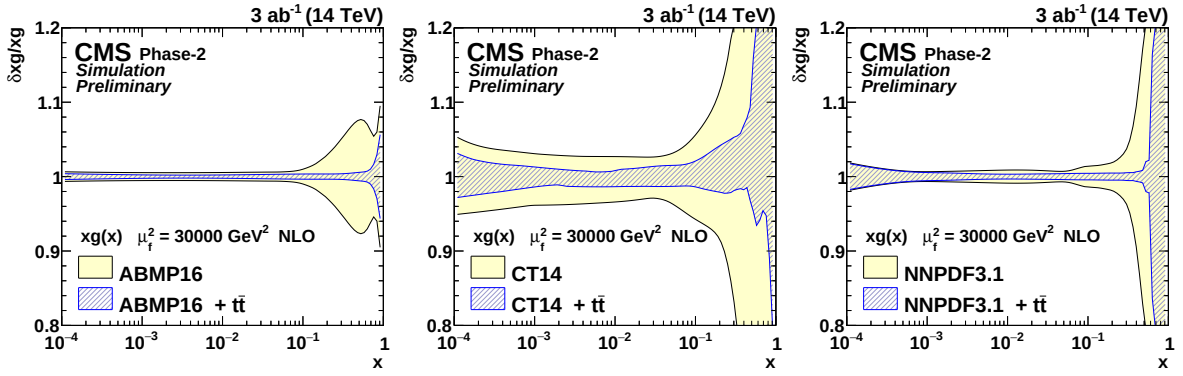

Fig. 74: The relative gluon PDF uncertainties of the original and profiled ABMP16 (left), CT14 (middle) and NNPDF3.1 (right) sets.

6.1.4 Forward top quark physics

Three measurements of top production have been performed by LHCb during Runs 1 and 2 of the LHC with a precision of (20-40)%, limited by the available data samples. As LHCb collects data at a lower rate than ATLAS and CMS, and has a limited acceptance, the measurements have focused on a partial reconstruction of the $\mathrm{t\bar{t}}$ final state in order to make optimal use of statistics. Additionally, as no estimate of missing energy is available, the measurements are performed at the level of the lepton and jets only, with no full top quark reconstruction performed. The first observation in the forward region was made in the μb final state, where the top quark is identified by the presence of a muon and a b-jet [554]. This

Table 33: The number of $t\bar{t}$ events expected to be reconstructed at LHCb per final state using a dataset corresponding to an integrated luminosity of 300 fb^{-1}. The mean value of Bjorken-x of the most energetic initiating parton is also shown for each final state.

Final state	300 fb^{-1}	$< x >$
ℓb	830k	0.295
$\ell b\bar{b}$	130k	0.368
μeb	12k	0.348
$\mu eb\bar{b}$	1.5k	0.415

final state has the highest signal yield, but suffers from the largest backgrounds, in particular from W boson production in association with a b-jet. It also cannot separate single top and top pair production, which both contribute to the final state. Measurements were also performed in the ℓbb final state [555] and μeb final state [556], which suffer from lower statistics but select the signal with a higher purity.

While current measurements in the top sector at LHCb have been statistically limited, the available dataset at the HL-LHC, where LHCb is expected to collect 300 fb-1, will permit precision measurements of the top quark pair production cross-section in the forward region, providing complementary information to ATLAS and CMS. The expected number of top pair events to be reconstructed at LHCb are given in Table 33, where the yields are obtained using next-to-leading predictions from the aMC@NLO generator interfaced with Pythia 8, with electroweak corrections are approximated as described in Ref. [557]. Leptons are required to satisfy $2.0 < \eta < 4.5$ and $p_{\rm T} > 20$ GeV, while jets are required to satisfy $2.2 < \eta < 4.2$ and $p_{\rm T} > 20$ GeV in all final states except the ℓb final state, where the $p_{\rm T}$ thereshold is raised to 60 GeV to combat the increased background. The detector efficiency is extrapolated from current measurements, where increases of between 10 and 50% are expected due to to improvements in the b-tagging algorithm and analysis techniques. Both muons and electrons are assumed to be employed for all analyses with similar efficiencies due to anticipated improvements in electron performance at LHCb during the HL-LHC. Measurements are expected to be made at sub-percent statistical precision in the ℓb final state, and at the percent level in the μeb and μebb final states. The dominant systematic uncertainties are expected to arise from the purity determination, particularly for the single lepton final states, and the knowledge of the b tagging efficiency, which are both expected to be at the level of a few percent.

As $\rm t\bar{t}$ production in the LHCb acceptance probes very large values of Bjorken-x, it has the potential to provide significant constraints on the gluon PDF in this region. The potential of the μeb final state was evaluated in Ref. [558], where reductions of 20% were found for a cross-section measurement with a precision of 4%. Even more stringent constraints can be obtained through precise differential cross-section measurements, and measurements in the μebb final state, both of which will only be possible with the data available at the HL-LHC.

6.1.5 Single top cross section: theoretical results

Although top quarks are predominantly produced in $t\bar{t}$ pairs through strong interactions, a substantial fraction of them is also produced through the exchange of electroweak bosons. In the latter case, only a single (anti-)top is produced per collision, hence one refers to these processes as "single-top" production. Despite their smaller rates w.r.t. pair production, single-top processes offer unique opportunities to study the electroweak structure of top interactions.

The purpose of this section is to summarize the state-of-the-art for the computation of single-top

production cross sections, and highlight what type of studies could be performed with an HL/HE LHC upgrade.

It is customary to categorize single-top production in the SM according to the virtuality of the W-boson involved in the leading-order $2 \to 2$ partonic process: the s-channel processes ($q\bar{q}' \to t\bar{b}$) involve the exchange of a time-like W boson, the t-channel processes $bq \to tq'$ involve the exchange of a space-like W, while associated Wt-production ($bg \to tW^-$) involves the production of a top quark in association with a W boson.

Although convenient, the above characterization suffers two theoretical issues:

- a classification in terms of underlying $2 \to 2$ processes implicitly assumes that the b-quark is treated as massless, i.e. the computations are performed in the so-called five-flavour number scheme (5FNS). This framework effectively resums large logarithms of the form $\ln m_b/Q$, where Q is a typical transverse scale of the process and as such it is particularly appropriate for observables that are only sensitive to large $p_T \gg m_b$ scales, like for example total cross sections. However, especially in the t-channel case, there are important observables which are sensitive to small transverse scales $p_T \sim m_b$ (e.g. the kinematics of the "spectator" b-jet which originates from initial state $g \to b\bar{b}$ splitting, particularly at small p_T). In this case, the 5FNS is not appropriate and it is important to treat the b-quark as massive, i.e. to work in four-flavour mass scheme (4FNS). In this scheme, the t-channel LO process becomes $2 \to 3$: $gq \to t\bar{b}q'$. The 4FNS and 5FNS are formally equivalent, but differences can arise when the perturbative expansion is truncated, and in practice these effects might be relevant for some observables [559–561]. Within this context, the advantages of a HL/HE upgrade is twofold. On the one hand, the larger dataset and increased energy would allow for more harsh selection cuts that would effectively remove regions of the phase space sensitive to small transverse scales. This would allow for a clean theoretical description using the 5FNS, which does not suffer from large logarithmic contaminations. On the other hand, it would allow one to explore with high accuracy the transition region between the range of validity of the 4FNS and 5FNS, thus providing important information on their interplay.
- once higher-order corrections are included, the distinction between s and t channels does not hold, due to interference effects. These interference effects first appear at order $\mathcal{O}(\alpha_s^2\alpha^2)$, i.e. at NNLO in the 5FNS, or at NLO in the 4FNS, and are color and (typically) kinematic suppressed. Given the large hierarchy and small kinematic overlap between t- and s- channels, interference effects are typically very small in pp collisions, but may in principle play a role if very high accuracy is required for specific observables. Moreover, once the W and top decay products are included, interferences arise also between $t\bar{t}$, single-top (with Wt-production, as well as t-channel in the 4FNS) and $WWb\bar{b}$ production, unless the narrow-width limit $\Gamma_t \to 0$ is taken. These effects can play a role for high precision studies, see e.g. [562, 563].

In spite of the above issues, as long as only NLO QCD corrections are considered, it is possible to compute well-defined cross-sections for s and t-channel in the 5FNS, and, by imposing a jet-veto on b-jets, to suppress the contamination of $t\bar{t}$ to the Wt process, thereby allowing for a sensible definition of the cross section for the latter channel as well. In table 34 we report the NLO cross sections for the 3 channels at the LHC, for centre-of-mass energies of 14 and 27 TeV. Scale and PDF uncertainties are also reported. At both energies, the t-channel is the dominant production mechanism. The relative importance of the s-channel decreases with the collider energy, while it increases for Wt associated production.

In figure 75 we also show, for the t-channel case, the cumulative cross section with a minimum $p_{T,\mathrm{min}}$ cut on the top, or antitop, transverse momentum, obtained at NLO in the 5FNS. The two horizontal bars in the plot correspond to the cross sections for which one has 100 events, by assuming an integrated luminosity of 3 ab^{-1} at 14 TeV (red) and of 15 ab^{-1} at 27 TeV (blue).

	14 TeV			27 TeV		
	σ [pb]	Δ_{μ_r,μ_f}	$\Delta_{\rm PDF}$	σ [pb]	Δ_{μ_r,μ_f}	$\Delta_{\rm PDF}$
t-channel (t)	156	$^{+3\%}_{-2.2\%}$	$\pm$ 2.3 %	447	$^{+3\%}_{-2.6\%}$	$\pm$ 2%
t-channel ($\bar{t}$)	94	$^{+3.1\%}_{-2.1\%}$	$\pm$ 3.1%	299	$^{+3.1\%}_{-2.5\%}$	$\pm$ 2.6%
s-channel (t)	6.8	$^{+2.7\%}_{-2.2\%}$	$\pm$ 1.7%	14.8	$^{+2.7\%}_{-3.2\%}$	$\pm$ 1.8%
s-channel ($\bar{t}$)	4.3	$^{+2.7\%}_{-2.2\%}$	$\pm$ 1.8%	10.4	$^{+2.7\%}_{-3.3\%}$	$\pm$ 1.8%
Wt-channel* (t or $\bar{t}$)	36	$^{+2.9\%}_{-4.4\%}$	$\pm$ 5%	137	$^{+3.8\%}_{-6.1\%}$	$\pm$ 4%

Table 34: Single-top inclusive cross sections at NLO for the LHC at 14 and 27 TeV, in the 5FNS. All results were obtained using PDF4LHC15_nlo_mc, the central value for the renormalization and factorizations scales (μ_r, μ_f) have been set equal to $m_t = 173.2$ GeV and varied by a factor of two, with the constraint $1/2 \leq \mu_r/\mu_f \leq 2$. * For Wt-channel, a jet-veto on b-jets has been used ($p_{t,b_j} < 50$ GeV), and the central value for μ_r and μ_f has been set to 50 GeV too. For these predictions, V_{tb} has been set to one.

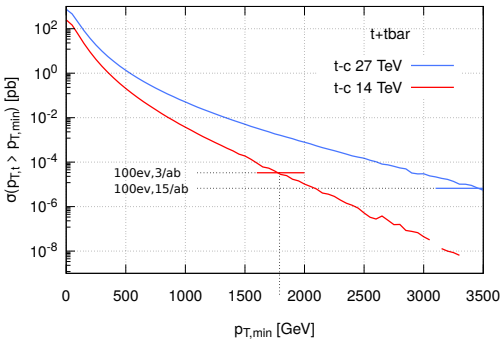

Fig. 75: Cumulative cross section for t-channel single-(anti)top production in the 5FNS at 14 and 27 TeV as a function of $p_{T,\rm min}$. The same settings used to obtain results in table 34 were used here.

For t-channel production, NNLO QCD corrections have also been computed in refs. [513, 564, 565].[18] These corrections have been obtained in the structure function approximations, where higher-order corrections to the light and heavy-quark lines ($q \to q'W$ and $b \to tW$, respectively) are computed separately. Within this approximation, the terms which are not included at NNLO are color suppressed ($1/N_c^2$), and hence estimated to be negligible for phenomenology, given the moderate size of NNLO effects. Moreover, when working in these approximations, interference effects between s and t-channel are also absent. The results obtained in refs [564, 565] indicate that NNLO QCD corrections are small: the total cross sections at NNLO increase by at most 2% with respect to the NLO result (when the latter is obtained with NLO PDFs), whereas the relative scale uncertainty is reduced by at least $\sim 50\%$. Moreover, the NNLO result is contained within the NLO uncertainty band, showing extremely good convergence for the perturbative expansion.[19] Despite the fact that the total cross section shows excellent perturbative stability, more sizeable effects can be noticed in some differential distributions, where

[18] NNLO QCD results were also obtained for s-channel, see ref. [566].

[19] When NLO corrections are computed with NNLO PDFs, the NNLO/NLO ratio is instead slightly smaller than one, but the conclusions remain the same.

NNLO/NLO corrections can reach $\mathcal{O}(10\%)$ in certain regions of the transverse momentum distributions of the top (anti-)quark and the pseudo-rapidity distributions of the leading jet. In these cases, scale variation may underestimate the actual theoretical uncertainty.

NNLO corrections to the top quark decay are also know [567, 568], and they can be combined with the NNLO correction to production using the "on-shell top-quark approximation" where the top width Γ_t is kept finite, but tree-level interference effects between the single top production and decay stage are neglected, as well as loop diagrams with a virtual gluon connecting the production and decay stages. This is an excellent approximation for inclusive-enough quantities, since omitted corrections are suppressed by a factor $\Gamma_t/m_t < 1\%$. [20] More details can be found in [513].

In presence of fiducial cuts, it is important to stress that QCD corrections are more pronounced, with NNLO effects amounting about 5% on total rates as well as differential distributions. In this case, corrections from pure decay are typically half of those from pure production. Finally, we note that NLO EW corrections to on-shell single top production are small, $\sim$ few permill, see e.g. [89]. EW effect can become more relevant in tails of distributions, or for observables highly sensitive to off-shell effects.

Single-top can also be produced in association with a Z boson (tZq). Although the cross section is smaller than in the aforementioned channels, a HL/HE upgrade at the LHC will allow one to measure well this production process too. QCD NLO corrections to tZq-production are known [570]. In table 35 we report the total cross sections at NLO in the SM, for centre-of-mass energies of 14 and 27 TeV.

	14 TeV	27 TeV
	σ [fb]	σ [fb]
tZq-channel (t)	639	2536
tZq-channel ($\bar{t}$)	350	1543

Table 35: Single-top production cross section in association with a Z boson, at NLO for the LHC at 14 and 27 TeV, in the 5FNS. All results were obtained using PDF4LHC15_nlo_mc, the renormalization and factorizations scales have been set equal to $m_t = 173.2$ GeV.

As far as phenomenology is concerned, single-top offers the possibility perform several studies within and beyond the SM. Within the "SM only" hypothesis, one can use it to extract information about the SM V_{tb} matrix element, as discussed for instance in ref. [571]. Setting constraints on the b-quark PDF might also be possible, by looking at charge ratios, i.e. ratios of $t/\bar{t}$ cross sections. These ratios depend in general upon the PDFs used, and notably, in the t-channel case, on the b-quark PDF. Moreover, they can be predicted quite accurately, as most of the theoretical uncertainties cancel out in the ratio, leaving a residual theoretical uncertainty from scale variation (at NNLO) of few percent for each PDF set, as shown for instance in fig. 29 of ref. [513]. Although the charge ratio for total cross sections $\sigma_t/\sigma_{\bar{t}}$ exhibits a dependence upon the PDF set [572,573], slightly more pronounced sensitivity might be obtained by looking at differential distributions, such as $(d\sigma/dy_t)/(d\sigma/dy_{\bar{t}})$ and $(d\sigma/dy_{\ell^+})/(d\sigma/dy_{\ell^-})$, which also allow one to constrain the u/d ratio in the proton. In figure 76 such a comparison among different PDF sets is shown, for LHC collisions at 14 and 27 TeV: differences among different PDF sets can be observed, especially at large rapidities. It is clear that a HL upgrade will allow one to reduce the statistical uncertainty at large rapidities, giving the chance to discriminate among different PDF sets. As the available phase space opens up, further sensitivity might be expected at 27 TeV.

[20] This is not the case for exclusive observables, which are sensitive to off-shell effects in the reconstructed top mass M_{Wb}, and beyond kinematic edges, see Ref. [569] for a thorough analysis.

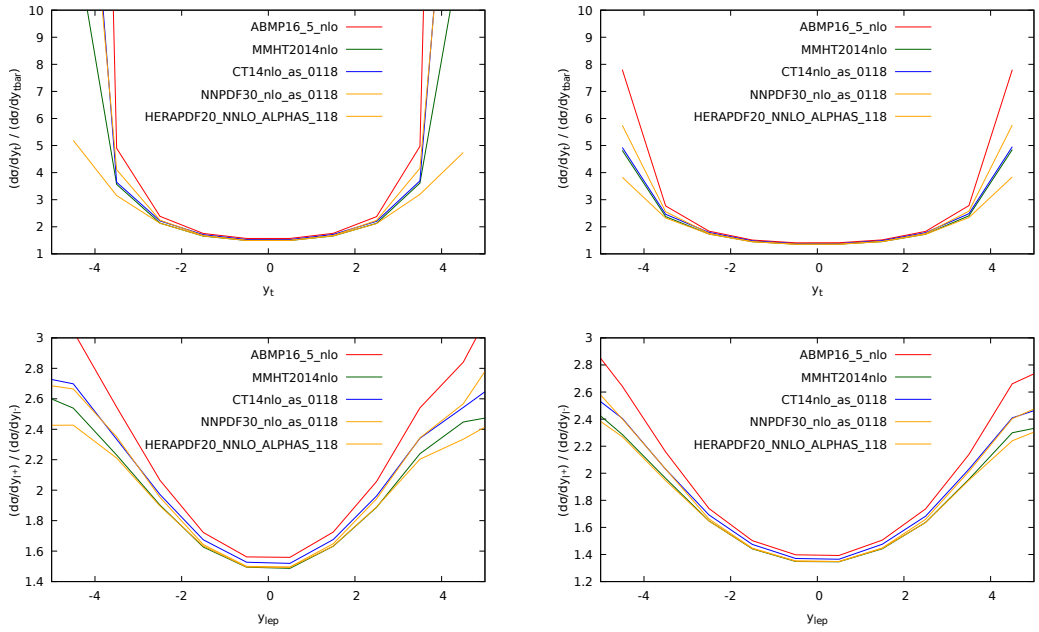

Fig. 76: Differential charge ratios $\mathcal{O}_t/\mathcal{O}_{\bar{t}}$ at 14 (left panels) and 27 (right panels) TeV for the top quark and charged lepton rapidities, in t-channel single-top production.

Single-top processes offer also several opportunities to probe some new-physics scenarios.[21] In order to systematically interpret potential deviations from the SM, it is particularly convenient to work in the SM Effective Field Theory (SMEFT) [574, 575], where the SM is augmented by a set of higher-dimension operators. If we limit the discussion to dimension-6 operators, the SMEFT Lagrangian has the form

$$\mathcal{L}_{\rm SMEFT} = \mathcal{L}_{\rm SM} + \sum_i \frac{C_i}{\Lambda^2}\mathcal{O}_i + \mathcal{O}(\Lambda^{-4}). \tag{40}$$

where the sum runs over all the dimension-6 operators that maintain the SM symmetries. The remarkable virtue of t-channel single-top production is that its cross section only depends upon a limited number of dimension-6 operators, thereby allowing to set bounds on them relatively easily. At LO and in the 5FNS only three operators contribute:

$$\mathcal{O}_{tW} = i\big(\bar{Q}\sigma^{\mu\nu}\,\tau_I\,t\big)\,\tilde{\phi}\,W^I_{\mu\nu} + \text{h.c.}\,, \tag{41}$$

$$\mathcal{O}^{(3)}_{\phi q} = i\big(\phi^\dagger \overleftrightarrow{D}_\mu \tau_I \phi\big)\big(\bar{q}_i\,\gamma^\mu\,\tau^I q_i\big) + \text{h.c.}\,, \tag{42}$$

$$\mathcal{O}^{(3,1)}_{Qq} = \big(\bar{q}_i\,\gamma_\mu\,\tau_I q_i\big)\big(\bar{Q}\,\gamma^\mu\,\tau^I Q\big)\,, \tag{43}$$

in agreement with the notation of [192]. The operators of eq. (41)-(42) modify the Wtb interaction in the following way

$$\begin{aligned}\mathcal{L}^{\rm dim-6}_{Wtb} &= -\frac{g}{\sqrt{2}}\bar{b}(x)\gamma^\mu P_L t(x)\,W_\mu(x)\left(1+\frac{C^{(3)}_{\varphi Q}v^2}{\Lambda^2}\right)\\ &+ \frac{2\,v\,C_{tW}}{\Lambda^2}\bar{b}(x)\sigma^{\mu\nu}P_R t(x)\,\partial_\nu W_\mu(x) + \text{h. c.}\,,\end{aligned} \tag{44}$$

[21] In the following we limit our discussion to the t-channel case, and the production in association with a Z boson.

where $v = 246$ GeV is the Higgs doublet vacuum expectation value, and y_t the top quark Yukawa coupling. Here and below we assume $V_{tb} = 1$. Note that the four-fermion operator of eq. (43) introduces a contact $udtb$ interaction. From eq. (44) it is clear that setting bounds on the SMEFT using single-top measurements allows to probe in detail the structure of the Wtb coupling. A comprehensive discussion can be found in [221], where a NLO study of the effect of these operators on total and differential distributions in single top production and decay is performed.

In the SMEFT, the single top cross section can be parametrised as

$$\sigma = \sigma_{SM} + \sum_i \frac{1\text{TeV}^2}{\Lambda^2} C_i \sigma_i + \sum_{i \leq j} \frac{1\text{TeV}^4}{\Lambda^4} C_i C_j \sigma_{ij}. \tag{45}$$

To establish the impact of the operators on single top production at HL/HE LHC, we show in table 36 the ratio $r_i = \sigma_i/\sigma_{SM}$ for 14 TeV and 27 TeV both for the inclusive cross section and the high transverse momentum region. Results are obtained in the 5FNS with NNPDF3.0 LO PDFs [159]. Central scales for μ_R, μ_F are chosen as m_t. We find that the impact of the operator in eq. (42) remains unchanged when going from 14 to 27 TeV, as its effect is to only rescale the SM coupling. The impact of the dipole operator (41) is only mildly affected by going to the HE-LHC, whereas the sensitivity to the four-fermion operator is the one which benefits most by probing the high p_T tail and by the HE-LHC.

	t-channel 14 TeV		t-channel 27 TeV	
		($p_T^t > 350$ GeV)		($p_T^t > 350$ GeV)
σ_{SM}	225 pb	0.746 pb	640 pb	3.40 pb
r_{tW}	0.025	0.052	0.022	0.040
$r_{tW,tW}$	0.014	0.31	0.016	0.34
$r_{\phi Q^{(3)}}$	0.12	0.12	0.12	0.12
$r_{\phi Q^{(3)},\phi Q^{(3)}}$	0.0037	0.0037	0.0037	0.0037
$r_{Qq^{(3,1)}}$	-0.36	-6.45	-0.39	-6.79
$r_{Qq^{(3,1)},Qq^{(3,1)}}$	0.135	18.8	0.222	26.8

Table 36: Comparison among the LO sensitivities of $t-$ channel single-top to the three operators described in eq. (41)-(43), for the inclusive cross-section and with a cut $p_T^t > 350$ GeV, at 14 and 27 TeV. Results are obtained in the 5FNS with NNPDF3.0 LO PDFs [159], the renormalization and factorizations scales have been set equal to $m_t = 173.2$ GeV. The interference term $r_i = \sigma_i/\sigma_{SM}$ (when non-zero) and the square $r_{i,i} = \sigma_{i,i}/\sigma_{SM}$ are given for each operator. σ_i and $\sigma_{i,i}$ are defined in eq. (45).

Production in association with a Z boson is also important in the BSM context. A complete study of its sensitivity to BSM effects was performed in ref. [220], where the interplay with t-channel single-top, as well as single-top production in association with a Higgs boson, is discussed thoroughly, and at NLO. Table 6 of [220] reports a comparison among the sensitivity of these processes to various operators. Current limits from other processes, as well as current and future projections for bounds that can be achieved looking into tZj production are also discussed (e.g. in fig. 6 of [220]). For some operators, notably $\mathcal{O}_{tW}$ and $\mathcal{O}_{\phi q}^{(3)}$, the improvement due to considering tZj measurements at HL are remarkable, especially when tails of distributions are considered. It is likely that even more promising results could be obtained at HE.

Another goal of a HL/HE upgrade is to extract bounds on (or find evidence of) WWZ anomalous gauge couplings, or FCNC. In this context, tZq is quite important both because it is sensitive to these effects, as well as because it's an irreducible background, as its production rate is competitive with $t\bar{t}Z$ production, where these effects are typically looked for.

6.2 Four top production at the HL/HE LHC

The production of four top quarks is one of the rare processes in top quark physics that has large sensitivity to variety of new physics effects (including effective field theory sensitivity and sensitivity to anomalous top-Higgs couplings), while at the same time it is interesting in the Standard Model context as a complex QCD process. The cross section is about one order of magnitude smaller than $t\bar{t}\gamma$ production, with multiple precision calculations predicting values of $\sigma_{t\bar{t}t\bar{t}} = 9.2^{+2.9}_{-2.4}$fb (NLO) and $\sigma_{t\bar{t}t\bar{t}} = 11.97^{+2.15}_{-2.51}$fb (NLO+EWK) [12, 115, 576].

ATLAS and CMS have published multiple papers where limits on $t\bar{t}t\bar{t}$ production were presented as SM-oriented searches [577–579] and/or derived as a side product of searches for new physics, typically coming from searches for vector-like quarks or MSSM SUSY signatures [580–584].

The production of $t\bar{t}t\bar{t}$ is a rare standard Model (SM) process that is expected to be discovered by future LHC runs, including HL-LHC and HE-LHC. The increase in collision energy is important for $t\bar{t}t\bar{t}$ production because the cross section is largely induced by gluons in the inital state, leading to a substantial improvement in the signal-to-background ratio when the collision energy of the LHC is increased. Analyses looking for the production of $t\bar{t}t\bar{t}$ also are well-suited for interpretation in SMEFT [192].

The $t\bar{t}t\bar{t}$ process has not yet been observed at the LHC. Once closer to observation, and considering the sensitivity of $t\bar{t}t\bar{t}$ production to new physics scenarios in the top quark and scalar section, it is prudent to instead consider how accurately the cross section can be measured with the analyses. Of course in the future analysis techniques are also expected to improve, and dedicated analyses will surely improve this sensitivity, but this is beyond the scope of this study. It is however important to keep in mind that such a sensitivity study is less sensitive to systematic uncertainties on the background determination, while being more sensitive to the signal modelling uncertainties and overall branching fraction and acceptance of the selection.

6.2.1 State-of-the art predictions in the SM: the complete NLO corrections

In this section we compute the so-called "complete"-NLO corrections to four-top production at the HE and HL LHC. Four-top production can proceed through different terms of order $\alpha_s^p\alpha^q$ with $p+q = 4,\ 5$ at LO and at NLO respectively. The term complete-NLO refers to computation of all terms with $p + q \leq 5$, which has been performed for the first time in Ref. [115] by employing the newely-released version of `MadGraph5_aMC@NLO` [12] capable of computing mixed QCD and Electroweak corrections [89]. Among the various contributions, the NLO QCD corrections ($p = 5$, $q = 0$) are also included, which have been known for some years [576, 585]. Despite that power-counting arguments suggest that the larger q the more suppressed a contribution is, it has been shown in Ref. [115] that this is not the case for $t\bar{t}t\bar{t}$ production. In fact, terms with up to two powers of α still contribute to several 10%s with respect to the $\mathcal{O}(\alpha_s^4)$ LO contribution. One of the reasons why this happens is because of the large Higgs-top Yukawa coupling; furthermore, important cancelations appear among these terms, which may be spoiled by non-SM effects.

In this short paragraph we report inclusive predictions for the HL and HE LHC, with a centre-of-mass energy of respectively 14 TeV and 27 TeV. For differential distributions, the qualitative and quantitative behaviour is very similar to the predictions at 13 TeV reported in Ref. [115] **We may add some if there is space**. We use the same setup and notation of Ref. [115], where the interested reader can find more details as well as predictions for 13 and 100 TeV.

We report in Tab. 37 the total-cross section for $t\bar{t}t\bar{t}$ production in different approximations, and in Tab. 38 the breakdown of the different orders contributing at LO and NLO, as fraction of the $\mathcal{O}(\alpha_s^4)$ LO contribution, LO_1. We observe that the pattern of relative corrections is rather similar between 14 and 27 TeV. In particular, besides NLO_1 which is entirely of QCD origin, and thus displays a strong

Table 37: Cross section for four-top production at the HL and HE LHC, in various approximations. See Ref. [115] for details.

σ[fb]		LO_{QCD}	$\text{LO}_{\text{QCD}} + \text{NLO}_{\text{QCD}}$	LO	LO + NLO	$\frac{\text{LO(+NLO)}}{\text{LO}_{\text{QCD}}\text{(+NLO}_{\text{QCD}})}$
$H_T/4$	14 TeV	$9.04^{+69\%}_{-38\%}$	$14.72^{+19\%}_{-23\%}$	$10.04^{+63\%}_{-35\%}$	$15.83^{+18\%}_{-21\%}$	1.11 (1.08)
	27 TeV	$81.87^{+62\%}_{-36\%}$	$135.19^{+19\%}_{-21\%}$	$91.10^{+56\%}_{-33\%}$	$143.93^{+17\%}_{-20\%}$	1.11 (1.06)

Table 38: $t\bar{t}t\bar{t}$: $\sigma_{\text{(N)LO}_i}/\sigma_{\text{LO}_{\text{QCD}}}$ ratios at 14 and 27 TeV, for different values of $\mu = \mu_r = \mu_f$. See Ref. [115] for details.

δ[%]	14 TeV			27 TeV		
	$\mu = H_T/8$	$\mu = H_T/4$	$\mu = H_T/2$	$\mu = H_T/8$	$\mu = H_T/4$	$\mu = H_T/2$
LO_2	-25.8	-28.1	-30.4	-23.6	-25.9	-28.2
LO_3	32.5	38.9	45.8	30.7	37.0	43.8
LO_4	0.2	0.3	0.4	0.1	0.2	0.2
LO_5	0.0	0.0	0.1	0.0	0.0	0.1
NLO_1	14.7	62.9	103.3	21.7	65.1	101.9
NLO_2	8.1	-3.5	-15.1	5.0	-4.4	-13.9
NLO_3	-10.0	1.8	15.8	-7.8	1.6	13.2
NLO_4	2.2	2.7	3.4	1.6	2.0	2.4
NLO_5	0.1	0.2	0.2	0.1	0.2	0.2
NLO_6	< 0.1	< 0.1	< 0.1	< 0.1	< 0.1	< 0.1
$\text{NLO}_2 + \text{NLO}_3$	-1.9	-1.7	0.7	-2.8	-2.8	-0.7

dependence on the renormalisation and factorisation scales, such a feature is present also for NLO_2 and NLO_3, which witnesses the fact that they receive an important contribution through QCD corrections from LO_2 and LO_3 respectively, on top of the electroweak corrections from LO_1 and LO_2. Furthermore, NLO_2 and NLO_3 tend to cancel each other almost exactly, leading to a complete-NLO prediction well within the uncertainty band of the one at NLO QCD accuracy. Such a feature may be spoiled by effects beyond the Standard Model, such as anomalous Higgs-top couplings. Thus, NLO corrections cannot be neglected when similar studies are performed, such as those presented in Sect. 6.3.2.

6.2.2 Plans for experimental measurements

6.2.2.1 ATLAS **To be updated**

ATLAS has studied the potential to measure the Standard Model $t\bar{t}t\bar{t}$ cross section using 3000 fb^{-1} of HL-LHC data in the channel with several leptons [**?**]. Events are selected if they contain at least two isolated leptons with the same charge or at least three isolated leptons. At least five jets among which at least two are b-tagged are required. In addition the scalar sum of the p_T of all selected jets and leptons (H_T) is requested to be $H_T > 500$ GeV and the missing transverse momentum $MET > 40$ GeV. In order to extract the measured $t\bar{t}t\bar{t}$ cross section a fit is performed to the H_T distributions in several signal regions according to the jets and b-jets multiplicities: at least 6 jets and exactly 2 b-jets, or at least 5 jets and exactly 3 b-jets, or at least 6 jets and at least 4 b jets. These regions are further split in events with two same sign leptons or with at least three leptons leading to 6 signal regions.

The background arises from $t\bar{t}V$, multiboson and $t\bar{t}H$ events as well as events with fake or non

prompt leptons. The rate of this difficult instrumental background is computed from the ATLAS 36 fb^{-1} analysis [584] in the relevant regions with different lepton and b-tagged jet multiplicities. The number of events selected in the different signal regions are shown in Figure 77.

The main sources of systematic uncertainties taken into account come from uncertainties on the fake lepton background and on the SM background and signal normalisations. A maximum-likelihood fit is performed simultaneously in the six signal regions to extract the $t\bar{t}t\bar{t}$ signal cross section normalised to the prediction from the SM. The impact of systematic uncertainties on the background expectations is described by nuisance parameters. As a result of the fit, the expected uncertainty on the measured $t\bar{t}t\bar{t}$ cross section is found to be XX%. The systematic uncertainty that impacts the precision the most is .... Overall the impact of the systematic uncertainties remain limited as a fit without systematic uncertainties leads to a precision of XX% on the extracted $t\bar{t}t\bar{t}$ cross section.

Fig. 77: Number of selected events in the different signal regions considered in the ATLAS analysis [**?**].

6.2.2.2 CMS

The most sensitive result of the CMS collaboration on the Standard Model $t\bar{t}t\bar{t}$ process [577] is based on an integrated luminosity of 35.9 fb^{-1}and a center of mass energy of 13 TeV, and relies on events with 2 same-sign leptons or 3 or more leptons. This Run 2 analysis sets an expected 95% CL upper limit on the $t\bar{t}t\bar{t}$ production cross section of $20.8^{+11.2}_{-6.9}$ fb, and an expected significance (based on a cross section of 9.2 fb) of 1.0 standard deviations above the background-only hypothesis.

The result of Ref. [577] is used to derive extrapolations for HL and HE-LHC, which are described in Ref. [586] and summarized below. The extrapolations rely on a simple rescaling of the signal and background cross sections, and make different assumptions on the systematic uncertainties. First the statistical uncertainties (*Stat. only*) are considered, then the same systematic uncertainties as the published result are used (*Run 2*), and finally these systematics are progressively reduced as a function of the integrated luminosity (*YR18*, *YR18+*).

The expected sensitivity on the $t\bar{t}t\bar{t}$ cross section for different HL and HE-LHC scenarios is listed in Tab. 39. Based on these results, evidence for $t\bar{t}t\bar{t}$ production will become possible with around 300 fb^{-1} of HL-LHC data at $\sqrt{s} = 14$ TeV, at which point the statistical uncertainty on the measured cross section will be of the order of 30% and the measurement will have a total uncertainty of around 33-43%, depending on the systematic uncertainty scenario considered. For larger datasets at HL-LHC, all scenarios considered become dominated by systematic uncertainties. With 3 ab^{-1} the cross section can be constrained to 9% statistical uncertainty, and the total uncertainty of a measurement ranges between 18% and 28% depending on the considered systematic uncertainties. At HE-LHC the $t\bar{t}t\bar{t}$ cross section is expected to be constrained to within a 1-2% statistical uncertainty, and the systematic uncertainties also decrease due to the improved signal to background ratio at $\sqrt{s} = 27$ TeV. Future changes to the analysis strategy might allow improvements based on optimizing the interplay between statistical and systematic uncertainties.

The $t\bar{t}t\bar{t}$ cross section measurements can also be used to constrain the Wilson coefficients of the $\mathcal{O}_R$, $\mathcal{O}_L^{(1)}$, $\mathcal{O}_B^{(1)}$ and $\mathcal{O}_B^{(8)}$ dimension-6 operators of the Effective-Field-Theory (EFT) Lagrangian. These constraints are included in Ref. [587] for both HL-LHC and HE-LHC scenarios.

6.3 Four top quarks as a probe of new physics

6.3.1 Limits on pseudoscalar colour-octets

Heavy coloured resonances decaying into a pair of top quarks are present in many new physics theories [588–592]. Such particles are typically pair-produced at large rate and their decay then leads to a

Table 39: Expected sensitivity for the production cross section of $t\bar{t}t\bar{t}$ production, in percent, at 68% confidence level. The fractional uncertainty on the cross section signal strength is given for various LHC upgrade scenarios. Cross sections are corrected for the changes expected by $\sqrt{s}$. For the 15 ab^{-1} 27 TeV scenario, the systematic uncertainty extrapolation is no longer valid, so only the statistical uncertainty is provided.

Int. Luminosity	$\sqrt{s}$	*Stat. only* (%)	*Run 2* (%)	*YR18* (%)	*YR18+* (%)
300 fb^{-1}	14 TeV	$+30, -28$	$+43, -39$	$+36, -34$	$+36, -33$
3 ab^{-1}	14 TeV	± 9	$+28, -24$	$+20, -19$	± 18
3 ab^{-1}	27 TeV	± 2	$+15, -12$	$+9, -8$	$+8, -7$
15 ab^{-1}	27 TeV	± 1			

substantial enhancement of four-top production. Current bounds on such a setup are driven by a recent CMS analysis of four-top events [577], using 35.9 fb^{-1} of LHC collisions at a centre-of-mass energy of 13 TeV. Those bounds should however strongly improve in the upcoming years, as illustrated in this contribution with the example of a scalar colour-octet field O, traditionally dubbed a sgluon. The effective Lagrangian describing the couplings of such a sgluon to the Standard model is given by [593]

$$\mathcal{L} \supset g_8 d_{abc} O^a G^b_{\mu\nu} G^{\mu\nu c} + \tilde{g}_8 d_{abc} O^a G^b_{\mu\nu} \tilde{G}^{\mu\nu c} + \left\{ \bar{q} \left[\mathbf{y_8^L} P_L + \mathbf{y_8^R} P_R \right] O^a T_a q + \text{h.c.} \right\} , \qquad (46)$$

where T^a and d_{abc} are respectively the fundamental representation matrices and symmetric structure constants of $SU(3)$. Moreover, flavour and fundamental colour indices are understood for simplicity and we denote the gluon field strength (dual field strength) tensor by $G^a_{\mu\nu}$ ($\tilde{G}^a_{\mu\nu}$). We focus on the case of a pseudoscalar sgluon with $g_8 = 0$ and purely imaginary $\mathbf{y_8}$ matrices, and additionally enforce $\tilde{g}_8 = 0$ as in Dirac gaugino supersymmetric scenarios. A non-vanishing $\tilde{g}_8$ coupling would however weaken the bounds by reducing the sgluon branching ratio into top quarks. In order to assess the impact of future search on the potential discovery of a sgluon, we follow the recasting strategy detailed in Ref. [594]. We generate an NLO UFO module [595] through FEYNRULES [596], NLOCT [597] and FEYNARTS [598] and use it to generate events within the MADGRAPH5_aMC@NLO framework [12], the hard-scattering matrix elements being convolved with the NNPDF3.0 NLO set of parton densities [159] and the sgluon decays being achieved with MADSPIN [364] and MADWIDTH [599]. Parton showering and hadronisation are performed by PYTHIA 8 [324] and we simulate the response of the CMS detector with DELPHES 3 [232] and FASTJET [303]. Finally, we mimic the four-top selection strategy of CMS [577] by using the MADANALYSIS 5 [600–602] framework.

The best signal region (SR6) from Ref. [577], in terms of constraints, focuses on a topology featuring one pair of same-sign leptons, at least 4 b-jets and at least 5 hard jets. We show the observed and expected limits on the pseudoscalar octet cross section times the corresponding branching ration into four top quarks in Fig. 78 (left). While the analysis of Ref. [577] targeted a Standard Model four-top signal, future studies adopting a new physics signal selection strategy relying on the large differences in the final-state kinematics could be more adapted and lead to sizeable improvement in the reach [594].

To calculate the projected sensitivity of the HL/HE LHC, we assume that the current selection efficiencies at 13 TeV are similar to the future ones, and moreover rescale the four-top and other SM backgrounds by the appropriate partonic luminosities relative to those at 13 TeV. The rescaling factor for the non-four-top SM background is taken to be the largest ratio of the ttZ and ttW background component, using the projected cross-sections from elsewhere in this report **ADD reference to ttW/Z sections**. We obtain factors of 1.3 and 12 for the 14 and 27 TeV cases, respectively. According to Sect. 6.2.1, the four-top cross section is then set to 15.83 fb and 144 fb at 14 and 27 TeV, respectively, recalling that the 13 TeV cross section is of 11.97 fb. The results for the projected mass limits are then given in the following Table 40, together with the 13 TeV value for reference.

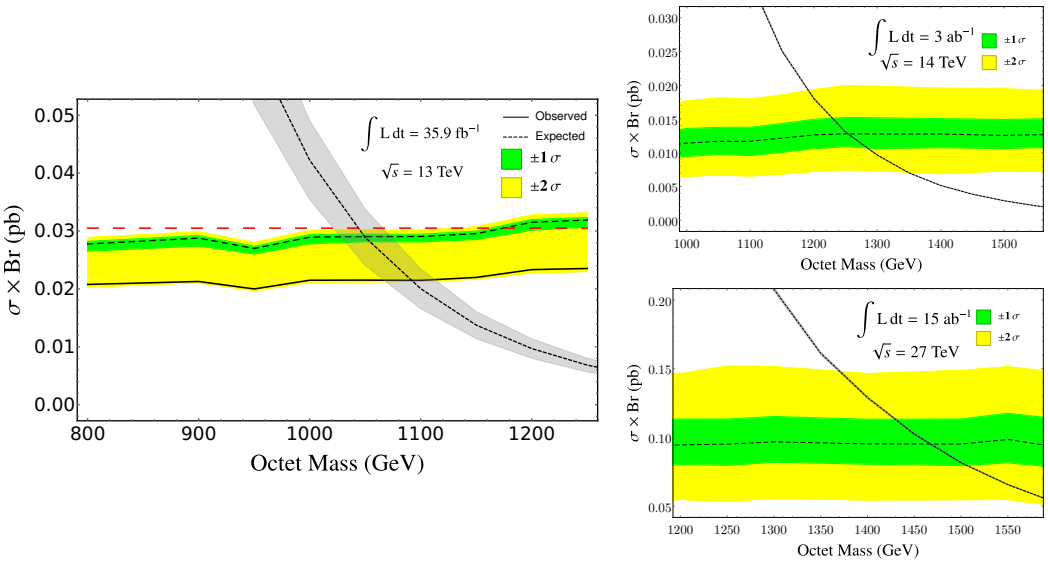

Fig. 78: Left: Expected (dashed) and observed (solid) pseudoscalar sgluon pair-production cross section excluded at the 95% confidence level when making use of the results associated with the SR6 region of the four-top CMS analysis of Ref. [577]. Theoretical predictions for the signal rate are indicated by the grey band. Right: expected limits for proton-proton collisions at centre-of-mass energies of 14 (top) and 27 (bottom) TeV, with the sgluon cross-section as the fine dotted line.

Table 40: Results for the projected mass limits on pseudo-scalar color octets.

	$35.9\,\text{fb}^{-1}$ @ 13 TeV	$3\,\text{ab}^{-1}$ @ 14 TeV	$15\,\text{ab}^{-1}$ @ 27 TeV
Octet mass (GeV)	1060	1260	1470

6.3.2 Limits on top-Higgs interaction from multi-top final state

Four top-quark ($t\bar{t}t\bar{t}$) production provides a powerful tool to probe the Top-quark Yukawa coupling (y_t) [603]. In the SM the $t\bar{t}t\bar{t}$ production can be induced either by the pure gauge interaction (involving the gluon, Z-boson or photon in the intermediate state) [604] or by the Higgs boson mediation [603]. Defining the general top-Higgs coupling as $y_t \equiv \kappa_t y_t^{\text{SM}}$ with y_t^{SM} the top-Yukawa coupling in the SM, the leading-order cross section of $t\bar{t}t\bar{t}$ production can be parameterized as

$$\sigma(t\bar{t}t\bar{t}) = \sigma(t\bar{t}t\bar{t})^{\text{SM}}_{g/Z/\gamma} + \kappa_t^2\sigma(t\bar{t}t\bar{t})^{\text{SM}}_{\text{int}} + \kappa_t^4\sigma(t\bar{t}t\bar{t})^{\text{SM}}_{H}, \tag{47}$$

where $\sigma(t\bar{t}t\bar{t})^{\text{SM}}_{g/Z,\gamma,\ H,\ \text{int}}$ denotes the cross section induced by the pure gauge interaction, Higgs-boson mediation and the interfere effect, respectively. Note that $\sigma^{\text{SM}}_{H,\text{int}}$ is comparable to $\sigma(t\bar{t}t\bar{t})^{\text{SM}}_{g/Z,\gamma}$ as $y_t^{\text{SM}} \sim 1$ in the SM. For example, the leading order calculation with the renormalization/factorization scale (μ) fixed to the dynamics scale [12] yields

$$\begin{aligned} \text{HL}-\text{LHC}\ (\sqrt{s} = 14\ \text{TeV}) \quad &: \quad \sigma(t\bar{t}t\bar{t}) = \ 13.14 - \ \ 2.01\kappa_t^2 + \ 1.52\kappa_t^4\ \ [\text{fb}] \\ \text{HE}-\text{LHC}\ (\sqrt{s} = 27\ \text{TeV}) \quad &: \quad \sigma(t\bar{t}t\bar{t}) = 115.10 - 15.57\kappa_t^2 + 11.73\kappa_t^4\ \ [\text{fb}] \end{aligned} \tag{48}$$

Clearly, $\sigma(t\bar{t}t\bar{t})$ depends only on κ_t such that it directly probes y_t without any assumption on Higgs boson. The above values suffer from a large μ dependence; when varying the scale by a factor 2, the cross section varies by about 50%. It is crucial to take the full next-to-leading order corrections [115,576] into account to get a realistic simulation. Here, we generate the tree level events and rescale the cross section to the NLO.

A special signature of the $t\bar{t}t\bar{t}$ events is the same-sign charged leptons (SSL) from the two same-sign top quarks. The other two top quarks are demanded to decay hadronically to maximize the event rate. Therefore, the topology of the signal event consists of two same-sign charged leptons, four b-quarks, four light-flavor quarks, and two invisible neutrinos. In practice it is challenging to identify four b-jets. Instead, we demand at least 5 (6) jets are tagged and three of them are identified as b-jets at the HL(HE)-LHC, respectively. The two invisible neutrinos appear as a missing transverse momentum ($\not{E}_T$) in the detector. The SM backgrounds contain $t\bar{t}+X$, $W^{\pm}W^{\pm}jj$ and $W^{\pm}W^{\pm}jj$ processes. See Ref. [603] for the details of those kinematic cuts used to disentangle the $t\bar{t}t\bar{t}$ signal from the huge backgrounds. We demand $\not{E}_T > 100$ GeV at the HL-LHC and $\not{E}_T > 150$ GeV at the HE-LHC. Table 41 displays the numbers of signal and background events after applying the kinematics cuts listed in each row sequentially. In Table 41, at the HL-LHC the $t\bar{t}t\bar{t}$ production cross section is multiplied by a constant K-factor of 1.27 with uncertainty 27% (see [576]), while at the HE-LHC the cross section is rescaled to NLO order of $143.93^{+17\%}_{-20\%}$ fb (see Tab. 37 in Sect. 6.2.1).

The MC simulation shows that the $t\bar{t}t\bar{t}$ production ($\kappa_t = 1$) can be discovery at a 5σ confidence level with an integrated luminosity of 2075 fb^{-1} at the HL-LHC and 146 (72, 216) fb^{-1} at the HE-LHC, respectively. The event rate is not enough for measuring y_t precisely at the HL/HE-LHC but it is good for bounding y_t; for example, we obtain a direct bound $\kappa_t \leq 1.41$ $[1.37, 1.47]$ at the HL-LHC and $\kappa_t \leq 1.15$ $[1.12, 1.17]$ (1.12 $[1.10, 1.13]$, 1.10 $[1.08, 1.12]$) with an luminosity of 10 (20, 30) ab^{-1} at the HE-LHC, respectively.

We conclude with a word of care on the interpretation of results from our study: as it has been discussed in Sect. 6.2.1, the complete-NLO corrections to $t\bar{t}t\bar{t}$ are large and can involve terms proportional to y_t^3, y_t^5 and y_t^6 (on top of y_t^2 and y_t^4 already present at LO). However, since in such corrections y_t is renormalised, an extension of our study will not be immediately possible at NLO.

Table 41: The numbers of signal and background events at the HL-LHC with an integrated luminosity of 300 fb^{-1} (left) and at the HE-LHC with an integrated luminosity of 1 ab^{-1}. The cuts listed in the row are applied sequentially [603].

HL-LHC	Basic	SSL	Jets	$\not{E}_T$	m_T	H_T
$t\bar{t}t\bar{t}_H$	577.22	9.82	4.68	2.43	1.33	1.21
$t\bar{t}t\bar{t}_{g/Z/\gamma}$	5006.34	78.15	37.02	19.25	11.09	10.16
$t\bar{t}t\bar{t}_{\text{int}}$	-764.67	-12.79	-6.19	-3.23	-1.93	-1.77
$t\bar{t}$	2.5×10^8	28802.4	44.1	18.9	0	0
$t\bar{t}W^+$	32670	2359.5	36.9	17.7	12.3	8.7
$t\bar{t}W^-$	16758	1397.1	49.5	9.9	4.5	4.5
$t\bar{t}Z$	24516	2309.4	20.1	10.8	10.8	9.3
$W^{\pm}W^{\pm}jj$	4187.7	1147.5	0.11	0	0	0

HE-LHC	Basic	SSL	Jets	$\not{E}_T$	m_T	H_T
$t\bar{t}t\bar{t}_H$	15174.4	260.09	84.61	27.92	15.42	15.17
$t\bar{t}t\bar{t}_{g/Z/\gamma}$	148898.	2421.08	814.77	268.02	168.55	166.77
$t\bar{t}t\bar{t}_{\text{int}}$	-20141.9	-347.81	-117.95	-36.17	-20.14	-19.66
$t\bar{t}$	3.3×10^7	130207	291.9	0	0	0
$t\bar{t}W^+$	1.3×10^6	11488.5	171.0	39.6	27.1	27.1
$t\bar{t}W^-$	7.6×10^5	7387.1	99.5	19.9	9.9	9.9
$t\bar{t}Z$	3.9×10^6	20748.7	507.2	129.7	70.8	70.8
$W^{\pm}W^{\pm}jj$	888700	7947.0	4.7	3.5	0	0

6.3.3 *Constraining four-fermion operators in the EFT*

The four-top total cross section measurement can be interpreted within the SMEFT framework [605]. Following the notation in Refs. [605] and [192], the relevant operators consist of four independent four-top-quark operator coefficients, $\tilde{C}_{\mathrm{tt}}$, $\tilde{C}^{(+)}_{\mathrm{QQ}}$, $\tilde{C}^{(1)}_{\mathrm{Qt}}$, $\tilde{C}^{(8)}_{\mathrm{Qt}}$, and fourteen independent two-light-two-top-quark ($qqtt$) operator coefficients, $\tilde{C}^{(8)}_{\mathrm{td}}$, $\tilde{C}^{(1)}_{\mathrm{td}}$, $\tilde{C}^{(8)}_{\mathrm{Qd}}$, $\tilde{C}^{(1)}_{\mathrm{Qd}}$, $\tilde{C}^{(8)}_{\mathrm{tu}}$, $\tilde{C}^{(1)}_{\mathrm{tu}}$, $\tilde{C}^{(8)}_{\mathrm{Qu}}$, $\tilde{C}^{(1)}_{\mathrm{Qu}}$, $\tilde{C}^{(8,1)}_{\mathrm{Qq}}$, $\tilde{C}^{(1,1)}_{\mathrm{Qq}}$, $\tilde{C}^{(8,3)}_{\mathrm{Qq}}$, $\tilde{C}^{(1,3)}_{\mathrm{Qq}}$, $\tilde{C}^{(8)}_{\mathrm{tq}}$, $\tilde{C}^{(1)}_{\mathrm{tq}}$. Here $\tilde{C}_i \equiv C_i/\Lambda^2$. O_{tG} is relevant but better constrained by other processes.

To estimate the projected limits on these coefficients, we make a few simple assumptions: 1) the effective operators do not significantly change the distribution of events, so the sensitivity mainly comes from inclusive measurements; 2) a kinematic cut M_{cut} of a few TeV can be applied to the total mass of the four tops to make sure the SMEFT can be matched to BSM models with scales larger than this energy (i.e. following Ref. [606]); and 3) M_{cut} does not significantly change the projected sensitivity on cross section measurements. By combining the expected experimental sensitivity discussed in Sect. 6.2.2 and the theoretical predictions presented in Sect. 6.2.1 we estimate that the total cross section can be determined with an uncertainty of 102%, 58%, and 40%, at 95% CL level, for the 13, 14 and 27 TeV runs respectively. The corresponding integrated luminosities are 300 fb^{-1}, 3 ab^{-1} and 15 ab^{-1}.

For illustration, in Figure 79 we show the signal strength dependence on two operator coefficients: one four-top coefficient (left) and one $qqtt$ coefficient (right), assuming a 3 TeV M_{cut}. The cross section becomes more sensitive to the four-top operator coefficient at larger energies. Together with smaller uncertainties, the limit on this coefficient is significantly improved with the 27 TeV run. On the other hand, the cross section becomes less sensitive to the $qqtt$ operator coefficient as the energy increases. The limits are thus not very much affected by energy. In Table 42 we present individual limits on all 18 operator coefficients, assuming $M_{cut} = 3$ TeV.

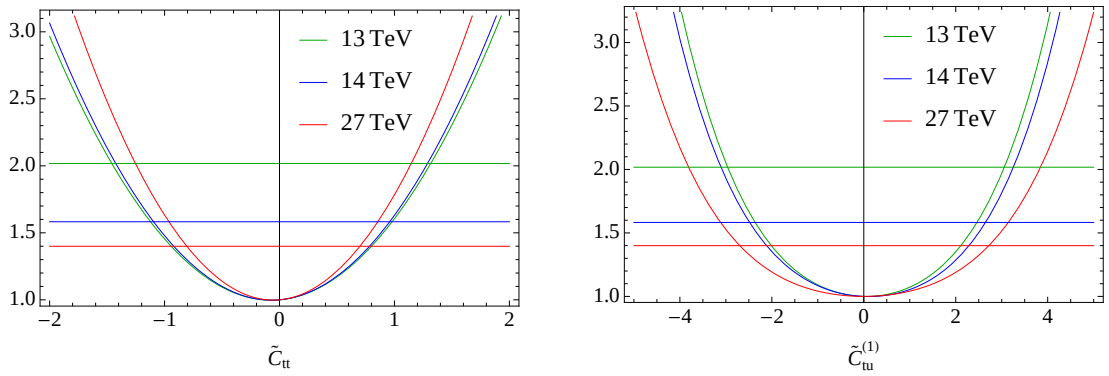

Fig. 79: Four-top signal strength as a function of operator coefficients, $\tilde{C}_{tt}$ (left) and $\tilde{C}^{(1)}_{tu}$ (right). Horizontal lines represent the expected measurements at each energy. $M_{cut} = 3$ TeV is applied.

6.3.4 *Accessing top quark flavour violating effects and dipole moment through multi-top production*

In this paragraph, we study the sensitivity of the four top quark production on the strong dipole moments of the top quark [607]. Within the SM framework, the top quark dipole moments are zero at tree level, however, higher-order corrections could generate non-zero strong dipole moments for the top quark. The top quark strong dipole moments have very small values in the SM, so that they would not be observable at the LHC experiments. However, there are extensions of the SM in which sizable contributions to these dipole moments arise, making them accessible by the experiments at the LHC [608, 609]. As a result, observation of any significant deviation of dipole moments from zero would point to beyond the SM physics. The most general effective Lagrangian describing the $gt\bar{t}$ coupling considering dimension-6

	13 TeV	14 TeV	27 TeV
$\tilde{C}_{\rm td}^{(8)}$	[-9.8, 6.4]	[-8.8, 5.4]	[-6.6, 5.4]
$\tilde{C}_{\rm td}^{(1)}$	[-3.9, 4.1]	[-3.3, 3.4]	[-3.3, 3.3]
$\tilde{C}_{\rm Qd}^{(8)}$	[-9.6, 6.2]	[-8.8, 5.2]	[-7.6, 5.2]
$\tilde{C}_{\rm Qd}^{(1)}$	[-4., 4.]	[-3.3, 3.3]	[-3.4, 3.3]
$\tilde{C}_{\rm tu}^{(8)}$	[-8.2, 4.8]	[-6.4, 4.3]	[-9.6, 4.5]
$\tilde{C}_{\rm tu}^{(1)}$	[-3., 3.1]	[-2.5, 2.6]	[-2.7, 2.7]
$\tilde{C}_{\rm Qu}^{(8)}$	[-7.8, 4.6]	[-7.8, 4.]	[-5.8, 4.2]
$\tilde{C}_{\rm Qu}^{(1)}$	[-3., 3.]	[-2.6, 2.6]	[-2.7, 2.7]
$\tilde{C}_{\rm Qq}^{(8,1)}$	[-7.5, 4.2]	[-6., 3.6]	[-6.5, 3.7]
$\tilde{C}_{\rm Qq}^{(1,1)}$	[-2.5, 2.7]	[-2.1, 2.3]	[-2.2, 2.3]
$\tilde{C}_{\rm Qq}^{(8,3)}$	[-5.8, 4.8]	[-4.7, 4.2]	[-5.4, 4.]
$\tilde{C}_{\rm Qq}^{(1,3)}$	[-2.6, 2.6]	[-2.1, 2.2]	[-2.2, 2.2]
$\tilde{C}_{\rm tq}^{(8)}$	[-7.1, 3.9]	[-6.9, 3.3]	[-5.1, 3.4]
$\tilde{C}_{\rm tq}^{(1)}$	[-2.6, 2.6]	[-2.2, 2.2]	[-2.3, 2.2]
$\tilde{C}_{\rm tt}$	[-1.5, 1.3]	[-1.1, 0.96]	[-0.81, 0.7]
$\tilde{C}_{\rm QQ}^{(+)}$	[-1.5, 1.3]	[-1.1, 0.96]	[-0.81, 0.7]
$\tilde{C}_{\rm Qt}^{(1)}$	[-2.4, 2.4]	[-1.8, 1.8]	[-1.3, 1.3]
$\tilde{C}_{\rm Qt}^{(8)}$	[-5.3, 4.4]	[-4.1, 3.1]	[-3., 2.3]

Table 42: Limits on 14 $qqtt$ operator coefficients and 4 four-top operator coefficients, expected at the 13, 14 and 27 TeV scenarios, at the 95% CL level.

operators can be parametrized as [610]:

$$\mathcal{L}_{gt\bar{t}} = -g_s\bar{t}\frac{\lambda^a}{2}\gamma^\mu t G_\mu^a - g_s\bar{t}\lambda^a\frac{i\sigma^{\mu\nu}q_\nu}{m_t}(d_V^g + id_A^g\gamma_5)tG_\mu^a,$$

where the chromomagnetic and chromoelectric dipole moments of the top quark are denoted by d_V^g and d_A^g (both are zero in the SM at leading order). Direct bounds on both d_V^g and d_A^g were obtained from the top quark pair cross section measurements at the LHC and the Tevatron. The bounds on the dipole moments using the $t\bar{t}$ cross section at the LHC and Tevatron were found to be: $-0.012 \leq d_V^g \leq 0.023$, $|d_A^g| \leq 0.087$ [611]. Four-top quark production is also affected by the $gt\bar{t}$ effective coupling and provides a powerful way to probe the chromomagnetic and chromoelectric dipole moments of the top quark. The representative Feynman diagrams with the effective $gt\bar{t}$ coupling denoted by filled red circles are shown in Fig. 80. The contribution of the top quark dipole moments to the $t\bar{t}t\bar{t}$ production cross section is determined with the `MadGraph5_aMC@NLO` package [12]. By taking into account at most an effective vertex in each diagram, the total four top cross section at $\sqrt{s} = 14$ TeV has the following form:

$$\begin{aligned}\sigma(pp \to t\bar{t}t\bar{t})(\text{fb}) &= \sigma_{\rm SM} + 154.8 \times d_V^g + 3404.4 \times (d_V^g)^2, \\ \sigma(pp \to t\bar{t}t\bar{t})(\text{fb}) &= \sigma_{\rm SM} + 2731.3 \times (d_A^g)^2, \end{aligned} \quad (49)$$

where the SM four top quark cross section is denoted by $\sigma_{\rm SM}$. The linear terms are due to the interference between the new physics and SM with the contribution of the order of Λ^{-2}. The quadratic terms suppressed by Λ^{-4} power are the pure contributions of the strong dipole moments. To estimate the

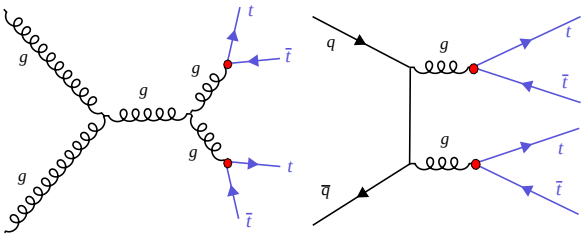

Fig. 80: Representative Feynman diagrams for the $t\bar{t}t\bar{t}$ production where the effects of the strong dipole moments are shown as filled red circles.

Coupling	HL-LHC, 14 TeV, 3 ab^{-1}	HE-LHC, 27 TeV, 15 ab^{-1}
d_V^g	[-0.084, 0.009]	[-0.063, 0.001]
d_A^g	[-0.030, 0.030]	[-0.011, 0.011]

Table 43: Limits at 95% CL on the chromoelectric and chromomagnetic dipole moments $d_V^{g,Z}$ at 95% CL for the HL-LHC and HE-LHC.

sensitivity of the four top process to dipole moments, we concentrate on the same-sign dilepton channel due to its clean signature and very low background contribution. The main background contributions come from the $t\bar{t}W$ and $t\bar{t}Z$ processes. Signal and the background processes are generated with the `MadGraph5_aMC@NLO` package at leading order. `Pythia 6` [612] is used for hadronization, showering and decay of unstable particles. Jets are reconstructed using the anti-k_t algorithm [233]. Signal events are selected by requiring exactly two same-sign charged leptons with $p_T^\ell > 25$ GeV and $|\eta^\ell| < 2.5$. The missing transverse energy has to be larger than 30 GeV. Each event is required to have at least eight jets with $p_T > 30$ GeV and $|\eta| < 2.5$ from which at least three should be b-tagged jets. All objects in the final state are required to be well isolated objects by requiring $\Delta R(i,j) > 0.4$. Table 43 presents limits at 95% CL on the chromoelectric (d_A^g) and chromomagnetic (d_V^g) dipole moments for the HL-LHC and HE-LHC. The HE-LHC improves the HL-LHC bound on d_A^g by about a factor of three and the upper bound on d_V^g by one order of magnitude. The four top-quark production at the HE-LHC would be able to tighten the upper limit on d_A^g (d_V^g) by a factor of two (eight) w.r.t. the top pair production at the HL-LHC [611].

6.4 The $t\bar{t}V$ production at the HL/HE LHC

6.4.1 Theoretical framework

$t\bar{t}Z$ cross sections at NLO QCD and EW

In this section we provide the cross section for $t\bar{t}Z$ production at the HL and HE LHC. Our result are accurate up to NLO QCD and NLO EW accuracy [99]. NLO QCD and EW corrections are computed simultaneously with `MadGraph5_aMC@NLO` [12], more specifically by using the recently-released version capable of mixed-coupling expansions [89]. We use the same setup as in Ref. [144] (see in particular Sect. 1.6.7.a), except for the PDF set, for which we will always employ the `PDF4LHC15_nlo_30_pdfas` set [153]. In fact, at variance with the predictions in Ref. [144], we do not include photon-initiated contributions, as recent studies on the photon distribution became avilable [180, 181], and the corresponding photon density gives negligible contributions for $t\bar{t}Z$. The quoted EW corrections include the LO term at $\mathcal{O}(\alpha^2\alpha_s)$ and the NLO one at $\mathcal{O}(\alpha^2\alpha_s^2)$. At variance with $t\bar{t}W$ production, for which other contributions, subleading in the couplings, turn instead to be relevant (see Sect. 6.4.1), it has been shown in Ref. [89] that such contributions can be safely neglected for $t\bar{t}Z$.

Cross-sections for $t\bar{t}Z$ are quoted in Tab. 44, together with the NLO/LO QCD K-factor, the relative impact of EW corrections, and the theory uncertainties. For the latter, we quote separately the uncertainty coming from scale variations, the PDF uncertainty and the α_s one.

Table 44: Cross section, in pb, for $t\bar{t}Z$ production at the HL and HE LHC. Uncertainties on the cross sections are at the per-mil level.

$\sqrt{s}$	$\sigma^{\rm NLO}_{\rm QCD}$	$\sigma^{\rm NLO}_{\rm QCD+EW}$	$K_{\rm QCD}$	$\delta_{\rm EW}$ [%]	scale [%]		PDF [%]	α_s [%]
14 TeV	1.018	1.015	1.40	-0.3	+9.6	-11.2	±2.7	± 2.8
27 TeV	4.90	4.81	1.45	-2.0	+9.9	-10.4	±2.0	± 2.0

The complete-NLO corrections to $t\bar{t}W$

In this section we compute the so-called "complete"-NLO corrections to $t\bar{t}W^{\pm}$ procution. This process can proceed through different terms of order $\alpha_s^p\alpha^{q+1}$ with $p+q=2,\ 3$ at LO and at NLO respectively. The term complete-NLO refers to compuatation of all terms with $p+q\leq 3$, which has been performed for the first time in Ref. [115] by employing the newely-released version of `MadGraph5_aMC@NLO` [12] capable of computing mixed QCD and Electroweak corrections [89]. Among the various contributions, the complete-NLO corrections include the NLO QCD ones ($p=3$, $q=0$) [382, 383, 613, 614], and the NLO EW corrections ($p=2$, $q=2$) [99]. In this short paragraph we report inclusive predictions for the HL and HE LHC, with a centre-of-mass energy of respectively 14 TeV and 27 TeV. We use the same setup and notation of Ref. [115], where the interested reader can find more details as well as predictions for 13 and 100 TeV.

Table 45: Cross section for $t\bar{t}W^{\pm}$ production at the HL and HE LHC, in various approximations. Number in parentheses are computed with a jet veto. See Ref. [115] for details.

σ[fb]		LO_{QCD}	$\text{LO}_{\text{QCD}}+\text{NLO}_{\text{QCD}}$	LO	LO + NLO	$\frac{\text{LO(+NLO)}}{\text{LO}_{\text{QCD}}\text{(+NLO}_{\text{QCD}}\text{)}}$
$H_T/2$	14 TeV	$414^{+23\%}_{-18\%}$	$628^{+11\%}_{-11\%}$ ($521^{+5\%}_{-7\%}$)	$418^{+23\%}_{-17\%}$	$670^{+12\%}_{-11\%}$ ($548^{+6\%}_{-7\%}$)	1.07 (1.05)
	27 TeV	$1182^{+21\%}_{-16\%}$	$2066^{+14\%}_{-11\%}$ ($1561^{+7\%}_{-7\%}$)	$1194^{+21\%}_{-16\%}$	$2329^{+14\%}_{-11\%}$ ($1750^{+7\%}_{-7\%}$)	1.13 (1.12)

We report in Tab. 45 the total-cross section for $t\bar{t}W^{\pm}$ production in different approximations, and in Tab. 46 the breakdown of the different orders contributing at LO and NLO, as fraction of the $\mathcal{O}(\alpha_s^2\alpha)$ LO contribution, LO_1. Number in parentheses are computed by vetoing hard central jets, with $p_T > 100\,\text{GeV}$ and $\eta < 2.5$. As it can be gathered from the tables, the jet veto is beneficial in order to reduce the NLO QCD corrections, in particular the large contribution coming from hard real emissions with a soft or collinear W boson. We can appreciate how the NLO_3 contribution is actually larger than the NLO_2 (the EW corrections) despite the extra power of α, and how such a contribution grows with the collider energy. As explained in Ref. [115], this is due to the $t-W$ scattering process [615]. Since the size of NLO_3 is not much affected by the jet veto, a measurement of the $t-W$ scattering from the $t\bar{t}W$ cross section should be possible.

Table 46: $t\bar{t}W$: $\sigma_{(\mathrm{N})\mathrm{LO}_i}/\sigma_{\mathrm{LO}_{\mathrm{QCD}}}$ ratios at 14 and 27 TeV, for different values of $\mu = \mu_r = \mu_f$. LO_2 is identically zero and is not quoted in the table. Number in parentheses are computed with a jet veto. See Ref. [115] for details.

$\delta[\%]$	14 TeV			27 TeV		
	$\mu = H_T/4$	$\mu = H_T/2$	$\mu = H_T$	$\mu = H_T/4$	$\mu = H_T/2$	$\mu = H_T$
LO_3	0.8	1.0	1.1	0.9	1.0	1.2
NLO_1	37.4 (7.7)	51.8 (25.9)	64.7 (41.9)	67.4 (18.4)	74.8 (32.0)	82.0 (44.3)
NLO_2	−4.5 (−4.7)	−4.3 (−4.5)	−4.1 (−4.3)	−5.1 (−5.4)	−5.0 (−5.2)	−4.8 (−5.1)
NLO_3	13.0 (9.7)	13.3 (9.9)	13.6 (10.1)	25.5 (19.8)	26.1 (20.2)	26.6 (20.6)
NLO_4	0.02 (−0.00)	0.03 (0.00)	0.05 (0.01)	0.06 (0.01)	0.08 (0.02)	0.10 (0.03)

6.5 Top mass

6.5.1 Theoretical issues

The typical errors currently quoted for the top mass measurements in the so called "direct measurements" at the LHC are of the order of 500-600 MeV, and with the prospect of the high luminosity operations, as can be seen from fig. 81 of the following section, the projected future experimental uncertainty is around 200 MeV. Such a high precision entails also a high level of scrutiny concerning the extracted top mass value. In direct measurements, the measured top mass is the value of the top mass parameter in the Monte Carlo generator that is used to fit top-mass sensitive distributions. In this respect, the scrutiny must also regard theoretical aspects dealing with how the Monte Carlo models the relevant mass sensitive distributions, keeping in mind that all effects that can lead to variations of the result in the 100 MeV range should be considered.

The top mass parameter, as all coupling constants characterizing the underlying field theory, requires renormalization, and its precise value depends upon the adopted renormalization scheme. The differences in the top mass in different renormalization prescriptions are of the order of $\alpha_s(m_t)m_t$, i.e. a value that can amount to several GeV's. It is thus clear that an experimental result, in order to be of any use, must specify to which scheme the measured value corresponds to.

At present, the experimental collaborations seem to have renounced to qualify direct mass measurements by also specifying a renormalization scheme. This is a consequence of the fact that no full agreement has been reached among theorists on this issue. Some authors have argued that, in view of the inherent leading-order nature of the Monte Carlo generators, no scheme can be specified for the mass measured in direct measurements, since at leading order all schemes are equivalent. This argument was also used to advocate alternative measurements where the mass-sensitive observable is directly computed in perturbation theory at NLO or NNLO accuracy, and is compared to experimental distributions already corrected for detector effects [616, 617]. For example, the total cross section for $t\bar{t}$ production is sensitive to the top mass, it has been computed up to the NNLO order in QCD [41], and can be used to extract a top mass value [618–620]. Similarly, in Ref. [616, 617], shape observables constructed out of the $t\bar{t} + \mathrm{jet}$ kinematics are used.

Several theoretical works have appeared proposing alternative techniques to measure the top mass, partly in order to avoid the "Monte Carlo Mass" issue mentioned above, and partly to circumvent other aspects of direct measurements that may be considered problematic. The authors of Ref. [621] presented a method, based upon the charged-lepton energy spectrum, that is not sensitive to top production kinematics, but only to top decay, and does not make use of jets. Since top decays have been computed at NNLO accuracy [567, 568], they argue that a very accurate measurement may be achieved in this way. Other authors have advocated the use of boosted top jets (see Ref. [622] and references therein). In

Ref. [623], the b-jet energy peak position is proposed as mass-sensitive observable, that is claimed to have a reduced sensitivity to production dynamics. In Ref. [624], the use of lowest Mellin moments of lepton kinematic distributions is discussed. In the leptonic channel, it is also possible to use distributions based on the "stransverse" mass variable [625], which generalizes the concept of transverse mass for a system with two identical decay branches [626, 627]. Some of these methods have been effectively exploited by the experimental collaborations [625, 628–631] to yield alternative determinations of $m_{\rm t}$. They are consistent within errors with direct measurements, and thus provide valuable checks. It turns out, however, that at the moment their errors are not competitive with direct measurements. Furthermore, in view of the larger errors, assessing their eventual theoretical issue is a less demanding task in comparison to the case of direct measurements.

The notion that the Monte Carlo mass parameter cannot be qualified as a field theoretical mass has extensively permeated the discussions regarding the interpretation of top mass measurements. It is not difficult to show, however, that it is a misleading statement. In reality, the accuracy of Shower Monte Carlo's depends upon the observables one considers. As a trivial example, the total or differential cross section for the production of top quarks is predicted at leading order by standard Shower Monte Carlo's, so that the value of the top mass extracted by fitting it to a measured production cross section would certainly carry inaccuracies of order $\alpha_s m_t$. Such measurement cannot be qualified by specifying any particular scheme.[22] This is not the case if one consider as an observable the mass of the top decay products. In ref. [632], for example, it is pointed out that, in the narrow width limit, a perturbative calculation of the mass of the top decay products performed in the pole mass scheme yields a result that is independent upon the perturbative order. Since Monte Carlo generators, when performing heavy particle decay, strictly conserve the mass of the decaying particle, we can infer that the Monte Carlo mass parameter should be identified with the pole mass up to non-perturbative effects[23] as far as the mass of the decay products is concerned. From an unrelated point of view, in ref. [633] it is argued that since the top-quark decay is treated with a Breit-Wigner form in the Monte Carlo generators, it should be close to top mass schemes that are compatible with the Breit-Wigner form. In turn, these schemes yield mass values that differ from the pole mass by terms of order $\alpha_s \Gamma_t$. In subsequent works, it is argued that, in the narrow width limit, one can relate the Monte Carlo mass parameter to a running mass (typically the $\rm MSr$ mass) evaluated at the scale of the Monte Carlo shower cutoff, that is typically below a GeV. This again yields to a Monte Carlo mass parameter differing from the top pole mass by a fraction of a GeV. We also stress that theoretical papers that make use of the measured top mass values (noticeably those on electroweak precision fits [366, 634], and calculations inherent to the issue of vacuum stability [635–637]) interpret the direct measurement results as being close to the pole mass measurements, up to a theoretical error of few hundred MeV's.

A problem that has received much attention is the presence of an infrared renormalon in the Pole Mass definition. It turns out that the expression of the pole mass in terms of the $\overline{\rm MS}$ one, in terms of a perturbative expansion in the strong coupling constant, has factorially divergent coefficients [638, 639]. This leads to an ambiguity of the order of a typical hadronic scale in the relation betwee the Pole and the $\overline{\rm MS}$ mass, Estimates of this inherent ambiguity vary from 110 to 250 MeV [640–643]. It should be stressed, however, that the finite width of the top screens the effects of soft radiation, so that this ambiguity *does not affect the physics* of top production and decay. In view of the considerable time ahead of us before the High Luminosity program is started, we can assume, for the purpouse of this workshop, that this ambiguity, if it ever becomes important, can in principle be circumvented, and will not discuss it further here.

[22] In fact, at the moment, Monte Carlo generators that achieve NLO accuracy for sufficiently inclusive cross section are routinely used in top mass studies.

[23] In the narrow width limit the top can propagate a long time before decay, and long-distance non-perturbative effects can manifest themselves there, and affect the mass by few hundred MeV's.

Even accepting the fact that the difference between the top mass in direct measurements and the top pole mass is of the order of few hundred MeV's, in view of the current and projected accuracy of the measurement, the problem of reaching a theoretical uncertainty that matches the experimental one remains unanswered. Attempts to better understand the "few hundred MeV" difference mentioned above have appeared in the literature. They basically exploit the fact that soft emissions effects both in Shower Monte Carlo and in full QCD can be computed, and can have impact on the mass measurement problem. The authors of refs. [633,644–646], attempted to find a relation between the Monte Carlo mass parameter and a well-defined short distance mass, typically the MSr mass [647] evaluated at a scale of the order of the shower cutoff. In essence, the mass of a highly boosted top jet[24] is computed by using a resummed analytic calculations performed in a SCET framework, and by using shower algorithms. The comparison of the two results yields a relation between the Shower mass parameter and the field theoretical one used in the SCET calculation.[25] In a late work [646], they also examined in detail the analytic structure of the shower algorithm as compared to the one used in the resummed calculation. The differences between the Monte Carlo mass parameter and a short distance mass (of the kind that are compatible with the resonance structure, like the MSr mass evaluated at low scales) are found to be typically of the order of $q_0\alpha_s(q_0)$, where q_0 is the shower cut-off.

A limitation of these studies is that they applies to an observable that is not quite what is used in direct measurements, where one considers jets of the top decay products rather than top jets. Furthermore whether corrections of this order should be considered independently of all remanining non-perturbative uncertainties is a matter of debate. The fact remains, however, that studies of this sort in the framework of direct measurements are needed, since they may expose corrections that should be included in order to match the experimental accuracy.

Direct measurements are not the only context where theoretical errors that are linear in the strong interaction scale, i.e. of the order of few hundred MeV, do arise. In ref. [648], the production and decay of a top quark is considered in a very simplified context, and in a particular approximation, such that non-perturbative corrections can be examined in relation to the factorial growth of the coefficients of the perturbative expansions. Linear power corrections are found to affect all observables that make use of jets. But it was also found that typical leptonic observables are also affected by linear power corrections. Notice that this implies that the total cross section is also affected by linear power corrections, as soon as selection cuts are imposed. These kind of studies can also be extended to more complex measurement procedure, eventually making use of jet calibration, in order to understand to what extent these theoretical limitations to the precision can be removed.

The discussion carried out so far has highlighted theoretical problems that should be studied in more depth in order to advance our understanding of the theoretical precision of the measurement. In essence these problems are related to the physics of soft emission, and thus allow to draw conclusions that are motivated by perturbation theory, extrapolated to some extent to low scales. On the other two extremes, there are aspect of the event simulations that only have to do with relatively hard scales, and others that are more related to the modeling of physical effects that we are not able to compute, i.e. to hadronization phenomena. There is a current research effort, aimed at improving the simulation of top production and decay, in both these directions. It includes both the improvement of perturbative accuracy [563], and the improvement in the overall shower-hadronization aspects, including those related to colour reconnection [649,650]. Furthermore, studies of the sensitivity of top-mass sensitive observables to the perturbative accuracy, to the shower implementation and to the hadronization model, are being carried out. In one such study [651], significant differences were found when comparing Herwig7 and Pythia8, where the former adopts an angular ordered shower, and the latter has a dipole shower, in the

[24] In fact the emisphere mass in very high energy $t\bar{t}$ production events in e^+e^- annihilation

[25] This procedure is often quoted as a form of calibration of the Monte Carlo mass parameter. Notice, however that the same terminology is used in completely different contexts, see for example [**?**].

description of top-mass sensitive observables. In general, there is a range of equally plausible simulation model than we can use to describe heavy quark production and decay, that will include different Monte Carlo generators, different Monte Carlo tunes in a given generator, and different implementation of some component of a generator, like for example the colour reconnection model. As more work is done by exploring different plausible simulation model, the range of model will enlarge, and potentially also the error in mass measurement will increase. This increase in the error should be contrasted by limiting the range of models, typically by requiring that some key observables are in reasonable agreement with data. An example of a study in this direction is given in ref. [652], where the sensitivity of the top-mass error upon the uncertainties in key Monte Carlo tuning parameters is studied, and a set of calibration observables strongly sensitive to the Monte Carlo parameters, but with very mild sensitivity to the top mass, is considered in order to reduce the parameters uncertainties.

A complementary way of reducing the error is to find variants of measurement methods that are likely to reduced the dependence of the extracted mass from the range of models. In situ jet calibration is routinely used by the experimental collaborations in top mass measurement. This procedure not only reduces the experimental error associated with the jet energy scale, but it may also reduces the theoretical error, by reducing the sensitivity of the measurements from features of jet simulations in the generators. More specific proposals in this direction have appeared in ref. [653] the impact of adopting jet grooming techniques to the jets in direct top mass measurements is examined.

As mentioned earlier, alternative techniques for mass measurements are currently explored, and will become more precise at the High Luminosity LHC. As shown in fig. 81 in the following subsection, the mass measurement from single top production will acquire a precision similar to the one available today from direct measurements. The end-point measurement using the J/Ψ will also reach a precision near 600 MeV. Thus, at High Luminosity we may end up having one highly precise measurement technique, plus a number of independent methods supporting its results. It should not be forgotten however, that high luminosity and/or high energy may also offer opportunities for new techniques. In ref. [622], the use of grooming techniques applied to boosted top jets is studied, with the goal of directly extracting a short distance mass. To what extent the high luminosit phase can make this technique feasible is a matter for future studies. Another example is given in the work of ref. [654], where it is argue that a glitch in the dilepton spectrum should be visible for a dilepton invariant mass near twice the top mass. This effect is due to the diphoton production subprocess $gg \to \gamma\gamma$ mediated by a top loop. The projected statistical error for the mass determination using this method is of 2-3 GeV for the High Luminosity LHC, and 0.3-0.6 GeV for the High Energy option. A 1 GeV error systematic from the EM calorimeter calibration should also accounted for. Furthermore, a complete study of the projected theoretical error is not yet available. It is nevertheless interesting to remember that transversal thinking may lead to progress in this area.

In summary, we have seen that, from a theoretical point of view, much work is needed to put the top mass measurements at the LHC on a solid ground. Such work should comprise more thorough experimental work aimed at understanding and reduce the sources of errors; theoretical work in the frameworks of Monte Carlo studies and simulation; and formal theoretical work aimed at understanding crucial aspects of the uncertainties. Such work has already started, and we can expect that much more will be understood by the time the High Luminosity program starts. Thus, in spite of the many difficulties, we see no reasons why a theoretical precision matching the foreseable experimental error should not be possible at the high luminosity LHC.

6.5.2 Top mass experimental projections

The measurement of the top quark mass m_{top} with high precision is a crucial task for the expected 3000 fb^{-1} of pp collision data expected in HL-LHC. The top quark mass is one of the free parameters within the Standard Model and its Yukawa coupling is predicted to be close to unity. Therefore it may

play a special role in the electroweak symmetry breaking. The top quark mass dominantly contributes to the quantum corrections of the Higgs field, which become important for any extrapolation of the Standard Model to extremely high energies, from a few hundred GeV and above. At these high energies some of the fundamental deficiencies of the Standard Model can be further investigated, such as the stability of the electroweak vacuum state in the Higgs potential. Thus, precise measurements of the top quark mass allow for consistency tests of the Standard Model and to look for signs of new physics beyond.

The top quark mass is measured using various techniques and in different decays channels by the ATLAS and CMS experiments following two different approaches. Firstly, direct m_{top} measurements are obtained exploiting information from the kinematic reconstruction of the measured top quark decay products, and their corresponding combinations. These informations are obtained from Monte Carlo (MC) simulated events using different assumed values for the top quark mass parameter in the program. Therefore, such results relate to measurements of the input parameter of MC event generators, and differences between different MC are covered by a specific systematic uncertainty. The relation between the measured quantity, the top quark MC mass $m_{\text{top}}^{\text{MC}}$, and the physical parameter of interest, the top quark pole mass, is affected by non-perturbative contributions which could be $\sim$ 1 GeV. Secondly, indirect determinations of m_{top} are obtained based on the comparison of inclusive or differential $t\bar{t}$ production cross-section to the corresponding theory calculations, thus sensitive to $m_{\text{top}}^{\text{pole}}$.

The input material for the top quark mass summary is collected in Ref [655, 656].

The methods exploited for the measurement of m_{top} directly using the kinematic properties of the $t\bar{t}$ (or single-top quark) decay products are the template, the matrix element and the ideogram methods. In the template method, based on a full ($t\bar{t}$ $\rightarrow$lepton+jets, $t\bar{t}$ $\rightarrow$all-jets) or partial ($t\bar{t}$ $\rightarrow$dilepton and single-top quark) reconstruction of the kinematics underlying the top-quark(s) decay, probability density functions (templates) for observables sensitive to the underlying m_{top}, and to additional parameters, are constructed based on MC simulation. These templates are fitted to functions interpolating between the different input values of m_{top}, fixing all other parameters of the functions. Finally, an unbinned likelihood fit to the observed data distribution of the observable is used to obtain the value of m_{top} describing the data best. Typically, for single top and dilepton events the $m(lb)$ variable is used, whereas for the lepton+jets events the $m_{\text{top}}^{\text{reco}}$ obtained from a kinematic fit is more appropriate. The ideogram method can be considered as a computational effective approximation of a matrix element method. After a kinematic fit of the decay products to a $t\bar{t}$ hypothesis, MC-based likelihood functions are exploited for each event (ideograms) that depend only on the parameters to be determined from the data. The ideograms reflect the compatibility of the kinematics of the event with a given decay hypothesis. As in the case of the template method, ideograms can be generalised in multiple dimensions depending on the number of input observables used.

The latest ATLAS combination of direct m_{top} measurements leads to of top quark mass value of $m_{\text{top}} = 172.69 \pm 0.48$ TeV with a total precision of $\sim 0.28\%$ [657]. The latest CMS combination of direct m_{top} measurements leads to of top quark mass value of $m_{\text{top}} = 172.44 \pm 0.48$ TeV with a total precision of $\sim 0.28\%$ [arXiv:1509.04044]. The precision in each of these analyses is primarily limited by systematic effects, in particular by the modelling of top quark production and decay and by the jet energy scale. Analysis techniques have been developed to use in-situ constraints from the data on a global jet energy scale factor or light jet and b-jet energy scale (3D fits) [657], which still suffer from statistical uncertainties, which will be reduced strongly at the HL-LHC. The total amount of 3000 fb^{-1} of 14 TeV data would clearly decrease the statistical uncertainty in these analyses. Therefore, the statistical precision in each analysis should be traded in various ways for a reduced total systematic uncertainty by cutting into phase space regions where the systematic uncertainties are high.

A variety of alternative methods are exploited to supplement the top quark mass measurements from direct mass reconstruction based on jet observables. One source of alternative observables is the

usage of the b-jet information in the $t\bar{t}$ decay, e.g. via final states featuring J/ψ produced in the b-hadron decays or secondary vertices in b-jets. With the alternative approaches, a large variety of other $m_{\text{top}}^{\text{MC}}$ measurements can be done, which have different sensitivities to the top quark production and decay mechanisms and making therefore different contributions to the systematic uncertainties. Compared to the template method with the standard final states, the sensitivity to the light-jet and b-jet energy scale (respectively JES and b-JES) is expected to be reduced. One of the limiting factors of this approach is the small branching fraction, $\mathcal{B}(t\bar{t} \to (W^+b)(W^-b) \to (\ell\nu_\ell J/\psi(\to \mu^+\mu^-)X)(qq'b) \sim 3.2 \times 10^{-4}$, where $\ell = e, \mu$. On the other hand the modelling of b-fragmentation and b-decay are expected to be among the dominating sources of systematic uncertainties of these two analyses and need to be studied extensively in a dedicated study to reduce the signal modelling uncertainties. Both measurements can contribute in different ways to the final combination to improve the precision measurement of m_{top}. Individual m_{top} results resting on various techniques and $t\bar{t}$ (or single-top quark) decay channels, have different sensitivities to statistical and systematic effects, and to the details of the MC simulation. To exploit the full physics potential of the available measurements, and to profit from their diversity and complementarity, they are combined, thereby further increasing our knowledge on m_{top}.

In some alternative techniques the top quark mass is exctracted by comparing cross sections or distributions that can be calculated directly in QCD at either NLO or NNLO, to corresponding distributions extracted from data. The mass parameter used in the NLO or NNLO calculation (either the $\overline{\text{MS}}$ or the Pole top mass) is obtained by fitting the theoretical cross section or distribution to the measured one. In this framework, mass measurements have been performed using as observables the inclusive $t\bar{t}$ cross-section [Ref], the differential decay rate in $t\bar{t}$+1 jet events [Ref], lepton and dilepton differential cross-sections [Ref].

Due to the changes of the detector performance for the HL-LHC, it is difficult to estimate precisely the effects of systematic uncertainties. The sources of uncertainty are assumed to be the same as the current ones. The estimated Run-2 uncertainties are scaled to align with HL-LHC extrapolations developed by the ATLAS and CMS Collaborations and documented in Ref. [658]. The impact of the experimental systematic uncertainties will likely be reduced relative to their effect on the Run-2 analysis given the large datasets available, allowing precise performance studies to be conducted. The jet reconstruction uncertainties on m_{top} are expected to be divided by a factor up to two, while uncertainties related to the reconstruction of electrons and muons remain the same as in Run-2. The theory modelling uncertainties are expected to be divided by a factor two compared to existing values. The larger HL-LHC dataset will allow for dedicated tuning and good understanding of NLO MC generators matched to parton showers, as already started with Run-2 data [388]. Another large contribution to the uncertainties stems from the modelling of QCD interactions, which can be investigated and constrained using differential measurements of the mass parameter itself or other ancillary measurements in parts of the phase space not yet accessible. These measurements are partially already being performed [659–661], but will benefit from more statistics, therefore strong constraints from the high statistics at the HL-LHC are expected.

6.5.3 Top mass in the J/psi channel ATLAS

Preliminary

For this report, ATLAS Collaboration presents projections for the top quark mass measurement accuracy using $\mathrm{t\bar{t}} \to$ lepton+jets events with $J/\psi \to \mu^+\mu^-$ in the final state. Samples of simulated events for signal and background processes are produced at 14 TeV centre-of-mass energy. They include the production of $\mathrm{t\bar{t}}$ pairs, single-top quarks and W boson/Z bosonbosons in association with jets. After the event generation step, a fast simulation of the trigger and detector effects is added with the dedicated ATLAS software framework. The event selection follows the analysis done at 8 TeV [662]. Events are required to have at least one charged isolated lepton with $p_{\mathrm{T}} > 25\ rmGeV$ and $|\eta| < 4$ and at least 4 jets with $p_{\mathrm{T}} > 25\ rmGeV$ and $|\eta| < 4.5$. No requirement is applied on the number of b-tagged

Method	Statistical	Systematic	Total(GeV)
$t\bar{t}$ lepton+jets	0.17	0.02	0.17
single-t t-channel	0.45	0.06	0.45
$m_{sv\ell}$	0.62	0.02	0.62
J/ψ	0.24	0.53	0.58
$\sigma_{t\bar{t}}$	0.4%(exp)	0.4%(theory)	1.2

Table 47: Projected total uncertainties on the top quark mass for 3 ab^{-1} and $\sqrt{s}$=14TeV obtained with different methods.

jets. J/Ψcandidates are reconstructed using all pairs of opposite charge sign soft muons with $p_{\mathrm{T}} > 4$ GeV and $|\eta| < 4.5$ The top quark mass is obtained from a template method with unbinned likelihood maximisation approach. A statistical uncertainty of 0.xx GeV is expected, with a systematic uncertainty of 0.xx GeV. The total amount of 3000 fb^{-1} of 14 TeV data would clearly decrease the statistical uncertainty in this analysis. However, the precision would be limited by systematic effects. Therefore, the statistical precision should be traded in various ways for a reduced total systematic uncertainty by cutting into phase space regions where the systematic uncertainties are high.

This paragraph discusses the potential of selected top quark mass measurements at the HL-LHC done by the CMS Collaboration, as described in detail in Ref [655]. The extrapolations are based on measurements performed at 7 and 8 TeV centre-of-mass energy using 5 fb^{-1} and 19.7 fb^{-1}, respectively. The numbers presented here do not include the possible ambiguity in the interpretation of the measured value with respect to a well defined renormalisation scheme. However, also the measurement of the pole mass from the inclusive $\mathrm{t\bar{t}}$ cross-section cross section is extrapolated to HL-LHC conditions.

Typically, the jet energy scale uncertainties play a dominant role for top quark mass measurements. The contribution from background processes, important only for the measurement using single top events, is expected to be well under control. For the extrapolation of the extraction of m_{top} from the total cross-section, the cross-section measurement is assumed to be ultimately limited by the luminosity uncertainty, here assumed to be 1.5%. For the prediction, no predictions beyond NNLO are assumed, such that the uncertainty due to scale variations is constant.

The resulting extrapolated uncertainties on the top quark mass measurements are summarised in Figure 81. The measurement using J/ψ mesons and using in general secondary vertices benefit the most from higher statistics. But also the other measurements improve significantly, mostly from more precise understanding of systematic uncertainties, as discussed above, such that ultimately, the precision will range between 0.1% (which is of the order of Λ_{QCD}) and 0.7%.

6.6 Top quark properties and couplings

6.6.1 Top quark charge asymmetries at LHCb

The top quark charge asymmetry present in quark-initiated production is diluted by the presence of gluon-gluon fusion and the increased quark content in the proton at forward rapidities gives LHCb additional sensitivity to this observable. As LHCb takes data at a lower rate than ATLAS and CMS, and has a limited acceptance, a partial reconstruction of the $t\bar{t}$ final state is anticipated in order to make optimal use of statistics, as described in Sec. 6.1.4. The expected differential single lepton asymmetry at LHCb, inferred from the rate of $\ell^+ b$ and $\ell^- b$ production as a function of lepton pseudorapidity, is shown in Fig. 82 [663]. The expected statistical precision of a dataset corresponding to 300 fb^{-1} of integrated luminosity, the total expected at LHCb during the HL-LHC, is shown, along with the theoretical uncertainties due to scale, α_s and PDF uncertainties. The projection indicates that LHCb

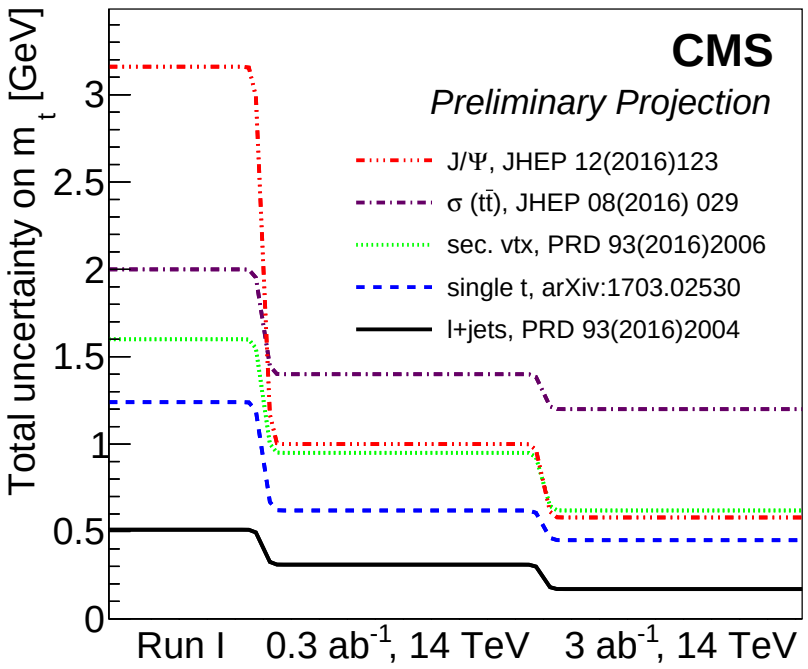

Fig. 81: The top mass measurement uncertainty for different methods as a function of integrated luminosity as obtained by CMS.

will have sufficient statistics to make a non-zero observation of the $t\bar{t}$ charge asymmetry at the HL-LHC. The dominant systematic uncertainty on the measurement is expected to come from the knowledge of the background contributions, particularly from W production in association with b-jets. Other final states, where an additional b-jet or lepton are required to be present will provide additional information as, despite the lower statistical precision, they probe larger values of Bjorken-x and select the data sample with a higher purity.

6.6.2 A method to determine $|V_{cb}|$ at the weak scale in top quark decays at the LHC

In a recent paper [664], a new method was proposed to measure the $|V_{cb}|$ element of the Cabibbo Kobayashi Maskawa (CKM) quark mixing matrix at the scale $q \simeq m_W$, using top decays at the LHC. To date, $|V_{cb}|$ has always been measured in B decays, i.e. at an energy scale $q \simeq \frac{m_b}{2}$, far below the weak scale, and it is currently known to an uncertainty of about 2% [665]:

$$|V_{cb}| = (42.2 \pm 0.8) \times 10^{-3}. \tag{50}$$

In the proposed measurement at the LHC, $|V_{cb}|$ will be measured at the scale $q \simeq m_W$, more representative of the weak scale. The motivation for such a measurement is that the traditional extraction of $|V_{cb}|$ in B decays relies heavily on the operator product expansion, and its sensitivity is significantly affected by theoretical uncertainties [665]. In contrast, in dealing with decays of on-shell Ws, as here, the theoretical situation is likely to be much cleaner and the systematic uncertainties will be very different. Moreover, there could be significant evolution of $|V_{cb}|$ between $q \simeq \frac{m_b}{2}$ and $q \simeq m_W$ due to radiative corrections: e.g. the application (somewhat inappropriately) of the Standard Model (SM) six-quark evolution equations [666] at two-loop order [667] to the CKM matrix between $q \simeq \frac{m_b}{2}$ and $q \simeq m_W$ yields

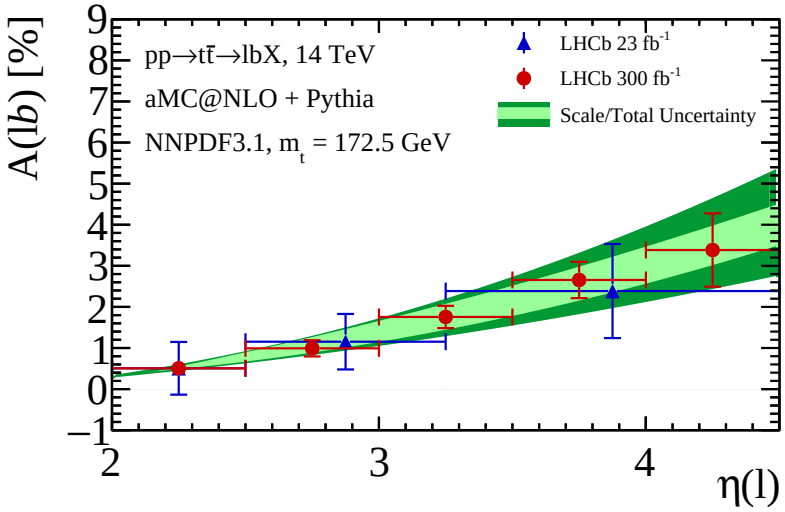

Fig. 82: The predicted SM asymmetry at LHCb as a function of lepton pseudorapidity in the ℓb final state at 14 TeV. The bands show the uncertainty on the theoretical predictions due to scale variations (light green) and due to combined scale, PDF and α_s variations (dark green). The expected statistical precision on measurements performed by LHCb using 23 and 300 fb^{-1} of data is indicated by the error bars on the points.

a fractional increase in $|V_{cb}|$ of $\simeq 5\%$, see fig. 83. While the correct treatment for SM evolution at such low energies is rather to use an effective field theory, integrating out the top quark below $q \sim m_t$ [668], such a calculation of the $|V_{cb}|$ running has not yet appeared in the literature. Thus the low-energy evolution of $|V_{cb}|$ is currently completely uncertain, while the naive calculation outlined above at least opens the possibility that its running might be observable, if $|V_{cb}|$ can be measured at or above the weak scale.

The proposed method uses the decays of tagged $t\bar{t}$ pairs with one semileptonic top decay, (the tag), $\bar{t} \to \bar{b}W^- \to \bar{b}\ell^-\bar{\nu}_\ell$, and the other a hadronic decay, $t \to bW \to b\bar{q}c$, where $\bar{q}$ is a charge $\frac{1}{3}$ antiquark (charge-conjugate decays will be assumed everywhere unless otherwise stated). The fraction of these in which $\bar{q} = \bar{b}$ is (up to negligible phase-space factors), exactly $|V_{cb}|^2$. Using this ratio, otherwise leading experimental uncertainties in most of the tagging efficiencies are cancelled. Thus the required signal will contain three tagged b-jets and a tagged c-jet, in addition to a charged lepton and missing transverse momentum.

Taking as a starting point, efficiencies from existing ATLAS and CMS $t\bar{t}$ cross-section analyses, already-achieved experimental tagging performances [669–674], and reasonable assumptions about backgrounds, it is estimated [664], that the fractional uncertainty on $|V_{cb}|$ which can be obtained at a single experiment using the Run 2 dataset is:

$$\frac{\Delta|V_{cb}|}{|V_{cb}|} \sim 0.07, \tag{51}$$

which is statistics-limited. Averaging the two experiments would give a fractional error of $\sim 5\%$.

Since the values of the systematic uncertainties on the tagging performances used to calculate eq. (51) were based roughly on their present determinations, the result is generalised in fig. 84, to show the dependence of the obtained fractional error on the systematic uncertainties as they vary. Also shown in fig. 84 are the results using larger datasets, corresponding to various future LHC luminosity scenarios. The systematics-limited regime is represented by the linear-sloping region towards the bottom-right

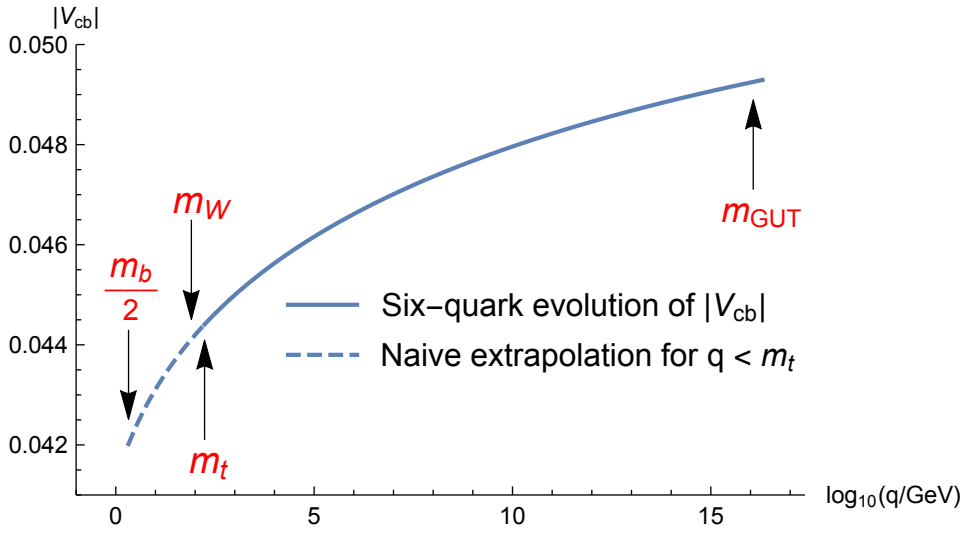

Fig. 83: Renomalisation Group evolution of $|V_{cb}|$ using the six-quark running scheme [666–668] between m_{GUT} and $\frac{m_b}{2}$. Previous publications stop at m_t, while a correct procedure would use a five-quark scheme for $q \lesssim m_t$. This naive procedure at least suggests the possibility of significant low-energy evolution of $|V_{cb}|$.

part of the figure, while the statistics-limited regime lies close to the y-axis, where the benefit of more statistics is most marked. The figure shows that making the measurement with future LHC data promises further improvements from both increased statistics and if tagging performance uncertainties can be reduced. E.g. if $\delta_{\mathcal{B}_1} = 3\delta_{\epsilon_b}$ can be reduced to $\simeq 0.05$, then at the end of Run 3, the uncertainty on $|V_{cb}|$ per experiment using this method could be as low as 4.5%, giving a fractional uncertainty on the average of the two $|V_{cb}|$ measurements of $\sim 3\%$. HL-LHC would then deliver a further reduction in the measurement uncertainty of better than a factor of 2. Either of these higher statistics measurements could give sensitivity for the first time to the renormalisation group running of $|V_{cb}|$.

6.7 Flavour changing neutral current

Processes with flavour-changing neutral currents (FCNC) are forbidden at tree level and are strongly suppressed in higher orders by the Glashow-Iliopoulos-Maiani (GIM) mechanism [675]. The SM predicts the branching fractions for top quark FCNC decays of $\mathcal{O}(10^{-12}$–$10^{-16})$ [676–678]. However, various extensions of the SM allow a significant enhancement of the FCNC top quark decay rates arising from possible contributions of new particles [678–680]. Any deviations from heavily suppressed top FCNC rates would be a clear sign of new physics. The FCNC interactions of the top quark with the SM gauge and Higgs bosons can be described through the following anomalous coupling Lagrangian:

$$\begin{aligned}\mathcal{L} = \sum_{q=u,c} \Big[& \sqrt{2} g_s \frac{\kappa_{gqt}}{\Lambda} \bar{t} \sigma^{\mu\nu} T_a (f_{Gq}^L P_L + f_{Gq}^R P_R) q G_{\mu\nu}^a + \\ & + \frac{g}{\sqrt{2} c_W} \frac{\kappa_{zqt}}{\Lambda} \bar{t} \sigma^{\mu\nu} (f_{Zq}^L P_L + f_{Zq}^R P_R) q Z_{\mu\nu} + \frac{g}{4 c_W} \zeta_{zqt} \bar{t} \gamma^{\mu} (f_{Zq}^L P_L + f_{Zq}^R P_R) q Z_{\mu} - \\ & - e \frac{\kappa_{\gamma qt}}{\Lambda} \bar{t} \sigma^{\mu\nu} (f_{\gamma q}^L P_L + f_{\gamma q}^R P_R) q A_{\mu\nu} + \\ & + \frac{g}{\sqrt{2}} \bar{t} \kappa_{Hqt} (f_{Hq}^L P_L + f_{Hq}^R P_R) q H \Big] + h.c., \end{aligned} \tag{52}$$

where P_L and P_R are chiral projection operators in spin space, κ_{Xqt} is the anomalous coupling for tXq

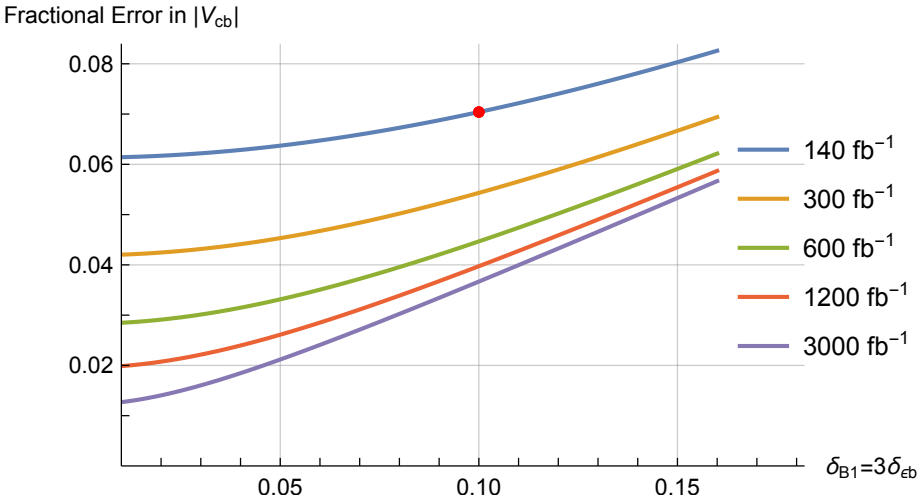

Fig. 84: Estimated fractional error in $|V_{cb}|^2$ as a function of the systematic uncertainties δ_{ϵ_b} in the b-jet tagging efficiency and $\delta_{\mathcal{B}_1}$ in the light-to-b jet flavour mis-tag probability, and integrated luminosity. For ease of presentation, we assume $\delta_{\mathcal{B}_1} \simeq 3\delta_{\epsilon_b}$ as it is at the time of writing. The top curve represents the Run 2 statistics and the red point on it indicates the illustrative values used to obtain eq. (51). The second curve corresponds to luminosity projections for Run 3, while the bottom curve is for the projected integrated luminosity for HL-LHC. We have allowed for a 15% increase in the $t\bar{t}$ cross-section in the lower three curves, corresponding to an increase in beam collision energy to 14 TeV.

vertex ($X = g, Z, \gamma, H$), ζ_{Zqt} is the additional anomalous coupling for tZq vertex, f_{Xq}^L and f_{Xq}^R are the left and right-handed complex chiral parameters with an unitarity constraint of $|f_{Xq}^L|^2 + |f_{Xq}^R|^2 = 1$. Each of the anomalous couplings can be probed in events with the top quark pair production where one of the top quark decays via FCNC interaction, as well as in events with the associated production of the single top quark with a gluon, Z boson, γ, or Higgs boson.

Signal modeling

The generation of signal events at ATLAS is done at NLO with MadGraph5_aMC@NLO [12, 681] and the effective field theory framework developed in the TopFCNC model is used [682, 683]. In the case of gqt coupling, the MEtop generator is used instead [684]. At CMS signal events are simulated at LO with MadGraph5_aMC@NLO with the effective lagrangian implemented by means of the FEYNRULES package, except in the simulation of signal events for gqt and γqt couplings where CompHEP [685] and PROTOS 2.0 [686] are used, respectively. In both experiments Pythia 8 is used to simulate the parton showering and hadronization. The generation of signal events is done under the assumption of only one non-vanishing FCNC coupling at a time.

Top-gluon

The gqt FCNC process was studied by ATLAS [687] and CMS [688] in single top quark events. The event signature includes the requirement of one isolated lepton and the presence of a significant amount of transverse missing energy (E_T^{miss}). The analysis at CMS requires exactly one b and one non-b jet to b present in the final state with the dominant background arising from the $t\bar{t}$+jets production, while the analysis at ATLAS vetoes any additional jets resulting in the dominant source of background associated with the W+jets production. A neural network-based technique is used to separate signal

from background events. The observed (expected) 95% CL upper limits in the CMS analysis are $\mathcal{B}(t \to gu) < 2.0\ (2.8) \times 10^{-5}$ and $\mathcal{B}(t \to gc) < 4.1\ (2.8) \times 10^{-4}$, while the resultant limits in case of ATLAS are $\mathcal{B}(t \to gu) < 4.0\ (3.5) \times 10^{-5}$ and $\mathcal{B}(t \to gc) < 2.0\ (1.8) \times 10^{-4}$. The projected limits for $3ab^{-1}$ are $\mathcal{B}(t \to gu) < 3.8 \times 10^{-6}$ and $\mathcal{B}(t \to gc) < 32.1 \times 10^{-6}$ [689].

Top-Z

ATLAS studied the sensitivity to the tqZ interaction, by performing an analysis [**?**] based on simulated samples and following both the strategy of its 13 TeV data analysis on the same subject [**?**] and of the general recommendations for this HL-LHC study. The study is performed in the three charged lepton final state of $t\bar{t}$ events, in which one of the top quarks decays to qZ, $(q = u, c)$ and the other one decays to bW ($t\bar{t} \to bWqZ \to b\ell\nu q\ell\ell$). The kinematics of the events are reconstructed through a χ^2 minimisation and dedicated control regions are used to normalize the main backgrounds and constrain systematic uncertainties. The main uncertainties, in both the background and signal estimations, are expected to come from theoretical normalization uncertainties and uncertainties in the modeling of background processes in the simulation. Different scenarios for the systematic uncertainties are considered, ranging from the full estimations obtained with the 13 TeV data analysis, to the ones expected with improvements in theoretical predictions, which should be half of the former ones. A binned likelihood function $L(\mu, \theta)$ is used to do the statistical analysis and extract the signal normalisation. An improvement by a factor of five is expected in relation to the current 13 TeV data analysis results. Obtained branching ratio limits are at the level of 4 to 5 $\times 10^{-5}$ depending on the considered scenarios for the systematic uncertainties.

Top-γ

The $t\gamma q$ anomalous interactions are probed by CMS at 8 TeV in events with single top quarks produced in association with a photon [690]. Event selection criteria includes the presence of one isolated lepton, one isolated photon, E_T^{miss}, and up to one b jet. The dominant $W\gamma$ and W+jets backgrounds are suppressed with a BDT. The resultant exclusion limits are $\mathcal{B}(t \to \gamma u) < 1.3\ (1.9) \times 10^{-4}$ and $\mathcal{B}(t \to \gamma c) < 2.0\ (1.7) \times 10^{-3}$. Preliminary projection studies yield $\mathcal{B}(t \to \gamma u) < 8.6 \times 10^{-6}$, $\mathcal{B}(t \to \gamma c) < 7.4 \times 10^{-5}$ [**?**].

Top-Higgs

The tHq interactions are studied by ATLAS in top quark pair events with $t \to qH, H \to \gamma\gamma$ [691] and $H \to WW$ [692] at 13 TeV. The former analysis explores the final state with two isolated photons. For leptonic top quark decays the selection criteria includes the requirement of one isolated lepton, exactly one b jet, and at least one non-b jet. In case of hadronic top quark decays the analysis selects events with no isolated leptons, at least one b jet, and at least three additional non-b jets. The dominant background processes are associated with the production of non-resonant $\gamma\gamma$+jets, $t\bar{t}$+jets and W+$\gamma\gamma$ events. The resultant limits are $\mathcal{B}(t \to Hu) < 2.4\ (1.7) \times 10^{-3}$ and $\mathcal{B}(t \to Hc) < 2.2\ (1.6) \times 10^{-3}$. The search for FCNC in $H \to WW$ includes the analysis of multilepton final states with either two same-sign or three leptons. The dominant backgrounds arising from the ttW, ttZ and non-prompt lepton production are suppressed with a BDT. The obtained limits are $\mathcal{B}(t \to Hu) < 1.9\ (1.5) \times 10^{-3}$ and $\mathcal{B}(t \to Hc) < 1.6\ (1.5) \times 10^{-3}$. The tHq anomalous couplings are probed by CMS in $H \to b\bar{b}$ channel in top quark pair events, as well as in single top associated production with a Higgs boson, at 13 TeV [693]. The event selection includes the requirement of one isolated lepton, at least two b jets, and at least one additional non-b jet. The dominant $t\bar{t}$ background is suppressed with a BDT discriminant to set the exclusion limits of $\mathcal{B}(t \to Hu) < 4.7\ (3.4) \times 10^{-3}$ and $\mathcal{B}(t \to Hc) < 4.7\ (4.4) \times 10^{-3}$. Preliminary projections suggest $\mathcal{B}(t \to Hq) < \mathcal{O}(10^{-4})$ [694, 695].

$\mathcal{B}$ limit at 95%C.L.	3 ab^{-1}, 14 TeV	15ab^{-1}, 27 TeV	Ref.
$t \to gu$	3.8×10^{-6}	5.6×10^{-7}	[689]
$t \to gc$	32.1×10^{-6}	19.1×10^{-7}	[689]
$t \to Zq$	4×10^{-5}		[?]
$t \to \gamma u$	8.6×10^{-6}		[?]
$t \to \gamma c$	7.4×10^{-5}		[?]
$t \to Hq$	10^{-4}		[694]

Table 48: Summary of the projected reach for the 95% C.L. limits on the branching ratio for anomalous flavor changing top couplings.

7 Effective coupling interpretations for top quark cross sections and properties

Effective Field Theory (SMEFT) [574, 575], where the SM is augmented by a set of higher-dimension operators

$$\mathcal{L}_{\rm SMEFT} = \mathcal{L}_{\rm SM} + \sum_i \frac{C_i}{\Lambda^2}\mathcal{O}_i + \mathcal{O}(\Lambda^{-4}). \tag{53}$$

As an example the relevant operators for the tWb vertex are:

$$\mathcal{O}_{tW} = i\left(\bar{Q}\sigma^{\mu\nu}\,\tau_I\,t\right)\tilde{\phi}\,W^I_{\mu\nu} + \text{h.c.} \tag{54}$$

$$\mathcal{O}^{(3)}_{\phi q} = i\left(\phi^\dagger \overleftrightarrow{D}_\mu \tau_I \phi\right)\left(\bar{q}_i\,\gamma^\mu\,\tau^I q_i\right) + \text{h.c.} \tag{55}$$

in agreement with the notation of [192].

The operators of eq. (54)-(55) modify the Wtb interaction in the following way

$$\begin{aligned}\mathcal{L}^{\rm dim-6}_{Wtb} &= -\frac{g}{\sqrt{2}}\bar{b}(x)\gamma^\mu P_L t(x)\,W_\mu(x)\left(1+\frac{C^{(3)}_{\varphi Q}v^2}{\Lambda^2}\right)\\ &+ \frac{2\,v\,C_{tW}}{\Lambda^2}\bar{b}(x)\sigma^{\mu\nu}P_R t(x)\,\partial_\nu W_\mu(x) + \text{h. c.}\,,\end{aligned} \tag{56}$$

where $v = 246$ GeV is the Higgs doublet vacuum expectation value, and y_t the top quark Yukawa coupling. Here and below we assume $V_{tb} = 1$. We remark that a slightly different approach [696–700], not using operators but anomalous couplings, has also been used in the literature. It is straightforward to connect the operator coefficients with the anomalous couplings description. The connection between the operator coefficients to the anomalous couplings is discussed in [610]. Wtb vertex can be probed in single top production ($t-, Wt, s-$channel top production), W helicity fractions and forward-backward asymmetries.

Similarly the coupling of the top to the Z and photon can be parametrised by the dimension-6 operators as discussed in [192], where the relevant degrees of freedom are discussed. The relevant degrees of freedom for the top-Z interaction $c^-_{\phi Q}, c^3_{\phi Q}, c_{\phi t}, c^{[I]}_{tZ}$ whilst the photon-top interaction depends on $c^{[I]}_{tA}$ as defined in [192]. Phenomenological studies of top production in association with a vector boson or a photon exist in the literature [217, 218, 701, 702] including NLO QCD corrections.

In this section we examine the prospects of probing top charged and neutral couplings at the HL-LHC.

7.1 The top quark couplings to the W boson

The latest and most precise measurements on single top quark production cross sections ($t-, Wt-$ and $s-$channels) [?, ?, 573, 703–709], W boson helicity fractions (F_0,F_L and F_R) [710, 711] and

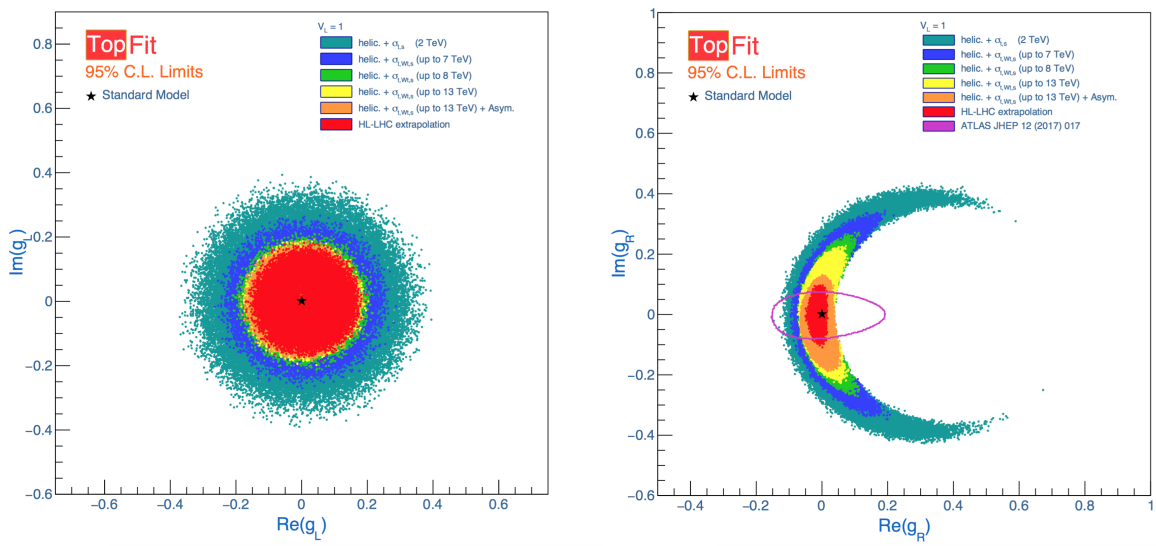

Fig. 85: Limits at 95% CL on the allowed regions for anomalous couplings. The *two*- dimensional distributions of the Re versus the Im components of g_L (left) and g_R (right), are shown.

forward-backward asymmetries (A_{FB}^{ℓ},A_{FB}^{N},A_{FB}^{T}) [712], measured at different centre-of-mass energies i.e., 2 TeV at Tevatron and 7, 8 and 13 TeV at the LHC, were used to set stringent 95% Confidence Level (CL) limits on possible new physics that affect the Wtb vertex structure. The results were extrapolated to the High-Luminosity (HL-LHC) phase of the LHC, by assuming the full expected luminosity (3000 fb^{-1}) and scaling the uncertainties obtained at the LHC for $\sqrt{s} = 13$ TeV (the central value of the observables were assumed to be the Standard Model prediction at 14 TeV). The statistical and simulation related uncertainties were scaled according to the total integrated luminosity at the HL-LHC. All generator and signal modelling related systematic uncertainties of these observables were extrapolated to be half of their current value, in accordance with the recent ATLAS and CMS official recommendations for the High-Luminosity studies. All experimental performance related uncertainties (leptons and jets, efficiencies, energy resolutions, etc.) were considered to maintain the current value at 13 TeV, at the exception of the efficiency of tagging jets from the hadronization of $b-$quarks ($b-tagging$), which is expected to be reduced by half. These extrapolated measurements were included in the global fit, in combination with the current measurements, in order to estimate expected limits on the real and imaginary components of the top quark couplings. The allowed regions of the new couplings are presented in Figure 85 and Table 49. Figure 85 allows also for a comparison between current LHC results and the HL-LHC projections.

HL-LHC	g_R	g_L	V_R
Allowed Region (Re)	[-0.05 , 0.02]	[-0.17 , 0.19]	[-0.28 , 0.32]
Allowed Region (Im)	[-0.11 , 0.10]	[-0.19 , 0.18]	[-0.30 , 0.30]

Table 49: 95% CL limits on the allowed regions of the real and imaginary components of the anomalous couplings. The combination of the measurements extrapolated to the HL-LHC (3000 fb^{-1}) is shown.

7.2 $t\bar{t}\gamma$

TO BE ADDED

7.3 $t\bar{t}Z$

Many beyond the Standard Model (BSM) predictions include anomalous couplings of the top quark to the electroweak gauge bosons [608, 713–718]. While we restrict this study to the $t\bar{t}Z$ channel and the CMS Phase-2 detector with a luminosity scenario of 3 ab^{-1}, we go beyond earlier work [702] and study the sensitivity of the $t\bar{t}Z$ process using differential cross section data. We interpret the result in terms of the SM effective field theory [192] and set limits on the relevant Wilson coefficients of the Warsaw basis [478] C_{tZ}, $C_{tZ}^{[Im]}$, $C_{\phi t}$ and $C_{\phi Q}$ [719, 720].

Event simulation

We generate events at the parton level at LO using `MADGRAPH5aMC@NLO` v2.3.3 [12], and decay them using `MadSpin` [364, 721]. Parton showering and hadronization are done using `PYTHIA` 8.2 [251, 324]. Fast detector simulation was performed using `Delphes` [232], with the CMS reconstruction efficiency parametrization for the Phase-2 upgrade with 200PU. Jets are reconstructed with the FastJet package [303] and using the anti-k_T algorithm [233] with a cone size $R = 0.4$. Besides the signals, we also generate the main backgrounds in the leptonic final states in order to achieve a realistic background prediction. The WZ, tZq, tWZ, $t\bar{t}\gamma$ and $t\bar{t}Z$ processes are normalized to cross sections calculated up to next-to-leading order (NLO) in perturbative QCD.

Event selection

From results on the inclusive $t\bar{t}Z$ cross section from ATLAS [722, 723] and CMS [724–727] it follows that the three lepton channel, where the Z and one of the W bosons originating from a top quark decay leptonically is the most sensitive search channel. We thus require three reconstructed leptons (e or μ) with $p_T(l)$ thresholds of 10, 20, and 40 GeV, respectively, and $|\eta(l)| < 3.0$. We furthermore require that there is among them a pair of opposite-sign same-flavor leptons consistent with the Z boson by requiring $|m(ll) - m_Z| < 10$ GeV. We remove reconstructed leptons within a cone of $\Delta R < 0.3$ to any reconstructed jet satisfying $p_T(j) > 30$ GeV. Furthermore, at least 3 jets are required with $p_T(j) > 30$ GeV and $|\eta(j)| < 4.0$, where one of the jets has been identified as a b-tag jet according to the `Delphes` specification.

We consider the distributions of the observables above in equally sized bins of the transverse Z boson momenta $p_T(Z)$ [701] and $\cos\theta_Z^*$, the relative angle of the negatively charged lepton to the Z boson direction of flight in the rest frame of the boson. The differential cross sections for the SM (black) and BSM (colored lines) interpretations in $t\bar{t}Z$ with respect to $p_T(Z)$ and $\cos\theta_Z^*$ are shown in Fig. 86 for C_{tZ} = 2.4 $(\Lambda/\text{TeV})^2$ and $C_{tZ}^{[Im]}$ = 2.4 $(\Lambda/\text{TeV})^2$. We normalize the BSM distributions to the SM yield in the plots to visualize the discriminating features of the parameters. The part of the signal which does not contain information on the Wilson coefficients is shown hatched, backgrounds are shown in solid colors.

Results

The predicted yields are estimated for the 3 ab^{-1} HL-LHC scenario at $\sqrt{s} = 13$ TeV and scaled to 14 TeV. We perform a binned profiled maximum log-likelihood fit of the ratio $q(r) = -2L(r, \hat{\theta}_r)/L(\hat{r}, \hat{\theta}))$, where θ are nuisance parameters and $\hat{\theta}_r$ maximize the likelihood function for a signal strength modifier r. $\hat{r}$ and $\hat{\theta}$ maximize L. Experimental uncertainties are estimated based on the expected performance of the Phase-2 CMS detector. In Fig. 87, the log-likelihood scan for the $t\bar{t}Z$ process is shown in the $C_{\phi Q}/C_{\phi t}$ parameter plane (left) and the dipole moment parameter plane $C_{tZ}/C_{tZ}^{[Im]}$ (right). The green (red) lines

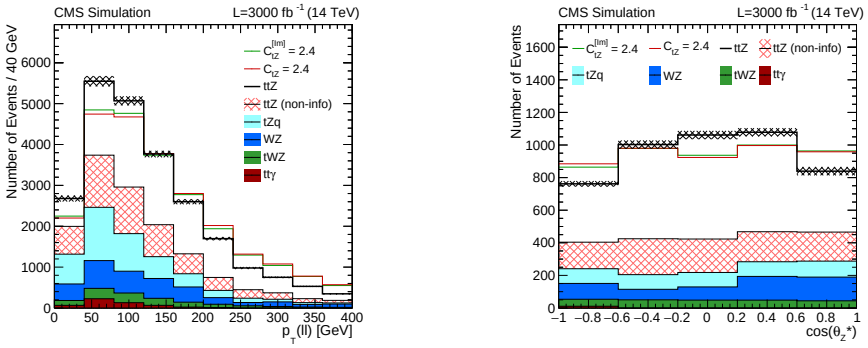

Fig. 86: Differential cross sections of $p_T(Z)$ (left) and $\cos\theta^*_Z$ (right) for the in the text mentioned selection and the Phase-2 scenario. For $\cos\theta^*_Z$, additionally $p_T(Z) > 200$ GeV is applied.

show the 1σ (2σ) contour line and the SM parameter point corresponds to $C_{\phi t} = C_{\phi Q} = 0$ and $C_{tZ} = C_{tZ}^{[Im]} = 0$.

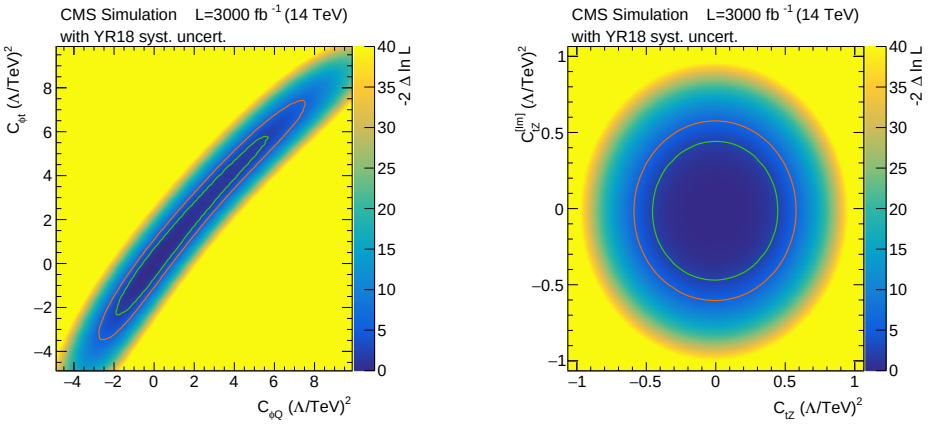

Fig. 87: Scan of the negative log-likelihood in the $C_{\phi Q}/C_{\phi t}$ (left) and $C_{tZ}/C_{tZ}^{[Im]}$ parameter planes (right) for the $t\bar{t}Z$ process. The $\pm1\sigma$ ($\pm2\sigma$) contour lines are given in green (red).

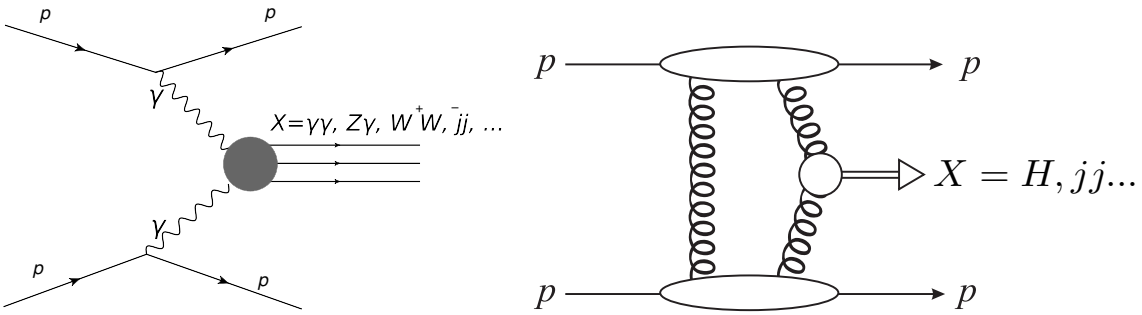

Fig. 88: Schematic diagram of the production of a system X in (left) two–photon (right) QCD–initiated central exclusive production.

8 Forward physics

8.1 Photon-induced collisions at the HL–LHC

Central exclusive production (CEP) corresponds to the production of central system X, and nothing else, with two outgoing intact protons:

$$pp \to p \; + \; X \; + \; p \; . \tag{57}$$

Such a process may be mediated by photon exchange, with the elastic photon emission vertex leaving the protons intact, see Fig. 88 (left). A range of SM (e.g. $X = \gamma\gamma$, $Z\gamma$, ZZ, $\ell\bar{\ell}$) and BSM states (e.g. $X =$ axion–like particles, monopoles, SUSY particles) may be produced in this way. These have the benefit of:

- The theoretical framework to model the underlying production mechanism, based on the equivalent photon approximation [728], is very well understood. Moreover, due to the peripheral nature of the interaction the possibility for additional inelastic proton–proton interactions (in other words of multiple–particle interactions) is very low.
- As the mass of the central system increases, the relative size of any contribution from QCD–initiated production, see Section 8.2, becomes increasingly small [729], due to the strong Sudakov suppression in vetoing on additional QCD radiation.

CEP therefore offers a unique opportunity at the LHC to observe the purely photon–initiated production of electromagnetically charged objects at the LHC in a clean and well understood environment; we in effect use the LHC as a photon–photon collider. The cross sections for such processes can be relatively small, in particular at higher mass, and therefore to select such events it is essential to run during nominal LHC running with tagged protons. The increased statistics available during the HL–LHC stage will allow these studies to push to higher masses and lower cross sections, increasing the discovery potential. A detailed study for the example case of anomalous quartic gauge couplings is discussed below.

8.1.1 Anomalous quartic gauge couplings with proton tagging at the HL-LHC

We discuss the discovery potential of anomalous quartic gauge interactions at the LHC via the measurement of central exclusive production. The central system X is reconstructed in the central detector (CMS, ATLAS) while the outgoing protons, which remain intact due to the coherent photon exchange, can be reconstructed with dedicated tracking detectors located in the very forward region at about $\pm$ 210 m (220 m) with respect to the interaction point of the CMS (ATLAS) experiment. The fractional momentum loss of the outgoing protons $\xi = \Delta p/p$ is reconstructed offline.Central exclusive production processes satisfy $m_X = m_X^{\text{fwd}} = \sqrt{\xi_1 \xi_2 s}$ and $y_X = y_X^{\text{fwd}} = \frac{1}{2}\log\left(\frac{\xi_1}{\xi_2}\right)$, where m_X and y_X are the mass

and rapidity of the system X reconstructed with the central detector, m_X^{fwd} and y_X^{fwd} are the mass and rapidity of the system X reconstructed with the forward detectors and $\sqrt{s}$ is the proton-proton center-of-mass energy. This relationship sets a powerful offline selection tool for background suppression, since non-exclusive events are not correlated to the forward protons.

For our projections, we assume that a similar set-up as with the CT-PPS and AFP detectors is possible at the HL-LHC. We will give an overview of the physics case for light-by-light scattering as the prototype example and the quartic $\gamma\gamma\gamma Z$ coupling as an instance of other gauge couplings that could be studied at the HL-LHC. Our projections consider also the impact of the difference of the measured time-of-flight for the intact protons with various timing precisions (on the order of 10 ps), which can be used to determine the longitudinal coordinate of the event vertex down to $\sim$ 2 mm. Time-of-flight measurements can help further reduce the background, especially at the HL-LHC where the number of interactions per bunch crossing will range from 140-200.

Scattering of light-by-light in p-p collisions

Under the assumption that there exists a New Physics energy scale Λ much heavier than the experimentally accessible energy E, new physics manifestations can be described using an effective Lagrangian valid for $\Lambda \gg E$. Among these operators, the pure photon dimension-eight operators $\mathcal{L}_{4\gamma} = \zeta_1^{4\gamma} F_{\mu\nu}F^{\mu\nu}F_{\rho\sigma}F^{\rho\sigma} + \zeta_2^{4\gamma} F_{\mu\nu}F^{\nu\rho}F_{\rho\lambda}F^{\lambda\mu}$ induce the $\gamma\gamma\gamma\gamma$ interaction. This coupling can be probed in $pp \to p(\gamma\gamma \to \gamma\gamma)p$ reactions. This sub-process and the SM light-by-light scattering one are implemented in the Forward Physics Monte Carlo (FPMC) event generator. The Equivalent Photon Approximation is used to calculate the emitted coherent photon flux off the protons.

With proton tagging, one can probe $\gamma\gamma \to \gamma\gamma$ collisions from about 300 GeV to 2 TeV. The mass acceptance on the photon pair is limited mainly by the acceptance of ξ of the proton taggers ($0.015 \leq \xi \leq 0.15$). The background is dominated by non-exclusive diphoton production events overlapped with uncorrelated events with intact protons coming from the secondary collisions occurring in the same bunch crossing. This background can be suppressed by looking at the central and forward systems kinematic correlations (the aforementioned mass and rapidity matching). The irreducible background coming from the SM exclusive diphoton production is negligible at large invariant masses. The background can be further suppressed if the time-of-flight difference of each of the scattered protons is measured. The precision of the event vertex longitudinal position determined with the time-of-flight measurement is given by $\delta z = c\,\delta t/\sqrt{2}$, where c is the speed of light and δt is the timing precision. For our projections, we have considered that the average pileup was of 200 collisions per bunch crossing.

The expected bounds on the anomalous couplings $\zeta_{1,2}^{4\gamma}$ at 95% CL are calculated based on the total expected background rate and can be seen in Fig. 89. The reach on the quartic couplings $\zeta_{1,2}^{4\gamma}$ down to $5 \cdot 10^{-14}$ GeV^{-4} with 300 fb^{-1} at 14 TeV, and down to $1 \cdot 10^{-14}$ GeV^{-4} at the HL-LHC with a luminosity of 3000 fb^{-1} without using time-of-flight information. The last bound can be improved by a factor of $\sim$ 1.2 if the timing precision is of 10 ps.

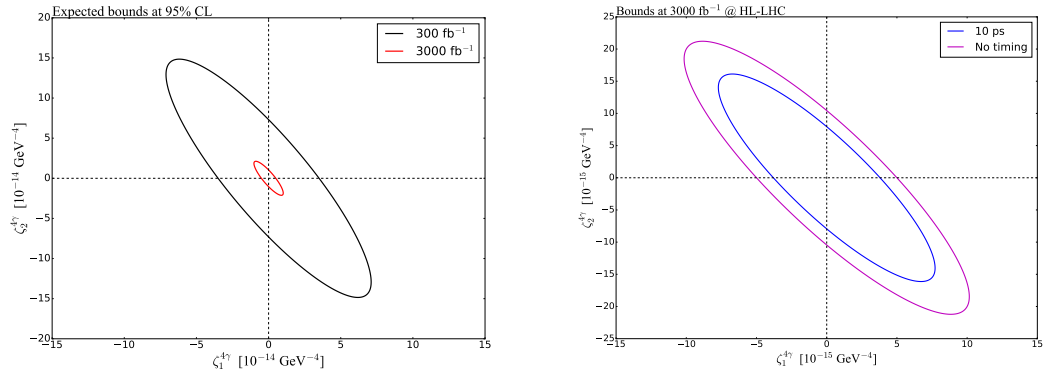

Fig. 89: Expected bounds at 95% CL on the anomalous quartic coupling for 300 fb^{-1} and at the HL-LHC with 3000 fb^{-1} (no time-of-flight measurement) (left). Expected bounds at 95%CL on the anomalous couplings at the HL-LHC with time-of-flight measurement with precision of 10 ps and without time-of-flight measurement (right).

Constraining $\gamma\gamma\gamma Z$ coupling via $pp \to p(\gamma\gamma \to \gamma Z)p$

The $\gamma\gamma\gamma Z$ interaction is induced at one-loop level in the SM via loops of fermions and $W^{\pm}$ bosons. Loops of heavy particles charged under $\mathrm{SU}(2)_L \times \mathrm{U}(1)_Y$ contribute to the $\gamma\gamma\gamma Z$ couplings. The dimension-eight effective operators are $\mathcal{L}_{\gamma\gamma\gamma Z} = \zeta_1^{3\gamma Z} F^{\mu\nu} F_{\mu\nu} F^{\rho\sigma} Z_{\rho\sigma} + \zeta_2^{3\gamma Z} F^{\mu\nu} \tilde{F}_{\mu\nu} F^{\rho\sigma} \tilde{Z}_{\rho\sigma}$, which induce the $\gamma\gamma\gamma Z$ interaction. This induces the anomalous $\gamma\gamma \to \gamma Z$ scattering and generates the rare SM decay $Z \to \gamma\gamma\gamma$. This coupling can be probed in $pp \to p(\gamma\gamma \to \gamma Z)p$ reactions. The sub-process was implemented in the FPMC event generator as well.

Since the exclusive channel is very clean, it allows the possibility of studying exclusive $Z\gamma$ production with the Z boson decaying into a charged lepton pair or to hadrons (dijet or large radius jet signature). The signature $(Z \to \ell\bar{\ell}) + \gamma$ is much cleaner, but has vastly fewer events than $(Z \to \text{hadrons}) + \gamma$ final states. We apply a similar event selection on the exclusive $Z\gamma$ production as in the exclusive $\gamma\gamma$ case. The sensitivity on the anomalous coupling at 95% CL combining both channels at 14 TeV with 300 fb^{-1} of data is on the order of $1 \cdot 10^{-13}$ GeV $^{-4}$ (see Fig. 90). For the HL-LHC with 3000 fb^{-1} it scales down to $1 \cdot 10^{-14}$ GeV^{-4} when combining both channels. The time-of-flight measurement can improve the expected bounds by a factor of ~ 2 .

8.2 Central exclusive production: QCD prospects

The CEP process may be mediated purely by the strong interaction, and in such a case if the mass of the central system is large enough a perturbative approach may be applied, via the diagram shown in Fig. 88 (right), see [730, 731] for reviews. As well as probing QCD in a novel regime, the exclusive nature of this process has the benefit that the produced object obeys a quantum number selection rule. Namely the object must be C even, while the production of P even states with $J_z = 0$ angular momentum projection on the beam axis is strongly dominant. From the point of view of the production of new BSM states or the understanding of existing QCD bound states (e.g. exotic quarkonia) this therefore

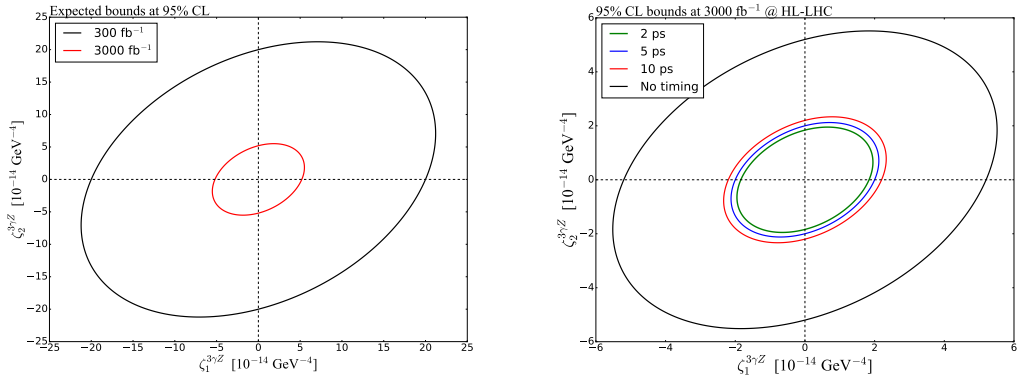

Fig. 90: Expected bounds on the anomalous couplings at 95%CL between 300 fb^{-1} and 3000 fb^{-1} at the HL-LHC (no time-of-flight measurement) (left). Expected bounds at 95%CL for timing precisions of $\delta t = 2,\ 5,\ 10$ ps at the HL-LHC (right).

has the benefit of identifying the produced object quantum numbers. The $J_z = 0$ selection implies that only certain helicity configurations in the underlying $gg \to X$ production process contribute, which also leads to unique phenomenological consequences. A detailed discussion of this selection rule can be found in [731] and the references therein. Two example processes, namely exclusive jet and Higgs boson production, are discussed briefly below. These represent higher mass test cases relevant to HL–LHC running with tagged protons at ATLAS/CMS. The possibilities for the observation of lower mass objects with the ALICE detector will be addressed in Section 8.4.

The exclusive production of jets provides a new and unexplored area of QCD phenomenology. While this process has been observed at the Tevatron [732, 733], so far no data has been taken at the LHC. The quantum number selection rule discussed above has a number of consequences that are quite distinct from the standard inclusive channels. In particular, the production of purely gluonic dijets is predicted to be strongly dominant, allowing a study of purely gg jets from a colour–singlet initial state. In the three–jet case the presence of 'radiation zeros' [734], that is a complete vanishing in the leading order amplitudes for certain kinematic configurations, is expected. This phenomena is well known in electroweak processes, but this is the only known example of a purely QCD process where this occurs. Some representative predictions for the HL–LHC are shown in Table 50. These are calculated using the `SuperChic 2.5` MC generator [735], which provides the most up to date predictions for CEP processes. The cross sections are suppressed relative to the inclusive case, but are nonetheless relatively large. On the other hand, in the three jet case, in particular in the invariant mass region that may be relevant for the acceptance of proton tagging detectors, the cross sections are lower and would clearly benefit from as large a data sample as possible for studies of novel features, such as radiation zeros and other jet shape variables.

The production of the Higgs boson through exclusive gg fusion would represent a completely new observation channel. As discussed in more detail in [731], this has the potential to shed light on the CP properties of the state, as well as its coupling to b quarks in a distinct way to inclusive channels. The cross section for a SM Higgs, as predicted by `SuperChic 2.5` [735], is $\sigma(|y_H| < 2.5) = (1 \overset{\times}{\div} 2)$ fb, where the dominant uncertainties are due to PDFs and modelling of the soft gap survival probability. The predicted

Table 50: Parton–level predictions for exclusive two and three jet production cross sections (in pb) at the LHC for different cuts on the minimum central system invariant mass M_X at $\sqrt{s} = 14$ TeV. The jets are required to have transverse momentum $p_\perp > 20$ GeV for $M_X(\mathrm{min}) = 75, 150$ GeV and $p_\perp > 40$ GeV for $M_X(\mathrm{min}) = 250$ GeV and pseudorapidity $|\eta| < 2.5$. The anti–k_t algorithm with jet radius $R = 0.6$ is used in the three jet case and the $q\bar{q}$ cross sections correspond to one massless quark flavour.

$M_X(\mathrm{min})$	gg	$q\bar{q}$	$b\bar{b}$	ggg	$gq\bar{q}$
75	130	0.032	0.082	5.0	0.11
150	4.5	6.1×10^{-4}	1.1×10^{-3}	0.70	0.019
250	0.15	2.2×10^{-5}	2.7×10^{-5}	0.016	4.3×10^{-4}

rate is therefore relatively small, and would again benefit both from the increased statistics available in HL running, and even more crucially from the potential installation of new tagging detectors at a larger distance from the ATLAS/CMS IPs (see Section 8.3), which would extend the existing mass acceptance into the Higgs region.

8.3 Tagged proton at the HL–LHC: experimental prospects

This section discusses possible locations for movable near-beam detectors along the outgoing beam lines near IP5, designed for detecting the leading protons from central production processes (Fig. 88, Eqn. (57)). While the results which follow consider the possibilities for detectors in association with the CMS experiment, we can expect qualitatively similar prospects in the case of the ATLAS detector, although this is not discussed explicitly here. After identifying the best-suited positions, the proton detection acceptance and hence the central-mass tagging reach is calculated for each of these positions as a function of beam parameters and based on present-day assumptions on optics (Version 1.3), collimation scheme and near-beam-detector insertion rules from machine protection arguments. Given that at the time of this article the crossing-angle plane in IP5 (horizontal as until LS3, or vertical) has not yet been decided, both options have been investigated. It has to be pointed out that the crossing planes of IP1 and IP5 have to be different: one will be horizontal, the other vertical.

While in the CT-PPS (later PPS) project [736] in Run 2 the near-beam detectors were Roman Pots inherited from the TOTEM experiment [737, 738] and upgraded for high-luminosity operation [739], no technological assumptions are made at this early stage of preparation for HL-LHC. The highly demanding engineering and detector physics challenges are not addressed here.

Possible Locations for Near-Beam Detectors

The search for suitable detector locations around IP5 is driven by the goal to cover the widest possible range of central masses M to be measured via the fractional momentum losses

$$\xi_{1/2} = \frac{\Delta p_{1/2}}{p} \tag{58}$$

of the two surviving protons using the relation

$$M^2 = \xi_1 \, \xi_2 \, s \, , \tag{59}$$

where $\sqrt{s} = 14\,\text{TeV}$ is the centre-of-mass energy.

The minimum accessible ξ of leading protons at a location z [26] along the beam line is given by

$$\xi_{\text{min}}(\alpha, \beta^*, z) = \frac{[n_{\text{TCT}}(\beta^*) + \Delta n]\sigma_{\text{XRP}}(\beta^*, z) + \Delta d + \delta}{D_{x,\text{XRP}}(\alpha, \xi_{\text{min}}, z)}\,, \tag{60}$$

where σ_x is the horizontal beam width depending on the optics (characterised by β^*), D_x is the horizontal dispersion depending on the crossing-angle α, n_{TCT} is the half-gap of the tertiary collimators (TCT) as defined by the collimation scheme, $\Delta n = 3$ is the retraction of the near-beam detector housings (e.g. Roman Pots) relative to the TCT position in terms of σ_x, $\Delta d = 0.3\,\text{mm}$ is an additional safety retraction to allow for beam orbit fluctuations, and the constant δ, typically 0.5 mm, accounts for any distance between the outer housing surface closest to the beam and the sensitive detector. The dependence of the dispersion on ξ implies that Eqn. (60) has to be resolved for ξ_{min} after parameterising $D_x(\xi)$.

The first step of the study is to plot the z-dependent quantities, σ_x and D_x, along the outgoing beam line for one typical HL-LHC optics configuration (Figure 91, left). The resulting ξ_{min} is shown in Figure 91 (right). Note that for vertical crosing smaller values are reached. The locations most suitable for the measurement of small $|\xi|$ values are marked in red. Closer layout inspection of the region around the minimum at 232 m (inside the quadrupole Q6) indicated two promising locations: at 220 m (just before the collimator TCL6) and at 234 m (after the exit of Q6). Even smaller momentum losses can be reached at 420 m (the "missing magnet" region already studied previously by the FP420 project [740]).

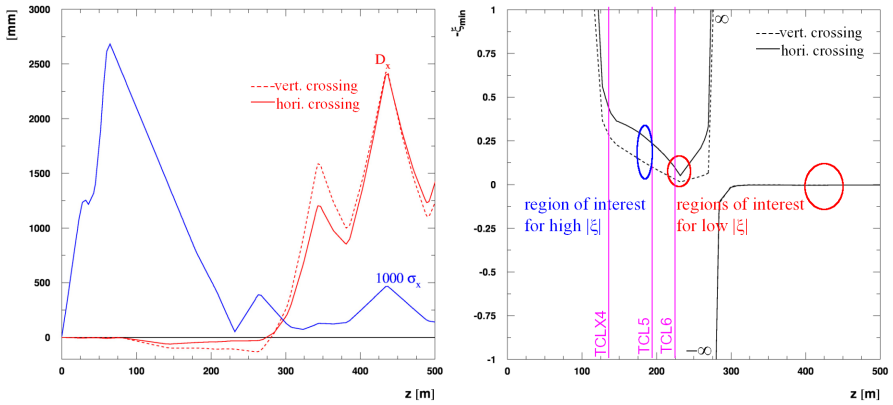

Fig. 91: horizontal dispersion and beam width (scaled by 1000) as a function of the distance s from IP5 for Beam 1, i.e. in LHC Sector 5-6 (left). Minimum accepted ξ as a function of z according to Eqn. (60) for $(\alpha/2, \beta^*) = (250\,\mu\text{rad}, 15\,\text{cm})$ and $n_{\text{TCT}} = 12.9$ (right). The TCL collimator positions are indicated. In both pictures the continuous and dashed lines represent horizontal and vertical crossing in IP5, respectively.

The apparent sign change of ξ_{min} at $z \approx 270\,\text{m}$ reflects the sign change of the dispersion at that location (as seen in the left panel of the figure). It means that the diffractive proton trajectories transition from $x > 0$ to $x < 0$. The implication for the potential detector location at 420 m is that detectors need to be placed in the confined space between the incoming and the outgoing beam pipes, excluding

[26] In this article the variable z is used for the longitudinal coordinate instead of s to avoid confusion with the Mandelstam s.

conventional Roman Pot technology. A further complication is that in this location the beam pipes are in a cryostat, necessitating more involved engineering changes.

A region of interest for the detection of higher masses lies at 196 m just upstream of the collimator TCL5 that intercepts protons with large $|\xi|$ (Section 8.3). Locations even further upstream, before TCLX4, would give an even higher upper mass cut but are excluded due to the prohibitively high low-mass limit leaving no acceptance interval.

In summary, for the more detailed discussions in the following sections, four detector locations have been retained: 196 m, 220 m, 234 m, 420 m.

Crossing-Angle and Optics Dependence of the Mass Acceptance Limits

In the previous section, only one specific combination of crossing-angle α and beam optics (β^*) was considered. However, at HL-LHC luminosity levelling will be performed in all fills by changing α and β^* in a pre-defined sequence. For the present study the $(\alpha/2,\, \beta^*)$ trajectories envisaged in [741] were used.

Minimum Mass

The minimum mass accepted at a location z for given α and β^* can be calculated using Eqns. (59) and (60). For simplicity, symmetric optics in the two beams, i.e. equal $\xi_{\rm min}$, are assumed:

$$M_{\rm min} = |\xi_{\rm min}|\,\sqrt{s}\,. \tag{61}$$

The α and ξ dependences of D_x can be parameterised based on simulations with MAD-X [742]. The α dependence is linear, and the ξ-dependence can be linearly approximated within the ξ-ranges relevant in practice.

The β^* dependence of $\sigma_{\rm XRP}$ was calculated analytically, profitting from invariance properties of the presently planned family of ATS optics. This is likely to change in the future and will need to be adapted.

The β^* dependence of $n_{\rm TCT}$ follows the presently foreseen collimation strategy [743] of keeping the TCT gap constant at $d_{\rm TCT} = 12.9\,\sigma_{\rm TCT}(\beta^* = 15\,{\rm cm})$ (for nominal emittance $\varepsilon_n = 2.5\,\mu$m rad), implying $n_{\rm TCT}(\beta^*) = \frac{d_{\rm TCT}}{\sigma_{\rm TCT}(\beta^*)}$, where an analytical expression for $\sigma_{\rm TCT}(\beta^*)$ can be derived.

The result of this calculation, contour lines of $M_{\rm min}$ in the beam parameter space $(\alpha/2, \beta^*)$, is shown in Fig. 92 for the four detector locations chosen in the previous section. Some possible luminosity-levelling trajectories are drawn, too. The start point at the beginning of the fill is always at the maximum β^* value.

From these graphs we draw the following conclusions:

- The main driving factor for the minimum mass is the dispersion which in turn is fully determined by the crossing-angle. The optics (via β^*) plays a minor role.
- If the 420 m location can be instrumented, the minimum mass is about 50 GeV with only a very weak dependence on the optics, the crossing-angle and its plane (horizontal or vertical).
- Without the 420 m location, vertical crossing gives a much better low-mass acceptance (210 GeV) than horizontal crossing (660 GeV).

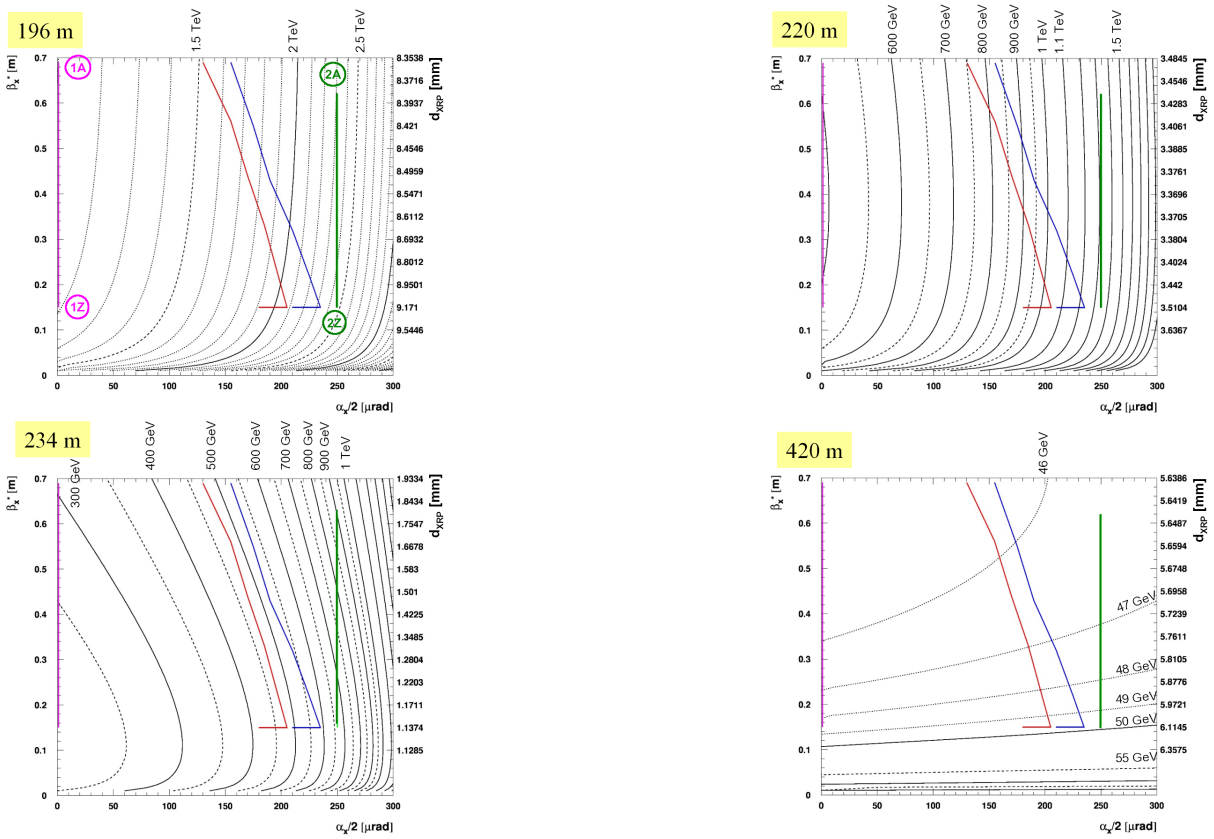

Fig. 92: Contour lines for the minimum accepted mass $M_{\text{min}} = |\xi|_{\text{min}}\sqrt{s}$ in the crossing-angle/optics parameter space $(\alpha/2, \beta^*)$. On the right-hand ordinate the XRP approach distance is calculated from β^*. The coloured lines represent possible luminosity-levelling trajectories [741]. For horizontal crossing: green = "baseline", blue = "relaxed adaptive", red = "aggressive adaptive"; for vertical crossing: violet = any trajectory. The labels (1A) – (2Z) in the first panel define the trajectory start and end points used in Figs. 94 and 95.

Maximum Mass

The maximum mass accepted at a location z is determined by the tightest aperture restriction d_A upstream of z and the dispersion there:

$$M_{\text{max}} = |\xi_{\text{max}}|\,\sqrt{s} = \frac{d_A}{D_A(\alpha, \xi_{\text{max}})}\,. \tag{62}$$

In the case of vertical beam crossing in IP5, both horizontal and vertical apertures may impose limitations, whereas in the case of horizontal crossing there is no substantial vertical dispersion and hence no acceptance loss from the vertical aperture. Fig. 93 shows the results of a complete aperture study. It was concluded that even for vertical crossing most limitations come from the horizontal aperture and that for all locations, except 420 m, this horizontal aperture is limited by the TCL collimators. At 420 m, on the other hand, the beam-pipe absorbs diffractive protons with $|\xi| > 0.012$. The highest

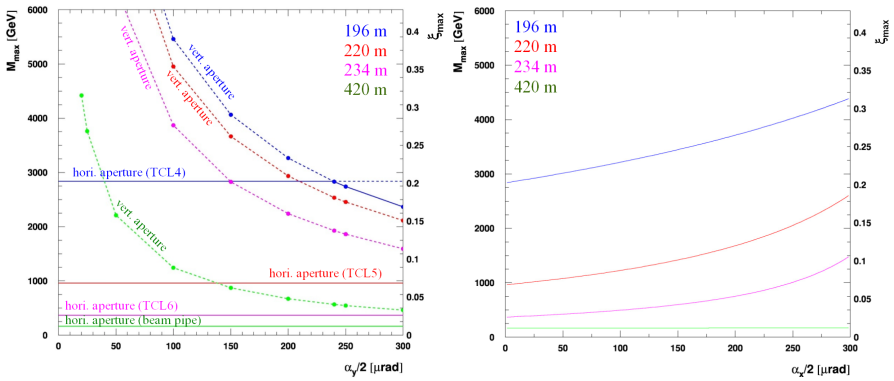

Fig. 93: Maximum accepted diffractive mass for each detector location as a function of the crossing-angle. Vertical crossing (left): both horizontal and vertical apertures contribute to the mass limits. The continuous lines denote the most restrictive, i.e. dominant, limitations. Horizontal crossing (right): only the horizontal apertures contribute.

masses are accepted by the unit at 196 m: up to 2.7 TeV for vertical crossing and up to 4 TeV for horizontal crossing.

Mass-Rapidity Acceptance

The CEP acceptance for a given point in the beam parameter space (α, β^*) can be visualised by drawing for every instrumented detector location the $|\xi|$-acceptance bands – whose limits are calculated according to the previous section – in the mass-rapidity plane

$$\left(\ln\frac{M}{\sqrt{s}}, y\right) = \left(\frac{1}{2}(\ln\xi_1 + \ln\xi_2), \frac{1}{2}(\ln\xi_1 - \ln\xi_2)\right) . \tag{63}$$

Fig. 94 shows these (M, y) contour plots for the start and end points of the two extreme levelling cases defined in Fig. 92: points (1A) and (1Z) for any trajectory with vertical crossing in IP5, points (2A) and (2Z) for the "Baseline" trajectory with horizontal crossing. The projections on the mass axis, under the approximation of flat rapidity distributions, are given in Fig. 95.

The following observations are made:

- The acceptance zones of the four detector locations are non-overlapping and separated by gaps. For horizontal crossing the gaps are wider than for vertical crossing.
- Although the double-arm acceptance has mass gaps at central rapidities, the mixed acceptance zones combining different detector units in the two arms of the experiment (e.g. 420 m left + 234 m right) fill some of these mass gaps by providing acceptance at forward rapidities.
- The gaps between the acceptances of 196 m, 220 m and 234 m can potentially be closed by opening TCL5 and TCL6 a little further if allowable from machine protection arguments. On the other hand, the gap between 234 m and 420 m is caused by the beam pipe at $z > 300$ m limiting the aperture. It could only be closed by adding a detector unit near 300 m.

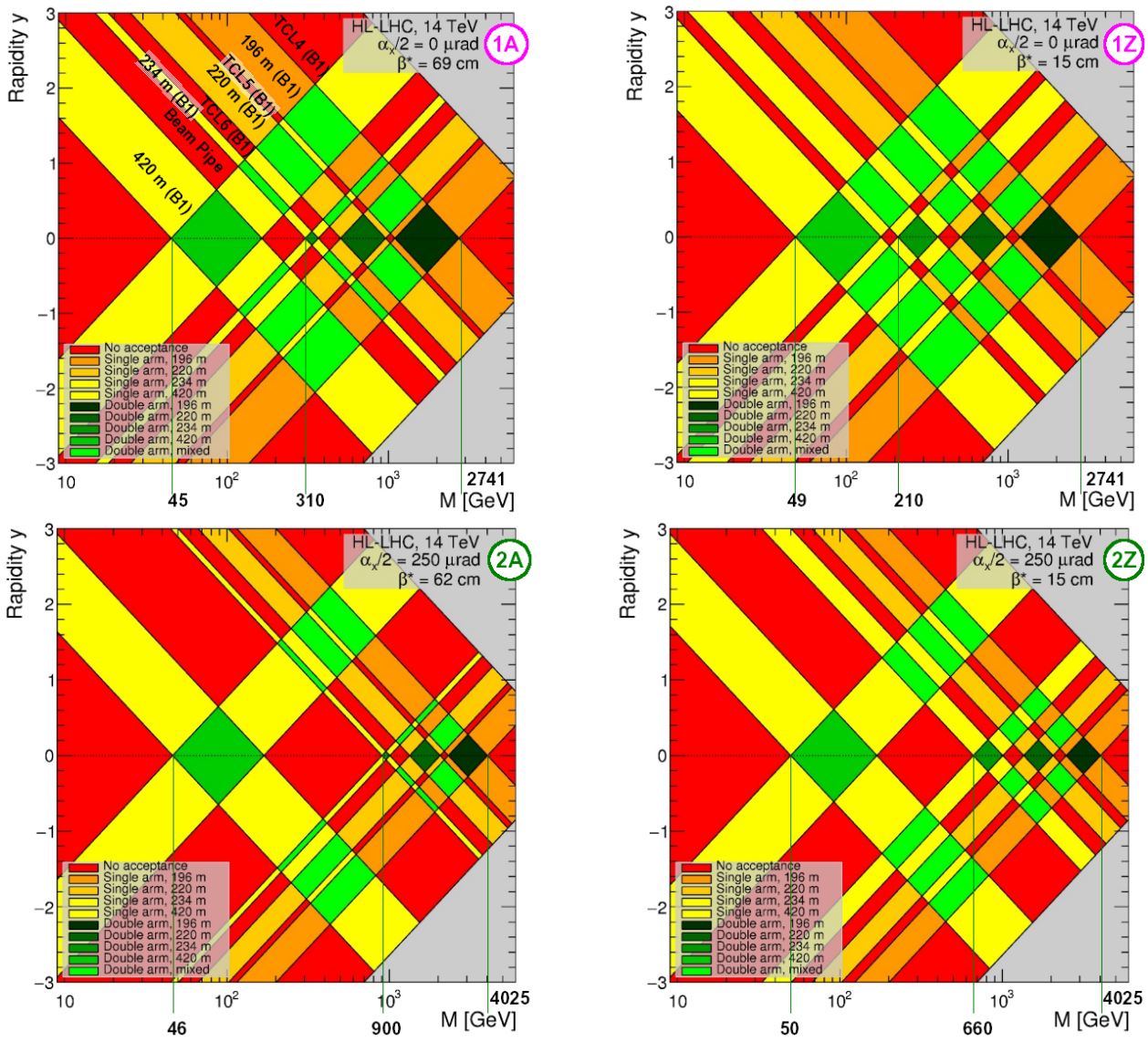

Fig. 94: Acceptance for the protons from central diffraction in the mass-rapidity plane. The yellow/orange colour tones mark single-arm proton acceptance, the green tones mark double-arm acceptance. Top: start and end point of any levelling trajectory for vertical crossing, bottom: start and end point of the baseline levelling trajectory for horizontal crossing.

8.4 Low-mass central exclusive production

Central exclusive production of low-mass diffractive states in pp collisions at the LHC may serve as a valuable source of information on the nonperturbative aspects of strong interaction. At low masses, CEP is usually described in terms of double pomeron exchange (DPE) mechanism. DPE is expected to be an ideal process for the investigation of meson resonances with $I^G(J^{PC}) = 0^+(0^{++}, 2^{++}, \ldots)$ quantum

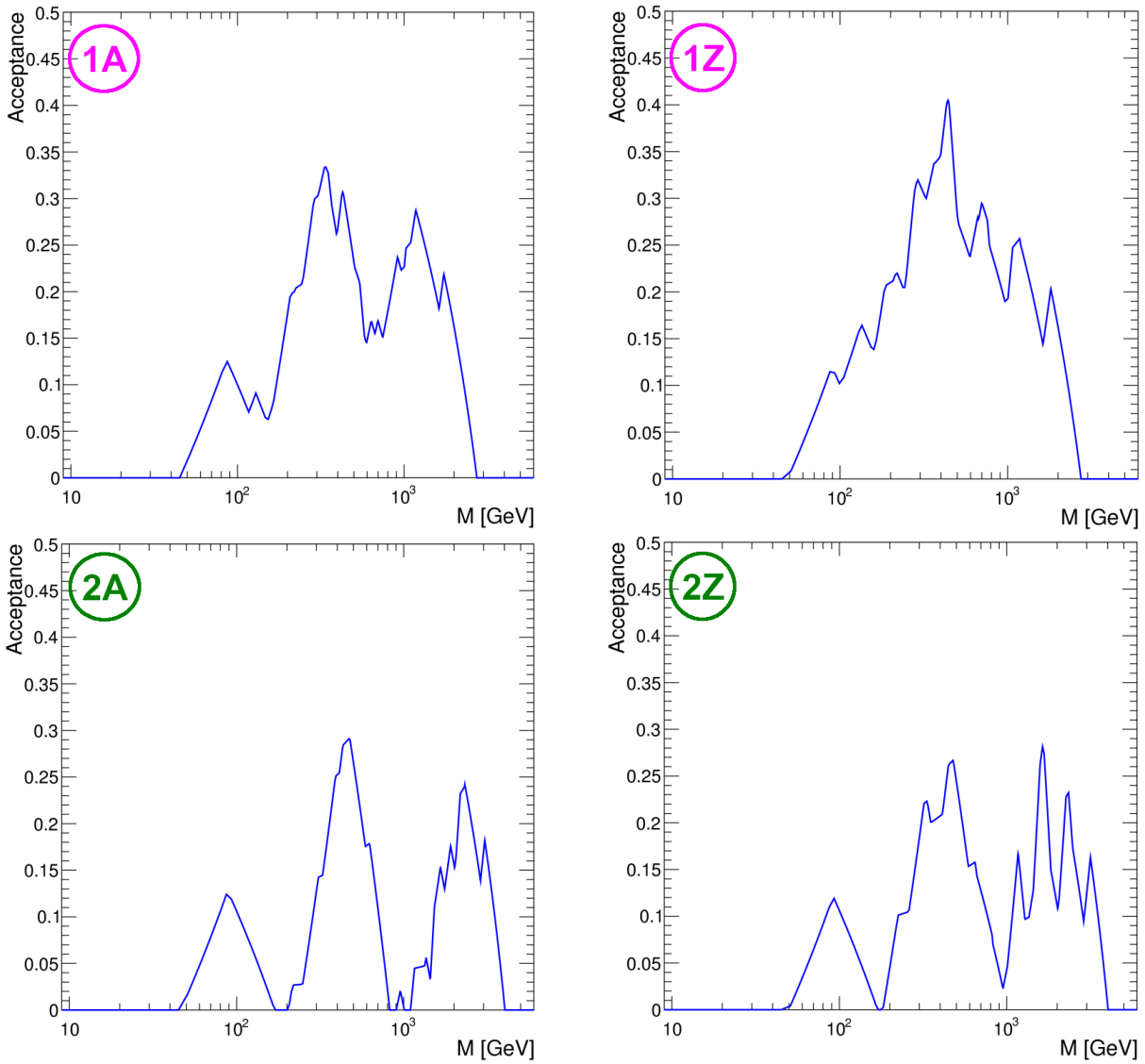

Fig. 95: Projection of the (M, y) acceptance on the mass axis, adding up all the double-arm areas of Fig. 94 for the same points in the (α, β^*) beam parameter space.

numbers and gluonic bound states. Glueball searches in CEP are of particular interest because lattice QCD calculations predict lightest glueballs to have masses $M_G(0^{++}) = 1710$ MeV and $M_G(2^{++}) = 2390$ MeV [744]. Pure glueballs are predicted to decay equally well into pair of pions, kaons or η mesons with suppressed two photon decays. However this simple signature is spoiled by the fact that glueballs are expected to mix with nearby $q\bar{q}$ states.

Central-exclusive production of low-mass resonances in $\pi\pi$ and KK channels has been extensively studied in fixed target experiments at CERN and Fermilab (see review in [730]) and recent collider experiments at RHIC [745], Tevatron [746] and the LHC [747]. The partial-wave analysis (PWA)

has been performed in several experiments to investigate the spin-parity nature of the centrally produced system [748–750]. There is a clear evidence of supernumerous light scalar meson states, not fitting well into the conventional groundstate $q\bar{q}$ nonet and suggesting that some of these states have significant gluonic component. $f_0(1370)$, $f_0(1500)$ and $f_0(1710)$ mesons are considered as most promising glueball-meson mixing state candidates but the nature of all these states is still open for discussion [751]. In the tensor sector, the lightest isoscalar $q\bar{q}$ states $f_2(1270)$ and $f_2'(1525)$ are well established however there are at least four additional reported tensor resonances requiring confirmation.

CEP can be also used to investigate the spin structure of the Pomeron and its coupling to hadrons. Historically, the Pomeron was considered as effective spin 1 quasiparticle supported by successful fits of total and differential pp cross sections [752]. Recently, an alternative approach based on the tensorial Pomeron has been developed [753] providing definitive predictions and restrictions of spin-parity, polarization and rapidity of the produced diffractive system in CEP at the LHC [754–756].

Multidifferential measurements and PWA of $\pi\pi$, KK and $p\bar{p}$ final states in a wide range of invariant masses in CEP at the LHC would also allow one to constrain poorly known Pomeron-meson couplings and form-factors in various phenomenological models [754, 757] and also build a transition to perturbative QCD models of hadron pair production in CEP [758] valid at high invariant masses and transverse momenta of the produced pair. Another important outcome of CEP measurements would be a determination of the absorptive corrections, the probability that the rapidity gaps would be filled with particles from accompanying initial- or final-state interactions. The central exclusive production of meson pairs therefore represents a process of much phenomenological interest, which can shed light on both perturbative and non–perturbative aspects of QCD.

Perturbative aspects of QCD can be also investigated in CEP of heavy quarkonium states [731]. Detailed studies of χ_c resonances in CEP at the LHC would provide a valuable input to test the ideas and methods of the QCD physics of bound states. Measurements of the outgoing proton momentum distributions, cross sections and relative abundances of χ_{c0}, χ_{c1} and χ_{c2} states would be important for the test of the overall theoretical formalism.

Measurements of CEP processes rely on the selection of events with only few tracks in an otherwise empty detector, therefore large pseudorapidity coverage and low pileup conditions are essential to guarantee the event emptiness. The ALICE detector nicely matches these requirements. Low material budget, access to low transverse momenta and excellent PID capabilities in ALICE serve as additional advantages. First CEP measurements have been already performed by ALICE in the LHC Run 1 and 2. Fig. 96 illustrates raw invariant mass spectra of $\pi^+\pi^-$ and K^+K^- pairs in CEP events collected by ALICE in proton-proton collisions at $\sqrt{s} = 13$ TeV, where one can easily identify several resonance structures. ALICE is going to collect a much larger sample of central exclusive events and significantly extend the scope of the CEP program in proton-proton collisions in LHC Run 3 with expected integrated luminosity of about 200 pb^{-1} and much better efficiency in the continuous readout mode. The CEP program includes glueball searches and precision hadron spectroscopy in $\pi^+\pi^-$, K^+K^-, $p\bar{p}$, $2\pi2K$, 4π and other channels. The expected high integrated luminosity will also allow ALICE to measure the spectrum of heavy quarkonium states in various decay channels, e.g. a yield of at least 50k $\chi_{c0} \to \pi^+\pi^-$ decays is expected in CEP events by the end of Run 3 based on cross section estimates from SuperChic generator [759].

The LHCb experiment can extend the CEP program to forward rapidities. High luminosity at moderate pileup and good hadron PID capabilities would be particularly useful for the studies of heavy

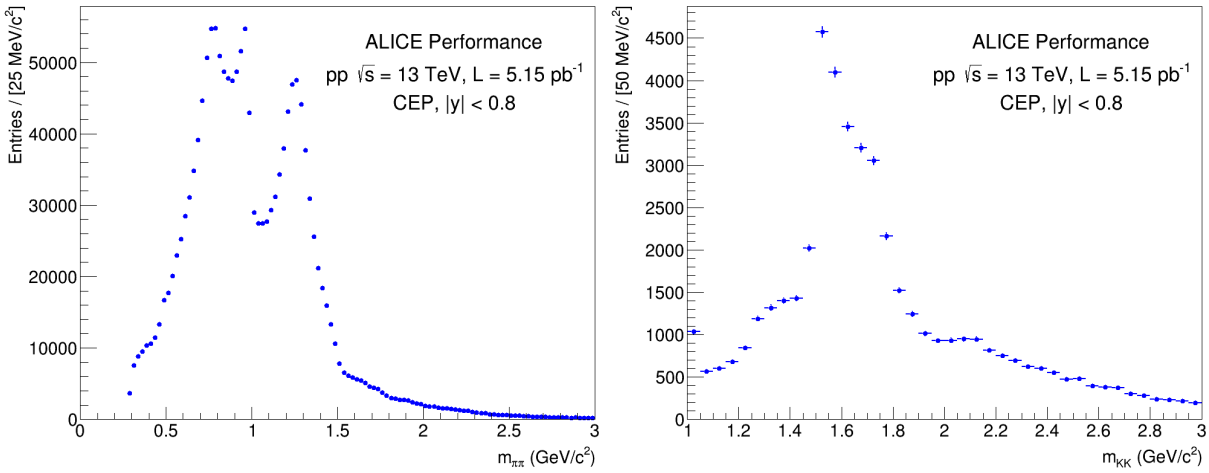

Fig. 96: Raw invariant mass spectra of $\pi^+\pi^-$ (left) and K^+K^- (right) pairs in CEP events collected by ALICE in proton-proton collisions at $\sqrt{s} = 13$ TeV.

quarkonium states in central exclusive events. Measurements of low-mass central exclusive production processes with proton tagging might be also possible with ATLAS and CMS detectors during low pile-up runs at high β^*.

References

[1] R. K. Ellis and G. Zanderighi, *Scalar one-loop integrals for QCD*, JHEP **02** (2008) 002, arXiv:0712.1851 [hep-ph].

[2] A. van Hameren, *OneLOop: For the evaluation of one-loop scalar functions*, Comput. Phys. Commun. **182** (2011) 2427–2438, arXiv:1007.4716 [hep-ph].

[3] S. Frixione, Z. Kunszt, and A. Signer, *Three jet cross-sections to next-to-leading order*, Nucl. Phys. **B467** (1996) 399–442, arXiv:hep-ph/9512328 [hep-ph].

[4] S. Catani and M. H. Seymour, *A General algorithm for calculating jet cross-sections in NLO QCD*, Nucl. Phys. **B485** (1997) 291–419, arXiv:hep-ph/9605323 [hep-ph]. [Erratum: Nucl. Phys.B510,503(1998)].

[5] R. Britto, F. Cachazo, and B. Feng, *Generalized unitarity and one-loop amplitudes in N=4 super-Yang-Mills*, Nucl. Phys. **B725** (2005) 275–305, arXiv:hep-th/0412103 [hep-th].

[6] G. Ossola, C. G. Papadopoulos, and R. Pittau, *Reducing full one-loop amplitudes to scalar integrals at the integrand level*, Nucl. Phys. **B763** (2007) 147–169, arXiv:hep-ph/0609007 [hep-ph].

[7] R. K. Ellis, W. T. Giele, Z. Kunszt, and K. Melnikov, *Masses, fermions and generalized D-dimensional unitarity*, Nucl. Phys. **B822** (2009) 270–282, arXiv:0806.3467 [hep-ph].

[8] W. T. Giele, Z. Kunszt, and K. Melnikov, *Full one-loop amplitudes from tree amplitudes*, JHEP **04** (2008) 049, arXiv:0801.2237 [hep-ph].

[9] R. K. Ellis, Z. Kunszt, K. Melnikov, and G. Zanderighi, *One-loop calculations in quantum field theory: from Feynman diagrams to unitarity cuts*, Phys. Rept. **518** (2012) 141–250, arXiv:1105.4319 [hep-ph].

[10] F. Cascioli, P. Maierhofer, and S. Pozzorini, *Scattering Amplitudes with Open Loops*, Phys. Rev. Lett. **108** (2012) 111601, arXiv:1111.5206 [hep-ph].

[11] G. Cullen et al., *GOSAM-2.0: a tool for automated one-loop calculations within the Standard Model and beyond*, Eur. Phys. J. **C74** (2014) no. 8, 3001, arXiv:1404.7096 [hep-ph].

[12] J. Alwall, R. Frederix, S. Frixione, V. Hirschi, F. Maltoni, O. Mattelaer, H. S. Shao, T. Stelzer, P. Torrielli, and M. Zaro, *The automated computation of tree-level and next-to-leading order differential cross sections, and their matching to parton shower simulations*, JHEP **07** (2014) 079, arXiv:1405.0301 [hep-ph].

[13] T. O. Eynck, E. Laenen, L. Phaf, and S. Weinzierl, *Comparison of phase space slicing and dipole subtraction methods for gamma* —> anti-Q*, Eur. Phys. J. **C23** (2002) 259–266, arXiv:hep-ph/0109246 [hep-ph].

[14] ATLAS Collaboration, G. Aad et al., *Measurement of W^+W^- production in pp collisions at $\sqrt{s} = 7$ TeV with the ATLAS detector and limits on anomalous WWZ and WWγ couplings*, Phys. Rev. **D87** (2013) no. 11, 112001, arXiv:1210.2979 [hep-ex]. [Erratum: Phys. Rev.D88,no.7,079906(2013)].

[15] CMS Collaboration, S. Chatrchyan et al., *Measurement of the W^+W^- Cross section in pp Collisions at $\sqrt{s} = 7$ TeV and Limits on Anomalous $WW\gamma$ and WWZ couplings*, Eur. Phys. J. **C73** (2013) no. 10, 2610, arXiv:1306.1126 [hep-ex].

[16] CMS Collaboration, S. Chatrchyan et al., *Measurement of W+W- and ZZ production cross sections in pp collisions at sqrt(s) = 8 TeV*, Phys. Lett. **B721** (2013) 190–211, arXiv:1301.4698 [hep-ex].

[17] G. Heinrich, *QCD calculations for the LHC: status and prospects*, in *5th Large Hadron Collider Physics Conference (LHCP 2017) Shanghai, China, May 15-20, 2017*. 2017. arXiv:1710.04998 [hep-ph].

[18] S. Dittmaier, *Standard Model Theory*, in *Proceedings, 2017 European Physical Society Conference on High Energy Physics (EPS-HEP 2017): Venice, Italy, July 5-12, 2017*. 2017. arXiv:1709.08564 [hep-ph]. https://pos.sissa.it/314/581/pdf.

[19] J. Currie, A. Gehrmann-De Ridder, T. Gehrmann, E. W. N. Glover, A. Huss, and J. Pires, *Precise predictions for dijet production at the LHC*, Phys. Rev. Lett. **119** (2017) no. 15, 152001, arXiv:1705.10271 [hep-ph].

[20] A. V. Kotikov, *Differential equations method: The Calculation of vertex type Feynman diagrams*, Phys. Lett. **B259** (1991) 314–322.

[21] A. V. Kotikov, *Differential equation method: The Calculation of N point Feynman diagrams*, Phys. Lett. **B267** (1991) 123–127. [Erratum: Phys. Lett.B295,409(1992)].

[22] J. M. Henn, *Multiloop integrals in dimensional regularization made simple*, Phys. Rev. Lett. **110** (2013) 251601, arXiv:1304.1806 [hep-th].

[23] C. G. Papadopoulos, *Simplified differential equations approach for Master Integrals*, JHEP **07** (2014) 088, arXiv:1401.6057 [hep-ph].

[24] S. P. Jones, M. Kerner, and G. Luisoni, *Next-to-Leading-Order QCD Corrections to Higgs Boson Plus Jet Production with Full Top-Quark Mass Dependence*, Phys. Rev. Lett. **120** (2018) no. 16, 162001, arXiv:1802.00349 [hep-ph].

[25] J. M. Lindert, K. Kudashkin, K. Melnikov, and C. Wever, *Higgs bosons with large transverse momentum at the LHC*, Phys. Lett. **B782** (2018) 210–214, arXiv:1801.08226 [hep-ph].

[26] L. Adams, C. Bogner, and S. Weinzierl, *The two-loop sunrise graph in two space-time dimensions with arbitrary masses in terms of elliptic dilogarithms*, J. Math. Phys. **55** (2014) no. 10, 102301, arXiv:1405.5640 [hep-ph].

[27] J. M. Henn, K. Melnikov, and V. A. Smirnov, *Two-loop planar master integrals for the production of off-shell vector bosons in hadron collisions*, JHEP **05** (2014) 090, arXiv:1402.7078 [hep-ph].

[28] F. Caola, J. M. Henn, K. Melnikov, and V. A. Smirnov, *Non-planar master integrals for the production of two off-shell vector bosons in collisions of massless partons*, JHEP **09** (2014) 043, arXiv:1404.5590 [hep-ph].

[29] T. Gehrmann, A. von Manteuffel, L. Tancredi, and E. Weihs, *The two-loop master integrals for* $q\bar{q} \to VV$, JHEP **06** (2014) 032, arXiv:1404.4853 [hep-ph].

[30] C. G. Papadopoulos, D. Tommasini, and C. Wever, *Two-loop Master Integrals with the Simplified Differential Equations approach*, JHEP **01** (2015) 072, arXiv:1409.6114 [hep-ph].

[31] C. G. Papadopoulos, D. Tommasini, and C. Wever, *The Pentabox Master Integrals with the Simplified Differential Equations approach*, JHEP **04** (2016) 078, arXiv:1511.09404 [hep-ph].

[32] E. Remiddi and L. Tancredi, *An Elliptic Generalization of Multiple Polylogarithms*, Nucl. Phys. **B925** (2017) 212–251, arXiv:1709.03622 [hep-ph].

[33] R. Bonciani, V. Del Duca, H. Frellesvig, J. M. Henn, F. Moriello, and V. A. Smirnov, *Two-loop planar master integrals for Higgs→ 3 partons with full heavy-quark mass dependence*, JHEP **12** (2016) 096, arXiv:1609.06685 [hep-ph].

[34] L. Adams, E. Chaubey, and S. Weinzierl, *Analytic results for the planar double box integral relevant to top-pair production with a closed top loop*, arXiv:1806.04981 [hep-ph].

[35] L. Adams, E. Chaubey, and S. Weinzierl, *Simplifying Differential Equations for Multiscale Feynman Integrals beyond Multiple Polylogarithms*, Phys. Rev. Lett. **118** (2017) no. 14, 141602, arXiv:1702.04279 [hep-ph].

[36] L. Adams, C. Bogner, A. Schweitzer, and S. Weinzierl, *The kite integral to all orders in terms of*

elliptic polylogarithms, J. Math. Phys. **57** (2016) no. 12, 122302, arXiv:1607.01571 [hep-ph].

[37] J. Ablinger, J. Blümlein, A. De Freitas, M. van Hoeij, E. Imamoglu, C. G. Raab, C. S. Radu, and C. Schneider, *Iterated Elliptic and Hypergeometric Integrals for Feynman Diagrams*, J. Math. Phys. **59** (2018) no. 6, 062305, arXiv:1706.01299 [hep-th].

[38] A. von Manteuffel and L. Tancredi, *A non-planar two-loop three-point function beyond multiple polylogarithms*, JHEP **06** (2017) 127, arXiv:1701.05905 [hep-ph].

[39] J. Broedel, C. Duhr, F. Dulat, B. Penante, and L. Tancredi, *Elliptic symbol calculus: from elliptic polylogarithms to iterated integrals of Eisenstein series*, JHEP **08** (2018) 014, arXiv:1803.10256 [hep-th].

[40] S. Becker and S. Weinzierl, *Direct numerical integration for multi-loop integrals*, Eur. Phys. J. **C73** (2013) no. 2, 2321, arXiv:1211.0509 [hep-ph].

[41] M. Czakon, P. Fiedler, and A. Mitov, *Total Top-Quark Pair-Production Cross Section at Hadron Colliders Through* $O(\alpha_S^4)$, Phys. Rev. Lett. **110** (2013) 252004, arXiv:1303.6254 [hep-ph].

[42] C. Bogner, A. Schweitzer, and S. Weinzierl, *Analytic continuation and numerical evaluation of the kite integral and the equal mass sunrise integral*, Nucl. Phys. **B922** (2017) 528–550, arXiv:1705.08952 [hep-ph].

[43] S. Borowka, G. Heinrich, S. Jahn, S. P. Jones, M. Kerner, J. Schlenk, and T. Zirke, *pySecDec: a toolbox for the numerical evaluation of multi-scale integrals*, Comput. Phys. Commun. **222** (2018) 313–326, arXiv:1703.09692 [hep-ph].

[44] A. Gehrmann-De Ridder, T. Gehrmann, and E. W. N. Glover, *Antenna subtraction at NNLO*, JHEP **09** (2005) 056, arXiv:hep-ph/0505111 [hep-ph].

[45] G. Heinrich, *A numerical method for NNLO calculations*, Nucl. Phys. Proc. Suppl. **116** (2003) 368–372, arXiv:hep-ph/0211144 [hep-ph]. [,368(2002)].

[46] M. Czakon, *A novel subtraction scheme for double-real radiation at NNLO*, Phys. Lett. **B693** (2010) 259–268, arXiv:1005.0274 [hep-ph].

[47] R. Boughezal, K. Melnikov, and F. Petriello, *A subtraction scheme for NNLO computations*, Phys. Rev. **D85** (2012) 034025, arXiv:1111.7041 [hep-ph].

[48] M. Czakon and D. Heymes, *Four-dimensional formulation of the sector-improved residue subtraction scheme*, Nucl. Phys. **B890** (2014) 152–227, arXiv:1408.2500 [hep-ph].

[49] F. Caola, K. Melnikov, and R. Röntsch, *Nested soft-collinear subtractions in NNLO QCD computations*, Eur. Phys. J. **C77** (2017) no. 4, 248, arXiv:1702.01352 [hep-ph].

[50] V. Del Duca, C. Duhr, A. Kardos, G. Somogyi, and Z. Trócsányi, *Three-Jet Production in Electron-Positron Collisions at Next-to-Next-to-Leading Order Accuracy*, Phys. Rev. Lett. **117** (2016) no. 15, 152004, arXiv:1603.08927 [hep-ph].

[51] M. Cacciari, F. A. Dreyer, A. Karlberg, G. P. Salam, and G. Zanderighi, *Fully Differential Vector-Boson-Fusion Higgs Production at Next-to-Next-to-Leading Order*, Phys. Rev. Lett. **115** (2015) no. 8, 082002, arXiv:1506.02660 [hep-ph]. [Erratum: Phys. Rev. Lett.120,no.13,139901(2018)].

[52] S. Catani, L. Cieri, G. Ferrera, D. de Florian, and M. Grazzini, *Vector boson production at hadron colliders: a fully exclusive QCD calculation at NNLO*, Phys. Rev. Lett. **103** (2009) 082001, arXiv:0903.2120 [hep-ph].

[53] R. Boughezal, C. Focke, X. Liu, and F. Petriello, *W-boson production in association with a jet at next-to-next-to-leading order in perturbative QCD*, Phys. Rev. Lett. **115** (2015) no. 6, 062002, arXiv:1504.02131 [hep-ph].

[54] J. Gaunt, M. Stahlhofen, F. J. Tackmann, and J. R. Walsh, *N-jettiness Subtractions for NNLO QCD Calculations*, JHEP **09** (2015) 058, arXiv:1505.04794 [hep-ph].

[55] S. Badger, H. Frellesvig, and Y. Zhang, *Hepta-Cuts of Two-Loop Scattering Amplitudes*, JHEP **04** (2012) 055, arXiv:1202.2019 [hep-ph].

[56] S. Badger, H. Frellesvig, and Y. Zhang, *A Two-Loop Five-Gluon Helicity Amplitude in QCD*, JHEP **12** (2013) 045, arXiv:1310.1051 [hep-ph].

[57] S. Badger, G. Mogull, A. Ochirov, and D. O'Connell, *A Complete Two-Loop, Five-Gluon Helicity Amplitude in Yang-Mills Theory*, JHEP **10** (2015) 064, arXiv:1507.08797 [hep-ph].

[58] T. Gehrmann, J. M. Henn, and N. A. Lo Presti, *Analytic form of the two-loop planar five-gluon all-plus-helicity amplitude in QCD*, Phys. Rev. Lett. **116** (2016) no. 6, 062001, arXiv:1511.05409 [hep-ph]. [Erratum: Phys. Rev. Lett.116,no.18,189903(2016)].

[59] S. Badger, G. Mogull, and T. Peraro, *Local integrands for two-loop all-plus Yang-Mills amplitudes*, JHEP **08** (2016) 063, arXiv:1606.02244 [hep-ph].

[60] D. C. Dunbar, G. R. Jehu, and W. B. Perkins, *Two-loop six gluon all plus helicity amplitude*, Phys. Rev. Lett. **117** (2016) no. 6, 061602, arXiv:1605.06351 [hep-th].

[61] S. Badger, C. Brønnum-Hansen, H. B. Hartanto, and T. Peraro, *First look at two-loop five-gluon scattering in QCD*, Phys. Rev. Lett. **120** (2018) no. 9, 092001, arXiv:1712.02229 [hep-ph].

[62] S. Abreu, F. Febres Cordero, H. Ita, B. Page, and M. Zeng, *Planar Two-Loop Five-Gluon Amplitudes from Numerical Unitarity*, Phys. Rev. **D97** (2018) no. 11, 116014, arXiv:1712.03946 [hep-ph].

[63] C. Anastasiou, C. Duhr, F. Dulat, E. Furlan, T. Gehrmann, F. Herzog, A. Lazopoulos, and B. Mistlberger, *High precision determination of the gluon fusion Higgs boson cross-section at the LHC*, JHEP **05** (2016) 058, arXiv:1602.00695 [hep-ph].

[64] B. Mistlberger, *Higgs boson production at hadron colliders at N^3LO in QCD*, JHEP **05** (2018) 028, arXiv:1802.00833 [hep-ph].

[65] F. A. Dreyer and A. Karlberg, *Vector-Boson Fusion Higgs Production at Three Loops in QCD*, Phys. Rev. Lett. **117** (2016) no. 7, 072001, arXiv:1606.00840 [hep-ph].

[66] W. Bizon, P. F. Monni, E. Re, L. Rottoli, and P. Torrielli, *Momentum-space resummation for transverse observables and the Higgs $p_\perp$ at N^3LL+NNLO*, JHEP **02** (2018) 108, arXiv:1705.09127 [hep-ph].

[67] X. Chen, T. Gehrmann, E. W. N. Glover, A. Huss, Y. Li, D. Neill, M. Schulze, I. W. Stewart, and H. X. Zhu, *Precise QCD Description of the Higgs Boson Transverse Momentum Spectrum*, arXiv:1805.00736 [hep-ph].

[68] W. Bizon, X. Chen, A. Gehrmann-De Ridder, T. Gehrmann, N. Glover, A. Huss, P. F. Monni, E. Re, L. Rottoli, and P. Torrielli, *Fiducial distributions in Higgs and Drell-Yan production at N^3LL+NNLO*, arXiv:1805.05916 [hep-ph].

[69] J. C. Collins, D. E. Soper, and G. F. Sterman, *Transverse Momentum Distribution in Drell-Yan Pair and W and Z Boson Production*, Nucl. Phys. **B250** (1985) 199–224.

[70] S. Catani, L. Trentadue, G. Turnock, and B. R. Webber, *Resummation of large logarithms in e+ e- event shape distributions*, Nucl. Phys. **B407** (1993) 3–42.

[71] C. W. Bauer, D. Pirjol, and I. W. Stewart, *Soft collinear factorization in effective field theory*, Phys. Rev. **D65** (2002) 054022, arXiv:hep-ph/0109045 [hep-ph].

[72] C. W. Bauer and P. F. Monni, *A numerical formulation of resummation in effective field theory*, arXiv:1803.07079 [hep-ph].

[73] M. Dasgupta, F. A. Dreyer, K. Hamilton, P. F. Monni, and G. P. Salam, *Logarithmic accuracy of parton showers: a fixed-order study*, JHEP **09** (2018) 033, arXiv:1805.09327 [hep-ph].

[74] Z. Nagy and D. E. Soper, *Effects of subleading color in a parton shower*, JHEP **07** (2015) 119, arXiv:1501.00778 [hep-ph].

[75] S. Jadach, A. Kusina, W. Placzek, and M. Skrzypek, *On the dependence of QCD splitting functions on the choice of the evolution variable*, JHEP **08** (2016) 092, arXiv:1606.01238 [hep-ph].

[76] S. Höche and S. Prestel, *Triple collinear emissions in parton showers*, Phys. Rev. **D96** (2017) no. 7, 074017, arXiv:1705.00742 [hep-ph].

[77] S. Höche and S. Prestel, *The midpoint between dipole and parton showers*, Eur. Phys. J. **C75** (2015) no. 9, 461, arXiv:1506.05057 [hep-ph].

[78] N. Fischer, S. Prestel, M. Ritzmann, and P. Skands, *Vincia for Hadron Colliders*, Eur. Phys. J. **C76** (2016) no. 11, 589, arXiv:1605.06142 [hep-ph].

[79] S. Alioli, C. W. Bauer, C. Berggren, F. J. Tackmann, J. R. Walsh, and S. Zuberi, *Matching Fully Differential NNLO Calculations and Parton Showers*, JHEP **06** (2014) 089, arXiv:1311.0286 [hep-ph].

[80] K. Hamilton, P. Nason, E. Re, and G. Zanderighi, *NNLOPS simulation of Higgs boson production*, JHEP **10** (2013) 222, arXiv:1309.0017 [hep-ph].

[81] S. Höche, Y. Li, and S. Prestel, *Drell-Yan lepton pair production at NNLO QCD with parton showers*, Phys. Rev. **D91** (2015) no. 7, 074015, arXiv:1405.3607 [hep-ph].

[82] S. Actis, A. Denner, L. Hofer, J.-N. Lang, A. Scharf, and S. Uccirati, *RECOLA: REcursive Computation of One-Loop Amplitudes*, Comput. Phys. Commun. **214** (2017) 140–173, arXiv:1605.01090 [hep-ph].

[83] S. Actis, A. Denner, L. Hofer, A. Scharf, and S. Uccirati, *Recursive generation of one-loop amplitudes in the Standard Model*, JHEP **04** (2013) 037, arXiv:1211.6316 [hep-ph].

[84] T. Gleisberg, S. Hoeche, F. Krauss, M. Schonherr, S. Schumann, F. Siegert, and J. Winter, *Event generation with SHERPA 1.1*, JHEP **02** (2009) 007, arXiv:0811.4622 [hep-ph].

[85] M. Schönherr, *An automated subtraction of NLO EW infrared divergences*, Eur. Phys. J. **C78** (2018) no. 2, 119, arXiv:1712.07975 [hep-ph].

[86] G. Cullen, N. Greiner, G. Heinrich, G. Luisoni, P. Mastrolia, G. Ossola, T. Reiter, and F. Tramontano, *Automated One-Loop Calculations with GoSam*, Eur. Phys. J. **C72** (2012) 1889, arXiv:1111.2034 [hep-ph].

[87] R. Frederix, T. Gehrmann, and N. Greiner, *Automation of the Dipole Subtraction Method in MadGraph/MadEvent*, JHEP **09** (2008) 122, arXiv:0808.2128 [hep-ph].

[88] T. Gehrmann and N. Greiner, *Photon Radiation with MadDipole*, JHEP **12** (2010) 050, arXiv:1011.0321 [hep-ph].

[89] R. Frederix, S. Frixione, V. Hirschi, D. Pagani, H. S. Shao, and M. Zaro, *The automation of next-to-leading order electroweak calculations*, JHEP **07** (2018) 185, arXiv:1804.10017 [hep-ph].

[90] J. R. Andersen et al., *Les Houches 2015: Physics at TeV Colliders Standard Model Working Group Report*, in *9th Les Houches Workshop on Physics at TeV Colliders (PhysTeV 2015) Les Houches, France, June 1-19, 2015*. 2016. arXiv:1605.04692 [hep-ph]. http://lss.fnal.gov/archive/2016/conf/fermilab-conf-16-175-ppd-t.pdf.

[91] J. R. Andersen et al., *Les Houches 2017: Physics at TeV Colliders Standard Model Working Group Report*, in *10th Les Houches Workshop on Physics at TeV Colliders (PhysTeV 2017) Les Houches, France, June 5-23, 2017*. 2018. arXiv:1803.07977 [hep-ph]. http://lss.fnal.gov/archive/2018/conf/fermilab-conf-18-122-cd-t.pdf.

[92] A. Denner, L. Hofer, A. Scharf, and S. Uccirati, *Electroweak corrections to lepton pair*

production in association with two hard jets at the LHC, JHEP **01** (2015) 094, arXiv:1411.0916 [hep-ph].

[93] A. Denner, R. Feger, and A. Scharf, *Irreducible background and interference effects for Higgs-boson production in association with a top-quark pair*, JHEP **04** (2015) 008, arXiv:1412.5290 [hep-ph].

[94] A. Denner and R. Feger, *NLO QCD corrections to off-shell top-antitop production with leptonic decays in association with a Higgs boson at the LHC*, JHEP **11** (2015) 209, arXiv:1506.07448 [hep-ph].

[95] S. Kallweit, J. M. Lindert, P. Maierhöfer, S. Pozzorini, and M. Schönherr, *NLO electroweak automation and precise predictions for W+multijet production at the LHC*, JHEP **04** (2015) 012, arXiv:1412.5157 [hep-ph].

[96] S. Frixione, V. Hirschi, D. Pagani, H. S. Shao, and M. Zaro, *Weak corrections to Higgs hadroproduction in association with a top-quark pair*, JHEP **09** (2014) 065, arXiv:1407.0823 [hep-ph].

[97] M. Chiesa, N. Greiner, and F. Tramontano, *Automation of electroweak corrections for LHC processes*, J. Phys. **G43** (2016) no. 1, 013002, arXiv:1507.08579 [hep-ph].

[98] S. Kallweit, J. M. Lindert, P. Maierhofer, S. Pozzorini, and M. Schönherr, *NLO QCD+EW predictions for V + jets including off-shell vector-boson decays and multijet merging*, JHEP **04** (2016) 021, arXiv:1511.08692 [hep-ph].

[99] S. Frixione, V. Hirschi, D. Pagani, H. S. Shao, and M. Zaro, *Electroweak and QCD corrections to top-pair hadroproduction in association with heavy bosons*, JHEP **06** (2015) 184, arXiv:1504.03446 [hep-ph].

[100] B. Biedermann, M. Billoni, A. Denner, S. Dittmaier, L. Hofer, B. Jäger, and L. Salfelder, *Next-to-leading-order electroweak corrections to $pp \to W^+W^- \to 4$ leptons at the LHC*, JHEP **06** (2016) 065, arXiv:1605.03419 [hep-ph].

[101] B. Biedermann, A. Denner, S. Dittmaier, L. Hofer, and B. Jäger, *Electroweak corrections to $pp \to \mu^+\mu^- e^+e^- + X$ at the LHC: a Higgs background study*, Phys. Rev. Lett. **116** (2016) no. 16, 161803, arXiv:1601.07787 [hep-ph].

[102] A. Denner and M. Pellen, *NLO electroweak corrections to off-shell top-antitop production with leptonic decays at the LHC*, JHEP **08** (2016) 155, arXiv:1607.05571 [hep-ph].

[103] B. Biedermann, A. Denner, and M. Pellen, *Large electroweak corrections to vector-boson scattering at the Large Hadron Collider*, Phys. Rev. Lett. **118** (2017) no. 26, 261801, arXiv:1611.02951 [hep-ph].

[104] B. Biedermann, A. Denner, S. Dittmaier, L. Hofer, and B. Jager, *Next-to-leading-order electroweak corrections to the production of four charged leptons at the LHC*, JHEP **01** (2017) 033, arXiv:1611.05338 [hep-ph].

[105] A. Denner, J.-N. Lang, M. Pellen, and S. Uccirati, *Higgs production in association with off-shell top-antitop pairs at NLO EW and QCD at the LHC*, JHEP **02** (2017) 053, arXiv:1612.07138 [hep-ph].

[106] R. Frederix, S. Frixione, V. Hirschi, D. Pagani, H.-S. Shao, and M. Zaro, *The complete NLO corrections to dijet hadroproduction*, JHEP **04** (2017) 076, arXiv:1612.06548 [hep-ph].

[107] D. Pagani, I. Tsinikos, and M. Zaro, *The impact of the photon PDF and electroweak corrections on $t\bar{t}$ distributions*, Eur. Phys. J. **C76** (2016) no. 9, 479, arXiv:1606.01915 [hep-ph].

[108] B. Biedermann, S. Bräuer, A. Denner, M. Pellen, S. Schumann, and J. M. Thompson, *Automation of NLO QCD and EW corrections with Sherpa and Recola*, Eur. Phys. J. **C77** (2017) 492, arXiv:1704.05783 [hep-ph].

[109] S. Kallweit, J. M. Lindert, S. Pozzorini, and M. Schönherr, *NLO QCD+EW predictions for $2\ell 2\nu$ diboson signatures at the LHC*, JHEP **11** (2017) 120, arXiv:1705.00598 [hep-ph].

[110] M. Chiesa, N. Greiner, M. Schönherr, and F. Tramontano, *Electroweak corrections to diphoton plus jets*, JHEP **10** (2017) 181, arXiv:1706.09022 [hep-ph].

[111] B. Biedermann, A. Denner, and M. Pellen, *Complete NLO corrections to W^+W^+ scattering and its irreducible background at the LHC*, JHEP **10** (2017) 124, arXiv:1708.00268 [hep-ph].

[112] B. Biedermann, A. Denner, and L. Hofer, *Next-to-leading-order electroweak corrections to the production of three charged leptons plus missing energy at the LHC*, JHEP **10** (2017) 043, arXiv:1708.06938 [hep-ph].

[113] M. Czakon, D. Heymes, A. Mitov, D. Pagani, I. Tsinikos, and M. Zaro, *Top-pair production at the LHC through NNLO QCD and NLO EW*, JHEP **10** (2017) 186, arXiv:1705.04105 [hep-ph].

[114] N. Greiner and M. Schönherr, *NLO QCD+EW corrections to diphoton production in association with a vector boson*, JHEP **01** (2018) 079, arXiv:1710.11514 [hep-ph].

[115] R. Frederix, D. Pagani, and M. Zaro, *Large NLO corrections in $t\bar{t}W^{\pm}$ and $t\bar{t}t\bar{t}$ hadroproduction from supposedly subleading EW contributions*, JHEP **02** (2018) 031, arXiv:1711.02116 [hep-ph].

[116] C. Gütschow, J. M. Lindert, and M. Schönherr, *Multi-jet merged top-pair production including electroweak corrections*, Eur. Phys. J. **C78** (2018) no. 4, 317, arXiv:1803.00950 [hep-ph].

[117] M. Schönherr, *Next-to-leading order electroweak corrections to off-shell WWW production at the LHC*, JHEP **07** (2018) 076, arXiv:1806.00307 [hep-ph].

[118] S. Dittmaier, A. Huss, and C. Schwinn, *Mixed QCD-electroweak $O(\alpha_s\alpha)$ corrections to Drell-Yan processes in the resonance region: pole approximation and non-factorizable corrections*, Nucl. Phys. **B885** (2014) 318–372, arXiv:1403.3216 [hep-ph].

[119] S. Dittmaier, A. Huss, and C. Schwinn, *Dominant mixed QCD-electroweak $O(\alpha_s\alpha)$ corrections to Drell–Yan processes in the resonance region*, Nucl. Phys. **B904** (2016) 216–252, arXiv:1511.08016 [hep-ph].

[120] A. Kotikov, J. H. Kuhn, and O. Veretin, *Two-Loop Formfactors in Theories with Mass Gap and Z-Boson Production*, Nucl. Phys. **B788** (2008) 47–62, arXiv:hep-ph/0703013 [HEP-PH].

[121] W. B. Kilgore and C. Sturm, *Two-Loop Virtual Corrections to Drell-Yan Production at order $\alpha_s\alpha^3$*, Phys. Rev. **D85** (2012) 033005, arXiv:1107.4798 [hep-ph].

[122] R. Bonciani, *Two-loop mixed QCD-EW virtual corrections to the Drell-Yan production of Z and W bosons*, PoS **EPS-HEP2011** (2011) 365.

[123] R. Bonciani, S. Di Vita, P. Mastrolia, and U. Schubert, *Two-Loop Master Integrals for the mixed EW-QCD virtual corrections to Drell-Yan scattering*, JHEP **09** (2016) 091, arXiv:1604.08581 [hep-ph].

[124] A. von Manteuffel and R. M. Schabinger, *Numerical Multi-Loop Calculations via Finite Integrals and One-Mass EW-QCD Drell-Yan Master Integrals*, JHEP **04** (2017) 129, arXiv:1701.06583 [hep-ph].

[125] R. Bonciani, F. Buccioni, R. Mondini, and A. Vicini, *Double-real corrections at $\mathcal{O}(\alpha\alpha_s)$ to single gauge boson production*, Eur. Phys. J. **C77** (2017) no. 3, 187, arXiv:1611.00645 [hep-ph].

[126] C. Anastasiou, R. Boughezal, and F. Petriello, *Mixed QCD-electroweak corrections to Higgs boson production in gluon fusion*, JHEP **04** (2009) 003, arXiv:0811.3458 [hep-ph].

[127] M. Bonetti, K. Melnikov, and L. Tancredi, *Higher order corrections to mixed QCD-EW contributions to Higgs boson production in gluon fusion*, Phys. Rev. **D97** (2018) no. 5, 056017,

arXiv:1801.10403 [hep-ph]. [Erratum: Phys. Rev.D97,no.9,099906(2018)].

[128] J. M. Lindert et al., *Precise predictions for $V+$ jets dark matter backgrounds*, Eur. Phys. J. **C77** (2017) no. 12, 829, arXiv:1705.04664 [hep-ph].

[129] A. Denner and S. Pozzorini, *One loop leading logarithms in electroweak radiative corrections. 1. Results*, Eur. Phys. J. **C18** (2001) 461–480, arXiv:hep-ph/0010201 [hep-ph].

[130] A. Denner and S. Pozzorini, *One loop leading logarithms in electroweak radiative corrections. 2. Factorization of collinear singularities*, Eur. Phys. J. **C21** (2001) 63–79, arXiv:hep-ph/0104127 [hep-ph].

[131] J.-y. Chiu, F. Golf, R. Kelley, and A. V. Manohar, *Electroweak Sudakov corrections using effective field theory*, Phys. Rev. Lett. **100** (2008) 021802, arXiv:0709.2377 [hep-ph].

[132] J.-y. Chiu, R. Kelley, and A. V. Manohar, *Electroweak Corrections using Effective Field Theory: Applications to the LHC*, Phys. Rev. **D78** (2008) 073006, arXiv:0806.1240 [hep-ph].

[133] M. L. Mangano et al., *Physics at a 100 TeV pp Collider: Standard Model Processes*, CERN Yellow Report (2017) no. 3, 1–254, arXiv:1607.01831 [hep-ph].

[134] C. Bernaciak and D. Wackeroth, *Combining NLO QCD and Electroweak Radiative Corrections to W boson Production at Hadron Colliders in the POWHEG Framework*, Phys. Rev. **D85** (2012) 093003, arXiv:1201.4804 [hep-ph].

[135] L. Barze, G. Montagna, P. Nason, O. Nicrosini, and F. Piccinini, *Implementation of electroweak corrections in the POWHEG BOX: single W production*, JHEP **04** (2012) 037, arXiv:1202.0465 [hep-ph].

[136] L. Barze, G. Montagna, P. Nason, O. Nicrosini, F. Piccinini, and A. Vicini, *Neutral current Drell-Yan with combined QCD and electroweak corrections in the POWHEG BOX*, Eur. Phys. J. **C73** (2013) no. 6, 2474, arXiv:1302.4606 [hep-ph].

[137] A. Mück and L. Oymanns, *Resonace-improved parton-shower matching for the Drell-Yan process including electroweak corrections*, JHEP **05** (2017) 090, arXiv:1612.04292 [hep-ph].

[138] F. Granata, J. M. Lindert, C. Oleari, and S. Pozzorini, *NLO QCD+EW predictions for HV and HV +jet production including parton-shower effects*, JHEP **09** (2017) 012, arXiv:1706.03522 [hep-ph].

[139] M. Chiesa, G. Montagna, L. Barze, M. Moretti, O. Nicrosini, F. Piccinini, and F. Tramontano, *Electroweak Sudakov Corrections to New Physics Searches at the LHC*, Phys. Rev. Lett. **111** (2013) no. 12, 121801, arXiv:1305.6837 [hep-ph].

[140] J. R. Christiansen and T. Sjöstrand, *Weak Gauge Boson Radiation in Parton Showers*, JHEP **04** (2014) 115, arXiv:1401.5238 [hep-ph].

[141] F. Krauss, P. Petrov, M. Schoenherr, and M. Spannowsky, *Measuring collinear W emissions inside jets*, Phys. Rev. **D89** (2014) no. 11, 114006, arXiv:1403.4788 [hep-ph].

[142] C. W. Bauer, N. Ferland, and B. R. Webber, *Standard Model Parton Distributions at Very High Energies*, JHEP **08** (2017) 036.

[143] J. Chen, T. Han, and B. Tweedie, *Electroweak Splitting Functions and High Energy Showering*, JHEP **11** (2017) 093, arXiv:1611.00788 [hep-ph].

[144] LHC Higgs Cross Section Working Group Collaboration, D. de Florian et al., *Handbook of LHC Higgs Cross Sections: 4. Deciphering the Nature of the Higgs Sector*, arXiv:1610.07922 [hep-ph].

[145] W. Beenakker, C. Borschensky, M. Kramer, A. Kulesza, E. Laenen, S. Marzani, and J. Rojo, *NLO+NLL squark and gluino production cross-sections with threshold-improved parton distributions*, Eur. Phys. J. **C76** (2016) no. 2, 53.

[146] S. Alioli, M. Farina, D. Pappadopulo, and J. T. Ruderman, *Precision Probes of QCD at High Energies*, JHEP **07** (2017) 097.

[147] M. Aaboud et al., *Measurement of the W-boson mass in pp collisions at $\sqrt{s} = 7$ TeV with the ATLAS detector*, Eur. Phys. J. **C78** (2018) no. 2, 110.

[148] CDF, D0 Collaboration, T. A. Aaltonen et al., *Tevatron Run II combination of the effective leptonic electroweak mixing angle*, Phys. Rev. **D97** (2018) no. 11, 112007, arXiv:1801.06283 [hep-ex].

[149] R. D. Ball, S. Carrazza, L. Del Debbio, S. Forte, Z. Kassabov, J. Rojo, E. Slade, and M. Ubiali, *Precision determination of the strong coupling constant within a global PDF analysis*, Eur. Phys. J. **C78** (2018) no. 5, 408.

[150] J. Gao, L. Harland-Lang, and J. Rojo, *The Structure of the Proton in the LHC Precision Era*, Phys. Rept. **742** (2018) 1–121.

[151] J. Rojo et al., *The PDF4LHC report on PDFs and LHC data: Results from Run I and preparation for Run II*, J. Phys. **G42** (2015) 103103.

[152] S. Forte and G. Watt, *Progress in the Determination of the Partonic Structure of the Proton*, Ann.Rev.Nucl.Part.Sci. **63** (2013) 291.

[153] J. Butterworth et al., *PDF4LHC recommendations for LHC Run II*, J. Phys. **G43** (2016) 023001, arXiv:1510.03865 [hep-ph].

[154] J. Gao and P. Nadolsky, *A meta-analysis of parton distribution functions*, JHEP **1407** (2014) 035.

[155] S. Carrazza, J. I. Latorre, J. Rojo, and G. Watt, *A compression algorithm for the combination of PDF sets*, Eur. Phys. J. **C75** (2015) 474.

[156] S. Carrazza, S. Forte, Z. Kassabov, J. I. Latorre, and J. Rojo, *An Unbiased Hessian Representation for Monte Carlo PDFs*, Eur. Phys. J. **C75** (2015) no. 8, 369.

[157] S. Dulat, T.-J. Hou, J. Gao, M. Guzzi, J. Huston, P. Nadolsky, J. Pumplin, C. Schmidt, D. Stump, and C. P. Yuan, *New parton distribution functions from a global analysis of quantum chromodynamics*, Phys. Rev. D **93** (2016) no. 3, 033006, arXiv:1506.07443 [hep-ph].

[158] L. A. Harland-Lang, A. D. Martin, P. Motylinski, and R. S. Thorne, *Parton distributions in the LHC era: MMHT 2014 PDFs*, Eur. Phys. J. C **75** (2015) no. 5, 204, arXiv:1412.3989 [hep-ph].

[159] NNPDF Collaboration, R. D. Ball et al., *Parton distributions for the LHC Run II*, JHEP **04** (2015) 040, arXiv:1410.8849 [hep-ph].

[160] A. Buckley, J. Ferrando, S. Lloyd, K. Nordström, B. Page, M. Rüfenacht, M. Schönherr, and G. Watt, *LHAPDF6: parton density access in the LHC precision era*, Eur. Phys. J. **C75** (2015) 132, arXiv:1412.7420 [hep-ph].

[161] M. Czakon, N. P. Hartland, A. Mitov, E. R. Nocera, and J. Rojo, *Pinning down the large-x gluon with NNLO top-quark pair differential distributions*, JHEP **04** (2017) 044.

[162] R. Boughezal, A. Guffanti, F. Petriello, and M. Ubiali, *The impact of the LHC Z-boson transverse momentum data on PDF determinations*, JHEP **07** (2017) 130.

[163] J. M. Campbell, J. Rojo, E. Slade, and C. Williams, *Direct photon production and PDF fits reloaded*, Eur. Phys. J. **C78** (2018) no. 6, 470.

[164] J. Currie, E. W. N. Glover, and J. Pires, *Next-to-Next-to Leading Order QCD Predictions for Single Jet Inclusive Production at the LHC*, Phys. Rev. Lett. **118** (2017) no. 7, 072002, arXiv:1611.01460 [hep-ph].

[165] NNPDF Collaboration, R. D. Ball et al., *Parton distributions from high-precision collider data*, Eur. Phys. J. C **77** (2017) 663, arXiv:1706.00428 [hep-ph].

[166] T. Carli, D. Clements, A. Cooper-Sarkar, C. Gwenlan, G. P. Salam, F. Siegert, P. Starovoitov, and

M. Sutton, *A posteriori inclusion of parton density functions in NLO QCD final-state calculations at hadron colliders: The* APPLGRID *project*, Eur. Phys. J. C **66** (2010) 503, arXiv:0911.2985 [hep-ph].

[167] M. Wobisch, D. Britzger, T. Kluge, K. Rabbertz, and F. Stober, *Theory-Data Comparisons for Jet Measurements in Hadron-Induced Processes*, .

[168] R. Boughezal, J. M. Campbell, R. K. Ellis, C. Focke, W. Giele, X. Liu, F. Petriello, and C. Williams, *Color singlet production at NNLO in MCFM*, Eur. Phys. J. **C77** (2017) no. 1, 7.

[169] Z. Nagy, *Three jet cross-sections in hadron hadron collisions at next-to-leading order*, Phys.Rev.Lett. **88** (2002) 122003.

[170] V. Bertone, R. Frederix, S. Frixione, J. Rojo, and M. Sutton, *aMCfast: automation of fast NLO computations for PDF fits*, JHEP **1408** (2014) 166.

[171] M. Czakon, D. Heymes, and A. Mitov, *Dynamical scales for multi-TeV top-pair production at the LHC*, JHEP **04** (2017) 071, arXiv:1606.03350 [hep-ph].

[172] M. Czakon, D. Heymes, and A. Mitov, *fastNLO tables for NNLO top-quark pair differential distributions*, .

[173] E. Bagnaschi, M. Cacciari, A. Guffanti, and L. Jenniches, *An extensive survey of the estimation of uncertainties from missing higher orders in perturbative calculations*, JHEP **02** (2015) 133.

[174] S. Moch, B. Ruijl, T. Ueda, J. A. M. Vermaseren, and A. Vogt, *Four-Loop Non-Singlet Splitting Functions in the Planar Limit and Beyond*, JHEP **10** (2017) 041.

[175] F. Dulat, B. Mistlberger, and A. Pelloni, *Differential Higgs production at N^3LO beyond threshold*, JHEP **01** (2018) 145.

[176] M. Bonvini, S. Marzani, J. Rojo, L. Rottoli, M. Ubiali, R. D. Ball, V. Bertone, S. Carrazza, and N. P. Hartland, *Parton distributions with threshold resummation*, JHEP **09** (2015) 191.

[177] R. D. Ball, V. Bertone, M. Bonvini, S. Marzani, J. Rojo, and L. Rottoli, *Parton distributions with small-x resummation: evidence for BFKL dynamics in HERA data*, Eur. Phys. J. **C78** (2018) no. 4, 321.

[178] M. Czakon, A. Ferroglia, D. Heymes, A. Mitov, B. D. Pecjak, D. J. Scott, X. Wang, and L. L. Yang, *Resummation for (boosted) top-quark pair production at NNLO+NNLL' in QCD*, JHEP **05** (2018) 149, arXiv:1803.07623 [hep-ph].

[179] K. Mishra et al., *Electroweak Corrections at High Energies*, in *Proceedings, 2013 Community Summer Study on the Future of U.S. Particle Physics: Snowmass on the Mississippi (CSS2013): Minneapolis, MN, USA, July 29-August 6, 2013*. 2013. http://inspirehep.net/record/1246902/files/arXiv:1308.1430.pdf.

[180] A. Manohar, P. Nason, G. P. Salam, and G. Zanderighi, *How bright is the proton? A precise determination of the photon parton distribution function*, Phys. Rev. Lett. **117** (2016) no. 24, 242002, arXiv:1607.04266 [hep-ph].

[181] A. V. Manohar, P. Nason, G. P. Salam, and G. Zanderighi, *The Photon Content of the Proton*, JHEP **12** (2017) 046, arXiv:1708.01256 [hep-ph].

[182] V. Bertone, S. Carrazza, N. P. Hartland, and J. Rojo, *Illuminating the photon content of the proton within a global PDF analysis*, .

[183] J. Rojo, *Parton Distributions at a 100 TeV Hadron Collider*, in *24th International Workshop on Deep-Inelastic Scattering and Related Subjects (DIS 2016) Hamburg, Germany, April 11-15, 2016*. 2016. http://inspirehep.net/record/1465838/files/arXiv:1605.08302.pdf.

[184] M. Bonvini, *Small-x phenomenology at the LHC and beyond: HELL 3.0 and the case of the Higgs cross section*, .

[185] B. Fornal, A. V. Manohar, and W. J. Waalewijn, *Electroweak Gauge Boson Parton Distribution*

Functions, JHEP **05** (2018) 106.

[186] T. Han, J. Sayre, and S. Westhoff, *Top-Quark Initiated Processes at High-Energy Hadron Colliders*, JHEP **04** (2015) 145.

[187] V. Bertone, A. Glazov, A. Mitov, A. Papanastasiou, and M. Ubiali, *Heavy-flavor parton distributions without heavy-flavor matching prescriptions*, JHEP **04** (2018) 046.

[188] P. Skands, S. Carrazza, and J. Rojo, *Tuning PYTHIA 8.1: the Monash 2013 Tune*, European Physical Journal C **74** (2014) 3024, arXiv:1404.5630 [hep-ph].

[189] R. Gauld and J. Rojo, *Precision determination of the small-x gluon from charm production at LHCb*, Phys. Rev. Lett. **118** (2017) no. 7, 072001.

[190] I. Brivio, Y. Jiang, and M. Trott, *The SMEFTsim package, theory and tools*, JHEP **12** (2017) 070, arXiv:1709.06492 [hep-ph].

[191] A. Dedes, W. Materkowska, M. Paraskevas, J. Rosiek, and K. Suxho, *Feynman rules for the Standard Model Effective Field Theory in R_x -gauges*, JHEP **06** (2017) 143, arXiv:1704.03888 [hep-ph].

[192] D. Barducci et al., *Interpreting top-quark LHC measurements in the standard-model effective field theory*, arXiv:1802.07237 [hep-ph].

[193] A. Alloul, B. Fuks, and V. Sanz, *Phenomenology of the Higgs Effective Lagrangian via FEYNRULES*, JHEP **04** (2014) 110, arXiv:1310.5150 [hep-ph].

[194] F. Maltoni, K. Mawatari, and M. Zaro, *Higgs characterisation via vector-boson fusion and associated production: NLO and parton-shower effects*, Eur. Phys. J. **C74** (2014) no. 1, 2710, arXiv:1311.1829 [hep-ph].

[195] F. Demartin, F. Maltoni, K. Mawatari, B. Page, and M. Zaro, *Higgs characterisation at NLO in QCD: CP properties of the top-quark Yukawa interaction*, Eur. Phys. J. **C74** (2014) no. 9, 3065, arXiv:1407.5089 [hep-ph].

[196] F. Demartin, F. Maltoni, K. Mawatari, and M. Zaro, *Higgs production in association with a single top quark at the LHC*, Eur. Phys. J. **C75** (2015) no. 6, 267, arXiv:1504.00611 [hep-ph].

[197] A. Falkowski, B. Fuks, K. Mawatari, K. Mimasu, F. Riva, and V. Sanz, *Rosetta: an operator basis translator for Standard Model effective field theory*, Eur. Phys. J. **C75** (2015) no. 12, 583, arXiv:1508.05895 [hep-ph].

[198] K. Mimasu, V. Sanz, and C. Williams, *Higher Order QCD predictions for Associated Higgs production with anomalous couplings to gauge bosons*, JHEP **08** (2016) 039, arXiv:1512.02572 [hep-ph].

[199] R. Grober, M. Muhlleitner, and M. Spira, *Higgs Pair Production at NLO QCD for CP-violating Higgs Sectors*, Nucl. Phys. **B925** (2017) 1–27, arXiv:1705.05314 [hep-ph].

[200] F. Goertz, A. Papaefstathiou, L. L. Yang, and J. Zurita, *Higgs boson pair production in the D=6 extension of the SM*, JHEP **04** (2015) 167, arXiv:1410.3471 [hep-ph].

[201] J. Bellm et al., *Herwig 7.0/Herwig++ 3.0 release note*, Eur. Phys. J. **C76** (2016) no. 4, 196, arXiv:1512.01178 [hep-ph].

[202] M. Spira, *HIGLU: A program for the calculation of the total Higgs production cross-section at hadron colliders via gluon fusion including QCD corrections*, arXiv:hep-ph/9510347 [hep-ph].

[203] M. Spira, *HIGLU and HDECAY: Programs for Higgs boson production at the LHC and Higgs boson decay widths*, Nucl. Instrum. Meth. **A389** (1997) 357–360, arXiv:hep-ph/9610350 [hep-ph].

[204] R. V. Harlander, S. Liebler, and H. Mantler, *SusHi Bento: Beyond NNLO and the heavy-top*

limit, Comput. Phys. Commun. **212** (2017) 239–257, arXiv:1605.03190 [hep-ph].

[205] H. Mantler and M. Wiesemann, *Hadronic Higgs production through NLO + PS in the SM, the 2HDM and the MSSM*, Eur. Phys. J. **C75** (2015) no. 6, 257, arXiv:1504.06625 [hep-ph].

[206] K. Arnold et al., *VBFNLO: A Parton level Monte Carlo for processes with electroweak bosons*, Comput. Phys. Commun. **180** (2009) 1661–1670, arXiv:0811.4559 [hep-ph].

[207] K. Arnold et al., *VBFNLO: A Parton Level Monte Carlo for Processes with Electroweak Bosons – Manual for Version 2.5.0*, arXiv:1107.4038 [hep-ph].

[208] A. Djouadi, J. Kalinowski, and M. Spira, *HDECAY: A Program for Higgs boson decays in the standard model and its supersymmetric extension*, Comput. Phys. Commun. **108** (1998) 56–74, arXiv:hep-ph/9704448 [hep-ph].

[209] R. Contino, M. Ghezzi, C. Grojean, M. Mühlleitner, and M. Spira, *eHDECAY: an Implementation of the Higgs Effective Lagrangian into HDECAY*, Comput. Phys. Commun. **185** (2014) 3412–3423, arXiv:1403.3381 [hep-ph].

[210] B. Gripaios and D. Sutherland, *DEFT: A program for operators in EFT*, arXiv:1807.07546 [hep-ph].

[211] J. Aebischer et al., *WCxf: an exchange format for Wilson coefficients beyond the Standard Model*, Comput. Phys. Commun. **232** (2018) 71–83, arXiv:1712.05298 [hep-ph].

[212] A. Celis, J. Fuentes-Martin, A. Vicente, and J. Virto, *DsixTools: The Standard Model Effective Field Theory Toolkit*, Eur. Phys. J. **C77** (2017) no. 6, 405, arXiv:1704.04504 [hep-ph].

[213] J. Aebischer, J. Kumar, and D. M. Straub, *Wilson: a Python package for the running and matching of Wilson coefficients above and below the electroweak scale*, arXiv:1804.05033 [hep-ph].

[214] C. Degrande, B. Fuks, K. Mawatari, K. Mimasu, and V. Sanz, *Electroweak Higgs boson production in the standard model effective field theory beyond leading order in QCD*, Eur. Phys. J. **C77** (2017) no. 4, 262, arXiv:1609.04833 [hep-ph].

[215] S. Alioli, W. Dekens, M. Girard, and E. Mereghetti, *NLO QCD corrections to SM-EFT dilepton and electroweak Higgs boson production, matched to parton shower in POWHEG*, JHEP **08** (2018) 205, arXiv:1804.07407 [hep-ph].

[216] D. Buarque Franzosi and C. Zhang, *Probing the top-quark chromomagnetic dipole moment at next-to-leading order in QCD*, Phys. Rev. **D91** (2015) no. 11, 114010, arXiv:1503.08841 [hep-ph].

[217] C. Zhang, *Single Top Production at Next-to-Leading Order in the Standard Model Effective Field Theory*, Phys. Rev. Lett. **116** (2016) no. 16, 162002, arXiv:1601.06163 [hep-ph].

[218] O. Bessidskaia Bylund, F. Maltoni, I. Tsinikos, E. Vryonidou, and C. Zhang, *Probing top quark neutral couplings in the Standard Model Effective Field Theory at NLO in QCD*, JHEP **05** (2016) 052, arXiv:1601.08193 [hep-ph].

[219] F. Maltoni, E. Vryonidou, and C. Zhang, *Higgs production in association with a top-antitop pair in the Standard Model Effective Field Theory at NLO in QCD*, JHEP **10** (2016) 123, arXiv:1607.05330 [hep-ph].

[220] C. Degrande, F. Maltoni, K. Mimasu, E. Vryonidou, and C. Zhang, *Single-top associated production with a Z or H boson at the LHC: the SMEFT interpretation*, JHEP **10** (2018) 005, arXiv:1804.07773 [hep-ph].

[221] M. de Beurs, E. Laenen, M. Vreeswijk, and E. Vryonidou, *Effective operators in t-channel single top production and decay*, arXiv:1807.03576 [hep-ph].

[222] E. Vryonidou and C. Zhang, *Dimension-six electroweak top-loop effects in Higgs production and decay*, JHEP **08** (2018) 036, arXiv:1804.09766 [hep-ph].

[223] G. Degrassi, P. P. Giardino, F. Maltoni, and D. Pagani, *Probing the Higgs self coupling via single Higgs production at the LHC*, JHEP **12** (2016) 080, arXiv:1607.04251 [hep-ph].

[224] W. Bizon, M. Gorbahn, U. Haisch, and G. Zanderighi, *Constraints on the trilinear Higgs coupling from vector boson fusion and associated Higgs production at the LHC*, JHEP **07** (2017) 083, arXiv:1610.05771 [hep-ph].

[225] S. Di Vita, C. Grojean, G. Panico, M. Riembau, and T. Vantalon, *A global view on the Higgs self-coupling*, JHEP **09** (2017) 069, arXiv:1704.01953 [hep-ph].

[226] C. Hartmann and M. Trott, *Higgs Decay to Two Photons at One Loop in the Standard Model Effective Field Theory*, Phys. Rev. Lett. **115** (2015) no. 19, 191801, arXiv:1507.03568 [hep-ph].

[227] C. Hartmann and M. Trott, *On one-loop corrections in the standard model effective field theory; the $\Gamma(h \to \gamma\,\gamma)$ case*, JHEP **07** (2015) 151, arXiv:1505.02646 [hep-ph].

[228] C. Hartmann, W. Shepherd, and M. Trott, *The Z decay width in the SMEFT: y_t and λ corrections at one loop*, JHEP **03** (2017) 060, arXiv:1611.09879 [hep-ph].

[229] S. Dawson and P. P. Giardino, *Higgs decays to ZZ and $Z\gamma$ in the standard model effective field theory: An NLO analysis*, Phys. Rev. **D97** (2018) no. 9, 093003, arXiv:1801.01136 [hep-ph].

[230] A. Dedes, M. Paraskevas, J. Rosiek, K. Suxho, and L. Trifyllis, *The decay $h \to \gamma\gamma$ in the Standard-Model Effective Field Theory*, JHEP **08** (2018) 103, arXiv:1805.00302 [hep-ph].

[231] S. Dawson and P. P. Giardino, *Electroweak Corrections to Higgs to $\gamma\gamma$ and W^+W^- in the SMEFT*, arXiv:1807.11504 [hep-ph].

[232] DELPHES 3 Collaboration, J. de Favereau, C. Delaere, P. Demin, A. Giammanco, V. Lemaître, A. Mertens, and M. Selvaggi, *DELPHES 3, A modular framework for fast simulation of a generic collider experiment*, JHEP **02** (2014) 057, arXiv:1307.6346 [hep-ex].

[233] M. Cacciari, G. P. Salam, and G. Soyez, *The Anti-k_t Jet Clustering Algorithm*, JHEP **04** (2008) 063, arXiv:0802.1189 [hep-ph].

[234] M. Cacciari, G. P. Salam, and G. Soyez, *FastJet User Manual*, Eur. Phys. J. **C72** (2012) 1896, arXiv:1111.6097 [hep-ph].

[235] ATLAS Collaboration, ATLAS Collaboration, *Expected performance of the ATLAS detector at HL-LHC*, in progress, CERN, Geneva, Dec, 2018.

[236] CMS Collaboration, CMS Collaboration, *Expected performance of the physics objects with the upgraded CMS detector at the HL-LHC*, in progress, CERN, Geneva, Dec, 2018.

[237] A. Collaboration, *Technical Design Report for the Phase-II Upgrade of the ATLAS TDAQ System*, CERN-LHCC-2017-020. ATLAS-TDR-029, CERN, Geneva, Sep, 2017. http://cds.cern.ch/record/2285584.

[238] C. Collaboration, *The Phase-2 Upgrade of the CMS L1 Trigger Interim Technical Design Report*, CERN-LHCC-2017-013. CMS-TDR-017, CERN, Geneva, Sep, 2017. https://cds.cern.ch/record/2283192. This is the CMS Interim TDR devoted to the upgrade of the CMS L1 trigger in view of the HL-LHC running, as approved by the LHCC.

[239] A. Collaboration, *Technical Design Report for the ATLAS Inner Tracker Pixel Detector*, CERN-LHCC-2017-021. ATLAS-TDR-030, CERN, Geneva, Sep, 2017. http://cds.cern.ch/record/2285585.

[240] A. Collaboration, *Technical Design Report for the ATLAS Inner Tracker Strip Detector*, CERN-LHCC-2017-005. ATLAS-TDR-025, CERN, Geneva, Apr, 2017. http://cds.cern.ch/record/2257755.

[241] CMS Collaboration, CMS Collaboration, *The Phase-2 Upgrade of the CMS Tracker*,

CERN-LHCC-2017-009. CMS-TDR-014, CERN, 2017.
https://cds.cern.ch/record/2272264.

[242] A. Collaboration, *Technical Design Report for the Phase-II Upgrade of the ATLAS LAr Calorimeter*, CERN-LHCC-2017-018. ATLAS-TDR-027, CERN, Geneva, Sep, 2017. http://cds.cern.ch/record/2285582.

[243] CMS Collaboration, CMS Collaboration, *The Phase-2 Upgrade of the CMS Barrel Calorimeters Technical Design Report*, CERN-LHCC-2017-011. CMS-TDR-015, CERN, 2017. https://cds.cern.ch/record/2283187.

[244] CMS Collaboration, *The Phase-2 Upgrade of the CMS Endcap Calorimeter*, CERN-LHCC-2017-023. CMS-TDR-019, 2017. https://cds.cern.ch/record/2293646.

[245] CMS Collaboration, *Technical Proposal for a MIP Timing Detector in the CMS Experiment Phase-2 Upgrade*, CERN-LHCC-2017-027. LHCC-P-009, 2017. https://cds.cern.ch/record/2296612.

[246] A. Collaboration, *Technical Design Report for the Phase-II Upgrade of the ATLAS Muon Spectrometer*, CERN-LHCC-2017-017. ATLAS-TDR-026, CERN, Geneva, Sep, 2017. http://cds.cern.ch/record/2285580.

[247] CMS Collaboration, *The Phase-2 Upgrade of the CMS Muon Detectors*, CERN-LHCC-2017-012. CMS-TDR-016, 2017. https://cds.cern.ch/record/2283189.

[248] A. Collaboration, *Technical Design Report for the Phase-II Upgrade of the ATLAS Tile Calorimeter*, CERN-LHCC-2017-019. ATLAS-TDR-028, CERN, Geneva, Sep, 2017. http://cds.cern.ch/record/2285583.

[249] CMS Collaboration, *Technical Proposal for the Phase-II Upgrade of the CMS Detector*, Cern-lhcc-2015-010, Geneva, Jun, 2015. https://cds.cern.ch/record/2020886.

[250] A. Collaboration, *Technical Proposal: A High-Granularity Timing Detector for the ATLAS Phase-II Upgrade*, CERN-LHCC-2018-023. LHCC-P-012, CERN, Geneva, Jun, 2018. http://cds.cern.ch/record/2623663.

[251] T. Sjostrand, S. Mrenna, and P. Z. Skands, *A Brief Introduction to PYTHIA 8.1*, Comput. Phys. Commun. **178** (2008) 852–867, arXiv:0710.3820 [hep-ph].

[252] I. Belyaev et al., *Handling of the generation of primary events in Gauss, the LHCb simulation framework*, J. Phys. Conf. Ser. **331** (2011) 032047.

[253] J. Pumplin, D. Stump, J. Huston, H. Lai, P. M. Nadolsky, et al., *New generation of parton distributions with uncertainties from global QCD analysis*, JHEP **07** (2002) 012, arXiv:hep-ph/0201195 [hep-ph].

[254] J. Allison et al., *Geant4 developments and applications*, IEEE Trans. Nucl. Sci. **53** (2006) 270.

[255] S. Agostinelli et al., *GEANT4: A Simulation Toolkit*, Nucl. Instrum. Meth. **A 506** (2003) 250.

[256] M. Clemencic et al., *The LHCb simulation application, Gauss: Design, evolution and experience*, J. Phys. Conf. Ser. **331** (2011) 032023.

[257] R. A. Khalek, S. Bailey, J. Gao, L. Harland-Lang, and J. Rojo, *Towards Ultimate Parton Distributions at the High-Luminosity LHC*, arXiv:1810.03639 [hep-ph].

[258] ATLAS Collaboration, G. Aad et al., *Measurement of $W^{\pm}$ and Z-boson production cross sections in pp collisions at $\sqrt{s} = 13$ TeV with the ATLAS detector*, Phys. Lett. **B759** (2016) 601–621, arXiv:1603.09222 [hep-ex].

[259] CMS Collaboration, A. M. Sirunyan et al., *Measurement of the $t\bar{t}$ production cross section using events with one lepton and at least one jet in pp collisions at $\sqrt{s}$ = 13 TeV*, JHEP **09** (2017) 051, arXiv:1701.06228 [hep-ex].

[260] G. Apollinari, O. BrÃŒning, T. Nakamoto, and L. Rossi, *High Luminosity Large Hadron*

Collider HL-LHC, CERN Yellow Report (2015) no. 5, 1–19, arXiv:1705.08830 [physics.acc-ph].

[261] H. Ogul and K. Dilsiz, *Cross Section Prediction for Inclusive Production of Z Boson in pp Collisions at* $\sqrt{s}$= 14 *TeV: A Study of Systematic Uncertainty Due to Scale Dependence*, Adv. High Energy Phys. **2017** (2017) 8262018, arXiv:1702.07206 [hep-ph].

[262] S. van der Meer, *Calibration of the effective beam height in the ISR*, CERN-ISR-PO-68-31. ISR-PO-68-31, CERN, Geneva, 1968. https://cds.cern.ch/record/296752.

[263] P. GrafstrÃ¶m and W. Kozanecki, *Luminosity determination at proton colliders*, Prog. Part. Nucl. Phys. **81** (2015) 97–148.

[264] H. Bartosik and G. Rumolo, *Production of single Gaussian bunches for Van der Meer scans in the LHC injector chain*, . https://cds.cern.ch/record/1590405.

[265] CMS Collaboration, *CMS luminosity measurement for the 2017 data-taking period at* $\sqrt{s} = 13$ TeV, CMS-PAS-LUM-17-004, CERN, Geneva, 2018. https://cds.cern.ch/record/2621960.

[266] ATLAS Collaboration, M. Aaboud et al., *Luminosity determination in pp collisions at* $\sqrt{s}$ = *8 TeV using the ATLAS detector at the LHC*, Eur. Phys. J. **C76** (2016) no. 12, 653, arXiv:1608.03953 [hep-ex].

[267] LHCb Collaboration, R. Aaij et al., *Precision luminosity measurements at LHCb*, JINST **9** (2014) no. 12, P12005, arXiv:1410.0149 [hep-ex].

[268] M. Hostettler and G. Papotti, *Beam Size Estimation from Luminosity Scans at the LHC During 2015 Proton Physics Operation*, in *Proceedings, 7th International Particle Accelerator Conference (IPAC 2016): Busan, Korea, May 8-13, 2016*, p. MOPMR025. 2016.

[269] O. Karacheban and T. Peter, *CMS emittance scans for luminosity calibration in 2017*, AYSS-2018: XXII International Scientific Conference of Young Scientists and Specialists (2018) .

[270] M. Hostettler, K. Fuchsberger, G. Papotti, T. Pieloni, and Y. Papaphilippou, *Luminosity Scans for Beam Diagnostics*, Phys. Rev. Accel. Beams **21** (Apr, 2018) 102801. 10 p. https://cds.cern.ch/record/2318252.

[271] CMS Collaboration, O. Karacheban and P. Tsrunchev, *CMS emittance scans for luminosity calibration in 2017*, CMS-CR-2018-062, CERN, Geneva, Jun, 2018. https://cds.cern.ch/record/2630628.

[272] J. Salfeld-Nebgen and D. Marlow, *Data-Driven Precision Luminosity Measurements with Z Bosons at the LHC and HL-LHC*, arXiv:1806.02184, Jun, 2018. http://cds.cern.ch/record/2641469.

[273] S. Alioli, P. Nason, C. Oleari, and E. Re, *A General Framework for Implementing NLO Calculations in Shower Monte Carlo Programs: the POWHEG BOX*, JHEP **06** (2010) 043, arXiv:1002.2581 [hep-ph].

[274] P. Nason and C. Oleari, *NLO Higgs boson production via vector-boson fusion matched with shower in POWHEG*, JHEP **02** (2010) 037, arXiv:0911.5299 [hep-ph].

[275] B. JÃ€ger, F. Schissler, and D. Zeppenfeld, *Parton-shower effects on Higgs boson production via vector-boson fusion in association with three jets*, JHEP **07** (2014) 125, arXiv:1405.6950 [hep-ph].

[276] M. Ciccolini, A. Denner, and S. Dittmaier, *Electroweak and QCD corrections to Higgs production via vector-boson fusion at the LHC*, Phys. Rev. **D77** (2008) 013002, arXiv:0710.4749 [hep-ph].

[277] M. Ciccolini, A. Denner, and S. Dittmaier, *Strong and electroweak corrections to the production*

of Higgs + 2jets via weak interactions at the LHC, Phys. Rev. Lett. **99** (2007) 161803, arXiv:0707.0381 [hep-ph].

[278] A. Denner, S. Dittmaier, S. Kallweit, and A. Muck, *Electroweak corrections to Higgs-strahlung off W/Z bosons at the Tevatron and the LHC with HAWK*, JHEP **03** (2012) 075, arXiv:1112.5142 [hep-ph].

[279] A. Denner, S. Dittmaier, S. Kallweit, and A. MÃŒck, *HAWK 2.0: A Monte Carlo program for Higgs production in vector-boson fusion and Higgs strahlung at hadron colliders*, Comput. Phys. Commun. **195** (2015) 161–171, arXiv:1412.5390 [hep-ph].

[280] J. Cruz-Martinez, T. Gehrmann, E. W. N. Glover, and A. Huss, *Second-order QCD effects in Higgs boson production through vector boson fusion*, arXiv:1802.02445 [hep-ph].

[281] M. Cacciari and G. P. Salam, *Dispelling the N^3 Myth for the k_t Jet-Finder*, Phys. Lett. **B 641** (2006) 57, arXiv:0512210 [hep-ph].

[282] X. Chen, T. Gehrmann, E. W. N. Glover, and M. Jaquier, *Precise QCD predictions for the production of Higgs + jet final states*, Phys. Lett. **B740** (2015) 147–150, arXiv:1408.5325 [hep-ph].

[283] X. Chen, J. Cruz-Martinez, T. Gehrmann, E. W. N. Glover, and M. Jaquier, *NNLO QCD corrections to Higgs boson production at large transverse momentum*, JHEP **10** (2016) 066, arXiv:1607.08817 [hep-ph].

[284] L. Cieri, X. Chen, T. Gehrmann, E. W. N. Glover, and A. Huss, *Higgs boson production at the LHC using the q_T subtraction formalism at N^3LO QCD*, arXiv:1807.11501 [hep-ph].

[285] T. Gehrmann et al., *Jet cross sections and transverse momentum distributions with NNLOJET*, in *13th International Symposium on Radiative Corrections: Application of Quantum Field Theory to Phenomenology (RADCOR 2017) St. Gilgen, Austria, September 24-29, 2017*. 2018. arXiv:1801.06415 [hep-ph]. https://inspirehep.net/record/1649093/files/arXiv:1801.06415.pdf.

[286] A. Gehrmann-De Ridder, T. Gehrmann, E. W. N. Glover, A. Huss, and T. A. Morgan, *Precise QCD predictions for the production of a Z boson in association with a hadronic jet*, Phys. Rev. Lett. **117** (2016) no. 2, 022001, arXiv:1507.02850 [hep-ph].

[287] J. Currie, T. Gehrmann, and J. Niehues, *Precise QCD predictions for the production of dijet final states in deep inelastic scattering*, Phys. Rev. Lett. **117** (2016) no. 4, 042001, arXiv:1606.03991 [hep-ph].

[288] A. Gehrmann-De Ridder, T. Gehrmann, E. W. N. Glover, A. Huss, and D. M. Walker, *Next-to-Next-to-Leading-Order QCD Corrections to the Transverse Momentum Distribution of Weak Gauge Bosons*, Phys. Rev. Lett. **120** (2018) no. 12, 122001, arXiv:1712.07543 [hep-ph].

[289] J. Currie, T. Gehrmann, E. W. N. Glover, A. Huss, J. Niehues, and A. Vogt, *N^3LO corrections to jet production in deep inelastic scattering using the Projection-to-Born method*, JHEP **05** (2018) 209, arXiv:1803.09973 [hep-ph].

[290] J. Niehues and D. M. Walker, *NNLO QCD Corrections to Jet Production in Charged Current Deep Inelastic Scattering*, arXiv:1807.02529 [hep-ph].

[291] J. Currie, A. Gehrmann-De Ridder, T. Gehrmann, E. W. N. Glover, A. Huss, and J. Pires, *Infrared sensitivity of single jet inclusive production at hadron colliders*, JHEP **10** (2018) 155, arXiv:1807.03692 [hep-ph].

[292] F. Campanario, T. M. Figy, S. PlÃ€tzer, and M. SjÃ¶dahl, *Electroweak Higgs Boson Plus Three Jet Production at Next-to-Leading-Order QCD*, Phys. Rev. Lett. **111** (2013) no. 21, 211802, arXiv:1308.2932 [hep-ph].

[293] F. Campanario, T. M. Figy, S. PlÃ€tzer, and M. SjÃ¶dahl, *NLO QCD Corrections to*

Electroweak Higgs Boson Plus Three Jet Production at the LHC, PoS **RADCOR2013** (2013) 042, arXiv:1311.5455 [hep-ph].

[294] F. Campanario, T. M. Figy, S. PlÃ€tzer, and M. Sjodahl, *Beyond the t-channel Approximation: Next-to-Leading Order QCD Corrections to Electroweak Higgs Boson Production Plus Three Jets Production at the LHC*, PoS **LL2014** (2014) 025, arXiv:1407.5050 [hep-ph].

[295] F. Campanario, T. M. Figy, S. Plätzer, M. Rauch, P. Schichtel, and M. Sjödahl, *Stress-testing the VBF approximation in multijet final states*, arXiv:1802.09955 [hep-ph].

[296] F. Campanario, *Towards pp -> VVjj at NLO QCD: Bosonic contributions to triple vector boson production plus jet*, JHEP **10** (2011) 070, arXiv:1105.0920 [hep-ph].

[297] M. Sjodahl, *ColorFull – a C++ library for calculations in SU(Nc) color space*, Eur. Phys. J. **C75** (2015) no. 5, 236, arXiv:1412.3967 [hep-ph].

[298] J. Baglio et al., *Release Note - VBFNLO 2.7.0*, arXiv:1404.3940 [hep-ph].

[299] T. Figy, V. Hankele, and D. Zeppenfeld, *Next-to-leading order QCD corrections to Higgs plus three jet production in vector-boson fusion*, JHEP **02** (2008) 076, arXiv:0710.5621 [hep-ph].

[300] S. Platzer and S. Gieseke, *Dipole Showers and Automated NLO Matching in Herwig++*, Eur. Phys. J. **C72** (2012) 2187, arXiv:1109.6256 [hep-ph].

[301] J. Bellm et al., *Herwig 7.1 Release Note*, arXiv:1705.06919 [hep-ph].

[302] M. Bähr, S. Gieseke, M. A. Gigg, D. Grellscheid, K. Hamilton, O. Latunde-Dada, S. Plätzer, P. Richardson, M. H. Seymour, A. Sherstnev, et al., *Herwig++ physics and manual*, The European Physical Journal C **58** (2008) no. 4, 639–707.

[303] M. Cacciari, G. P. Salam, and G. Soyez, *FastJet User Manual*, Eur. Phys. J. **C72** (2012) 1896, arXiv:1111.6097 [hep-ph].

[304] A. Buckley, J. Butterworth, L. Lonnblad, D. Grellscheid, H. Hoeth, J. Monk, H. Schulz, and F. Siegert, *Rivet user manual*, Comput. Phys. Commun. **184** (2013) 2803–2819, arXiv:1003.0694 [hep-ph].

[305] J. Towns, T. Cockerill, M. Dahan, I. Foster, K. Gaither, A. Grimshaw, V. Hazlewood, S. Lathrop, D. Lifka, G. D. Peterson, et al., *XSEDE: accelerating scientific discovery*, Computing in Science & Engineering **16** (2014) no. 5, 62–74.

[306] R. Pordes, D. Petravick, B. Kramer, D. Olson, M. Livny, A. Roy, P. Avery, K. Blackburn, T. Wenaus, F. Würthwein, et al., *The open science grid*, in *Journal of Physics: Conference Series*, vol. 78, p. 012057, IOP Publishing. 2007.

[307] I. Sfiligoi, D. C. Bradley, B. Holzman, P. Mhashilkar, S. Padhi, and F. Wurthwein, *The pilot way to grid resources using glideinWMS*, in *Computer Science and Information Engineering, 2009 WRI World Congress on*, vol. 2, pp. 428–432, IEEE. 2009.

[308] J. Bagger, V. D. Barger, K.-m. Cheung, J. F. Gunion, T. Han, G. A. Ladinsky, R. Rosenfeld, and C. P. Yuan, *The Strongly interacting WW system: Gold plated modes*, Phys. Rev. D **49** (1994) 1246–1264, arXiv:hep-ph/9306256.

[309] J. Bagger, V. D. Barger, K.-m. Cheung, J. F. Gunion, T. Han, G. A. Ladinsky, R. Rosenfeld, and C. P. Yuan, *CERN LHC analysis of the strongly interacting WW system: Gold plated modes*, Phys. Rev. D **52** (1995) 3878–3889, arXiv:hep-ph/9504426.

[310] CMS Collaboration, *Observation of a new boson at a mass of 125 GeV with the CMS experiment at the LHC*, Phys. Lett. B **716** (2012) 30–61, arXiv:1207.7235 [hep-ex].

[311] M. J. G. Veltman, *Second Threshold in Weak Interactions*, Acta Phys. Polon. B **8** (1977) 475.

[312] B. W. Lee, C. Quigg, and H. B. Thacker, *The Strength of Weak Interactions at Very High-Energies and the Higgs Boson Mass*, Phys. Rev. Lett. **38** (1977) 883–885.

[313] B. W. Lee, C. Quigg, and H. B. Thacker, *Weak Interactions at Very High-Energies: The Role of*

the Higgs Boson Mass, Phys. Rev. D **16** (1977) 1519.

[314] HEPAP Subcommittee Collaboration, HEPAP Subcommittee Collaboration, *Building for Discovery: Strategic Plan for U.S. Particle Physics in the Global Context*, . http://science.energy.gov/~/media/hep/hepap/pdf/May-2014/FINAL_P5_Report_053014.pdf.

[315] R. Aleksan, P. Braun-Munzinger, P. Chomaz, K. Desch, C. De Clercq, M. Diemoz, K. Huitu, P. Jenni, M. Krammer, Y. Kuno, P. McBride, T. Nakada, E. Tsesmelis, D. Wark, A. F. Zarnecki, F. Zwirner, P. Brun, E. Fernandez Martinez, R. Forty, E. Garutti, K. Kutak, A. Lister, P. Slavich, and F. Zimmermann, *Physics Briefing Book: Input for the Strategy Group to draft the update of the European Strategy for Particle Physics*, . https://cds.cern.ch/record/1628377. Open Symposium held in Cracow from 10th to 12th of September 2012.

[316] E. Accomando, A. Ballestrero, S. Bolognesi, E. Maina, and C. Mariotti, *Boson-boson scattering and Higgs production at the LHC from a six fermion point of view: Four jets + l nu processes at* $\mathcal{O}(\alpha_{em}^6)$, JHEP **03** (2006) 093, arXiv:hep-ph/0512219.

[317] B. Zhu, P. Govoni, Y. Mao, C. Mariotti, and W. Wu, *Same Sign WW Scattering Process as a Probe of Higgs Boson in pp Collision at* $\sqrt{s} = 10$ *TeV*, Eur. Phys. J. C **71** (2011) 1514, arXiv:1010.5848 [hep-ex].

[318] ATLAS Collaboration, ATLAS Collaboration, *Observation of electroweak production of a same-sign* W *boson pair in association with two jets in pp collisions at* $\sqrt{s} = 13$ *TeV with the ATLAS detector*, ATLAS-CONF-2018-030, CERN, Geneva, Jul, 2018. https://cds.cern.ch/record/2629411.

[319] CMS Collaboration, A. M. Sirunyan et al., *Observation of electroweak production of same-sign W boson pairs in the two jet and two same-sign lepton final state in proton-proton collisions at* $\sqrt{s} = 13$ *TeV*, Phys. Rev. Lett. **120** (2018) no. 8, 081801, arXiv:1709.05822 [hep-ex].

[320] ATLAS Collaboration, A. Collaboration, *Prospects for the measurement of the* $W^{\pm}W^{\pm}$ *scattering cross section and extraction of the longitudinal scattering component in pp collisions at the High-Luminosity LHC with the ATLAS experiment*, 2018.

[321] CMS Collaboration, C. Collaboration, *Study of* $W^{\pm}W^{\pm}$ *production via vector boson scattering at the HL-LHC with the upgraded CMS detector*, 2018.

[322] S. Frixione and B. R. Webber, *Matching NLO QCD computations and parton shower simulations*, JHEP **06** (2002) 029, arXiv:hep-ph/0204244 [hep-ph].

[323] R. D. Ball et al., *Parton distributions with LHC data*, Nucl. Phys. B **867** (2013) 244, arXiv:1207.1303 [hep-ph].

[324] T. Sjöstrand, S. Ask, J. R. Christiansen, R. Corke, N. Desai, P. Ilten, S. Mrenna, S. Prestel, C. O. Rasmussen, and P. Z. Skands, *An Introduction to PYTHIA 8.2*, Comput. Phys. Commun. **191** (2015) 159–177, arXiv:1410.3012 [hep-ph].

[325] J. M. Campbell, R. K. Ellis, P. Nason, and E. Re, *Top-Pair Production and Decay at NLO Matched with Parton Showers*, JHEP **04** (2015) 114, arXiv:1412.1828 [hep-ph].

[326] ATLAS Collaboration, ATLAS Collaboration, *Expected performance of the ATLAS detector at HL-LHC*, in progress, CERN, Geneva, Oct, 2018.

[327] M. Cacciari, G. P. Salam, G. Soyez, *The anti-*k_t *jet clustering algorithm*, JHEP **04** (2008) 063, arXiv:0802.1189 [hep-ph].

[328] D. Bertolini, P. Harris, M. Low, and N. Tran, *Pileup Per Particle Identification*, JHEP **10** (2014) 059, arXiv:1407.6013 [hep-ph].

[329] D. Guest, J. Collado, P. Baldi, S.-C. Hsu, G. Urban, and D. Whiteson, *Jet flavor classification in high-energy physics with deep neural networks*, Phys. Rev. D **94** (Dec, 2016) 112002. https://link.aps.org/doi/10.1103/PhysRevD.94.112002.

[330] D. Rainwater, R. Szalapski, and D. Zeppenfeld, *Probing color-singlet exchange in $Z + 2$-jet events at the CERN LHC*, Phys. Rev. D **54** (Dec, 1996) 6680–6689. https://link.aps.org/doi/10.1103/PhysRevD.54.6680.

[331] J. Searcy, L. Huang, M.-A. Pleier, and J. Zhu, *Determination of the WW polarization fractions in $pp \to W^{\pm}W^{\pm}jj$ using a deep machine learning technique*, Phys. Rev. D **93** (2016) no. 9, 094033, arXiv:1510.01691 [hep-ph].

[332] D. Gonçalves, T. Plehn, and J. M. Thompson, *Weak boson fusion at 100 TeV*, Phys. Rev. **D95** (2017) no. 9, 095011, arXiv:1702.05098 [hep-ph].

[333] B. Jäger, L. Salfelder, M. Worek, and D. Zeppenfeld, *Physics opportunities for vector-boson scattering at a future 100 TeV hadron collider*, Phys. Rev. **D96** (2017) no. 7, 073008, arXiv:1704.04911 [hep-ph].

[334] B. Jäger, C. Oleari, and D. Zeppenfeld, *Next-to-leading order QCD corrections to W^+W^- production via vector-boson fusion*, JHEP **07** (2006) 015, arXiv:hep-ph/0603177 [hep-ph].

[335] B. Jäger, C. Oleari, and D. Zeppenfeld, *Next-to-leading order QCD corrections to Z boson pair production via vector-boson fusion*, Phys. Rev. **D73** (2006) 113006, arXiv:hep-ph/0604200 [hep-ph].

[336] G. Bozzi, B. Jäger, C. Oleari, and D. Zeppenfeld, *Next-to-leading order QCD corrections to W^+Z and W^-Z production via vector-boson fusion*, Phys. Rev. **D75** (2007) 073004, arXiv:hep-ph/0701105 [hep-ph].

[337] B. Jäger, C. Oleari, and D. Zeppenfeld, *Next-to-leading order QCD corrections to W^+W^+jj and W^-W^-jj production via weak-boson fusion*, Phys. Rev. **D80** (2009) 034022, arXiv:0907.0580 [hep-ph].

[338] B. Jäger and G. Zanderighi, *NLO corrections to electroweak and QCD production of W^+W^+ plus two jets in the POWHEGBOX*, JHEP **11** (2011) 055, arXiv:1108.0864 [hep-ph].

[339] A. Denner, L. Hošeková, and S. Kallweit, *NLO QCD corrections to W^+W^+jj production in vector-boson fusion at the LHC*, Phys. Rev. **D86** (2012) 114014, arXiv:1209.2389 [hep-ph].

[340] M. Rauch, *Vector-Boson Fusion and Vector-Boson Scattering*, arXiv:1610.08420 [hep-ph].

[341] A. Ballestrero et al., *Precise predictions for same-sign W-boson scattering at the LHC*, Eur. Phys. J. **C78** (2018) no. 8, 671, arXiv:1803.07943 [hep-ph].

[342] C. Oleari and D. Zeppenfeld, *QCD corrections to electroweak $\ell\nu_\ell jj$ and $\ell^+\ell^-jj$ production*, Phys. Rev. **D69** (2004) 093004, arXiv:hep-ph/0310156 [hep-ph].

[343] D. Yu. Bardin, A. Leike, T. Riemann, and M. Sachwitz, *Energy-dependent width effects in e^+e^--annihilation near the Z-boson pole*, Phys. Lett. **B206** (1988) 539–542.

[344] A. Denner, S. Dittmaier, M. Roth, and D. Wackeroth, *Electroweak radiative corrections to $e^+e^- \to WW \to 4$ fermions in double-pole approximation: The RACOONWW approach*, Nucl. Phys. **B587** (2000) 67–117, arXiv:hep-ph/0006307 [hep-ph].

[345] A. Denner et al., *Predictions for all processes $e^+e^- \to 4$fermions $+\gamma$*, Nucl. Phys. **B560** (1999) 33–65, arXiv:hep-ph/9904472.

[346] A. Denner et al., *Electroweak corrections to charged-current $e^+e^- \to 4$ fermion processes: Technical details and further results*, Nucl. Phys. **B724** (2005) 247–294, arXiv:hep-ph/0505042.

[347] A. Denner and S. Dittmaier, *The complex-mass scheme for perturbative calculations with unstable particles*, Nucl. Phys. Proc. Suppl. **160** (2006) 22–26, arXiv:hep-ph/0605312 [hep-ph]. [,22(2006)].

[348] ATLAS Collaboration, G. Aad et al., *Evidence for Electroweak Production of $W^{\pm}W^{\pm}jj$ in pp Collisions at $\sqrt{s} = 8$ TeV with the ATLAS Detector*, Phys. Rev. Lett. **113** (2014) no. 14, 141803,

arXiv:1405.6241 [hep-ex].

[349] ATLAS Collaboration, M. Aaboud et al., *Measurement of $W^{\pm}W^{\pm}$ vector-boson scattering and limits on anomalous quartic gauge couplings with the ATLAS detector*, Phys. Rev. **D96** (2017) 012007, arXiv:1611.02428 [hep-ex].

[350] CMS Collaboration, V. Khachatryan et al., *Study of vector boson scattering and search for new physics in events with two same-sign leptons and two jets*, Phys. Rev. Lett. **114** (2015) no. 5, 051801, arXiv:1410.6315 [hep-ex].

[351] CMS Collaboration, *Observation of electroweak production of same-sign W boson pairs in the two jet and two same-sign lepton final state in proton-proton collisions at 13 TeV*, . CMS-PAS-SMP-17-004.

[352] ATLAS Collaboration, *Studies on the impact of an extended Inner Detector tracker and a forward muon tagger on $W^{\pm}W^{\pm}$ scattering in pp collisions at the High-Luminosity LHC with the ATLAS experiment*, . https://cds.cern.ch/record/2298958.

[353] C. Schwan, *NLO EW corrections for W and Z scattering at the LHC*, 2018. https://indico.cern.ch/event/702614/.

[354] A. Denner, S. Dittmaier, P. Maierhöfer, M. Pellen, and C. Schwan, *NLO QCD and EW corrections to WZ scattering*, In preparation .

[355] A. Ballestrero, B. Biedermann, S. Brass, A. Denner, S. Dittmaier, R. Frederix, P. Govoni, M. Grossi, B. Jäger, A. Karlberg, E. Maina, M. Pellen, G. Pelliccioli, S. Plätzer, M. Rauch, D. Rebuzzi, J. Reuter, V. Rothe, C. Schwan, H.-S. Shao, P. Stienemeier, G. Zanderighi, M. Zaro, and D. Zeppenfeld, *Precise predictions for same-sign W-boson scattering at the LHC*, The European Physical Journal C **78** (Aug, 2018) 671. https://doi.org/10.1140/epjc/s10052-018-6136-y.

[356] ATLAS Collaboration, A. Collaboration, *Observation of electroweak W±Z boson pair production in association with two jets in pp collisions at sqrt(s) = 13 TeV with the ATLAS detector*, 2018.

[357] CMS Collaboration, C. Collaboration, *Measurement of electroweak WZ production and search for new physics in pp collisions at sqrt(s) = 13 TeV*, 2018.

[358] T. Gleisberg et al., *Event generation with Sherpa 1.1*, JHEP **02** (2009) 007, arXiv:0811.4622 [hep-ph].

[359] J. Alwall, M. Herquet, F. Maltoni, O. Mattelaer, and T. Stelzer, *MadGraph 5: going beyond*, JHEP **06** (2011) 128, arXiv:1106.0522 [hep-ph].

[360] CMS Collaboration, T. Sirunyan et al., *Measurement of vector boson scattering and constraints on anomalous quartic couplings from events with four leptons and two jets in proton-proton collisions at sqrt(s) = 13 TeV.*, Phys. Lett. B **774** (Aug, 2017) 682–705. 24 p, arXiv:1708.02812.

[361] NNPDF Collaboration, R. D. Ball et al., *Parton distributions for the LHC Run II*, JHEP **04** (2015) 040, arXiv:1410.8849 [hep-ph].

[362] J. Alwall, R. Frederix, S. Frixione, V. Hirschi, F. Maltoni, O. Mattelaer, H.-S. Shao, T. Stelzer, P. Torielli, and M. Zaro, *The automated computation of tree-level and next-to-leading order differential cross sections, and their matching to parton shower simulations*, JHEP **07** (2014) 079, arXiv:1405.0301 [hep-ph].

[363] R. Frederix and S. Frixione, *Merging meets matching in MC@NLO*, JHEP **12** (2012) 061, arXiv:1209.6215 [hep-ph].

[364] P. Artoisenet, R. Frederix, O. Mattelaer, and R. Rietkerk, *Automatic spin-entangled decays of heavy resonances in Monte Carlo simulations*, JHEP **03** (2013) 015, arXiv:1212.3460 [hep-ph].

[365] J. M. Campbell and R. K. Ellis, *MCFM for the Tevatron and the LHC*, Nucl. Phys. B Proc. Suppl. **205-206** (2010) 10, arXiv:1007.3492 [hep-ph].

[366] Particle Data Group Collaboration, C. Patrignani et al., *Review of Particle Physics*, Chin. Phys. **C40** (2016) no. 10, 100001.

[367] ATLAS Collaboration, *Expected performance for an upgraded ATLAS detector at High-Luminosity LHC*, ATL-PHYS-PUB-2016-026, 2016. https://cds.cern.ch/record/2223839.

[368] D. Rainwater, R. Szalapski, and D. Zeppenfeld, *Probing color singlet exchange in Z+2-jet events at the CERN LHC*, Phys. Rev. D **54** (1996) 6680, arXiv:hep-ph/9605444 [hep-ph].

[369] CMS Collaboration, V. Khachatryan et al., *Measurement of electroweak production of two jets in association with a Z boson in proton–proton collisions at $\sqrt{s} = 8$ TeV*, Eur. Phys. J. C **75** (2015) 66, arXiv:1410.3153 [hep-ex].

[370] *Expected performance for an upgraded ATLAS detector at High-Luminosity LHC*, ATL-PHYS-PUB-2016-026, CERN, Geneva, Aug, 2016. https://cds.cern.ch/record/2223839.

[371] M. Cacciari, C. P. Salam and G. Soyez, *The anti-k_t jet clustering algorithm*, JHEP **04** (2008) 063.

[372] D. Krohn, J. Thaler, and L.-T. Wang, *Jet Trimming*, JHEP **02** (2010) 084, arXiv:0912.1342 [hep-ph].

[373] ATLAS Collaboration, *Identification of boosted, hadronically decaying W bosons and comparisons with ATLAS data taken at $\sqrt{s}$=8 TeV*, JHEP **n/a** (2015) n/a, arXiv:1510.05821 [hep-ex].

[374] *Identification of boosted, hadronically-decaying W and Z bosons in $\sqrt{s} = 13$ TeV Monte Carlo Simulations for ATLAS*, ATL-PHYS-PUB-2015-033, CERN, Geneva, Aug, 2015. https://cds.cern.ch/record/2041461.

[375] A. Hoecker, P. Speckmayer, J. Stelzer, J. Therhaag, E. von Toerne, and H. Voss, *TMVA: Toolkit for Multivariate Data Analysis*, PoS **ACAT** (2007) 040, arXiv:physics/0703039.

[376] G. Cowan, K. Cranmer, E. Gross, and O. Vitells, *Asymptotic formulae for likelihood-based tests of new physics*, Eur. Phys. J. **C71** (2011) 1554, arXiv:1007.1727 [physics.data-an]. [Erratum: Eur. Phys. J.C73,2501(2013)].

[377] The DELPHES 3 Collaboration, de Favereau, J., Delaere, C. *et al.*, *DELPHES 3: a modular framework for fast simulation of a generic collider experiment*, JHEP **02** (2014) 057, arXiv:1307.6346 [hep-ex].

[378] The project is partially supported by the EC as FP7 HiLumi LHC Design Study under grant no. 284404 Collaboration, L. Rossi and O. Bruning, *High Luminosity Large Hadron Collider: A description for the European Strategy Preparatory Group*, Geneva, Aug, 2012. https://cds.cern.ch/record/1471000.

[379] I. Bejar Alonso and L. Rossi, *HiLumi LHC Technical Design Report: Deliverable: D1.10*, Nov, 2015. https://cds.cern.ch/record/2069130.

[380] ATLAS Collaboration, *Prospect studies for the production of three massive vector bosons with the ATLAS detector at the High-Luminosity LHC*, ATL-PHYS-PUB-2018-030, CERN, Geneva, Nov, 2018. https://cds.cern.ch/record/2647220.

[381] A. Lazopoulos, T. McElmurry, K. Melnikov, and F. Petriello, *Next-to-Leading Order QCD Corrections to $t\bar{t}Z$ Production at the LHC*, Phys. Lett. **B 666** (2008) 62, arXiv:0804.2220 [hep-ph].

[382] M. Garzelli, A. Kardos, C. Papadopoulos, and Z. Trocsanyi, *$t\bar{t}W^{\pm}$ and $t\bar{t}Z$ Hadroproduction at*

NLO Accuracy in QCD with Parton Shower and Hadronization Effects, JHEP **11** (2012) 056, arXiv:1208.2665 [hep-ph].

[383] J. M. Campbell and R. K. Ellis, *$t\bar{t}W^{\pm}$ Production and Decay at NLO*, JHEP **07** (2012) 052, arXiv:1204.5678 [hep-ph].

[384] ATLAS Collaboration, *Multi-Boson Simulation for 13 TeV ATLAS Analyses*, ATL-PHYS-PUB-2017-005, 2017. https://cds.cern.ch/record/2261933.

[385] P. Nason, *A New Method for Combining NLO QCD with Shower Monte Carlo Algorithms*, JHEP **11** (2004) 040, arXiv:0409146 [hep-ph].

[386] S. Frixione, P. Nason, and C. Oleari, *Matching NLO QCD Computations with Parton Shower Simulations: the POWHEG Method*, JHEP **11** (2007) 070, arXiv:0709.2092 [hep-ph].

[387] T. Sjostrand, S. Mrenna, and P. Z. Skands, *PYTHIA 6.4 Physics and Manual*, JHEP **05** (2006) 026, arXiv:0603175 [hep-ph].

[388] ATLAS Collaboration, *Improvements in $t\bar{t}$ modelling using NLO+PS Monte Carlo generators for Run 2*, ATL-PHYS-PUB-2018-009, 2018. https://cds.cern.ch/record/2630327.

[389] ATLAS Collaboration, *Modelling of the $t\bar{t}H$ and $t\bar{t}V(V = W, Z)$ processes for $\sqrt{s} = 13$ TeV ATLAS analyses*, ATL-PHYS-PUB-2016-005, 2016. https://cds.cern.ch/record/2120826.

[390] M. Czakon and A. Mitov, *Top++: A Program for the Calculation of the Top-Pair Cross-Section at Hadron Colliders*, Comput. Phys. Commun. **185** (2014) 2930, arXiv:1112.5675 [hep-ph].

[391] ATLAS Collaboration, *Expected performance of the ATLAS detector at HL-LHC", In progress.*, ATL-PHYS-PUB-2018-xxx, 2018. https://cds.cern.ch/record/xxx.

[392] ATLAS Collaboration, M. Aaboud et al., *Search for triboson $W^{\pm}W^{\pm}W^{\mp}$ production in pp collisions at $\sqrt{s} = 8$ TeV with the ATLAS detector*, Eur. Phys. J. **C77** (2017) no. 3, 141, arXiv:1610.05088 [hep-ex].

[393] E. Bothmann, M. Schönherr, and S. Schumann, *Reweighting QCD matrix-element and parton-shower calculations*, Eur. Phys. J. **C76** (2016) no. 11, 590, arXiv:1606.08753 [hep-ph].

[394] G. Heinrich, S. Jahn, S. P. Jones, M. Kerner, and J. Pires, *NNLO predictions for Z-boson pair production at the LHC*, JHEP **03** (2018) 142, arXiv:1710.06294 [hep-ph].

[395] I. W. Stewart, F. J. Tackmann, and W. J. Waalewijn, *Factorization at the LHC: From PDFs to Initial State Jets*, Phys. Rev. **D81** (2010) 094035, arXiv:0910.0467 [hep-ph].

[396] R. Boughezal, C. Focke, W. Giele, X. Liu, and F. Petriello, *Higgs boson production in association with a jet at NNLO using jettiness subtraction*, Phys. Lett. **B748** (2015) 5–8, arXiv:1505.03893 [hep-ph].

[397] T. Gehrmann, A. von Manteuffel, and L. Tancredi, *The two-loop helicity amplitudes for $q\bar{q}' \to V_1V_2 \to 4$ leptons*, JHEP **09** (2015) 128, arXiv:1503.04812 [hep-ph].

[398] S. Alioli, F. Caola, G. Luisoni, and R. Röntsch, *ZZ production in gluon fusion at NLO matched to parton-shower*, Phys. Rev. **D95** (2017) no. 3, 034042, arXiv:1609.09719 [hep-ph].

[399] M. Grazzini, S. Kallweit, M. Wiesemann, and J. Y. Yook, *ZZ production at the LHC: NLO QCD corrections to the loop-induced gluon fusion channel*, arXiv:1811.09593 [hep-ph].

[400] M. Grazzini, S. Kallweit, D. Rathlev, and A. Torre, *$Z\gamma$ production at hadron colliders in NNLO QCD*, Phys. Lett. **B731** (2014) 204–207, arXiv:1309.7000 [hep-ph].

[401] M. Grazzini, S. Kallweit, and D. Rathlev, *$W\gamma$ and $Z\gamma$ production at the LHC in NNLO QCD*, JHEP **07** (2015) 085, arXiv:1504.01330 [hep-ph].

[402] F. Cascioli, T. Gehrmann, M. Grazzini, S. Kallweit, P. Maierhöfer, A. von Manteuffel,

S. Pozzorini, D. Rathlev, L. Tancredi, and E. Weihs, *ZZ production at hadron colliders in NNLO QCD*, Phys. Lett. **B735** (2014) 311–313, arXiv:1405.2219 [hep-ph].

[403] M. Grazzini, S. Kallweit, and D. Rathlev, *ZZ production at the LHC: fiducial cross sections and distributions in NNLO QCD*, Phys. Lett. **B750** (2015) 407–410, arXiv:1507.06257 [hep-ph].

[404] T. Gehrmann, M. Grazzini, S. Kallweit, P. Maierhöfer, A. von Manteuffel, S. Pozzorini, D. Rathlev, and L. Tancredi, *W^+W^- Production at Hadron Colliders in Next to Next to Leading Order QCD*, Phys. Rev. Lett. **113** (2014) no. 21, 212001, arXiv:1408.5243 [hep-ph].

[405] M. Grazzini, S. Kallweit, S. Pozzorini, D. Rathlev, and M. Wiesemann, *W^+W^- production at the LHC: fiducial cross sections and distributions in NNLO QCD*, JHEP **08** (2016) 140, arXiv:1605.02716 [hep-ph].

[406] M. Grazzini, S. Kallweit, D. Rathlev, and M. Wiesemann, *$W^\pm Z$ production at hadron colliders in NNLO QCD*, Phys. Lett. **B761** (2016) 179–183, arXiv:1604.08576 [hep-ph].

[407] M. Grazzini, S. Kallweit, D. Rathlev, and M. Wiesemann, *$W^\pm Z$ production at the LHC: fiducial cross sections and distributions in NNLO QCD*, JHEP **05** (2017) 139, arXiv:1703.09065 [hep-ph].

[408] S. Kallweit and M. Wiesemann, *ZZ production at the LHC: NNLO predictions for $2\ell 2\nu$ and 4ℓ signatures*, Phys. Lett. **B786** (2018) 382–389, arXiv:1806.05941 [hep-ph].

[409] M. Grazzini, S. Kallweit, D. Rathlev, and M. Wiesemann, *Transverse-momentum resummation for vector-boson pair production at NNLL+NNLO*, JHEP **08** (2015) 154, arXiv:1507.02565 [hep-ph].

[410] E. Re, M. Wiesemann, and G. Zanderighi, *NNLOPS accurate predictions for W^+W^- production*, arXiv:1805.09857 [hep-ph].

[411] A. Denner, S. Dittmaier, and L. Hofer, *COLLIER - A fortran-library for one-loop integrals*, PoS **LL2014** (2014) 071, arXiv:1407.0087 [hep-ph].

[412] A. Denner, S. Dittmaier, and L. Hofer, COLLIER*: a fortran-based Complex One-Loop LIbrary in Extended Regularizations*, Comput. Phys. Commun. **212** (2017) 220–238, arXiv:1604.06792 [hep-ph].

[413] G. Ossola, C. G. Papadopoulos, and R. Pittau, *CutTools: A Program implementing the OPP reduction method to compute one-loop amplitudes*, JHEP **03** (2008) 042, arXiv:0711.3596 [hep-ph].

[414] F. Buccioni, S. Pozzorini, and M. Zoller, *On-the-fly reduction of open loops*, Eur. Phys. J. **C78** (2018) no. 1, 70, arXiv:1710.11452 [hep-ph].

[415] K. J. F. Gaemers and G. J. Gounaris, *Polarization Amplitudes for e+ e- —> W+ W- and e+ e- —> Z Z*, Z. Phys. **C1** (1979) 259.

[416] K. Hagiwara, R. D. Peccei, D. Zeppenfeld, and K. Hikasa, *Probing the Weak Boson Sector in e+ e- —> W+ W-*, Nucl. Phys. **B282** (1987) 253–307.

[417] T. Melia et al., *W^+W^-, WZ and ZZ production in the POWHEG BOX*, JHEP **11** (2011) 078, arXiv:1107.5051 [hep-ph].

[418] P. Nason and G. Zanderighi, *W^+W^- , WZ and ZZ production in the POWHEG-BOX-V2*, Eur. Phys. J. **C74** (2014) no. 1, 2702, arXiv:1311.1365 [hep-ph].

[419] J. Baglio, S. Dawson, and I. M. Lewis, *An NLO QCD effective field theory analysis of W^+W^- production at the LHC including fermionic operators*, Phys. Rev. **D96** (2017) no. 7, 073003, arXiv:1708.03332 [hep-ph].

[420] A. Alves, N. Rosa-Agostinho, O. J. P. Éboli, and M. C. Gonzalez-Garcia, *Effect of Fermionic Operators on the Gauge Legacy of the LHC Run I*, Phys. Rev. **D98** (2018) no. 1, 013006, arXiv:1805.11108 [hep-ph].

[421] ATLAS Collaboration, G. Aad et al., *Measurement of total and differential W^+W^- production cross sections in proton-proton collisions at $\sqrt{s} = 8$ TeV with the ATLAS detector and limits on anomalous triple-gauge-boson couplings*, JHEP **09** (2016) 029, arXiv:1603.01702 [hep-ex].

[422] CMS Collaboration, V. Khachatryan et al., *Measurement of the $\mathrm{W}^+\mathrm{W}^-$ cross section in pp collisions at $\sqrt{s} = 8$ TeV and limits on anomalous gauge couplings*, Eur. Phys. J. **C76** (2016) no. 7, 401, arXiv:1507.03268 [hep-ex].

[423] C. Grojean, M. Montull, and M. Riembau, *Diboson at the LHC vs LEP*, arXiv:1810.05149 [hep-ph].

[424] ATLAS Collaboration, *Technical Design Report for the ATLAS Inner Tracker Strip Detector*, . http://cdsweb.cern.ch/record/2257755. CERN-LHCC-2017-005.

[425] F. Zimmermann, *HE-LHC Overview, Parameters and Challenges*, ICFA Beam Dyn. Newslett. **72** (2017) 138–141.

[426] ATLAS Collaboration, ATLAS Collaboration, *Prospects for the measurement of the W-boson mass at the HL- and HE-LHC*, . https://cds.cern.ch/record/2645431. ATL-PHYS-PUB-2018-026.

[427] H.-L. Lai, M. Guzzi, J. Huston, Z. Li, P. M. Nadolsky, et al., *New parton distributions for collider physics*, Phys. Rev. D **82** (2010) 074024, arXiv:1007.2241 [hep-ph].

[428] ATLAS Collaboration, *Measurement of the Z/γ^* boson transverse momentum distribution in pp collisions at $\sqrt{s} = 7$ TeV with the ATLAS detector*, JHEP **09** (2014) 145, arXiv:1406.3660 [hep-ex].

[429] N. Davidson, T. Przedzinski, and Z. Was, *PHOTOS interface in C++: Technical and Physics Documentation*, Comput. Phys. Commun. **199** (2016) 86–101, arXiv:1011.0937 [hep-ph].

[430] M. Klein and V. Radescu, *Partons from the LHeC*, . https://cds.cern.ch/record/1564929.

[431] LHeC Study Group Collaboration, J. L. Abelleira Fernandez et al., *A Large Hadron Electron Collider at CERN: Report on the Physics and Design Concepts for Machine and Detector*, J. Phys. **G39** (2012) 075001, arXiv:1206.2913 [physics.acc-ph].

[432] ATLAS Collaboration, *Measurement of the transverse momentum and ϕ^*_η distributions of Drell-Yan lepton pairs in proton–proton collisions at $\sqrt{s} = 8$ TeV with the ATLAS detector*, Eur. Phys. J. C **76** (2016) 291, arXiv:1512.02192 [hep-ex].

[433] ATLAS Collaboration, *Measurement of the W-boson mass in pp collisions at $\sqrt{s} = 7$ TeV with the ATLAS detector*, Eur. Phys. J. C **78** (2018) 110, arXiv:1701.07240 [hep-ex].

[434] A. Valassi, *Combining correlated measurements of several different physical quantities*, Nucl. Instrum. Meth. A **500** (2003) 391–405.

[435] J. C. Collins and D. E. Soper, *Angular Distribution of Dileptons in High-Energy Hadron Collisions*, Phys. Rev. D **16** (1977) 2219.

[436] SLD Electroweak Group, DELPHI, ALEPH, SLD, SLD Heavy Flavour Group, OPAL, LEP Electroweak Working Group, L3 Collaboration, S. Schael et al., *Precision electroweak measurements on the Z resonance*, Phys. Rept. **427** (2006) 257, arXiv:hep-ex/0509008 [hep-ex].

[437] CMS Collaboration, S. Chatrchyan et al., *Measurement of the weak mixing angle with the Drell-Yan process in proton-proton collisions at the LHC*, Phys. Rev. D **84** (2011) 112002, arXiv:1110.2682 [hep-ex].

[438] ATLAS Collaboration, G. Aad et al., *Measurement of the forward-backward asymmetry of electron and muon pair-production in pp collisions at $\sqrt{s}$ = 7 TeV with the ATLAS detector*, JHEP **09** (2015) 049, arXiv:1503.03709 [hep-ex].

[439] LHCb Collaboration, R. Aaij et al., *Measurement of the forward-backward asymmetry in*

$Z/\gamma^* \to \mu^+\mu^-$ *decays and determination of the effective weak mixing angle*, JHEP **11** (2015) 190, arXiv:1509.07645 [hep-ex].

[440] CDF Collaboration, T. A. Aaltonen et al., *Indirect measurement of* $\sin^2\theta_W$ *(or* M_W*) using* $\mu^+\mu^-$ *pairs from* γ^*/Z *bosons produced in* $p\bar{p}$ *collisions at a center-of-momentum energy of 1.96 TeV*, Phys. Rev. D **89** (2014) 072005, arXiv:1402.2239 [hep-ex].

[441] CDF Collaboration, T. A. Aaltonen et al., *Measurement of* $\sin^2\theta_{\rm eff}^{\rm lept}$ *using* e^+e^- *pairs from* γ^*/Z *bosons produced in* $p\bar{p}$ *collisions at a center-of-momentum energy of 1.96 TeV*, Phys. Rev. D **93** (2016) 112016, arXiv:1605.02719 [hep-ex].

[442] D0 Collaboration, V. M. Abazov et al., *Measurement of the effective weak mixing angle in* $p\bar{p} \to Z/\gamma^* \to e^+e^-$ *events*, Phys. Rev. Lett. **115** (2015) 041801, arXiv:1408.5016 [hep-ex].

[443] W. T. Giele and S. Keller, *Implications of hadron collider observables on parton distribution function uncertainties*, Phys. Rev. D **58** (1998) 094023, arXiv:hep-ph/9803393 [hep-ph].

[444] N. Sato, J. F. Owens, and H. Prosper, *Bayesian Reweighting for Global Fits*, Phys. Rev. D **89** (2014) 114020, arXiv:1310.1089 [hep-ph].

[445] A. Bodek, J. Han, A. Khukhunaishvili, and W. Sakumoto, *Using Drell-Yan forward-backward asymmetry to reduce PDF uncertainties in the measurement of electroweak parameters*, Eur. Phys. J. C **76** (2016) 115, arXiv:1507.02470 [hep-ex].

[446] H. Paukkunen and P. Zurita, *PDF reweighting in the Hessian matrix approach*, JHEP **12** (2014) 100, arXiv:1402.6623 [hep-ph].

[447] ATLAS Collaboration, *Prospect for a measurement of the Weak Mixing Angle in* $pp \to Z/\gamma^* \to e^+e^-$ *events with the ATLAS detector at the High Luminosity Large Hadron Collider*, ATL-PHYS-PUB-2018-037, CERN, Geneva, Nov, 2018. https://cds.cern.ch/record/2649330.

[448] CMS Collaboration, *Measurement of the weak mixing angle with the forward-backward asymmetry of Drell-Yan events at 8 TeV*, CMS-PAS-SMP-16-007, CERN, Geneva, 2017. http://cds.cern.ch/record/2273392.

[449] W. J. Barter, *Prospects for measurement of the weak mixing angle at LHCb*, LHCb-PUB-2018-013. CERN-LHCb-PUB-2018-013, CERN, Geneva, Nov, 2018. https://cds.cern.ch/record/2647836.

[450] S. Alioli, P. Nason, C. Oleari, and E. Re, *NLO vector-boson production matched with shower in POWHEG*, JHEP **07** (2008) 060, arXiv:0805.4802 [hep-ph].

[451] P. Nason, *A new method for combining NLO QCD with shower Monte Carlo algorithms*, JHEP **11** (2004) 040, arXiv:hep-ph/0409146 [hep-ph].

[452] S. Frixione, P. Nason, and C. Oleari, *Matching NLO QCD computations with parton shower simulations: the POWHEG method*, JHEP **11** (2007) 070, arXiv:0709.2092 [hep-ph].

[453] S. Alioli, P. Nason, C. Oleari, and E. Re, *A general framework for implementing NLO calculations in shower Monte Carlo programs: the POWHEG BOX*, JHEP **06** (2010) 043, arXiv:1002.2581 [hep-ph].

[454] NNPDF Collaboration, R. D. Ball et al., *Parton distributions for the LHC Run II*, JHEP **04** (2015) 040, arXiv:1410.8849 [hep-ph].

[455] LHCb Collaboration, R. Aaij et al., *LHCb Detector Performance*, Int. J. Mod. Phys. **A30** (2015) no. 07, 1530022, arXiv:1412.6352 [hep-ex].

[456] ATLAS Collaboration, ATLAS Collaboration, *ATLAS Phase-II Upgrade Scoping Document*, Cern-lhcc-2015-020, Geneva, Sep, 2015. http://cds.cern.ch/record/2055248.

[457] S. Catani, L. Cieri, G. Ferrera, D. de Florian, and M. Grazzini, *Vector Boson Production at*

Hadron Colliders: A Fully Exclusive QCD Calculation at Next-to-Next-to-Leading Order, Phys. Rev. Lett. **103** (Aug, 2009) 082001. https://link.aps.org/doi/10.1103/PhysRevLett.103.082001.

[458] ATLAS Collaboration, M. Aaboud et al., *Measurement of the Drell-Yan triple-differential cross section in pp collisions at $\sqrt{s} = 8$ TeV*, JHEP **12** (2017) 059, arXiv:1710.05167 [hep-ex].

[459] S. Alekhin et al., *HERAFitter*, Eur. Phys. J. **C75** (2015) no. 7, 304, arXiv:1410.4412 [hep-ph].

[460] ATLAS Collaboration, ATLAS Collaboration, *Measurement of the effective leptonic weak mixing angle using electron and muon pairs from Z-boson decay in the ATLAS experiment at $\sqrt{s} = 8$ TeV*, ATLAS-CONF-2018-037, CERN, Geneva, Jul, 2018. https://cds.cern.ch/record/2630340.

[461] HEPfit *Collaboration*, http://hepfit.roma1.infn.it.

[462] A. Caldwell, D. Kollar, and K. Kroninger, *BAT: The Bayesian Analysis Toolkit*, Comput. Phys. Commun. **180** (2009) 2197–2209, arXiv:0808.2552 [physics.data-an].

[463] I. Dubovyk, A. Freitas, J. Gluza, T. Riemann, and J. Usovitsch, *The two-loop electroweak bosonic corrections to $\sin^2\theta^b_{eff}$* , Phys. Lett. **B762** (2016) 184–189, arXiv:1607.08375 [hep-ph].

[464] I. Dubovyk, A. Freitas, J. Gluza, T. Riemann, and J. Usovitsch, *Complete electroweak two-loop corrections to Z boson production and decay*, Phys. Lett. **B783** (2018) 86–94, arXiv:1804.10236 [hep-ph].

[465] J. de Blas, M. Ciuchini, E. Franco, S. Mishima, M. Pierini, L. Reina, and L. Silvestrini, *Electroweak precision observables and Higgs-boson signal strengths in the Standard Model and beyond: present and future*, JHEP **12** (2016) 135, arXiv:1608.01509 [hep-ph].

[466] J. de Blas, M. Ciuchini, E. Franco, S. Mishima, M. Pierini, L. Reina, and L. Silvestrini, *Electroweak precision constraints at present and future colliders*, PoS **ICHEP2016** (2017) 690, arXiv:1611.05354 [hep-ph].

[467] J. de Blas, M. Ciuchini, E. Franco, S. Mishima, M. Pierini, L. Reina, and L. Silvestrini, *The Global Electroweak and Higgs Fits in the LHC era*, PoS **EPS-HEP2017** (2017) 467, arXiv:1710.05402 [hep-ph].

[468] A. Keshavarzi, D. Nomura, and T. Teubner, *Muon $g-2$ and $\alpha(M_Z^2)$: a new data-based analysis*, Phys. Rev. **D97** (2018) no. 11, 114025, arXiv:1802.02995 [hep-ph].

[469] CMS Collaboration, A. M. Sirunyan et al., *Measurement of the top quark mass using single top quark events in proton-proton collisions at $\sqrt{s} = 8$ TeV*, Eur. Phys. J. **C77** (2017) no. 5, 354, arXiv:1703.02530 [hep-ex].

[470] ATLAS Collaboration, *Measurement of the top quark mass in the $t\bar{t}$ lepton+jets channel from $\sqrt{s}$=8 TeV ATLAS data*, ATLAS-CONF-2017-071, CERN, Geneva, 2017.

[471] CMS Collaboration, A. M. Sirunyan et al., *Measurement of the top quark mass with lepton+jets final states using* p p *collisions at $\sqrt{s} = 13$ TeV*, Eur. Phys. J. **C78** (2018) no. 11, 891, arXiv:1805.01428 [hep-ex].

[472] CMS Collaboration, A. M. Sirunyan et al., *Measurements of properties of the Higgs boson decaying into the four-lepton final state in pp collisions at $\sqrt{s} = 13$ TeV*, JHEP **11** (2017) 047, arXiv:1706.09936 [hep-ex].

[473] ATLAS Collaboration, M. Aaboud et al., *Measurement of the Higgs boson mass in the $H \to ZZ^* \to 4\ell$ and $H \to \gamma\gamma$ channels with $\sqrt{s} = 13$ TeV pp collisions using the ATLAS detector*, Phys. Lett. **B784** (2018) 345–366, arXiv:1806.00242 [hep-ex].

[474] CMS Collaboration, CMS Collaboration, *Measurement of the weak mixing angle using the*

forward-backward asymmetry of Drell-Yan events in pp collisions at 8 TeV, arXiv:1806.00863 [hep-ex].

[475] ATLAS Collaboration, *Measurement of the effective leptonic weak mixing angle using electron and muon pairs from Z-boson decay in the ATLAS experiment at $\sqrt{s} = 8$ TeV*, ATLAS-CONF-2018-037, CERN, Geneva, 2018.

[476] S. Dawson et al., *Working Group Report: Higgs Boson*, in *Proceedings, 2013 Community Summer Study on the Future of U.S. Particle Physics: Snowmass on the Mississippi (CSS2013): Minneapolis, MN, USA, July 29-August 6, 2013*. 2013. arXiv:1310.8361 [hep-ex]. http://www.slac.stanford.edu/econf/C1307292/docs/EnergyFrontier/Higgs-18.pdf.

[477] M. E. Peskin and T. Takeuchi, *Estimation of oblique electroweak corrections*, Phys. Rev. **D46** (1992) 381–409.

[478] B. Grzadkowski, M. Iskrzynski, M. Misiak, and J. Rosiek, *Dimension-Six Terms in the Standard Model Lagrangian*, JHEP **10** (2010) 085, arXiv:1008.4884 [hep-ph].

[479] ATLAS Collaboration, *Jet energy scale measurements and their systematic uncertainties in proton–proton collisions at $\sqrt{s}$=13 TeV with the ATLAS detector*, Phys. Rev. D **96** (2017) 072002, arXiv:1703.09665 [hep-ex].

[480] ATLAS Collaboration, *A measurement of the calorimeter response to single hadrons and determination of the jet energy scale uncertainty using LHC Run-1 pp-collision data with the ATLAS detector*, Eur. Phys. J. C **77** (2017) 26, arXiv:1607.08842 [hep-ex].

[481] ATLAS Collaboration, *Measurement of the inclusive $W^{\pm}$ and Z/gamma cross sections in the electron and muon decay channels in pp collisions at $\sqrt{s} = 7$ TeV with the ATLAS detector*, Phys. Rev. **D85** (2012) 072004, arXiv:1109.5141 [hep-ex].

[482] ATLAS Collaboration, *Measurement of the cross section for top-quark pair production in pp collisions at $\sqrt{s} = 7$ TeV with the ATLAS detector using final states with two high-pt leptons*, JHEP **05** (2012) 059, arXiv:1202.4892 [hep-ex].

[483] ATLAS Collaboration, *Measurement of inclusive jet and dijet production in pp collisions at $\sqrt{s} = 7$ TeV using the ATLAS detector*, Phys. Rev. **D86** (2012) 014022, arXiv:1112.6297 [hep-ex].

[484] S. Alekhin, J. Blümlein, S. Moch, and R. Placakyte, *Parton distribution functions, α_s, and heavy-quark masses for LHC Run II*, Phys. Rev. **D96** (2017) no. 1, 014011, arXiv:1701.05838 [hep-ph].

[485] ATLAS, *Dynamics of isolated-photon plus jet production in pp collisions at $\sqrt{s} = 7$ TeV with the ATLAS detector*, Nucl. Phys. B **875** (2013) 483, arXiv:1307.6795 [hep-ex].

[486] ATLAS, *High-E_T isolated-photon plus jets production in pp collisions at $\sqrt{s} = 8$ TeV with the ATLAS detector*, Nucl. Phys. B **918** (2017) 257, arXiv:1611.06586 [hep-ex].

[487] S. Catani, M. Fontannaz, J. Ph. Guillet and E. Pilon, *Cross section of isolated prompt photons in hadron-hadron collisions*, JHEP **0205** (2002) 028, arXiv:hep-ph/0204023 [hep-ph].

[488] P. Aurenche, M. Fontannaz, J. Ph. Guillet, E. Pilon and M. Werlen, *A new critical study of photon production in hadronic collisions*, Phys. Rev. D **73** (2006) 094007, arXiv:hep-ph/0602133 [hep-ph]. and references therein.

[489] L.A. Harland-Lang, A.D. Martin, P. Motylinski and R.S. Thorne, *Parton distributions in the LHC era: MMHT 2014 PDFs*, Eur. Phys. J. **C 75** (2015) 204, arXiv:1412.3989 [hep-ph].

[490] L. Bourhis, M. Fontannaz and J.Ph. Guillet, *Quark and gluon fragmentation functions into photons*, Eur. Phys. J. C **2** (1998) 529, arXiv:hep-ph/9704447 [hep-ph].

[491] ATLAS, *Measurement of the cross section for inclusive isolated-photon production in pp collisions at $\sqrt{s}$=13 TeV using the ATLAS detector*, Phys. Lett. B **770** (2017) 473,

arXiv:1701.06882 [hep-ex].

[492] ATLAS, *Measurement of the cross section for isolated-photon plus jet production in pp collisions at $\sqrt{s}$=13 TeV using the ATLAS detector*, Phys. Lett. B **780** (2018) 578, arXiv:1801.00112 [hep-ex].

[493] CDF Collaboration, T. Aaltonen et al., *Measurement of the Cross Section for Prompt Isolated Diphoton Production in $p\bar{p}$ Collisions at $\sqrt{s} = 1.96$ TeV*, Phys. Rev. **D84** (2011) 052006, arXiv:1106.5131 [hep-ex].

[494] ATLAS Collaboration, M. Aaboud et al., *Measurements of integrated and differential cross sections for isolated photon pair production in pp collisions at $\sqrt{s} = 8$ TeV with the ATLAS detector*, Phys. Rev. **D95** (2017) no. 11, 112005, arXiv:1704.03839 [hep-ex].

[495] ATLAS Collaboration, G. Aad et al., *Search for diphoton events with large missing transverse momentum in 7 TeV proton-proton collision data with the ATLAS detector*, Phys. Lett. **B718** (2012) 411–430, arXiv:1209.0753 [hep-ex].

[496] CMS Collaboration, V. Khachatryan et al., *Search for diphoton resonances in the mass range from 150 to 850 GeV in pp collisions at $\sqrt{s} = 8$ TeV*, Phys. Lett. **B750** (2015) 494–519, arXiv:1506.02301 [hep-ex].

[497] S. Catani, L. Cieri, D. de Florian, G. Ferrera, and M. Grazzini, *Diphoton production at the LHC: a QCD study up to NNLO*, JHEP **04** (2018) 142, arXiv:1802.02095 [hep-ph].

[498] L. Cieri, *Diphoton isolation studies*, Nucl. Part. Phys. Proc. **273-275** (2016) 2033–2039, arXiv:1510.06873 [hep-ph].

[499] J. R. Andersen et al., *Les Houches 2013: Physics at TeV Colliders: Standard Model Working Group Report*, arXiv:1405.1067 [hep-ph].

[500] S. Frixione, *Isolated photons in perturbative QCD*, Phys. Lett. **B429** (1998) 369–374, arXiv:hep-ph/9801442 [hep-ph].

[501] S. Frixione and W. Vogelsang, *Isolated photon production in polarized pp collisions*, Nucl. Phys. **B568** (2000) 60–92, arXiv:hep-ph/9908387 [hep-ph].

[502] S. Catani et al., *QCD*, in *1999 CERN Workshop on standard model physics (and more) at the LHC, CERN, Geneva, Switzerland, 25-26 May: Proceedings*. 2000. arXiv:hep-ph/0005025 [hep-ph]. http://weblib.cern.ch/abstract?CERN-TH-2000-131.

[503] ATLAS Collaboration, G. Aad et al., *Measurement of isolated-photon pair production in pp collisions at $\sqrt{s} = 7$ TeV with the ATLAS detector*, JHEP **01** (2013) 086, arXiv:1211.1913 [hep-ex].

[504] CMS Collaboration, S. Chatrchyan et al., *Measurement of differential cross sections for the production of a pair of isolated photons in pp collisions at $\sqrt{s} = 7$ TeV*, Eur. Phys. J. **C74** (2014) no. 11, 3129, arXiv:1405.7225 [hep-ex].

[505] M. Grazzini, S. Kallweit, and M. Wiesemann, *Fully differential NNLO computations with MATRIX*, Eur. Phys. J. **C78** (2018) no. 7, 537, arXiv:1711.06631 [hep-ph].

[506] J. L. Abelleira Fernandez et al., *On the Relation of the LHeC and the LHC*, .

[507] L. A. Harland-Lang, V. A. Khoze, and M. G. Ryskin, *Exclusive LHC physics with heavy ions: SuperChic 3*, arXiv:1810.06567 [hep-ph].

[508] W. Stirling and E. Vryonidou, *Charm production in association with an electroweak gauge boson at the LHC*, Phys.Rev.Lett. **109** (2012) 082002.

[509] S. Chatrchyan et al., *Measurement of the muon charge asymmetry in inclusive pp to WX production at $\sqrt{s}$ = 7 TeV and an improved determination of light parton distribution functions*, Phys.Rev. **D90** (2014) 032004.

[510] D. d'Enterria and J. Rojo, *Quantitative constraints on the gluon distribution function in the*

proton from collider isolated-photon data, Nucl.Phys. **B860** (2012) 311–338.

[511] J. Rojo, *Improving quark flavor separation with forward W and Z production at LHCb*, PoS **DIS2017** (2018) 198.

[512] J. Rojo, *Constraints on parton distributions and the strong coupling from LHC jet data*, Int. J. Mod. Phys. **A30** (2015) 1546005.

[513] E. L. Berger, J. Gao, and H. X. Zhu, *Differential Distributions for t-channel Single Top-Quark Production and Decay at Next-to-Next-to-Leading Order in QCD*, JHEP **11** (2017) 158, arXiv:1708.09405 [hep-ph].

[514] V. Khachatryan et al., *Measurement of the differential cross section for top quark pair production in pp collisions at* $\sqrt{s} = 8$ *TeV*, Eur. Phys. J. **C75** (2015) no. 11, 542.

[515] G. Aad et al., *Measurements of top-quark pair differential cross-sections in the lepton+jets channel in pp collisions at* $\sqrt{s} = 8$ *TeV using the ATLAS detector*, Eur. Phys. J. **C76** (2016) no. 10, 538.

[516] *Measurement of associated production of W bosons with charm quarks in proton-proton collisions at* $\sqrt{s} = 13$ TeV *with the CMS experiment at the LHC*, CMS-PAS-SMP-17-014, CERN, Geneva, 2018. https://cds.cern.ch/record/2314570.

[517] G. Aad et al., *Measurement of the transverse momentum and* ϕ^*_η *distributions of Drell-Yan lepton pairs in proton-proton collisions at* $\sqrt{s} = 8$ *TeV with the ATLAS detector*, Eur. Phys. J. **C76** (2016) no. 5, 291.

[518] G. Aad et al., *Measurement of the double-differential high-mass Drell-Yan cross section in pp collisions at* $\sqrt{s} = 8$ *TeV with the ATLAS detector*, JHEP **08** (2016) 009.

[519] M. Aaboud et al., *Measurement of the cross section for inclusive isolated-photon production in pp collisions at* $\sqrt{s} = 13$ *TeV using the ATLAS detector*, Phys. Lett. **B770** (2017) 473–493.

[520] R. Aaij et al., *Measurement of forward W and Z boson production in pp collisions at* $\sqrt{s} = 8$ *TeV*, JHEP **01** (2016) 155.

[521] CMS Collaboration, V. Khachatryan et al., *Measurement of the double-differential inclusive jet cross section in proton–proton collisions at* $\sqrt{s} = 13$ *TeV*, Eur. Phys. J. **C76** (2016) no. 8, 451, arXiv:1605.04436 [hep-ex].

[522] R. D. Ball, V. Bertone, F. Cerutti, L. Del Debbio, S. Forte, et al., *Reweighting and Unweighting of Parton Distributions and the LHC W lepton asymmetry data*, Nucl.Phys. **B855** (2012) 608–638.

[523] NNPDF Collaboration, R. D. Ball, V. Bertone, F. Cerutti, L. Del Debbio, S. Forte, A. Guffanti, J. I. Latorre, J. Rojo, and M. Ubiali, *Reweighting NNPDFs: the W lepton asymmetry*, Nucl. Phys. B **849** (2011) 112–143, arXiv:1012.0836 [hep-ph]. [Erratum: Nucl. Phys.B855,927(2012)].

[524] B. C. Allanach et al., *SUSY Les Houches Accord 2*, Comput. Phys. Commun. **180** (2009) 8–25.

[525] M. Diehl, D. Ostermeier, and A. Schafer, *Elements of a theory for multiparton interactions in QCD*, JHEP **03** (2012) 089, arXiv:1111.0910 [hep-ph]. [Erratum: JHEP03,001(2016)].

[526] M. Diehl, J. R. Gaunt, D. Ostermeier, P. Plößl, and A. Schäfer, *Cancellation of Glauber gluon exchange in the double Drell-Yan process*, JHEP **01** (2016) 076, arXiv:1510.08696 [hep-ph].

[527] M. Diehl, J. R. Gaunt, and K. Schönwald, *Double hard scattering without double counting*, JHEP **06** (2017) 083, arXiv:1702.06486 [hep-ph].

[528] M. G. A. Buffing, M. Diehl, and T. Kasemets, *Transverse momentum in double parton scattering: factorisation, evolution and matching*, JHEP **01** (2018) 044, arXiv:1708.03528 [hep-ph].

[529] B. Blok, Yu. Dokshitser, L. Frankfurt, and M. Strikman, *pQCD physics of multiparton*

interactions, Eur. Phys. J. **C72** (2012) 1963, arXiv:1106.5533 [hep-ph].

[530] A. V. Manohar and W. J. Waalewijn, *A QCD Analysis of Double Parton Scattering: Color Correlations, Interference Effects and Evolution*, Phys. Rev. **D85** (2012) 114009, arXiv:1202.3794 [hep-ph].

[531] F. A. Ceccopieri, M. Rinaldi, and S. Scopetta, *Parton correlations in same-sign W pair production via double parton scattering at the LHC*, Phys. Rev. **D95** (2017) no. 11, 114030, arXiv:1702.05363 [hep-ph].

[532] C. Collaboration, *The Phase-2 Upgrade of the CMS Muon Detectors*, CERN-LHCC-2017-012. CMS-TDR-016, CERN, Geneva, Sep, 2017. https://cds.cern.ch/record/2283189.

[533] J. R. Gaunt and W. J. Stirling, *Double Parton Distributions Incorporating Perturbative QCD Evolution and Momentum and Quark Number Sum Rules*, JHEP **03** (2010) 005, arXiv:0910.4347 [hep-ph].

[534] T. Kasemets and M. Diehl, *Angular correlations in the double Drell-Yan process*, JHEP **01** (2013) 121, arXiv:1210.5434 [hep-ph].

[535] S. Cotogno, T. Kasemets, and M. Myska, *A spin on same-sign W-boson pair production*, arXiv:1809.09024 [hep-ph].

[536] M. Diehl and T. Kasemets, *Positivity bounds on double parton distributions*, JHEP **05** (2013) 150, arXiv:1303.0842 [hep-ph].

[537] S. Cotogno, *Polarized partons in hadrons at high energy*. PhD thesis, VU Amsterdam, 2018. https://www.nikhef.nl/pub/services/biblio/theses_pdf/thesis_S_Cotogno.pdf.

[538] M. Diehl, T. Kasemets, and S. Keane, *Correlations in double parton distributions: effects of evolution*, JHEP **05** (2014) 118, arXiv:1401.1233 [hep-ph].

[539] ATLAS Collaboration, *Measurement of underlying event characteristics using charged particles in pp collisions at $\sqrt{s} = 900GeV$ and 7 TeV with the ATLAS detector*, Phys. Rev. **D83** (2011) 112001, arXiv:1012.0791 [hep-ex].

[540] M. Bahr et al., *Herwig++ Physics and Manual*, Eur. Phys. J. **C58** (2008) 639–707, arXiv:0803.0883 [hep-ph].

[541] ATLAS Collaboration, *Measurement of charged-particle distributions sensitive to the underlying event in $\sqrt{s} = 13$ TeV proton-proton collisions with the ATLAS detector at the LHC*, JHEP **03** (2017) 157, arXiv:1701.05390 [hep-ex].

[542] M. Czakon, D. Heymes, and A. Mitov, *High-precision differential predictions for top-quark pairs at the LHC*, Phys. Rev. Lett. **116** (2016) no. 8, 082003, arXiv:1511.00549 [hep-ph].

[543] CMS Collaboration, V. Khachatryan et al., *Measurement of differential cross sections for top quark pair production using the lepton+jets final state in proton-proton collisions at 13 TeV*, Phys. Rev. D **95** (2017) 092001, arXiv:1610.04191 [hep-ex].

[544] CMS Collaboration, A. M. Sirunyan et al., *Measurement of differential cross sections for the production of top quark pairs and of additional jets in lepton+jets events from pp collisions at $\sqrt{s} = 13$ TeV*, Phys. Rev. D **97** (2018) 112003, arXiv:1803.08856 [hep-ex].

[545] CMS Collaboration, *The Phase-2 Upgrade of the CMS Tracker*, Technical Report CERN-LHCC-2017-009, 2017. https://cds.cern.ch/record/2272264.

[546] CMS Collaboration, *The Phase-2 Upgrade of the CMS Barrel Calorimeters Technical Design Report*, Technical Report CERN-LHCC-2017-011, 2017. https://cds.cern.ch/record/2283187.

[547] CMS Collaboration, *The Phase-2 Upgrade of the CMS Endcap Calorimeter*, Technical Report CERN-LHCC-2017-023, 2017. https://cds.cern.ch/record/2293646.

[548] CMS Collaboration, *The Phase-2 Upgrade of the CMS Muon Detectors*, Technical Report

CERN-LHCC-2017-012, 2017. https://cds.cern.ch/record/2283189.

[549] D. Bertolini, P. Harris, M. Low, and N. Tran, *Pileup Per Particle Identification*, JHEP (2014) 059, arXiv:1407.6013 [hep-ph].

[550] B. A. Betchart, R. Demina, and A. Harel, *Analytic solutions for neutrino momenta in decay of top quarks*, Nucl. Instrum. Meth. **A736** (2014) 169–178, arXiv:1305.1878 [hep-ph].

[551] V. Bertone, R. Frederix, S. Frixione, J. Rojo, and M. Sutton, *aMCfast: automation of fast NLO computations for PDF fits*, JHEP **08** (2014) 166, arXiv:1406.7693 [hep-ph].

[552] S. Alekhin, J. Blümlein, and S. Moch, *NLO PDFs from the ABMP16 fit*, Eur. Phys. J. **C78** (2018) no. 6, 477, arXiv:1803.07537 [hep-ph].

[553] CMS Collaboration, A. M. Sirunyan et al., *Measurement of double-differential cross sections for top quark pair production in pp collisions at $\sqrt{s} = 8$ TeV and impact on parton distribution functions*, Eur. Phys. J. **C77** (2017) no. 7, 459, arXiv:1703.01630 [hep-ex].

[554] LHCb collaboration, R. Aaij et al., *First observation of top quark production in the forward region*, Phys. Rev. Lett. **115** (2015) 112001 LHCb-PAPER-2015-022, CERN-PH-EP-2015-132, arXiv:1506.00903 [hep-ex].

[555] LHCb collaboration, R. Aaij et al., *Measurement of the $t\bar{t}$, $W + b\bar{b}$ and $W + c\bar{c}$ production cross sections in pp collisions at $\sqrt{s} = 8$ TeV*, Phys. Lett. **B767** (2017) 110 LHCb-PAPER-2016-038, CERN-EP-2016-232, arXiv:1610.08142 [hep-ex].

[556] LHCb collaboration, R. Aaij et al., *Measurement of forward top pair production in the dilepton channel in pp collisions at $\sqrt{s} = 13$ TeV*, LHCb-PAPER-2017-050, CERN-EP-2018-022, arXiv:1803.05188 [hep-ex]. submitted to JHEP.

[557] R. Gauld, *Leptonic top-quark asymmetry predictions at LHCb*, Phys. Rev. **D91** (2015) 054029, arXiv:1409.8631 [hep-ph].

[558] R. Gauld, *Feasibility of top quark measurements at LHCb and constraints on the large-x gluon PDF*, JHEP **02** (2014) 126, arXiv:1311.1810 [hep-ph].

[559] J. M. Campbell, R. Frederix, F. Maltoni, and F. Tramontano, *NLO predictions for t-channel production of single top and fourth generation quarks at hadron colliders*, JHEP **10** (2009) 042, arXiv:0907.3933 [hep-ph].

[560] J. M. Campbell, R. Frederix, F. Maltoni, and F. Tramontano, *Next-to-Leading-Order Predictions for t-Channel Single-Top Production at Hadron Colliders*, Phys. Rev. Lett. **102** (2009) 182003, arXiv:0903.0005 [hep-ph].

[561] R. Frederix, E. Re, and P. Torrielli, *Single-top t-channel hadroproduction in the four-flavour scheme with POWHEG and aMC@NLO*, JHEP **09** (2012) 130, arXiv:1207.5391 [hep-ph].

[562] F. Cascioli, S. Kallweit, P. Maierhöfer, and S. Pozzorini, *A unified NLO description of top-pair and associated Wt production*, PoS **LL2014** (2014) 026.

[563] T. Ježo, J. M. Lindert, P. Nason, C. Oleari, and S. Pozzorini, *An NLO+PS generator for $t\bar{t}$ and Wt production and decay including non-resonant and interference effects*, Eur. Phys. J. **C76** (2016) no. 12, 691, arXiv:1607.04538 [hep-ph].

[564] M. Brucherseifer, F. Caola, and K. Melnikov, *On the NNLO QCD corrections to single-top production at the LHC*, Phys. Lett. **B736** (2014) 58–63, arXiv:1404.7116 [hep-ph].

[565] E. L. Berger, J. Gao, C. P. Yuan, and H. X. Zhu, *NNLO QCD Corrections to t-channel Single Top-Quark Production and Decay*, Phys. Rev. **D94** (2016) no. 7, 071501, arXiv:1606.08463 [hep-ph].

[566] Z. L. Liu and J. Gao, *s -channel single top quark production and decay at next-to-next-to-leading-order in QCD*, Phys. Rev. **D98** (2018) no. 7, 071501, arXiv:1807.03835 [hep-ph].

[567] J. Gao, C. S. Li, and H. X. Zhu, *Top Quark Decay at Next-to-Next-to Leading Order in QCD*, Phys. Rev. Lett. **110** (2013) no. 4, 042001, arXiv:1210.2808 [hep-ph].

[568] M. Brucherseifer, F. Caola, and K. Melnikov, *$\mathcal{O}(\alpha_s^2)$ corrections to fully-differential top quark decays*, JHEP **04** (2013) 059, arXiv:1301.7133 [hep-ph].

[569] A. S. Papanastasiou, R. Frederix, S. Frixione, V. Hirschi, and F. Maltoni, *Single-top t-channel production with off-shell and non-resonant effects*, Phys. Lett. **B726** (2013) 223–227, arXiv:1305.7088 [hep-ph].

[570] J. Campbell, R. K. Ellis, and R. Röntsch, *Single top production in association with a Z boson at the LHC*, Phys. Rev. **D87** (2013) 114006, arXiv:1302.3856 [hep-ph].

[571] J. Alwall, R. Frederix, J. M. Gerard, A. Giammanco, M. Herquet, S. Kalinin, E. Kou, V. Lemaitre, and F. Maltoni, *Is $V(_{tb}) \simeq 1$?*, Eur. Phys. J. **C49** (2007) 791–801, arXiv:hep-ph/0607115 [hep-ph].

[572] ATLAS Collaboration, M. Aaboud et al., *Measurement of the inclusive cross-sections of single top-quark and top-antiquark t-channel production in pp collisions at $\sqrt{s}$ = 13 TeV with the ATLAS detector*, JHEP **04** (2017) 086, arXiv:1609.03920 [hep-ex].

[573] CMS Collaboration, A. M. Sirunyan et al., *Cross section measurement of t-channel single top quark production in pp collisions at $\sqrt{s} = 13$ TeV*, Phys. Lett. **B772** (2017) 752–776, arXiv:1610.00678 [hep-ex].

[574] S. Weinberg, *Phenomenological Lagrangians*, Physica **A96** (1979) no. 1-2, 327–340.

[575] W. Buchmuller and D. Wyler, *Effective Lagrangian Analysis of New Interactions and Flavor Conservation*, Nucl. Phys. **B268** (1986) 621–653.

[576] G. Bevilacqua and M. Worek, *Constraining BSM Physics at the LHC: Four top final states with NLO accuracy in perturbative QCD*, JHEP **07** (2012) 111, arXiv:1206.3064 [hep-ph].

[577] CMS Collaboration, A. M. Sirunyan et al., *Search for standard model production of four top quarks with same-sign and multilepton final states in proton–proton collisions at $\sqrt{s} = 13$ TeV*, Eur. Phys. J. **C78** (2018) no. 2, 140, arXiv:1710.10614 [hep-ex].

[578] CMS Collaboration, A. M. Sirunyan et al., *Search for standard model production of four top quarks in proton-proton collisions at $\sqrt{s}$ = 13 TeV*, Phys. Lett. **B772** (2017) 336–358, arXiv:1702.06164 [hep-ex].

[579] CMS Collaboration, V. Khachatryan et al., *Search for Standard Model Production of Four Top Quarks in the Lepton + Jets Channel in pp Collisions at $\sqrt{s}$ = 8 TeV*, JHEP **11** (2014) 154, arXiv:1409.7339 [hep-ex].

[580] CMS Collaboration, V. Khachatryan et al., *Search for new physics in same-sign dilepton events in proton–proton collisions at $\sqrt{s} = 13$ TeV*, Eur. Phys. J. **C76** (2016) no. 8, 439, arXiv:1605.03171 [hep-ex].

[581] ATLAS Collaboration, G. Aad et al., *Search for supersymmetry at $\sqrt{s}$=8 TeV in final states with jets and two same-sign leptons or three leptons with the ATLAS detector*, JHEP **06** (2014) 035, arXiv:1404.2500 [hep-ex].

[582] ATLAS Collaboration, G. Aad et al., *Search for production of vector-like quark pairs and of four top quarks in the lepton-plus-jets final state in pp collisions at $\sqrt{s} = 8$ TeV with the ATLAS detector*, JHEP **08** (2015) 105, arXiv:1505.04306 [hep-ex].

[583] ATLAS Collaboration, M. Aaboud et al., *Search for pair production of up-type vector-like quarks and for four-top-quark events in final states with multiple b-jets with the ATLAS detector*, JHEP **07** (2018) 089, arXiv:1803.09678 [hep-ex].

[584] ATLAS Collaboration, M. Aaboud et al., *Search for new phenomena in events with same-charge leptons and b-jets in pp collisions at $\sqrt{s} = 13$ TeV with the ATLAS detector*,

arXiv:1807.11883 [hep-ex].

[585] F. Maltoni, D. Pagani, and I. Tsinikos, *Associated production of a top-quark pair with vector bosons at NLO in QCD: impact on* $t\bar{t}H$ *searches at the LHC*, JHEP **02** (2016) 113, arXiv:1507.05640 [hep-ph].

[586] CMS Collaboration, *Projections of sensitivities for tttt production at HL-LHC and HE-LHC*, CMS PAS-FTR-18-031, 2018. https://cds.cern.ch/record/2650211.

[587] CMS Collaboration, CMS Collaboration, *Projections of sensitivities for tttt production at HL-LHC and HE-LHC*, .

[588] P. J. Fox, A. E. Nelson, and N. Weiner, *Dirac gaugino masses and supersoft supersymmetry breaking*, JHEP **08** (2002) 035, arXiv:hep-ph/0206096 [hep-ph].

[589] G. Burdman, B. A. Dobrescu, and E. Ponton, *Resonances from two universal extra dimensions*, Phys. Rev. **D74** (2006) 075008, arXiv:hep-ph/0601186 [hep-ph].

[590] G. D. Kribs, E. Poppitz, and N. Weiner, *Flavor in supersymmetry with an extended R-symmetry*, Phys. Rev. **D78** (2008) 055010, arXiv:0712.2039 [hep-ph].

[591] K. Benakli and M. D. Goodsell, *Dirac Gauginos in General Gauge Mediation*, Nucl. Phys. **B816** (2009) 185–203, arXiv:0811.4409 [hep-ph].

[592] C. Kilic, T. Okui, and R. Sundrum, *Vectorlike Confinement at the LHC*, JHEP **02** (2010) 018, arXiv:0906.0577 [hep-ph].

[593] S. Calvet, B. Fuks, P. Gris, and L. Valery, *Searching for sgluons in multitop events at a center-of-mass energy of 8 TeV*, JHEP **04** (2013) 043, arXiv:1212.3360 [hep-ph].

[594] L. Darmé, B. Fuks, and M. Goodsell, *Cornering sgluons with four-top-quark events*, Phys. Lett. **B784** (2018) 223–228, arXiv:1805.10835 [hep-ph].

[595] C. Degrande, C. Duhr, B. Fuks, D. Grellscheid, O. Mattelaer, and T. Reiter, *UFO - The Universal FeynRules Output*, Comput. Phys. Commun. **183** (2012) 1201–1214, arXiv:1108.2040 [hep-ph].

[596] A. Alloul, N. D. Christensen, C. Degrande, C. Duhr, and B. Fuks, *FeynRules 2.0 - A complete toolbox for tree-level phenomenology*, Comput. Phys. Commun. **185** (2014) 2250–2300, arXiv:1310.1921 [hep-ph].

[597] C. Degrande, *Automatic evaluation of UV and R2 terms for beyond the Standard Model Lagrangians: a proof-of-principle*, Comput. Phys. Commun. **197** (2015) 239–262, arXiv:1406.3030 [hep-ph].

[598] T. Hahn, *Generating Feynman diagrams and amplitudes with FeynArts 3*, Comput. Phys. Commun. **140** (2001) 418–431, arXiv:hep-ph/0012260 [hep-ph].

[599] J. Alwall, C. Duhr, B. Fuks, O. Mattelaer, D. G. Öztürk, and C.-H. Shen, *Computing decay rates for new physics theories with FeynRules and MadGraph5_aMC@NLO*, Comput. Phys. Commun. **197** (2015) 312–323, arXiv:1402.1178 [hep-ph].

[600] E. Conte, B. Fuks, and G. Serret, *MadAnalysis 5, A User-Friendly Framework for Collider Phenomenology*, Comput. Phys. Commun. **184** (2013) 222–256, arXiv:1206.1599 [hep-ph].

[601] E. Conte, B. Dumont, B. Fuks, and C. Wymant, *Designing and recasting LHC analyses with MadAnalysis 5*, Eur. Phys. J. **C74** (2014) no. 10, 3103, arXiv:1405.3982 [hep-ph].

[602] B. Dumont, B. Fuks, S. Kraml, S. Bein, G. Chalons, E. Conte, S. Kulkarni, D. Sengupta, and C. Wymant, *Toward a public analysis database for LHC new physics searches using MADANALYSIS 5*, Eur. Phys. J. **C75** (2015) no. 2, 56, arXiv:1407.3278 [hep-ph].

[603] Q.-H. Cao, S.-L. Chen, and Y. Liu, *Probing Higgs Width and Top Quark Yukawa Coupling from* $t\bar{t}H$ *and* $t\bar{t}t\bar{t}$ *Productions*, Phys. Rev. **D95** (2017) no. 5, 053004, arXiv:1602.01934 [hep-ph].

[604] V. D. Barger, A. L. Stange, and R. J. N. Phillips, *Four heavy quark hadroproduction*, Phys. Rev. **D44** (1991) 1987–1996.

[605] C. Zhang, *Constraining $qqtt$ operators from four-top production: a case for enhanced EFT sensitivity*, Chin. Phys. **C42** (2018) no. 2, 023104, arXiv:1708.05928 [hep-ph].

[606] R. Contino, A. Falkowski, F. Goertz, C. Grojean, and F. Riva, *On the Validity of the Effective Field Theory Approach to SM Precision Tests*, JHEP **07** (2016) 144, arXiv:1604.06444 [hep-ph].

[607] M. Malekhosseini, M. Ghominejad, H. Khanpour, and M. Mohammadi Najafabadi, *Constraining top quark flavor violation and dipole moments through three and four-top quark productions at the LHC*, arXiv:1804.05598 [hep-ph].

[608] T. Ibrahim and P. Nath, *The Top quark electric dipole moment in an MSSM extension with vector like multiplets*, Phys. Rev. **D82** (2010) 055001, arXiv:1007.0432 [hep-ph].

[609] B. Yang, J. Han, and X. Zhang, *Production of $Zt\bar{t}$ and $Zt\bar{T}$ in the littlest Higgs model with T-parity at High Energy Colliders*, Eur. Phys. J. **C73** (2013) no. 12, 2639.

[610] J. A. Aguilar-Saavedra, *A Minimal set of top anomalous couplings*, Nucl. Phys. **B812** (2009) 181–204, arXiv:0811.3842 [hep-ph].

[611] J. A. Aguilar-Saavedra, B. Fuks, and M. L. Mangano, *Pinning down top dipole moments with ultra-boosted tops*, Phys. Rev. **D91** (2015) 094021, arXiv:1412.6654 [hep-ph].

[612] T. Sjostrand, L. Lonnblad, S. Mrenna, and P. Z. Skands, *Pythia 6.3 physics and manual*, arXiv:hep-ph/0308153 [hep-ph].

[613] V. Hirschi, R. Frederix, S. Frixione, M. V. Garzelli, F. Maltoni, and R. Pittau, *Automation of one-loop QCD corrections*, JHEP **05** (2011) 044, arXiv:1103.0621 [hep-ph].

[614] F. Maltoni, M. L. Mangano, I. Tsinikos, and M. Zaro, *Top-quark charge asymmetry and polarization in $t\bar{t}W^{\pm}$ production at the LHC*, Phys. Lett. **B736** (2014) 252–260, arXiv:1406.3262 [hep-ph].

[615] J. A. Dror, M. Farina, E. Salvioni, and J. Serra, *Strong tW Scattering at the LHC*, JHEP **01** (2016) 071, arXiv:1511.03674 [hep-ph].

[616] S. Alioli, P. Fernandez, J. Fuster, A. Irles, S.-O. Moch, P. Uwer, and M. Vos, *A new observable to measure the top-quark mass at hadron colliders*, Eur. Phys. J. **C73** (2013) 2438, arXiv:1303.6415 [hep-ph].

[617] G. Bevilacqua, H. B. Hartanto, M. Kraus, M. Schulze, and M. Worek, *Top quark mass studies with $t\bar{t}j$ at the LHC*, JHEP **03** (2018) 169, arXiv:1710.07515 [hep-ph].

[618] CMS Collaboration, V. Khachatryan et al., *Measurement of the t-tbar production cross section in the e-mu channel in proton-proton collisions at sqrt(s) = 7 and 8 TeV*, JHEP **08** (2016) 029, arXiv:1603.02303 [hep-ex].

[619] ATLAS Collaboration, G. Aad et al., *Measurement of the $t\bar{t}$ production cross-section using $e\mu$ events with b-tagged jets in pp collisions at $\sqrt{s}$ = 7 and 8 TeV with the ATLAS detector*, Eur. Phys. J. **C74** (2014) no. 10, 3109, arXiv:1406.5375 [hep-ex]. [Addendum: Eur. Phys. J.C76,no.11,642(2016)].

[620] U. Langenfeld, S. Moch, and P. Uwer, *Measuring the running top-quark mass*, Phys. Rev. **D80** (2009) 054009, arXiv:0906.5273 [hep-ph].

[621] S. Kawabata, Y. Shimizu, Y. Sumino, and H. Yokoya, *Weight function method for precise determination of top quark mass at Large Hadron Collider*, Phys. Lett. **B741** (2015) 232–238, arXiv:1405.2395 [hep-ph].

[622] A. H. Hoang, S. Mantry, A. Pathak, and I. W. Stewart, *Extracting a Short Distance Top Mass with Light Grooming*, arXiv:1708.02586 [hep-ph].

[623] K. Agashe, R. Franceschini, D. Kim, and M. Schulze, *Top quark mass determination from the energy peaks of b-jets and B-hadrons at NLO QCD*, Eur. Phys. J. **C76** (2016) no. 11, 636, arXiv:1603.03445 [hep-ph].

[624] S. Frixione and A. Mitov, *Determination of the top quark mass from leptonic observables*, JHEP **09** (2014) 012, arXiv:1407.2763 [hep-ph].

[625] CMS Collaboration, A. M. Sirunyan et al., *Measurement of the top quark mass in the dileptonic $t\bar{t}$ decay channel using the mass observables $M_{b\ell}$, M_{T2}, and $M_{b\ell\nu}$ in pp collisions at $\sqrt{s} = 8$ TeV*, Phys. Rev. **D96** (2017) no. 3, 032002, arXiv:1704.06142 [hep-ex].

[626] C. G. Lester and D. J. Summers, *Measuring masses of semiinvisibly decaying particles pair produced at hadron colliders*, Phys. Lett. **B463** (1999) 99–103, arXiv:hep-ph/9906349 [hep-ph].

[627] A. J. Barr, B. Gripaios, and C. G. Lester, *Transverse masses and kinematic constraints: from the boundary to the crease*, JHEP **11** (2009) 096, arXiv:0908.3779 [hep-ph].

[628] CMS Collaboration, C. Collaboration, *Determination of the normalised invariant mass distribution of $\mathrm{t\bar{t}}$+jet and extraction of the top quark mass*, .

[629] CMS Collaboration, C. Collaboration, *Measurement of the top-quark mass from the b jet energy spectrum*, .

[630] ATLAS Collaboration, G. Aad et al., *Determination of the top-quark pole mass using $t\bar{t}$ + 1-jet events collected with the ATLAS experiment in 7 TeV pp collisions*, JHEP **10** (2015) 121, arXiv:1507.01769 [hep-ex].

[631] ATLAS Collaboration, M. Aaboud et al., *Measurement of lepton differential distributions and the top quark mass in $t\bar{t}$ production in pp collisions at $\sqrt{s} = 8$ TeV with the ATLAS detector*, Eur. Phys. J. **C77** (2017) no. 11, 804, arXiv:1709.09407 [hep-ex].

[632] P. Nason, *The Top Mass in Hadronic Collisions*, in *From My Vast Repertoire ...: Guido Altarelli's Legacy*, A. Levy, S. Forte, and G. Ridolfi, eds., pp. 123–151. 2019. arXiv:1712.02796 [hep-ph].

[633] A. H. Hoang and I. W. Stewart, *Top Mass Measurements from Jets and the Tevatron Top-Quark Mass*, Nucl. Phys. Proc. Suppl. **185** (2008) 220–226, arXiv:0808.0222 [hep-ph].

[634] Gfitter Group Collaboration, M. Baak, J. Cúth, J. Haller, A. Hoecker, R. Kogler, K. Mönig, M. Schott, and J. Stelzer, *The global electroweak fit at NNLO and prospects for the LHC and ILC*, Eur. Phys. J. **C74** (2014) 3046, arXiv:1407.3792 [hep-ph].

[635] G. Degrassi, S. Di Vita, J. Elias-Miro, J. R. Espinosa, G. F. Giudice, G. Isidori, and A. Strumia, *Higgs mass and vacuum stability in the Standard Model at NNLO*, JHEP **08** (2012) 098, arXiv:1205.6497 [hep-ph].

[636] D. Buttazzo, G. Degrassi, P. P. Giardino, G. F. Giudice, F. Sala, A. Salvio, and A. Strumia, *Investigating the near-criticality of the Higgs boson*, JHEP **12** (2013) 089, arXiv:1307.3536 [hep-ph].

[637] A. Andreassen, W. Frost, and M. D. Schwartz, *Scale Invariant Instantons and the Complete Lifetime of the Standard Model*, Phys. Rev. **D97** (2018) no. 5, 056006, arXiv:1707.08124 [hep-ph].

[638] I. I. Y. Bigi, M. A. Shifman, N. G. Uraltsev, and A. I. Vainshtein, *The Pole mass of the heavy quark. Perturbation theory and beyond*, Phys. Rev. **D50** (1994) 2234–2246, arXiv:hep-ph/9402360 [hep-ph].

[639] M. Beneke and V. M. Braun, *Heavy quark effective theory beyond perturbation theory: Renormalons, the pole mass and the residual mass term*, Nucl. Phys. **B426** (1994) 301–343, arXiv:hep-ph/9402364 [hep-ph].

[640] M. Beneke, P. Marquard, P. Nason, and M. Steinhauser, *On the ultimate uncertainty of the top quark pole mass*, Phys. Lett. **B775** (2017) 63–70, arXiv:1605.03609 [hep-ph].

[641] A. H. Hoang, C. Lepenik, and M. Preisser, *On the Light Massive Flavor Dependence of the Large Order Asymptotic Behavior and the Ambiguity of the Pole Mass*, JHEP **09** (2017) 099, arXiv:1706.08526 [hep-ph].

[642] A. Pineda, *Determination of the bottom quark mass from the Upsilon(1S) system*, JHEP **06** (2001) 022, arXiv:hep-ph/0105008 [hep-ph].

[643] G. S. Bali, C. Bauer, A. Pineda, and C. Torrero, *Perturbative expansion of the energy of static sources at large orders in four-dimensional SU(3) gauge theory*, Phys. Rev. **D87** (2013) 094517, arXiv:1303.3279 [hep-lat].

[644] A. H. Hoang, *The Top Mass: Interpretation and Theoretical Uncertainties*, in *Proceedings, 7th International Workshop on Top Quark Physics (TOP2014): Cannes, France, September 28-October 3, 2014*. 2014. arXiv:1412.3649 [hep-ph].

[645] M. Butenschoen, B. Dehnadi, A. H. Hoang, V. Mateu, M. Preisser, and I. W. Stewart, *Top Quark Mass Calibration for Monte Carlo Event Generators*, Phys. Rev. Lett. **117** (2016) no. 23, 232001, arXiv:1608.01318 [hep-ph].

[646] A. H. Hoang, S. Plätzer, and D. Samitz, *On the Cutoff Dependence of the Quark Mass Parameter in Angular Ordered Parton Showers*, JHEP **10** (2018) 200, arXiv:1807.06617 [hep-ph].

[647] A. H. Hoang, A. Jain, C. Lepenik, V. Mateu, M. Preisser, I. Scimemi, and I. W. Stewart, *The MSR mass and the $\mathcal{O}\left(\Lambda_{\rm QCD}\right)$ renormalon sum rule*, JHEP **04** (2018) 003, arXiv:1704.01580 [hep-ph].

[648] S. Ferrario Ravasio, P. Nason, and C. Oleari, *All-orders behaviour and renormalons in top-mass observables*, arXiv:1810.10931 [hep-ph].

[649] S. Argyropoulos and T. Sjöstrand, *Effects of color reconnection on $t\bar{t}$ final states at the LHC*, JHEP **11** (2014) 043, arXiv:1407.6653 [hep-ph].

[650] J. R. Christiansen and P. Z. Skands, *String Formation Beyond Leading Colour*, JHEP **08** (2015) 003, arXiv:1505.01681 [hep-ph].

[651] S. Ferrario Ravasio, T. Ježo, P. Nason, and C. Oleari, *A theoretical study of top-mass measurements at the LHC using NLO+PS generators of increasing accuracy*, Eur. Phys. J. **C78** (2018) no. 6, 458, arXiv:1801.03944 [hep-ph].

[652] G. Corcella, R. Franceschini, and D. Kim, *Fragmentation Uncertainties in Hadronic Observables for Top-quark Mass Measurements*, Nucl. Phys. **B929** (2018) 485–526, arXiv:1712.05801 [hep-ph].

[653] A. Andreassen and M. D. Schwartz, *Reducing the Top Quark Mass Uncertainty with Jet Grooming*, JHEP **10** (2017) 151, arXiv:1705.07135 [hep-ph].

[654] S. Kawabata and H. Yokoya, *Top-quark mass from the diphoton mass spectrum*, Eur. Phys. J. **C77** (2017) no. 5, 323, arXiv:1607.00990 [hep-ph].

[655] CMS Collaboration, *ECFA 2016: Prospects for selected standard model measurements with the CMS experiment at the High-Luminosity LHC*, CMS PAS-FTR-16-006, 2017. https://cds.cern.ch/record/2262606.

[656] ATLAS Collaboration, *Projection of the top quark mass measurement accuracy using $J/\psi \to \mu^+\mu^-$ in $t\bar{t}$ events in proton-proton collisions with 3000 fb^{-1} at the HL-LHC*, ANA-TOPQ-2018-33-PUB, 2018. https://cds.cern.ch/record/2628125.

[657] ATLAS Collaboration, *Measurement of the top quark mass in the $t\bar{t} \to$lepton+jets channel from $\sqrt{s} = 8$TeV ATLAS data and combination with previous results*, subm. Eur. Phys. J. C , arXiv:1810.01772 [hep-ex].

[658] *Recommendations on systematic uncertainties for HL-LHC*, https://twiki.cern.ch/twiki/bin/view/LHCPhysics/HLHELHCCommonSystematics.

[659] CMS Collaboration, C. Collaboration, *Study of the underlying event, b-quark fragmentation and hadronization properties in tbart events*, .

[660] CMS Collaboration, C. Collaboration, *Measurement of the top quark mass using the B-hadron lifetime technique*, .

[661] CMS Collaboration, C. Collaboration, *Underlying event measurement with ttbar+X events with p-p collision data at sqrt(s)=13 TeV*, .

[662] ATLAS Collaboration, *Reconstruction of J/ψ mesons in $t\bar{t}$ final states in proton–proton collisions at $\sqrt{s} = 8$ TeV with the ATLAS detector*, ATLAS-CONF-2015-040, 2015. https://cds.cern.ch/record/2046216.

[663] LHCb collaboration, *Physics case for an LHCb Upgrade II — Opportunities in flavour physics, and beyond, in the HL-LHC era*, arXiv:1808.08865 [hep-ex].

[664] P. F. Harrison and V. E. Vladimirov, *A Method to Determine $|V_{cb}|$ at the Weak Scale in Top Decays at the LHC*, arXiv:1810.09424 [hep-ph].

[665] Tanabashi, M. et al. (Particle Data Group), *Review of Particle Physics*, Phys. Rev. **D98** (2018) no. 3, 030001.

[666] T. P. Cheng, E. Eichten, and L.-F. Li, *Higgs Phenomena in Asymptotically Free Gauge Theories*, Phys. Rev. **D9** (1974) 2259.

[667] M. E. Machacek and M. T. Vaughn, *Two Loop Renormalization Group Equations in a General Quantum Field Theory. 2. Yukawa Couplings*, Nucl. Phys. **B236** (1984) 221–232.

[668] C. Balzereit, T. Mannel, and B. Plumper, *The Renormalization group evolution of the CKM matrix*, Eur. Phys. J. **C9** (1999) 197–211, arXiv:hep-ph/9810350 [hep-ph].

[669] ATLAS Collaboration, *Optimisation of the ATLAS b-tagging performance for the 2016 LHC Run*, ATL-PHYS-PUB-2016-012, CERN, 2016.

[670] ATLAS Collaboration, M. Aaboud et al., *Measurements of b-jet tagging efficiency with the ATLAS detector using $t\bar{t}$ events at $\sqrt{s} = 13$ TeV*, JHEP **08** (2018) 089, arXiv:1805.01845 [hep-ex].

[671] ATLAS Collaboration, *Measurement of b-tagging Efficiency of c-jets in $t\bar{t}$ Events Using a Likelihood Approach with the ATLAS Detector*, ATLAS-CONF-2018-001, CERN, 2018.

[672] ATLAS Collaboration, *Calibration of light-flavour jet b-tagging rates on ATLAS proton-proton collision data at $\sqrt{s} = 13$ TeV*, ATLAS-CONF-2018-006, CERN, 2018.

[673] ATLAS Collaboration, M. Aaboud et al., *Search for the Decay of the Higgs Boson to Charm Quarks with the ATLAS Experiment*, Phys. Rev. Lett. **120** (2018) no. 21, 211802, arXiv:1802.04329 [hep-ex].

[674] CMS Collaboration, A. M. Sirunyan et al., *Identification of heavy-flavour jets with the CMS detector in pp collisions at 13 TeV*, JINST **13** (2018) no. 05, P05011, arXiv:1712.07158 [physics.ins-det].

[675] S. L. Glashow, J. Iliopoulos, and L. Maiani, *Weak Interactions with Lepton-Hadron Symmetry*, Phys. Rev. D **2** (Oct, 1970) 1285–1292. https://link.aps.org/doi/10.1103/PhysRevD.2.1285.

[676] G. Eilam, J. L. Hewett, and A. Soni, *Rare decays of the top quark in the standard and two-Higgs-doublet models*, Phys. Rev. D **44** (Sep, 1991) 1473–1484. https://link.aps.org/doi/10.1103/PhysRevD.44.1473.

[677] B. Mele, S. Petrarca, and A. Soddu, *A New evaluation of the t —> cH decay width in the standard model*, Phys. Lett. **B435** (1998) 401–406, arXiv:hep-ph/9805498 [hep-ph].

[678] J. A. Aguilar-Saavedra, *Top flavor-changing neutral interactions: Theoretical expectations and experimental detection*, Acta Phys. Polon. **B35** (2004) 2695–2710, arXiv:hep-ph/0409342 [hep-ph].

[679] F. Larios, R. Martinez, and M. A. Perez, *New physics effects in the flavor-changing neutral couplings of the top quark*, Int. J. Mod. Phys. **A21** (2006) 3473–3494, arXiv:hep-ph/0605003 [hep-ph].

[680] Top Quark Working Group Collaboration, K. Agashe et al., *Working Group Report: Top Quark*, in *Proceedings, 2013 Community Summer Study on the Future of U.S. Particle Physics: Snowmass on the Mississippi (CSS2013): Minneapolis, MN, USA, July 29-August 6, 2013*. 2013. arXiv:1311.2028 [hep-ph]. http://www.slac.stanford.edu/econf/C1307292/docs/Top-21.pdf.

[681] M. L. Mangano, M. Moretti, F. Piccinini, and M. Treccani, *Matching matrix elements and shower evolution for top-quark production in hadronic collisions*, JHEP **01** (2007) 013, arXiv:hep-ph/0611129 [hep-ph].

[682] C. Degrande, F. Maltoni, J. Wang, and C. Zhang, *Automatic computations at next-to-leading order in QCD for top-quark flavor-changing neutral processes*, Phys. Rev. **D91** (2015) 034024, arXiv:1412.5594 [hep-ph].

[683] G. Durieux, F. Maltoni, and C. Zhang, *Global approach to top-quark flavor-changing interactions*, Phys. Rev. **D91** (2015) no. 7, 074017, arXiv:1412.7166 [hep-ph].

[684] R. Coimbra, A. Onofre, R. Santos, and M. Won, *MEtop - a generator for single top production via FCNC interactions*, Eur. Phys. J. **C72** (2012) 2222, arXiv:1207.7026 [hep-ph].

[685] CompHEP Collaboration, E. Boos, V. Bunichev, M. Dubinin, L. Dudko, V. Ilyin, A. Kryukov, V. Edneral, V. Savrin, A. Semenov, and A. Sherstnev, *CompHEP 4.4: Automatic computations from Lagrangians to events*, Nucl. Instrum. Meth. **A534** (2004) 250–259, arXiv:hep-ph/0403113 [hep-ph].

[686] J. A. Aguilar-Saavedra, *Zt, gamma t and t production at hadron colliders via strong flavour-changing neutral couplings*, Nucl. Phys. **B837** (2010) 122–136, arXiv:1003.3173 [hep-ph].

[687] ATLAS Collaboration, G. Aad et al., *Search for single top-quark production via flavour-changing neutral currents at 8 TeV with the ATLAS detector*, Eur. Phys. J. **C76** (2016) no. 2, 55, arXiv:1509.00294 [hep-ex].

[688] CMS Collaboration, V. Khachatryan et al., *Search for anomalous Wtb couplings and flavour-changing neutral currents in t-channel single top quark production in pp collisions at $\sqrt{s} = 7$ and 8 TeV*, JHEP **02** (2017) 028, arXiv:1610.03545 [hep-ex].

[689] CMS Collaboration, C. Collaboration, *Prospects for the search for gluon-mediated FCNC in top quark production with the CMS Phase-2 detector at the HL-LHC*, .

[690] CMS Collaboration, V. Khachatryan et al., *Search for Anomalous Single Top Quark Production in Association with a Photon in pp Collisions at $\sqrt{s} = 8$ TeV*, JHEP **04** (2016) 035, arXiv:1511.03951 [hep-ex].

[691] ATLAS Collaboration, M. Aaboud et al., *Search for top quark decays $t \to qH$, with $H \to \gamma\gamma$, in $\sqrt{s} = 13$ TeV pp collisions using the ATLAS detector*, JHEP **10** (2017) 129, arXiv:1707.01404 [hep-ex].

[692] ATLAS Collaboration, M. Aaboud et al., *Search for flavor-changing neutral currents in top quark decays $t \to Hc$ and $t \to Hu$ in multilepton final states in proton-proton collisions at $\sqrt{s} = 13$ TeV with the ATLAS detector*, Phys. Rev. **D98** (2018) no. 3, 032002, arXiv:1805.03483 [hep-ex].

[693] CMS Collaboration, A. M. Sirunyan et al., *Search for the flavor-changing neutral current*

interactions of the top quark and the Higgs boson which decays into a pair of b quarks at $\sqrt{s} =$ *13 TeV*, JHEP **06** (2018) 102, arXiv:1712.02399 [hep-ex].

[694] ATLAS Collaboration, *Expected sensitivity of ATLAS to FCNC top quark decays* $t \to Zu$ *and* $t \to Hq$ *at the High Luminosity LHC*, ATL-PHYS-PUB-2016-019, CERN, Geneva, Aug, 2016. https://cds.cern.ch/record/2209126.

[695] *Sensitivity of ATLAS at HL-LHC to flavour changing neutral currents in top quark decays* $t \to cH$*, with* $H \to \gamma\gamma$, ATL-PHYS-PUB-2013-012, CERN, Geneva, Sep, 2013. http://cds.cern.ch/record/1604506.

[696] J. A. Aguilar-Saavedra, J. Carvalho, N. F. Castro, F. Veloso, and A. Onofre, *Probing anomalous Wtb couplings in top pair decays*, Eur. Phys. J. **C50** (2007) 519–533, arXiv:hep-ph/0605190 [hep-ph].

[697] J. A. Aguilar-Saavedra, *Single top quark production at LHC with anomalous Wtb couplings*, Nucl. Phys. **B804** (2008) 160–192, arXiv:0803.3810 [hep-ph].

[698] J. A. Aguilar-Saavedra and S. Amor Dos Santos, *New directions for top quark polarization in the* t*-channel process*, Phys. Rev. **D89** (2014) no. 11, 114009, arXiv:1404.1585 [hep-ph].

[699] A. Prasath V, R. M. Godbole, and S. D. Rindani, *Longitudinal top polarisation measurement and anomalous* Wtb *coupling*, Eur. Phys. J. **C75** (2015) no. 9, 402, arXiv:1405.1264 [hep-ph].

[700] A. Jueid, *Probing anomalous* Wtb *couplings at the LHC in single* t*-channel top quark production*, Phys. Rev. **D98** (2018) no. 5, 053006, arXiv:1805.07763 [hep-ph].

[701] R. Röntsch and M. Schulze, *Constraining couplings of top quarks to the Z boson in* $t\bar{t}$ *+ Z production at the LHC*, JHEP **07** (2014) 091, arXiv:1404.1005 [hep-ph]. [Erratum: JHEP09,132(2015)].

[702] R. Röntsch and M. Schulze, *Probing top-Z dipole moments at the LHC and ILC*, JHEP **08** (2015) 044, arXiv:1501.05939 [hep-ph].

[703] CDF, D0 Collaboration, T. A. Aaltonen et al., *Tevatron Combination of Single-Top-Quark Cross Sections and Determination of the Magnitude of the Cabibbo-Kobayashi-Maskawa Matrix Element* $\mathbf{V_{tb}}$, Phys. Rev. Lett. **115** (2015) no. 15, 152003, arXiv:1503.05027 [hep-ex].

[704] CDF, D0 Collaboration, T. A. Aaltonen et al., *Observation of s-channel production of single top quarks at the Tevatron*, Phys. Rev. Lett. **112** (2014) 231803, arXiv:1402.5126 [hep-ex].

[705] ATLAS Collaboration, M. Aaboud et al., *Fiducial, total and differential cross-section measurements of* t*-channel single top-quark production in* pp *collisions at 8 TeV using data collected by the ATLAS detector*, Eur. Phys. J. **C77** (2017) no. 8, 531, arXiv:1702.02859 [hep-ex].

[706] ATLAS Collaboration, G. Aad et al., *Evidence for single top-quark production in the* s*-channel in proton-proton collisions at* $\sqrt{s}$ *=8 TeV with the ATLAS detector using the Matrix Element Method*, Phys. Lett. **B756** (2016) 228–246, arXiv:1511.05980 [hep-ex].

[707] CMS Collaboration, S. Chatrchyan et al., *Measurement of the single-top-quark* t*-channel cross section in* pp *collisions at* $\sqrt{s} = 7$ *TeV*, JHEP **12** (2012) 035, arXiv:1209.4533 [hep-ex].

[708] CMS Collaboration, S. Chatrchyan et al., *Evidence for associated production of a single top quark and W boson in* pp *collisions at* $\sqrt{s}$ *= 7 TeV*, Phys. Rev. Lett. **110** (2013) 022003, arXiv:1209.3489 [hep-ex].

[709] CMS Collaboration, V. Khachatryan et al., *Search for s channel single top quark production in* pp *collisions at* $\sqrt{s} = 7$ *and 8 TeV*, JHEP **09** (2016) 027, arXiv:1603.02555 [hep-ex].

[710] CDF, D0 Collaboration, T. Aaltonen et al., *Combination of CDF and D0 measurements of the* W *boson helicity in top quark decays*, Phys. Rev. **D85** (2012) 071106, arXiv:1202.5272 [hep-ex].

[711] ATLAS Collaboration, M. Aaboud et al., *Measurement of the W boson polarisation in $t\bar{t}$ events from pp collisions at $\sqrt{s}$ = 8 TeV in the lepton + jets channel with ATLAS*, Eur. Phys. J. **C77** (2017) no. 4, 264, arXiv:1612.02577 [hep-ex].

[712] ATLAS Collaboration, M. Aaboud et al., *Analysis of the Wtb vertex from the measurement of triple-differential angular decay rates of single top quarks produced in the t-channel at $\sqrt{s}$ = 8 TeV with the ATLAS detector*, JHEP **12** (2017) 017, arXiv:1707.05393 [hep-ex].

[713] W. Hollik, J. I. Illana, S. Rigolin, C. Schappacher, and D. Stockinger, *Top dipole form-factors and loop induced CP violation in supersymmetry*, Nucl. Phys. **B551** (1999) 3–40, arXiv:hep-ph/9812298 [hep-ph]. [Erratum: Nucl. Phys.B557,407(1999)].

[714] K. Agashe, G. Perez, and A. Soni, *Collider Signals of Top Quark Flavor Violation from a Warped Extra Dimension*, Phys. Rev. **D75** (2007) 015002, arXiv:hep-ph/0606293 [hep-ph].

[715] A. L. Kagan, G. Perez, T. Volansky, and J. Zupan, *General Minimal Flavor Violation*, Phys. Rev. **D80** (2009) 076002, arXiv:0903.1794 [hep-ph].

[716] T. Ibrahim and P. Nath, *The Chromoelectric Dipole Moment of the Top Quark in Models with Vector Like Multiplets*, Phys. Rev. **D84** (2011) 015003, arXiv:1104.3851 [hep-ph].

[717] C. Grojean, O. Matsedonskyi, and G. Panico, *Light top partners and precision physics*, JHEP **10** (2013) 160, arXiv:1306.4655 [hep-ph].

[718] F. Richard, *Can LHC observe an anomaly in $t\bar{t}Z$ production?*, arXiv:1304.3594 [hep-ph].

[719] J. Brehmer, K. Cranmer, F. Kling, and T. Plehn, *Better Higgs boson measurements through information geometry*, Phys. Rev. **D95** (2017) no. 7, 073002, arXiv:1612.05261 [hep-ph].

[720] J. Brehmer, *New Ideas for Effective Higgs Measurements*. PhD thesis, U. Heidelberg (main), 2017. http://www.thphys.uni-heidelberg.de/~plehn/includes/theses/brehmer_d.pdf.

[721] S. Frixione, E. Laenen, P. Motylinski, and B. R. Webber, *Angular correlations of lepton pairs from vector boson and top quark decays in Monte Carlo simulations*, JHEP **04** (2007) 081, arXiv:hep-ph/0702198 [HEP-PH].

[722] ATLAS Collaboration, G. Aad et al., *Measurement of the $t\bar{t}W$ and $t\bar{t}Z$ production cross sections in pp collisions at $\sqrt{s} = 8$ TeV with the ATLAS detector*, JHEP **11** (2015) 172, arXiv:1509.05276 [hep-ex].

[723] ATLAS Collaboration, M. Aaboud et al., *Measurement of the $t\bar{t}Z$ and $t\bar{t}W$ production cross sections in multilepton final states using 3.2 fb^{-1} of pp collisions at $\sqrt{s}$ = 13 TeV with the ATLAS detector*, Eur. Phys. J. **C77** (2017) no. 1, 40, arXiv:1609.01599 [hep-ex].

[724] CMS Collaboration, S. Chatrchyan et al., *Measurement of associated production of vector bosons and top quark-antiquark pairs at sqrt(s) = 7 TeV*, Phys. Rev. Lett. **110** (2013) 172002, arXiv:1303.3239 [hep-ex].

[725] CMS Collaboration, V. Khachatryan et al., *Measurement of top quark-antiquark pair production in association with a W or Z boson in pp collisions at $\sqrt{s} = 8$ TeV*, Eur. Phys. J. **C74** (2014) no. 9, 3060, arXiv:1406.7830 [hep-ex].

[726] CMS Collaboration, V. Khachatryan et al., *Observation of top quark pairs produced in association with a vector boson in pp collisions at $\sqrt{s} = 8$ TeV*, JHEP **01** (2016) 096, arXiv:1510.01131 [hep-ex].

[727] CMS Collaboration, A. M. Sirunyan et al., *Measurement of the cross section for top quark pair production in association with a W or Z boson in proton-proton collisions at $\sqrt{s} = 13$ TeV*, JHEP **08** (2018) 011, arXiv:1711.02547 [hep-ex].

[728] V. M. Budnev, I. F. Ginzburg, G. V. Meledin, and V. G. Serbo, *The Two photon particle production mechanism. Physical problems. Applications. Equivalent photon approximation*,

Phys.Rept. **15** (1975) 181–281.

[729] V. A. Khoze, A. D. Martin, and M. G. Ryskin, *Prospects for new physics observations in diffractive processes at the LHC and Tevatron*, Eur.Phys.J. **C23** (2002) 311–327, arXiv:hep-ph/0111078 [hep-ph].

[730] M. G. Albrow, T. D. Coughlin, and J. R. Forshaw, *Central Exclusive Particle Production at High Energy Hadron Colliders*, Prog.Part.Nucl.Phys. **65** (2010) 149–184, arXiv:1006.1289 [hep-ph].

[731] L. A. Harland-Lang, V. A. Khoze, M. G. Ryskin, and W. Stirling, *Central exclusive production within the Durham model: a review*, Int.J.Mod.Phys. **A29** (2014) 1430031, arXiv:1405.0018 [hep-ph].

[732] CDF Collaboration, T. Aaltonen et al., *Observation of Exclusive Dijet Production at the Fermilab Tevatron $p\bar{p}$ Collider*, Phys.Rev. **D77** (2008) 052004, arXiv:0712.0604 [hep-ex].

[733] D0 Collaboration, V. M. Abazov et al., *High mass exclusive diffractive dijet production in $\mathbf{p\bar{p}}$ collisions at $\sqrt{\mathbf{s}}$ = 1.96 TeV*, Phys.Lett. **B705** (2011) 193–199, arXiv:1009.2444 [hep-ex].

[734] L. A. Harland-Lang, *Planar radiation zeros in five-parton QCD amplitudes*, JHEP **1505** (2015) 146, arXiv:1503.06798 [hep-ph].

[735] L. A. Harland-Lang, V. A. Khoze, and M. G. Ryskin, *Exclusive physics at the LHC with SuperChic 2*, Eur. Phys. J. **C76** (2016) no. 1, 9, arXiv:1508.02718 [hep-ph].

[736] The CMS and TOTEM Collaborations, *CMS-TOTEM Precision Proton Spectrometer Technical Design Report*, CERN-LHCC-2014-021.

[737] TOTEM Collaboration, *Technical Design Report*, CERN-LHCC-2004-002; addendum CERN-LHCC-2004-020.

[738] G. Anelli et al., *The TOTEM Experiment at the CERN Large Hadron Collider*, JINST **3** (2008) S08007.

[739] TOTEM Collaboration, *TOTEM Upgrade Proposal*, CERN-LHCC-2013-009.

[740] M.G. Albrow et al., *The FP420 R&D Project: Higgs and New Physics with forward protons at the LHC*, JINST **4** (2009) T10001, arXiv:0806.0302 [hep-ex].

[741] N. Karastathis et al., *Field quality to achieve the required lifetime goals (with beam-beam)*, 7th HL-LHC Collaboration Meeting, 15.11.2017, https://indico.cern.ch/event/647714/contributions/2646093/ .

[742] CERN, *The MAD-X Program*. http://www.cern.ch/madx/ .

[743] D. Mirarchi et al., *TCL/TCTs setting scenarios for HL-LHC*, Collimation Upgrade Specification Meeting #83, 24.02.2017, https://indico.cern.ch/event/614887/ .

[744] C. J. Morningstar and M. J. Peardon, *The Glueball spectrum from an anisotropic lattice study*, Phys. Rev. **D60** (1999) 034509, arXiv:hep-lat/9901004 [hep-lat].

[745] STAR Collaboration, R. Sikora, *Recent results on Central Exclusive Production with the STAR detector at RHIC*, in *Diffraction and Low-x 2018 (Difflowx2018) Reggio Calabria, Italy, August 26-September 1, 2018*. 2018. arXiv:1811.03315 [hep-ex].

[746] CDF Collaboration, T. A. Aaltonen et al., *Measurement of central exclusive $\pi^+\pi^-$ production in $p\bar{p}$ collisions at $\sqrt{s} = 0.9$ and 1.96 TeV at CDF*, Phys. Rev. **D91** (2015) no. 9, 091101, arXiv:1502.01391 [hep-ex].

[747] CMS Collaboration, V. Khachatryan et al., *Exclusive and semi-exclusive pi+pi- production in proton-proton collisions at sqrt(s) = 7 TeV*, arXiv:1706.08310 [hep-ex].

[748] E690 Collaboration, M. A. Reyes et al., *Partial wave analysis of the centrally produced K(s) K(s) system at 800-GeV/c*, Phys. Rev. Lett. **81** (1998) 4079–4082.

[749] WA102 Collaboration, D. Barberis et al., *A Partial wave analysis of the centrally produced K+*

K- and K0(S) K0(S) systems in p p interactions at 450-GeV/c and new information on the spin of the f(J)(1710), Phys. Lett. **B453** (1999) 305–315, arXiv:hep-ex/9903042 [hep-ex].

[750] WA102 Collaboration, D. Barberis et al., *A Partial wave analysis of the centrally produced pi0 pi0 system in p p interactions at 450-GeV/c*, Phys. Lett. **B453** (1999) 325–332, arXiv:hep-ex/9903044 [hep-ex].

[751] V. Crede and C. A. Meyer, *The Experimental Status of Glueballs*, Prog. Part. Nucl. Phys. **63** (2009) 74–116, arXiv:0812.0600 [hep-ex].

[752] F. E. Close and G. A. Schuler, *Evidence that the pomeron transforms as a nonconserved vector current*, Phys. Lett. **B464** (1999) 279–285, arXiv:hep-ph/9905305 [hep-ph].

[753] P. Lebiedowicz, O. Nachtmann, and A. Szczurek, *Exclusive central diffractive production of scalar and pseudoscalar mesons tensorial vs. vectorial pomeron*, Annals Phys. **344** (2014) 301–339, arXiv:1309.3913 [hep-ph].

[754] P. Lebiedowicz, O. Nachtmann, and A. Szczurek, *Central exclusive diffractive production of $\pi^+\pi^-$ continuum, scalar and tensor resonances in pp and $p\bar{p}$ scattering within tensor pomeron approach*, Phys. Rev. **D93** (2016) no. 5, 054015, arXiv:1601.04537 [hep-ph].

[755] P. Lebiedowicz, O. Nachtmann, and A. Szczurek, *Towards a complete study of central exclusive production of K^+K^- pairs in proton-proton collisions within the tensor Pomeron approach*, Phys. Rev. **D98** (2018) 014001, arXiv:1804.04706 [hep-ph].

[756] P. Lebiedowicz, O. Nachtmann, and A. Szczurek, *Central exclusive diffractive production of $p\bar{p}$ pairs in proton-proton collisions at high energies*, Phys. Rev. **D97** (2018) no. 9, 094027, arXiv:1801.03902 [hep-ph].

[757] L. A. Harland-Lang, V. A. Khoze, and M. G. Ryskin, *Modelling exclusive meson pair production at hadron colliders*, Eur. Phys. J. **C74** (2014) 2848, arXiv:1312.4553 [hep-ph].

[758] L. A. Harland-Lang, V. A. Khoze, M. G. Ryskin, and W. J. Stirling, *Central exclusive meson pair production in the perturbative regime at hadron colliders*, Eur. Phys. J. **C71** (2011) 1714, arXiv:1105.1626 [hep-ph].

[759] L. A. Harland-Lang, V. A. Khoze, and M. G. Ryskin, SuperChic2*: a New Monte Carlo for Central Exclusive Production*, Acta Phys. Polon. Supp. **8** (2015) 751–756.